

School of Earth and Planetary Sciences

**Nanoscale geochemistry and geochronology of xenotime: application to
Earth sciences**

Cilva Joseph

0000-0002-2555-2536

**This thesis is presented for the Degree of
Doctor of Philosophy
of
Curtin University**


November 2023

Declaration

To the best of my knowledge and belief, this thesis contains no material previously published by any other person except where due acknowledgement has been made.

This thesis contains no material which has been accepted for the award of any other degree or diploma in any university.

Cilva Joseph

Signature: 

Date: 28-11-2023

Dedication

I dedicate this thesis to my dear parents, Achachan and Ammachi.

Abstract

Geochronology is a fundamental field of geology; it is the science of quantifying time. Geochronology is of utmost importance to understand the evolution of our universe and geological processes that shaped our planet Earth. The quantification of time for geological processes is primarily done by measuring parent and daughter isotopes (absolute dating) stored in specific mineral reservoirs, called geochronometers. In nature geological processes such as metamorphism, fluid activity, and deformation can affect the isotope system and be recorded in the minerals as a disturbance. All these processes can form complex textures at different length scales. Conventional analytical techniques do not always have the spatial resolution to deconvolve these complicated textures and the behaviour of elements in minerals. The use of advanced analytical techniques with near-absolute spatial resolution, such as atom probe tomography (APT) and correlative microscopy techniques, represents a step-change in mineral geochemistry. Nanoscale data provide complimentary information to lower spatial resolution, high-precision analytical techniques and combined use of these techniques helps in comprehending the mineral systems and changing the face of modern geochronology.

Previous studies on geochronometers using APT revealed nanoscale heterogeneities and found many mineralogical processes that affect the trace element distribution and redistribution of radiogenic isotopes in them. However, complex intrinsic properties of minerals, such as radiation damage and convoluted geological histories, hinder our understanding of mineralogical processes responsible for nanoscale heterogeneities. This PhD project focuses on the mineral xenotime from different geological settings and applies a multiscale analytical approach in order to unravel these mineralogical processes. Xenotime is a widespread accessory mineral in low to high-grade geological settings and is a commonly used geochronometer to date igneous, metamorphic, and hydrothermal processes.

Chapter one focuses on the optimisation of xenotime analysis using atom probe tomography (APT) in order to acquire quality data and develop xenotime nanogeochronology method. For this purpose, four xenotime standards (BS-1, MG-1, xtc and Y1) were investigated with different instrumental parameters to find the optimum working conditions for data yield, data quality and nanogeochronology. Several protocols were established with a fractionation correction method for U-Pb dating and two background correction methods for Pb-Pb systematics. Xenotime is the first geochronometer where both U-Pb and Pb-Pb isotope information can be extracted for the same nanoscale volume ($< 0.008 \mu\text{m}^3$) by APT.

Chapter three undertakes combined microscale imaging, geochronology, and nanoscale analysis of a fluid-altered xenotime sample from a pegmatite dyke of the Central Gneiss Belt of Grenville Province, Canada. Textural domains in the grain indicate fluid-assisted dissolution reprecipitation process, however no U-Pb disturbance can be attributed to fluid resetting from Sensitive high-resolution ion microprobe (SHRIMP) analysis. Nanoscale analysis of a domain beyond the fluid-related textures reveals nanoscale apatite inclusions enriched with radiogenic Pb. APT analysis also reveals a dislocation enriched in fluid mobile elements such as Cl, Li, Na, and Ca, evidence for fluid activity beyond the typical dissolution-reprecipitation texture. The apatite inclusions are proposed to form due to fluid activity around ~ 150 Ma years after crystallisation as determined from U-Pb nanogeochronology. This study shows that fluid activity in xenotime can be pervasive and forms nanoscale Pb* rich domains. The findings explain the resilience of xenotime in fluid active settings by trapping Pb* in apatite inclusions.

Chapter four examines the controls of the formation of apatite inclusions in xenotime. Previous studies indicate that these Ca-Pb* apatite inclusions are a common occurrence in phosphates. The samples used for this project were pegmatite xenotime grain Y1, Western Australia and metamorphic xenotime samples collected from different metamorphic grades of a contact aureole, Fanad, Ireland. Nanoscale analysis of the samples showed the presence of apatite inclusions (Ca-Pb*) in pegmatite samples and no heterogeneities in terms of Ca and Pb distribution in metamorphic samples. Combined micro and nanoscale investigations suggest that in xenotime, Ca and Pb* behaviour is tightly linked, and Ca concentration influences apatite formation. However, high-temperature metamorphism is not a major factor influencing the exsolution of nanoscale apatite inclusions. This is different from other geochronometers where Pb* nanoscale heterogeneities are attributed to high-temperature metamorphism. This study shows that in xenotime, composition and fluid alteration processes are the main drivers of Pb* redistribution.

Chapter five presents a comprehensive micro to nanoscale investigation of the U-Pb system in shock-deformed xenotime and explores the potential of xenotime as an impact geochronometer. Samples used in this study are sourced from Vredefort (South Africa), Santa Fe (USA) and Araguainha (Brazil). Electron back scatter diffraction (EBSD) analysis of the samples showed a variety of microstructures, including shock diagnostic {112} twins, and other microstructures such as planar deformation bands (PDB), planar fractures (PF), low angle boundaries (LAB), crystallographic misorientation and neoblastic texture. Xenotime grains with neoblastic texture showed U-Pb disturbance, and a correlation between resetting and degree of recrystallisation is apparent. The results indicate that neoblastic texture is shock-

induced and yielded impact age from xenotime for the first time from the Araguinha impact structure in Brazil. APT results from neoblasts suggested grain boundary migration for the formation of neoblasts in xenotime and the mobility of Pb.

The integrated outcome of this PhD thesis primarily helped to understand the mineral system xenotime in detail, the processes controlling its geochemical and geochronological behaviour in different geological settings using a multi-scale approach. The xenotime nanogeochronology method developed can be used to constrain ages from any small textural domains. Furthermore, this project presents a foundational study on shock metamorphism on xenotime, documenting micro to nanoscale observations, which helps in future studies on xenotime and also other geochronometers.

Acknowledgements

The PhD journey must be one of the most extraordinary experiences of my life. There were so many first times, travelling alone internationally, living alone in a different country, conversing in a different language daily, learning new techniques, and the list goes on. None of this would have been possible without the support of so many people to whom I wish to extend my sincere gratitude. First, I thank my Lord God for all the blessings showered over me, especially during these PhD days.

I am eternally grateful to my principal supervisor, Dr Denis Fougerouse, for choosing me for this position and guiding me in every point of this venture. Thank you for your patience, belief, understanding, teaching, weekly meetings, quickest replies, and invitations to your family. My associate supervisor Prof. Steven M. Reddy, for his constant encouragement, giving confidence before any presentation and constructive comments on my drafts. Thank you, Denis and Steve, for teaching me how to think and be a scientist.

I wish to thank all my collaborators who contributed to this project. Firstly, our geoscience atom probe group in Curtin for scientific and mental support - Will for teaching me the complicated instrument ever and for the constant support through every FIB session. David, for unravelling the atom probe world, answering every stupid question, and coming to my help in the lab for every mistake I make. Tommaso, thank you for your mental support as a friend and for helping me in my first year with FIB and atom probe analysis and scientific discussions. Xiao, for helping me during the FIB sessions, especially TEM sample preparations. Rick for his help with my first project and as a friend.

Hugo, for always having the door open and helping me with all SHRIMP analyses. Aaron, for providing samples to the most exciting project of this PhD and teaching me the basics of amazing EBSD. Steven Denyszyn (Memorial University of Newfoundland), Aaron Dodd (TEM), Ian Schipper (EPMA – University of Wellington), and Allen Kennedy (SHRIMP – John de Laeter Centre, Curtin) all contributed with instrumental and writing inputs in different projects of this PhD. I would also like to thank the Microscopy and Microanalysis Facility staff for all the support throughout this PhD.

I can't thank my mentors enough, Tomson Sir, Nilanjana Mam, and Anand Sir, for their constant inspiration and motivation to pursue this PhD and for giving advice for my academic and personal growth. I would also like to remember my dear teachers during my bachelor's and master's courses for introducing me to the amazing world of geoscience and research,

especially Anto Sir, Suraj Sir, Dilip Sir, Anish Sir, Praveen Sir, Krishnakumar Sir, Priya Miss, Ajith Sir, and Ajay Sir.

My dear friends here in Perth and back in India have always been very supportive throughout the process. My dear fellow colleagues, who made this journey smooth, especially during the pandemic when we were separated from our families for more than two and a half years. We became a family. Isabel – thank you for taking care of me in the emergency room for the whole night without even sleeping a wink, thank you for all the fun trips together, especially Kalbarri, coffee breaks, and you are the purest soul I have seen. Raiza and Jojo – thank you for all the morning coffees, movie nights, cooking nights, outside uni writing sessions, long walks and more. Thank you for the unbeatable support and love. Taryn - Thank you for all the motivating words when I felt the lowest in my PhD life, all the random hallway meetings and long conversations. David – for being the fun friend, all the food you bought for me, and the productive evening times we spent together. Other respectable members of my “office of world-class research”, Tony – for making me cakes, Riley, and Vickie – for the puzzling times together, Sean – for being the resource person of our office. Thanks to Kathy, Han, Jonas, Julian, and Max. Thanks to my friends in India who gave me the mental support and checked on me every time. Big thanks to my guardian in Perth Renjini chechi for the immeasurable support during the course of my PhD.

Finally, I want to thank my family – Achachan, Ammachi, Stephy chechi, Chris chechi, Monu, Siju chettan and Richie chettan. Achachan for his endless support, belief, prayers and sacrifices which made me stand here. Ammachi for hearing me all the time, for the never-ending conversations over phone when I feel alone here and for everything. Words cannot express my gratitude towards you. Stephychechi for being my second mother and guide, Chris chechi for the utmost care and Monu for being the mature younger but older sister for me. Thanks, and love to my dear husband and Pappa and Amma. Allen, my Achayan – thanks for being there for me from the very first day of this PhD journey starting from pushing me to apply for this position when I doubted myself, helping me to get processed through all formalities, overcoming my fears, all day long practice sessions for my presentations, editing my thesis and being the best in everything.

Thank you.

List of publications

Published

- Joseph C., Fougrouse D., Saxey D. W., Verberne R., Reddy S. M. and Rickard W. D. A. (2021) Xenotime at the Nanoscale: U-Pb Geochronology and Optimisation of Analyses by Atom Probe Tomography. *Geostandards and Geoanalytical Research*. 45, 443–456.
- Joseph C., Fougrouse D., Reddy S. M., Olierook H. K. H., Tacchetto T., Kennedy A., Saxey D. W., Rickard W. D. A., Denyszyn S. and Dodd A. (2023) Radiogenic Pb in xenotime trapped in nanoscale inclusions of apatite during fluid alteration. *Chemical Geology*, 121444.

In preparation for submission

- Joseph C., Fougrouse D., Cavosie A. J., Olierook H. K. H., Reddy S. M., Quintero R. R., Kennedy A., Saxey D. W., Rickard W. D. A., Towards a new impact geochronometer: Deformation microstructures and U-Pb systematics of shocked xenotime.
- Joseph C., Fougrouse D., Reddy S. M., Olierook H. K. H., Schipper C. I., Saxey D. W., Rickard W. D. A. Fluid alteration and Ca composition control the formation of nanoscale Ca-Pb clusters in xenotime, not high-temperature metamorphism.

Other relevant co-authored manuscript

- Olierook H. K. H., Crook K., Sinclair P., Fougrouse D., Joseph C., Kirkland C. L., Kennedy A., Gao H., Evans N. J., McDonald B. J., Quintero R. R., Kumara A. S., Cameron G., Walsh B., Roberts M. P. and McInnes B. I. A. (2023) Xenotime reveals Caledonian hydrothermal overprint on Neoproterozoic Cu mineralization, East Greenland. *Journal of the Geological Society of London*., jgs2022-141.

Attribution Statements

Table I. Attribution statement table for chapter 2: Xenotime at the Nanoscale: U-Pb Geochronology and Optimisation of Analyses by Atom Probe Tomography

Chapter 2	Conception and Design	Acquisition of Data and Method	Data Conditioning and Manipulation	Analysis and Statistical Method	Interpretation and Discussion
Co-Author 1 Cilva Joseph	✓	✓	✓	✓	✓
Co-Author 1 Acknowledgment: I acknowledge that these represent my contribution to the above research output, and I have approved the final version. <div style="text-align: right;">Signed:</div>					
Co-Author 2 Denis Fougrouse	✓	✓	✓	✓	✓
Co-Author 2 Acknowledgment: I acknowledge that these represent my contribution to the above research output, and I have approved the final version. <div style="text-align: right;">Signed:</div>					
Co-Author 3 David W. Saxey		✓	✓	✓	✓
Co-Author 3 Acknowledgment: I acknowledge that these represent my contribution to the above research output, and I have approved the final version. <div style="text-align: right;">Signed:</div>					
Co-Author 4 Rick Verberne			✓	✓	✓
Co-Author 4 Acknowledgment: I acknowledge that these represent my contribution to the above research output, and I have approved the final version. <div style="text-align: right;">Signed:</div>					
Co-Author 5 Steven M. Reddy	✓		✓	✓	✓
Co-Author 5 Acknowledgment: I acknowledge that these represent my contribution to the above research output, and I have approved the final version. <div style="text-align: right;">Signed:</div>					
Co-Author 6 William D.A. Rickard		✓			✓
Co-Author 6 Acknowledgment: I acknowledge that these represent my contribution to the above research output, and I have approved the final version. <div style="text-align: right;">Signed:</div>					

Table II. Attribution statement table for chapter 3: Radiogenic Pb in xenotime trapped in nanoscale inclusions of apatite during fluid alteration.

Chapter 3	Conception and Design	Acquisition of Data and Method	Data Conditioning and Manipulation	Analysis and Statistical Method	Interpretation and Discussion
Co-Author 1 Cilva Joseph	✓	✓	✓	✓	✓
Co-Author 1 Acknowledgment: I acknowledge that these represent my contribution to the above research output, and I have approved the final version. <div style="text-align: right;">Signed:</div>					
Co-Author 2 Denis Fougrouse	✓	✓	✓	✓	✓
Co-Author 2 Acknowledgment: I acknowledge that these represent my contribution to the above research output, and I have approved the final version. <div style="text-align: right;">Signed:</div>					
Co-Author 3 Steven M. Reddy			✓	✓	✓
Co-Author 3 Acknowledgment: I acknowledge that these represent my contribution to the above research output, and I have approved the final version. <div style="text-align: right;">Signed:</div>					
Co-Author 4 Hugo K. H. Olierook		✓	✓	✓	✓
Co-Author 4 Acknowledgment: I acknowledge that these represent my contribution to the above research output, and I have approved the final version. <div style="text-align: right;">Signed:</div>					
Co-Author 5 Tommaso Tacchetto			✓	✓	✓
Co-Author 5 Acknowledgment: I acknowledge that these represent my contribution to the above research output, and I have approved the final version. <div style="text-align: right;">Signed:</div>					
Co-Author 6 Allen Kennedy		✓			✓
Co-Author 6 Acknowledgment: I acknowledge that these represent my contribution to the above research output, and I have approved the final version. <div style="text-align: right;">Signed:</div>					

Co-Author 7 David W. Saxey		✓	✓	✓	
<p>Co-Author 7 Acknowledgment: I acknowledge that these represent my contribution to the above research output, and I have approved the final version.</p> <p style="text-align: right;">Signed:</p>					
Co-Author 8 William D.A. Rickard		✓			✓
<p>Co-Author 8 Acknowledgment: I acknowledge that these represent my contribution to the above research output, and I have approved the final version.</p> <p style="text-align: right;">Signed:</p>					
Co-Author 9 Steven Denyszyn			✓	✓	✓
<p>Co-Author 9 Acknowledgment: I acknowledge that these represent my contribution to the above research output, and I have approved the final version.</p> <p style="text-align: right;">Signed:</p>					
Co-Author 10 Aaron Dodd		✓	✓		
<p>Co-Author 10 Acknowledgment: I acknowledge that these represent my contribution to the above research output, and I have approved the final version.</p> <p style="text-align: right;">Signed:</p>					

Table III. Attribution statement table for chapter 4: Fluid alteration and Ca composition control the formation of nanoscale Ca-Pb clusters in xenotime, not high-temperature metamorphism.

Chapter 4	Conception and Design	Acquisition of Data and Method	Data Conditioning and Manipulation	Analysis and Statistical Method	Interpretation and Discussion
Co-Author 1 Cilva Joseph	✓	✓	✓	✓	✓
Co-Author 1 Acknowledgment: I acknowledge that these represent my contribution to the above research output, and I have approved the final version. <p style="text-align: right;">Signed:</p>					
Co-Author 2 Denis Fougrouse	✓	✓	✓	✓	✓
Co-Author 2 Acknowledgment: I acknowledge that these represent my contribution to the above research output, and I have approved the final version. <p style="text-align: right;">Signed:</p>					
Co-Author 3 Steven M. Reddy	✓		✓	✓	✓
Co-Author 3 Acknowledgment: I acknowledge that these represent my contribution to the above research output, and I have approved the final version. <p style="text-align: right;">Signed:</p>					
Co-Author 4 Hugo K. H. Olierook		✓	✓	✓	✓
Co-Author 4 Acknowledgment: I acknowledge that these represent my contribution to the above research output, and I have approved the final version. <p style="text-align: right;">Signed:</p>					
Co-Author 5 Ian Schipper		✓	✓	✓	✓
Co-Author 5 Acknowledgment: I acknowledge that these represent my contribution to the above research output, and I have approved the final version. <p style="text-align: right;">Signed:</p>					
Co-Author 6 David Saxey				✓	✓
Co-Author 6 Acknowledgment: I acknowledge that these represent my contribution to the above research output, and I have approved the final version. <p style="text-align: right;">Signed:</p>					

Co-Author 7 William M. Rickard		✓		✓	✓
Co-Author 7 Acknowledgment: I acknowledge that these represent my contribution to the above research output, and I have approved the final version. <div style="text-align: right;">Signed:</div>					

Table IV. Attribution statement table for chapter 5: Towards a new impact geochronometer: Deformation microstructures and U-Pb systematics of shocked xenotime.

Chapter 5	Conception and Design	Acquisition of Data and Method	Data Conditioning and Manipulation	Analysis and Statistical Method	Interpretation and Discussion
Co-Author 1 Cilva Joseph	✓	✓	✓	✓	✓
Co-Author 1 Acknowledgment: I acknowledge that these represent my contribution to the above research output, and I have approved the final version. <p style="text-align: right;">Signed:</p>					
Co-Author 2 Denis Fougrouse	✓	✓	✓	✓	✓
Co-Author 2 Acknowledgment: I acknowledge that these represent my contribution to the above research output, and I have approved the final version. <p style="text-align: right;">Signed:</p>					
Co-Author 3 Aaron J. Cavosie	✓	✓	✓	✓	✓
Co-Author 3 Acknowledgment: I acknowledge that these represent my contribution to the above research output, and I have approved the final version. <p style="text-align: right;">Signed:</p>					
Co-Author 4 Hugo K. H. Olierook		✓	✓	✓	✓
Co-Author 4 Acknowledgment: I acknowledge that these represent my contribution to the above research output, and I have approved the final version. <p style="text-align: right;">Signed:</p>					
Co-Author 5 Steven M. Reddy			✓	✓	✓
Co-Author 5 Acknowledgment: I acknowledge that these represent my contribution to the above research output, and I have approved the final version. <p style="text-align: right;">Signed:</p>					
Co-Author 6 Tommaso Tacchetto				✓	✓
Co-Author 6 Acknowledgment: I acknowledge that these represent my contribution to the above research output, and I have approved the final version. <p style="text-align: right;">Signed:</p>					

Co-Author 7 Raiza R. Quintero		✓		✓	✓
<p>Co-Author 7 Acknowledgment: I acknowledge that these represent my contribution to the above research output, and I have approved the final version.</p> <p style="text-align: right;">Signed:</p>					
Co-Author 8 Allen Kennedy		✓			✓
<p>Co-Author 8 Acknowledgment: I acknowledge that these represent my contribution to the above research output, and I have approved the final version.</p> <p style="text-align: right;">Signed:</p>					
Co-Author 9 David W. Saxey			✓	✓	✓
<p>Co-Author 9 Acknowledgment: I acknowledge that these represent my contribution to the above research output, and I have approved the final version.</p> <p style="text-align: right;">Signed:</p>					
Co-Author 10 William D.A. Rickard		✓	✓		
<p>Co-Author 10 Acknowledgment: I acknowledge that these represent my contribution to the above research output, and I have approved the final version.</p> <p style="text-align: right;">Signed:</p>					

Table of Contents

Declaration.....	i
Dedication.....	ii
Abstract.....	iii
Acknowledgements.....	vi
List of publications.....	viii
Attribution Statements.....	ix
List of Figures.....	xxii
List of Tables.....	xxix
List of Appendices.....	xxx
Chapter 1 : Introduction.....	1
1.1 Geochronometers at the nanoscale.....	3
1.2 Xenotime – the neglected geochronometer.....	4
1.3 New frontiers in geochronology – Atom probe tomography.....	7
1.4 Research objectives.....	8
1.5 Thesis structure.....	9
1.6 References.....	11
Chapter 2 : Xenotime at the nanoscale: U-Pb geochronology and optimisation of analyses by Atom Probe Tomography.....	18
Abstract.....	19
2.1 Introduction.....	20
2.2 Samples and methodology.....	21
2.2.1 Samples.....	21
2.2.2 FIB-SEM.....	22
2.2.3 APT.....	22
2.2.4 Isotope quantification.....	25
2.3 Results.....	26

2.3.1 Characteristics of xenotime APT analysis	26
2.3.2 Pb-Pb systematics	29
2.3.3 U-Pb systematics.....	31
2.4 Discussion	34
2.4.1 Xenotime analysis in APT	34
2.4.2 ²⁰⁷ Pb/ ²⁰⁶ Pb age.....	35
2.4.3 U-Pb age.....	36
2.5 Recommendations and conclusions	37
2.6 Acknowledgements.....	38
2.7 References.....	39
Chapter 3 : Radiogenic Pb in xenotime trapped in nanoscale inclusions of apatite during fluid alteration	47
Abstract.....	48
3.1 Introduction.....	49
3.2 Sample and geological background	50
3.3 Methods.....	51
3.3.1 Scanning electron microscopy (SEM)	51
3.3.2 Sensitive high-resolution ion micro-probe (SHRIMP).....	51
3.3.3 Focused ion beam (FIB).....	53
3.3.4 Transmission electron microscopy (TEM)	53
3.3.5 Atom probe tomography (APT).....	53
3.4 Results.....	54
3.4.1 Scanning electron microscopy	54
3.4.2 Sensitive high-resolution ion micro-probe.....	56
3.4.3 Transmission electron microscopy	56
3.4.4 Atom probe tomography	57
3.5 Discussion.....	61
3.5.1 Fluid alteration microstructures and geochronology	61

3.5.2 Nanoscale compositional heterogeneities in xenotime	63
3.5.3 Formation mechanism of apatite nanoscale inclusions.....	66
3.5.4 Summary and geochronological implications.....	68
3.6 Acknowledgments.....	69
3.7 References.....	70
Chapter 4 : Fluid alteration and Ca composition control the formation of nanoscale Ca-Pb clusters in xenotime, not high-temperature metamorphism.....	80
Abstract.....	81
4.1 Introduction.....	82
4.2 Samples and geological history	83
4.2.1 Y1 – Yinnietharra pegmatite, Gascoyne province.....	83
4.2.2 Fanad contact aureole, Ireland.	84
4.3 Methods.....	85
4.3.1 Xenotime imaging.....	85
4.3.2 Xenotime compositions	86
4.3.3 U-Pb geochronology using SHRIMP.....	86
4.3.4 Nanoscale geochemistry – sample preparation and analysis	87
4.4 Results.....	88
4.4.1 Y1 - Textural, geochemical, and geochronological characterisation.....	88
4.4.2 Fanad contact aureole - Petrological, textural, and geochemical characterisation. 90	
4.4.2.1 Sample 1606.....	90
4.4.2.2 Sample 1621.....	91
4.4.2.3 Sample 1630.....	91
4.4.2.4 Sample 1642.....	92
4.4.3 Insights from atom probe tomography analyses	95
4.4.3.1 Y1 - Gascoyne Province	95
4.4.3.2 Fanad contact aureole.	96
4.5 Discussion.....	98

4.5.1	Microscale texture and geochemistry of xenotime	98
4.5.1.1	Y1 - Gascoyne Province, Western Australia	98
4.5.1.2	Fanad contact aureole, Ireland.	98
4.5.2	Influence of composition and cooling rate in the formation of nanoscale clusters	100
4.6	Conclusion	104
4.7	Acknowledgements.....	104
4.8	References.....	105
Chapter 5 : Towards a new impact geochronometer: Deformation microstructures and U-Pb systematics of shocked xenotime.....		112
	Abstract.....	113
5.1	Introduction.....	114
5.2	Samples.....	116
5.2.1	Vredefort impact structure, South Africa.....	116
5.2.2	Santa Fe impact structure, USA.....	116
5.2.3	Araguainha impact structure, Brazil	117
5.3	Methods.....	118
5.3.1	Sample mounting	118
5.3.2	Scanning electron microscope-electron backscatter diffraction (SEM-EBSD)....	119
5.3.3	Sensitive high resolution ion microprobe (SHRIMP) and Electron micro probe analyser (EMPA)	119
5.3.4	Atom probe tomography (APT).....	120
5.4	Results.....	121
5.4.1	Microstructural characterisation of shocked xenotime.....	121
5.4.1.1	Vredefort impact structure	121
5.4.1.2	Santa Fe impact structure.....	124
5.4.1.3	Araguainha impact structure	125
5.4.2	SIMS U-Pb geochronology.....	127

5.4.3 Nanoscale characterisation.....	130
5.4.3.1 Vredefort xenotime (grain 14DG14)	131
5.4.3.2 Santa Fe xenotime (grain SFx5)	134
5.4.3.3 Araguainha xenotime (grain X3)	135
5.5 Discussion.....	136
5.5.1 Shock microstructures in xenotime.....	136
5.5.1.1 Planar fractures (PF)	137
5.5.1.2 Planar deformation bands (PDB).....	137
5.5.1.3 Deformation twins in {112}	138
5.5.1.4 Recrystallisation to neoblastic texture	138
5.5.2 SIMS U-Pb geochronology of shock microstructures in xenotime	139
5.5.2.1 Shocked twins, PDB and PF in xenotime (Vredefort and Santa Fe)	139
5.5.2.2 Neoblast formation in Araguainha – Pb mobility and age resetting.....	140
5.5.2.3 Significance of the Vredefort xenotime lower discordia intercept	141
5.5.3 Nanoscale heterogeneities in shock-deformed xenotime.....	142
5.5.3.1 Nanoscale analysis of twins and neoblasts from Vredefort and Santa Fe	142
5.5.3.2 Nanoscale analysis of neoblasts from Araguainha	143
5.6 Summary and Concluding remarks.....	146
5.7 Acknowledgements.....	147
5.8 References.....	148
Chapter 6 : Synthesis and future work.....	161
6.1 Optimisation of xenotime analysis using APT and nanogeochronology method.....	162
6.2 Pb mobility mechanisms in xenotime: insights from nanoscale analysis	163
6.2.1 Fluid activity	164
6.2.2 Phase immiscibility	165
6.2.3 Recrystallisation.....	165
6.3 Geochronometers in nanoscale: a revisit	166
6.4 Scope of future work.....	168

6.5 References.....	171
Chapter 7 : Bibliography.....	176
Appendices	206

List of Figures

- Figure 1.1 (a) Structure of REE site. (Y,HREE) cation in red, occupied in regular (Y,REE)O₈ dodecahedron provides an appropriate site for Y and the smaller, heavy REE. Modified after Engi, (2017). (b) Polyhedral projections down [100] showing xenotime structure, red – REO₈ polyhedra and blue PO₄ tetrahedra. Modified after Ni et al., (1995).4
- Figure 1.2: A schematic illustration of APT, including the alternative modes of voltage-pulsing and laser-pulsing operation. Location and timing information from the position-sensitive detector is used to reconstruct the original atomic structure in three dimensions and time of flight to identify the evaporated species.8
- Figure 2.1: (a) Atom probe mass spectra of xenotime (sample – xtc). Peaks are colour-coded by atomic/molecular species. (b) UO₂²⁺ and UO²⁺ molecular peaks used for fractionation correction. (c) Location of major U peak (UO³⁺) at the tail of YPO₃²⁺ peak.24
- Figure 2.2: (a) Atom probe mass spectrum showing Pb²⁺ peaks of reference material Y1. Shows the constant background before and after ²⁰⁶Pb²⁺ is comparable/consistent, which is illustrated in the inset. Negligible thermal peak tail influence. (b) Atom probe mass spectrum showing Pb²⁺ peaks of reference material xtc. Blue indicates the background. The figure shows the elevated background in between ²⁰⁶Pb²⁺ and ²⁰⁷Pb²⁺ peaks due to the influence of the thermal peak tail of ²⁰⁶Pb²⁺ compared with the constant background (101–102 Da). An illustration of the background correction technique is shown in the inset.26
- Figure 2.3: Three-dimensional reconstructed atom probe maps of Pb (²⁰⁶Pb + ²⁰⁷Pb + ²⁰⁸Pb), U (UO₂) and Ca of four reference materials xtc (a), Y1 (b), MG-1 (c), BS-1 (d). One sphere represents one atom. (b) Y1 shows the presence of Ca-rich clusters in the specimen. Concentration showed in atomic percentage.27
- Figure 2.4: All parameters are plotted against laser pulse energy. Specimens are colour coded. (a) ²⁰⁶Pb charge state ratio of xtc and Y1. (b) Background counts measured in ppm ns⁻¹. (c) Percentage of single hits for every analysis. (d) ThPO₃³⁺ counts per million ions.29
- Figure 2.5: ²⁰⁷Pb/²⁰⁶Pb ratios of xtc and Y1 plotted against laser pulse energy. Errors plotted in 2s. (a) Graph showing the results of ²⁰⁷Pb/²⁰⁶Pb ages of xtc and Y1 using constant

background correction. (b) $^{207}\text{Pb}/^{206}\text{Pb}$ ratios of xtc using a variable approximation method.....	31
Figure 2.6: (a) $^{206}\text{Pb}^{2+}/^{238}\text{UO}_2^{2+}$ ratio plotted against laser pulse energy. (b) $\text{UO}_2^{2+}/\text{UO}^{2+}$ ratio against laser pulse energy. Uncertainties at $2s$ are smaller than the symbols.....	33
Figure 2.7: The $\text{UO}_2^{2+}/\text{UO}^{2+}$ ratio correlated with $^{206}\text{Pb}/^{238}\text{U}$ fractionation (%) for xtc and Y1 samples. Linear regression through all data points gives an R^2 value of 0.984 and is defined by the equation $y = 12.06(\pm 0.621)x + 27.442(\pm 0.826)$. The grey band represents the 95% prediction band.	33
Figure 2.8: Weighted mean data of (a) xtc (orange) and (b) Y1 (green). The solid line represents the weighted mean age obtained from the data and the dotted lines represent the actual age of the specimens. The square band represents the uncertainties plotted ($2s$).....	37
Figure 3.1: Lithotectonic map of the Central Gneiss Belt, Grenville province, Ontario. The location of the sample studied is indicated with a star symbol. Inset showing first-order subdivisions of Grenville province in Canada. GFTZ – Grenville Front Tectonic Zone, ABT – Allocthon Boundary Thrust, CAB – Composite Arc Belt. Modified from Culshaw et al., 2016; Kerckhove, 2016).....	51
Figure 3.2: (a) Backscattered electron (BSE) image of grain z6413 showing altered and unaltered regions in xenotime. SHRIMP, TEM and APT sample locations are shown in the sample. SHRIMP spots colour code: yellow - unaltered region, Red - dark altered domains. (b) The grain shows altered mottled texture with planar features and submicron porosity. (c) Showing BSE dark domains of altered xenotime, mostly seen in the outer portions of the grain with U-Th rich inclusions precipitated in the boundary of altered and unaltered domains and larger pores ($2\text{--}3\ \mu\text{m}$). (d) Tera-Wasserburg diagram SHRIMP results with weighted mean $^{207}\text{Pb}/^{206}\text{Pb}$ age. The error bars are 2σ , with the point matches to the colour-coded of grain textural domains.....	55
Figure 3.3: (a) High Angle Annular Dark Field (HAADF) image of sample z6413 showing bright spherical domains distributed in the xenotime matrix. The location of c and d is indicated with a dashed orange area. (b) Diffraction pattern obtained from the same region in higher resolution (HR) mode showing circular rings along with the xenotime crystal diffraction pattern. (c) and (d) EDS X-ray element maps collected with the scanning transmission electron microscope (STEM).	57

Figure 3.4: (a) APT 3d reconstruction of specimens from sample z6413. Each sphere represents an atom of Ca (orange) and Pb (teal). Ca-Pb* apatite inclusions are distributed heterogeneously in the xenotime matrix. (b) close up of apatite inclusion and proximity histogram showing the concentration Ca and Pb in the cluster. Error 1σ	59
Figure 3.5: Diameter of the apatite inclusions versus Ca+Pb concentration. The composition of the smaller clusters is affected by local magnification effect during atom probe analysis leading underestimation of the composition of the clusters. Local magnification is resultant of evaporation difference between the host and the precipitate (cluster).....	59
Figure 3.6: (a) M1 specimen showing distribution of Ca, Pb, Cl, Li, and Na in the dislocation; (b) Proximity histogram of elements in the dislocation, errors are 1σ . Values of Li and Na plotted in the secondary axis.	60
Figure 3.7: APT $^{206}\text{Pb}/^{238}\text{U}$ weighted mean data of sample z6413. Green colour represents the data from whole specimen and brown represents age of the matrix, excluding the clusters. The solid line denotes the weighted mean age obtained from the data and the dotted line represent the crystallisation age determined by TIMS. The coloured bands represent the uncertainties plotted at 2σ	61
Figure 4.1: (a) Simplified regional geology of the Gascoyne Province bounded by E-W trending faults. Inset showing tectonic divisions of Western Australia. PC: Pilbara Craton, YC: Yilgarn Craton, KC: Kimberly Craton. Modified from Piechocka et al. (2017). (b) Geological map of the area around Glinsk, Fanad, County Donegal showing sample locations. Inset showing the sample location in Ireland modified after Kerrick (1987).....	85
Figure 4.2: Backscattered electron (BSE) image of grain Y1. BSE image showing BSE bright, BSE dark and BSE intermediate zones in the grain. BSE dark domains are associated with U-Th rich inclusions. SHRIMP and APT locations are marked.....	89
Figure 4.3: Tera-Wasserburg diagram plotting results from the Y1 SHRIMP data with weighted mean $^{207}\text{Pb}/^{206}\text{Pb}$ age.....	90
Figure 4.4: BSE images of representative xenotime grains from each metamorphic grade from Fanad contact aureole.	93
Figure 4.5: Graph plotting U concentration vs U/Th ratio from the samples, distinguishing xenotime from different metamorphic grades.....	94
Figure 4.6: EPMA x-ray compositional maps of grain 1642-1	94

Figure 4.7: EPMA x-ray compositional maps of grain 1642-2.95

Figure 4.8: (a) APT 3D reconstruction profile showing distributions of Ca and Pb from sample Y1. The needle contains numerous Ca-rich clusters and few Ca-Pb* rich clusters. (b) Closer look of Ca-rich clusters with proximity histogram showing Ca and Pb concentration. Error 1σ . (c) Closer look of Ca-Pb* rich cluster with proximity histogram showing Ca and Pb concentration in Pb* rich clusters.96

Figure 4.9: (a) Location of APT specimens from xenotime grain from sample 1606 corresponding to host xenotime grain. (b) APT 3D reconstruction profile showing distributions of Si, U, Ca and Pb from specimens M1 and M2. (c) and (d) Xenotime grains showing APT sample locations, sourced from contact zone. (e) APT 3D reconstruction profile showing distributions of Ca and Pb from both core and rim of the grains.....97

Figure 4.10: Box and whisker graph showing the Ca concentration of samples studied. 103

Figure 4.11: Summary diagram illustrating processes that affected the samples. (a) Crystallisation of high Ca pegmatite xenotime. Exsolution of Ca rich apatite inclusions during cooling of the crystal with minor Pb*. Later fluid alteration causing selective Pb* mobility into the previously formed apatite inclusions, forming of Ca-Pb* rich apatite inclusions. (b) Crystallisation of xenotime from garnet breakdown (xtm host) in the host metapelite. Coarsening of xenotime grains by increasing metamorphic grade and forming new xenotime rims due to contact metamorphism. Host xenotime exists as core, having low Ca concentration is affected by high-temperature metamorphism. However, no formation of apatite inclusions at this high temperature. (Colour code: orange – Ca atom, green – Pb atom)..... 104

Figure 5.1: Simplified geological maps of the three impact structures with sample locations. (a) The central uplift of the Vredefort dome, South Africa (modified after (Cavosie et al., 2010) with inset showing the location in South Africa (SA – South Africa, JB – Johannesburg, NAM – Namibia, BW – Botswana). (b) Map showing shocked rocks that define the Santa Fe impact structure (modified after Bauer et al., 1996; Montalvo et al., 2019) with inset showing the location of Santa Fe impact structure in New Mexico (NM – New Mexico). (c) Map of the Araguainha impact crater (modified after (Lana et al., 2008)) with inset showing location of Araguainha impact structure in Brazil. 118

Figure 5.2: Microstructures of Vredefort xenotime grain 14DG14. (a) Backscattered electron (BSE) image. Four orientations of planar fractures (PF1 – PF4) are visible. SHRIMP

spots and atom probe sample locations are indicated. (b) Electron backscatter diffraction (EBSD) grain orientation map (inverse pole figure, z projection [IPFz]). Deformation features are indicated, deformation twin lamellae (t) parallel to PF. Inset pole figure showing 3 sets of {112} twins (t1, t2, t3) and the host (lower-hemisphere, equal-area projection). (c) Texture component map showing low angle boundaries ($< 10^\circ$ in white color), planar deformation bands (PDB) oriented mostly parallel to the t2 twin direction, and also parallel to t1 twin direction (dark blue dashed line). The grain shows up to 12° of misorientation from the reference point (red cross left side). SHRIMP spots targeting PDB and twins are shown in red and yellow ellipses shows SHRIMP spots targeted the areas in the grain with $< 10^\circ$ of misorientation. (d) Inverse pole figure (IPFz) map showing location of atom probe sample APT 1, where the grain showing recrystallised neoblasts. (e) Inverse pole figure map showing location of atom probe sample APT 2, which targeted the segmented twin lamellae (t3). Four segments define disorientations close to, but different from, the {112} twin orientation, including $72^\circ/\langle 342 \rangle$, $68^\circ/\langle 232 \rangle$, $70^\circ/\langle 341 \rangle$, and $70^\circ/\langle 340 \rangle$; one segment records the {112} twin direction ($65^\circ/\langle 110 \rangle$). (f) Pole figures showing the twin and host relations from E. 123

Figure 5.3: Microstructures of Santa Fe xenotime grains SFx3, SFx4 and SFx5. (a), (b) and (c) Backscattered electron (BSE) images showing directions of planar fractures (indicated by arrows). SHRIMP spots are indicated, along with ages in Ma. (d), (e) and (f) Texture component maps showing relative misorientation from a reference point (red cross) with inset pole figures of (001) (lower-hemisphere, equal-area projection). (d) Grain SFx3 showing up to 5° misorientation (e) Grain SFx4 showing one {112} twin lamella and up to 5° misorientation (f) Grain SFx5 showing three sets of {112} twin lamellae (t1, t2, t3), up to 6° of misorientation, and planar deformation band (PDB). (g) Location of atom probe samples in grain SFx5 (h) Pole figure of G, recording the {112} twin and host relationship. 124

Figure 5.4: Microstructures of three xenotime grains from the Araguainha impact structure. (a), (b) and (c) EBSD band contrast (BC) maps with SHRIMP spots and U-Pb ages in Ma indicated. (d), (e) and (f) EBSD grain orientation maps (inverse pole figure, x projection [IPFx]) with insets showing orientation distribution of the recrystallised neoblasts from pole figures (lower-hemisphere, equal-area projection). (g) Close-up IPFx map showing location of atom probe samples from grain X3. (h) Grain reference orientation deviation (GROD) angle map of the area shown in G to up to 10° , showing the deviation

of orientation from the average orientation of the grain. Note the lobate texture between neoblasts at the A4 atom probe specimen location, in which the larger grain (α) with no misorientation is grown into grain with higher internal misorientation (β). Dashed lines represent contact between neoblasts showing lobate texture..... 126

Figure 5.5: EBSD maps of grain X1 from Araguainha. (a) Texture component map of X1 showing up to $\sim 20^\circ$ cumulative misorientation in the host domain of the grain. (b) EBSD grain orientation map of grain X1 (inverse pole figure, z projection [IPFz]). (c) Pole figures (lower-hemisphere, equal area projections) from (b), showing orientation relationship between the host domain with neoblast clusters. The neoblast orientations preserve the same orientations as $\{112\}$ twin lamellae. 127

Figure 5.6: SHRIMP U-Pb geochronology results plotted on Tera-Wasserburg diagrams. (a) Results for Vredefort xenotime grain 14DG14. Red ellipses – spots targeting twins and planar deformation bands; yellow ellipses – spots targeting areas with $< 10^\circ$ misorientation. The lower intercept of the discordia is 1803 ± 270 Ma. (b) Results for Santa Fe xenotime grains. 129

Figure 5.7: SHRIMP U-Pb geochronology results from Araguainha xenotime grains plotted on Tera-Wasserburg diagram. (a) Combined results from grain X1, X2 and X3. (b), (c) and (d) plotting results from grains X1, X2 and X3 respectively..... 130

Figure 5.8: Atom probe 3D reconstruction of representative specimens from Vredefort xenotime grain 14DG14 and Santa Fe grain SFx5. Each sphere represents an atom of the indicated element. (a) Specimen V1, host xenotime from the high strain domain of the grain showing Ca and Pb* enriched clusters and a dislocation enriched in Ca, Na, Al, and OH. Cl is also distributed heterogeneously in clusters. Specimen V4 from a neoblast from the recrystallised domain of the grain showing Ca and Pb* enriched clusters. (b) Specimen SF1, SF2 from host and both SF3 and SF4 the twin domains. Host and specimen showing numerous Ca clusters with $< 1\%$ Pb* clusters. Note that Pb* enriched Ca clusters is only present in specimen from twin domain. 133

Figure 5.9: (a) Summary of both Pb-Pb and U-Pb nanogeochronology results obtained from the different domains (neoblastic and twin) of the Vredefort grain (¹ - Kamo et al., 1996)(WS – Whole atom probe specimen). (b) U-Pb nanogeochronology results from the four specimens from Santa Fe..... 134

Figure 5.10: Specimen A4 from Araguainha showing grain boundary enriched in elements such as Si, Mg, Ca, Cl, Na, Al. The specimen also shows the presence of Si-Mg clusters distributed variably in different grains.....136

Figure 5.11: Illustration of the grain boundary migration forming the lobate texture between the recrystallised neoblasts at the grain scale (left) and nanoscale (right). Large crystal α has a lower dislocation density, less number of clusters hence less crystal distortion. Crystal β has a higher cluster density, with internal misorientation. With time, more deformed crystal is consumed, by atoms from β reorganise to fit the crystal lattice of α forming a interfingering lobate texture. 146

List of Tables

Table 2.1: Composition and age of reference materials	22
Table 2.2: Reference material description, analytical parameters and measurement results for U-Pb geochronology	23
Table 2.3: $^{207}\text{Pb}/^{206}\text{Pb}$ geochronology measurement results using constant and variable background estimation.	30

List of Appendices

Chapter 2

Appendix 2.1: Analysis on surface diffusion in xenotime during APT analysis	207
Appendix 2.1: Charge state ratio of PO versus laser pulse energy	212

Chapter 3

Appendix 3.1: SHRIMP U-Pb results of sample z6413	214
Appendix 3.2: SHRIMP spot location on sample z6413	227
Appendix 3.3: APT mass spectrum of sample z6413	228
Appendix 3.4: APT U-Pb nanogeochronology results	229

Chapter 4

Appendix 4.1 EPMA results from Fanad xenotime grains	230
Appendix 4.2 Y1 SHRIMP results	243
Appendix 4.3 EPMA x-ray compositional maps of 1642-3 and 1642-4 xenotime grains	244
Appendix 4.4 APT 3d reconstruction profiles of specimens from Fanad	245

Chapter 5

Appendix 5.1 EBSD working conditions	246
Appendix 5.2 SHRIMP results from three impact locations	247
Appendix 5.3 GROD angle map of grain X3 from Araguainha	252
Appendix 5.4 APT 3d reconstruction profiles of specimens from Vredefort and Araguainha	253
Appendix 5.5 APT nanogeochronology results	255

Chapter 1

Introduction

“It is perhaps a little indelicate to ask of our Mother Earth her age.”

Arthur Holmes (1913)

This year 2023, celebrates 110 years of modern isotope geochronology. In 1913, Nobel Prize laureate Frederick Soddy published an article in Nature Journal about the discovery of isotopes mentioned as “radio elements non-separable” (Soddy, 1913). In the same year, Arthur Holmes, considered the father of modern geochronology, published the book ‘Age of the Earth’ in which he describes how radioactivity can be used to date rocks and quantify geologic time (Holmes, 1913). From there, the field of isotope geochronology unravelled many mysteries about Earth, other planets in the solar system and greatly contributed to understanding the evolution of the universe.

Isotope geochronology is based on quantifying the rate of radioactive decay of the unstable isotopes stored in the minerals of rocks. Several isotope systems, such as U-Pb, Sm-Nd, Lu-Hf, Rb-Sr, K-Ar, and Re-Os are routinely and among those U-Pb system is the most used and well-studied isotopic system used to obtain the geochronological information from the rocks. To measure the isotopic composition of rocks and minerals, several techniques are available where the analytical volume changes from the whole rock to individual minerals. However, the geochronology data we obtain from these analyses is well precise, are often complex and difficult to understand. Most of the times this complexity in data is attributed to complex textures in the minerals which is unsolvable with limited spatial resolution of conventional techniques. Nonetheless complex textures in minerals formed by different geological processes present a brilliant opportunity to study the behaviour of mineral systems, namely the behaviour of isotopes during these processes in nature. With the advancement of technology, using instruments like atom probe tomography (APT), we are now able to measure the isotopic ratios of minerals from a sub-domain of grain, such as twins, small-scale alteration, and deformation microstructures, informing the behaviour isotopic systems in geochronometers and thereby shedding light on how large-scale geological processes affect geochronometers starting from nanoscale.

Using APT and other correlative microscopic techniques such as transmission electron microscopy (TEM), allows the analysis of individual atoms in minerals. This finer resolution informs mineralogical processes occurring at the atomic scale, which is fundamental to the understanding of the any geochemical behaviour of minerals. The combined capability of atom probe to analyse the chemistry and the nanoscale distribution of elements in 3d allows identifying element migration processes associated with microstructures and crystal defects.

The isotopic characterisation of nanoscale domains can reveal the timing of element mobility and the geological process responsible for it. Atom probe tomography is a complementary tool for geochemists to higher precision, lower spatial resolution analytical techniques (for a full review, see (Reddy et al., 2020)).

1.1 Geochronometers at the nanoscale

The first published study reporting atom probe analyses of a geochronometer was conducted on Hadean zircon grains and revealed Y, Pb* nanoscale clusters (Valley et al., 2014). In this study, the mobility of radiogenic Pb and the formation of clusters was attributed to volume diffusion of Pb into non-annealed radiation-damaged domains during metamorphic heating (Valley et al., 2014, 2015). Since, more nanoscale studies have been conducted on geochronometers with different geological history, and from different geological contexts, highlighting several mechanisms responsible for nanoscale heterogeneities in minerals. As expected, a lot of nanoscale studies have been conducted on zircon, and found that crystal defects produced by radiation damage result in enhanced mobility of trace elements, including Pb*, into discrete nanoscale reservoirs (Peterman et al., 2016, 2019; Piazzolo et al., 2016; Reddy et al., 2016; La Fontaine et al., 2017)

Similar studies investigating baddeleyite determined Pb* mobility as a result of phase transition during shock metamorphism and diffusion of Pb* into defects (White et al., 2017, 2018, 2019; Moser et al., 2019). Nanoscale study on rutile has shown the formation of Pb* enriched clusters, along with Al, Cr, and V, trapped in the transient radiation damage cores (Verberne et al., 2020). Atom probe studies on titanite have displayed distribution of common Pb associated with deformation-related defects (Kirkland et al., 2018). Similar to zircon, monazite has been studied extensively. Radiogenic Pb-enriched apatite inclusions have been proposed to form in monazite by the process of phase immiscibility (Fougerouse et al., 2018; Seydoux-Guillaume et al., 2019). Furthermore britholite and galena nanoscale inclusions were documented to have formed in monazite during fluid alteration (Fougerouse et al., 2021a; Turuani et al., 2022). Still in monazite, deformation microstructures and twin formation were linked with Pb* mobility, recording the time of their formation (Fougerouse et al., 2021b).

All the nanoscale studies on the geochronometers have revealed one important aspect, minerals are not as homogeneous as previously thought and several mineralogical mechanisms can be responsible for nanoscale heterogeneities. Both intrinsic defect properties of the mineral, such as radiation damage, and extrinsic factors such as deformation, fluid activity,

metamorphism causes these heterogeneities in minerals (Reddy et al., 2020). It is therefore crucial to study these mechanisms in order to improve our understanding of geochronometers and the geochronological data they produce.

This thesis focuses on a comparatively simple mineral, xenotime, a widely used geochronometer, in order to deconvolve complex mineralogical mechanisms that can affect minerals.

1.2 Xenotime – the neglected geochronometer

Xenotime is an yttrium phosphate (YPO_4), a widespread accessory mineral found in igneous rocks, especially felsic units (Förster, 1998; Bea and Montero, 1999; Schaltegger et al., 2005; Breiter and Förster, 2021), metapelites (Franz et al., 1996; Rasmussen et al., 2011), hydrothermal assemblages (Brown et al., 2002; Aleinikoff et al., 2012), as authigenic overgrowths on zircon in sedimentary rocks (McNaughton et al., 1999; Rasmussen, 2005), and as a component in detrital mineral placers (Van Emden et al., 1997). Xenotime has a tetragonal crystal structure in which Y is coordinated to eight oxygen ions forming YO_8 polyhedra forming chains in the b directions linked in the c direction by PO_4 tetrahedra (Figure 1.1a) (Ni et al., 1995; Engi, 2017). Due to the similarity in ionic radius, heavy rare earth elements (Gd-Lu; HREE) substitute for Y^{3+} by simple substitution mechanism, making xenotime a target for rare earth element extraction in heavy mineral sand deposits and carbonatites (Ni et al., 1995).

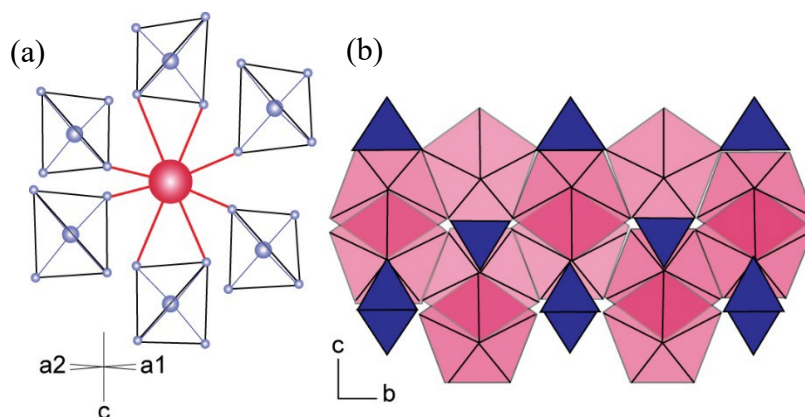
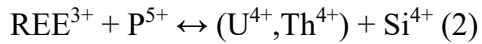
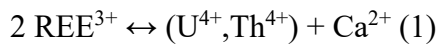


Figure 1.1 (a) Structure of REE site. (Y,HREE) cation in red, occupied in regular (Y,REE) O_8 dodecahedron provides an appropriate site for Y and the smaller, heavy REE. Modified after Engi, (2017). (b) Polyhedral projections down [100] showing xenotime structure, red – REO_8 polyhedra and blue PO_4 tetrahedra. Modified after Ni et al., (1995).

Two important coupled element substitution mechanisms have been defined in xenotime (Spear and Pyle, 2002; Engi, 2017). These mechanisms allow the incorporation of significant concentration of actinides, especially U compared to Th due to its smaller size.



Studies show that huttonite exchange (2) dominates in xenotime due to the fact that Si^{4+} is smaller than Ca^{2+} and preferentially gets incorporated replacing P^{5+} ion (Van Emden et al., 1997; Engi, 2017; Spear and Pyle, 2002). Igneous xenotime is found to be highest in actinide concentrations, whereas diagenetic and hydrothermal xenotime is usually lower in actinide concentrations (McNaughton and Rasmussen, 2018). Based on REE pattern and actinide concentration, the formation environment of xenotime can be constrained, a useful tool in routine geochemical and geochronologic analysis (Aleinikoff et al., 2015; McNaughton and Rasmussen, 2018).

Xenotime makes an excellent geochronometer due to its inherent properties and widespread presence. As mentioned above, xenotime incorporates high actinide content, especially U. Xenotime incorporates only negligible amounts of common Pb during growth, and this is primarily because of larger Pb^{2+} cation size compared to the small $(\text{Y}, \text{HREE})^{3+}$ cation site in xenotime (Donovan et al., 2003). Additionally, the Pb diffusion rate in xenotime is slower than other accessory phases such as zircon or monazite and a high closure temperature of ~ 900 °C as been determined (Cherniak, 2006, 2010). Xenotime is resistant to radiation damage, despite the high actinide concentration and no metamict xenotime has been documented in nature (Harrison et al., 2002). This is attributed to the low activation energy for annealing of the structure and which persist in moderate crustal conditions (Lenz et al., 2019).

Conventionally, xenotime is analysed using isotope dilution method (Hawkins and Bowring, 1999; Stern and Rayner, 2003), ion microprobe (McNaughton et al., 1999; Vallini et al., 2002; Cross and Williams, 2018), electron microprobe (Asami et al., 2002; Suzuki and Kato, 2008), and laser ablation ICP-MS (Liu et al., 2011). In igneous settings xenotime generally forms large and homogeneous grains, however in diagenetic and hydrothermal environments form small grain sizes and complicated texture, makes it more challenging to analyse using conventional techniques (Rasmussen, 2005). With its wide occurrence, xenotime has potential to uncover unresolved geological mysteries which cannot be achieved by other geochronometers.

One of the most notable application of xenotime is for the dating of diagenesis in Proterozoic sedimentary basins (Fletcher et al., 2000; Rasmussen et al., 2004; Rasmussen, 2005). Xenotime is one of the only U-Pb geochronometer forming during early diagenesis of sedimentary rocks, as syntaxial outgrowths on zircon. Even though there are many phases and isotopic systems used to constrain diagenetic ages other than xenotime, it has its own limitations. For example, apatite is another diagenetic mineral datable using U-Pb method. However, apatite is very prone to fluid alteration and incorporates high amounts of common Pb (Kirkland et al., 2018), which is a major hindrance when it comes to accurately date older sediments. Because xenotime remains isotopically closed up to amphibolite facies, it can be used to constrain diagenetic ages from Precambrian strata (Rasmussen, 2005). With episodic growths associated with fluid flow, hydrothermal event, and metamorphism, younger xenotime rim can form around diagenetic cores, and careful textural analysis can yield the basin history (Rasmussen, 2005).

Another application of xenotime is in the dating of highly fractionated granites, mainly because zircon in those suites will be damaged due to high actinide content and radiation damage (Li et al., 2013). Xenotime is resistant to radiation damage, even at high U concentrations (Harrison et al., 2002).

In metamorphic systems, xenotime is abundant in metapelites and is one of the major reservoir of HREEs (Spear and Pyle, 2002). The growth and consumption of xenotime is tightly linked to garnet and can be used as a geothermometer (Pyle and Spear, 2000, 2003). The Y content in xenotime and monazite in equilibrium is also used as a geothermometer in metapelites (Heinrich et al., 1997; Andrehs and Heinrich, 1998; Gratz and Heinrich, 1998). Being a geochronometer and geothermometer in metapelites and its survivability into higher grades, makes xenotime ideal to study the metamorphic history of the terrain.

In hydrothermal mineral assemblage settings, xenotime forms as a result of hydrothermal events and has been used to date Sn-W deposits, gold deposits, base metal, iron and uranium deposits (Brown et al., 2002; Schaltegger et al., 2005; Vallini et al., 2007; Rasmussen et al., 2010; Muhling et al., 2012).

With its unique capabilities, the geochronometer is still less studied due to the limitations of analytical techniques. For example, the diagenetic xenotime overgrowths on zircon are generally small grains (<10 μm), and analysis of the grains using conventional techniques with low spatial resolution is a challenge. Nevertheless, with cutting edge technology APT, it is now possible to target specific areas of interest in a mineral, e.g., micro

twins, deformation bands, fine overgrowths, and other textural features which can resolve complex geological questions, starting from its formation, associated trace element mobility and its geological implications.

1.3 New frontiers in geochronology – Atom probe tomography

Technological advance in science have enabled the visualisation of materials at the atomic scale. Atom probe tomography is such a technique, which allows three-dimensional nanoscale chemical mapping of individual atoms (Larson et al., 2013). Initially developed for material science research, the technique has now the capability of analysing non-conductive materials, including geological materials. APT works on the field evaporation of specimens under high electric field where the identification of evaporated species is obtained from time-of-flight mass spectrometry (TOF-MS). The APT specimen is prepared as a sharp (< 100 nm) needle to enhance field evaporation under high electric field. For conductive materials a voltage pulse, and for non-conducting materials a laser pulse, triggers the controlled evaporation of ionic species. The evaporated ions are then targeted to a position sensitive detector, recording the x,y coordinates of the location where the ion impacts the detector. The z coordinate is obtained from the time of arrival of the ion, also providing the stop time for TOF-MS. This way, the x,y,z coordinates are recorded and enables to build a 3d reconstruction of the sample analysed, with identification of evaporated species by time of flight (Gault et al., 2012; Larson et al., 2013; Reddy et al., 2020) (Figure 1.2). The needle-shaped specimen is prepared with a tip radius of 50–100 nm, this small sample size permits to target microstructures and any region of interest in a mineral to obtain both structural (distribution of elements) and chemical information including isotopic ratios. More information can be found in (Gault et al., 2012; Larson et al., 2013; Reddy et al., 2020), and chapter one which discusses, APT and analysis of xenotime.

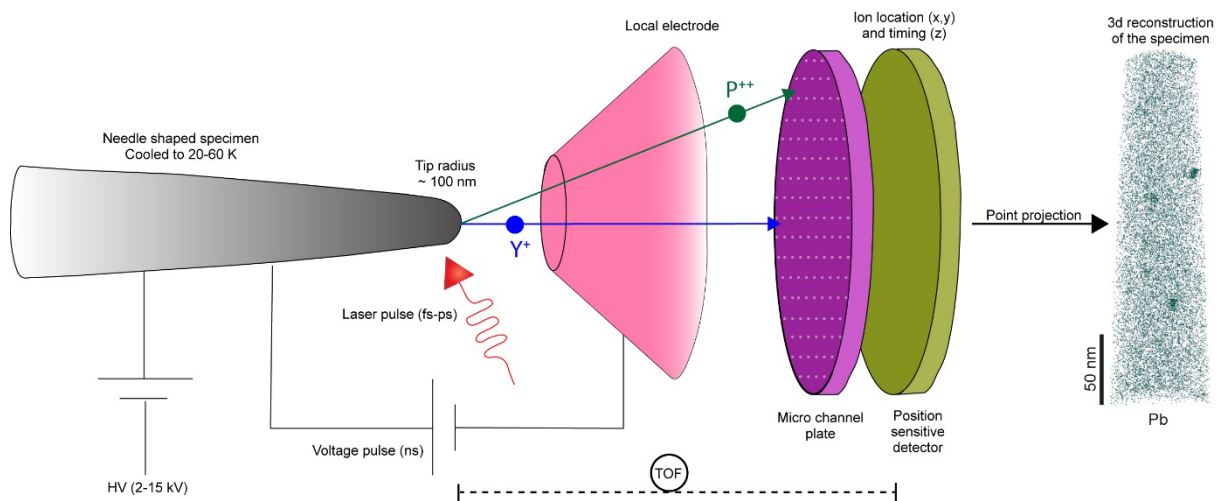


Figure 1.2: A schematic illustration of APT, including the alternative modes of voltage-pulsing and laser-pulsing operation. Location and timing information from the position-sensitive detector is used to reconstruct the original atomic structure in three dimensions and time of flight to identify the evaporated species.

1.4 Research objectives

The broader aim of the projects is to identify and understand different mineralogical processes affecting geochronometers, using the mineral xenotime as a proxy. To achieve the aim, xenotime from different geological settings were selected and studied in detail. In order to make nanoscale observations representative of a global process, the analytical workflow starts with microscale characterisation of the sample with petrography, scanning electron microscopy (SEM), and electron probe microanalysis (EPMA). Geochronological characterisation of selected xenotime grains was performed by sensitive high-resolution ion microprobe (SHRIMP). Using these data, region of interests for nanoscale analysis were selected for specimen preparation using focused ion beam SEM (FIB-SEM) and analysed using APT and / or transmitted electron microscopy (TEM). The detailed methodology is described in each chapter of this thesis.

In order to achieve the overarching aim of this project, specific objectives of this project were defined:

1. Optimisation of running conditions of xenotime analysis using APT and developing nanogeochronology methodology applied to xenotime to constrain age information from samples.

2. Study of xenotime sample affected by fluid alteration to document the nanoscale manifestation of fluid alteration in xenotime, as xenotime is believed to be resilient to fluid alteration and age resetting.
3. Examining the mineralogical controls of nanoscale heterogeneities in xenotime, especially apatite inclusions by studying samples sourced from a pegmatite and metapelites affected by contact metamorphism.
4. Investigate the response of U-Pb system with different shock metamorphic conditions, and deformation microstructures. Xenotime samples were sourced from three impact structures.

1.5 Thesis structure

This thesis is presented as a hybrid thesis, contains 4 core chapters in which two chapters are published in peer-reviewed journals and another two chapters. Each chapter have been prepared as stand-alone publication and each contains an introduction, followed by methods, results and discussion that are specific to the respective chapters. Supplementary information for each chapter is provided in the appendix at the end of the thesis.

Chapter II: *Xenotime at the Nanoscale: U-Pb Geochronology and Optimisation of Analyses by Atom Probe Tomography*

This chapter details the optimisation of xenotime analysis using APT and more importantly bring forwards the nanogeochronology method developed to constrain age information. Optimising xenotime analyses was the primary step, as xenotime this study was the first report of xenotime analysis by APT. Four routinely used xenotime standards were selected for this purpose, BS-1, MG-1, xtc, and Y1. There are several analytical conditions were tuned to improve the data yield and improve geochemical isotopic data. Both U-Pb and Pb-Pb method were developed, which were not attained for other minerals, due to isobaric interferences in the APT mass spectra or low concentration of actinides. This chapter is published in the journal *Geostandards and Geoanalytical Research*, May 2021.

Chapter III: *Radiogenic Pb in xenotime trapped in nanoscale inclusions of apatite during fluid alteration.*

This chapter is a multiscale analysis of fluid alteration textures in xenotime, as xenotime is presumed to be resistant fluid alteration. The sample is sourced from a pegmatite from Central Gneiss Belt, Grenville province, Ontario, Canada. Named as z6413, the sample is a

widely used xenotime standard in Secondary-ion mass spectrometry (SIMS) geochronology. Microscale characterisation revealed fluid alteration textures, however SIMS U-Pb analyses showed no correlation between textures and geochronology data. Further nanoscale analyses were done on the unaltered domain, and revealed a dislocation enriched in fluid mobile elements and numerous Pb*-rich apatite nanoscale inclusions. The apatite inclusions likely formed by fluid alteration, in grain area beyond the obvious textural expression of fluid activity observable at the microscale. A model is suggested where during fluid alteration, Pb* is trapped in apatite inclusions, thereby preserving the crystallisation age at the scale of conventional analytical techniques. This chapter is published in the journal *Chemical Geology*, July 2023.

Chapter IV: Fluid alteration and Ca composition control the formation of nanoscale Ca-Pb clusters in xenotime, not high-temperature metamorphism.

The observation of apatite inclusions from the analysis of pegmatite sample from chapter three, invoked the need of finding the controlling factors in the formation of apatite inclusions in xenotime, and therefore redistributing radiogenic Pb. For this purpose, two case studies were selected, Y1 – sourced from pegmatite, Gascoyne province of Western Australia, and xenotime from different metamorphic grades from a contact aureole, Fanad, Ireland. Both samples have different geological history and composition. Petrographic observations were followed by SIMS and EPMA analyses of the samples for further characterisation and finally APT nanoscale analysis. The results indicate that the high level of impurity (Ca concentration) and fluid activity are the main mechanisms affecting the formation of apatite inclusions in xenotime.

Chapter V: Towards a new impact geochronometer: Deformation microstructures and U-Pb systematics of shocked xenotime.

This chapter presents a comprehensive study on xenotime samples from three impact Vredefort (South Africa), Santa Fe (USA), and Araguainha (Brazil) with different physical conditions of impact and age. The study uses techniques such as SEM, EBSD, SHRIMP, and APT. The microstructures were primarily characterized using SEM-EBSD and identified targets for SHRIMP and APT analyses. This study identified a new shock diagnostic neoblastic texture from xenotime and the first ever impact age that is obtained from xenotime U-Pb analysis. Nanogeochronology of the samples were done and documented different generations of Pb signature from a small domain (twins, neoblasts) of the samples. APT analysis on the neoblasts proposes grain boundary migration for the formation of neoblasts.

Chapter VI: *Thesis synthesis and future work*

This chapter synthesise the findings of the different projects and its implications and possibilities of future work.

1.6 References

- Aleinikoff J. N., Lack J. F. S., Lund K., Evans K. V., Fanning C. M., Mazdab F. K., Wooden J. L. and Pillers R. M. (2012) Constraints on the timing of Co-Cu ± Au mineralization in the Blackbird district, Idaho, using SHRIMP U-Pb ages of monazite and xenotime plus zircon ages of related Mesoproterozoic orthogneisses and metasedimentary rocks. *Econ. Geol.* **107**, 1143–1175.
- Aleinikoff J. N., Lund K. and Fanning C. M. (2015) SHRIMP U-Pb and REE data pertaining to the origins of xenotime in belt supergroup rocks: Evidence for ages of deposition, hydrothermal alteration, and metamorphism. *Can. J. Earth Sci.* **52**, 722–745.
- Andrehs G. and Heinrich W. (1998) Experimental determination of REE distributions between monazite and xenotime: potential for temperature-calibrated geochronology. *Chem. Geol.* **149**, 83–96.
- Asami M., Suzuki K. and Grew E. S. (2002) Chemical Th-U-total Pb dating by electron microprobe analysis of monazite, xenotime and zircon from the Archean Napier complex, East Antarctica: Evidence for ultra-high-temperature metamorphism at 2400 Ma. *Precambrian Res.* **114**, 249–275.
- Bea F. and Montero P. (1999) Behavior of accessory phases and redistribution of Zr, REE, Y, Th, and U during metamorphism and partial melting of metapelites in the lower crust: An example from the Kinzigite Formation of Ivrea-Verbano, NW Italy. *Geochim. Cosmochim. Acta* **63**, 1133–1153.
- Breiter K. and Förster H. (2021) Compositional Variability of Monazite–Cheralite–Huttonite Solid Solutions, Xenotime, and Uraninite in Geochemically Distinct Granites with Special Emphasis to the Strongly Fractionated Peraluminous Li–F–P-Rich Podlesí Granite System (Erzgebirge/Krušné Hor. *Minerals* **11**, 127.
- Brown S. M., Fletcher I. R., Stein H. J., Snee L. W. and Groves D. I. (2002) Geochronological Constraints on Pre-, Syn-, and Postmineralization Events at the World-Class Cleo Gold Deposit, Eastern Goldfields Province, Western Australia. *Econ. Geol.* **97**, 541–559.

- Cherniak D. J. (2006) Pb and rare earth element diffusion in xenotime. *Lithos* **88**, 1–14.
- Cherniak D. J. (2010) Diffusion in accessory minerals: Zircon, titanite, apatite, monazite and xenotime. *Rev. Mineral. Geochemistry* **72**, 827–869.
- Cross A. J. and Williams I. S. (2018) SHRIMP U–Pb–Th xenotime (YPO₄) geochronology: A novel approach for the correction of SIMS matrix effects. *Chem. Geol.* **484**, 81–108.
- Donovan J. J., Hanchar J. M., Picolli P. M., Schrier M. D., Boatner L. A. and Jarosewich E. (2003) A re-examination of the rare-earth-element orthophosphate standards in use for electron-microprobe analysis. *Can. Mineral.* **41**, 221–232.
- Engi M. (2017) Petrochronology Based on REE-Minerals: Monazite, Allanite, Xenotime, Apatite. *Rev. Mineral. Geochemistry* **83**, 365–418.
- Fletcher I. R., Rasmussen B. and McNaughton N. J. (2000) SHRIMP U-Pb geochronology of authigenic xenotime and its potential for dating sedimentary basins. *Aust. J. Earth Sci.* **47**, 845–859.
- Förster H. J. (1998) The chemical composition of REE-Y-Th-U-rich accessory minerals in peraluminous granites of the Erzgebirge-Fichtelgebirge region, Germany. Part II: Xenotime. *Am. Mineral.* **83**, 1302–1315.
- Fougerouse D., Cavosie A. J., Erickson T., Reddy S. M., Cox M. A., Saxey D. W., Rickard W. D. A. and Wingate M. T. D. (2021a) A new method for dating impact events – Thermal dependency on nanoscale Pb mobility in monazite shock twins. *Geochim. Cosmochim. Acta* **314**, 381–396.
- Fougerouse D., Reddy S. M., Saxey D. W., Erickson T. M., Kirkland C. L., Rickard W. D. A., Seydoux-Guillaume A.-M., Clark C. and Buick I. S. (2018) Nanoscale distribution of Pb in monazite revealed by atom probe microscopy. *Chem. Geol.* **479**, 251–258.
- Fougerouse D., Reddy S. M., Seydoux-Guillaume A.-M., Kirkland C. L., Erickson T. M., Saxey D. W., Rickard W. D. A., Jacob D., Leroux H. and Clark C. (2021b) Mechanical twinning of monazite expels radiogenic lead. *Geology* **49**, 417–421.
- Franz G., Andrehs G. and Rhede D. (1996) Crystal chemistry of monazite and xenotime from Saxothuringian-Moldanubian metapelites, NE Bavaria, Germany. *Eur. J. Mineral.* **8**, 1097–1118.
- Gault B., Moody M. P., Cairney J. M. and Ringer S. P. (2012) Atom Probe Microscopy.,

Springer New York, New York, NY.

- Gratz R. and Heinrich W. (1998) Monazite-xenotime thermometry. III. Experimental calibration of the partitioning of gadolinium between monazite and xenotime. *Eur. J. Mineral.* **10**, 579–588.
- Harrison T. M., Catlos E. J. and Montel J.-M. (2002) U-Th-Pb Dating of Phosphate Minerals. *Rev. Mineral. Geochemistry* **48**, 524–558.
- Hawkins D. P. and Bowring S. A. (1999) U-Pb monazite, xenotime and titanite geochronological constraints on the prograde to post-peak metamorphic thermal history of Paleoproterozoic migmatites from the Grand Canyon, Arizona. *Contrib. to Mineral. Petrol.* **134**, 150–169.
- Heinrich W., Andrehs G. and Franz G. (1997) Monazite-xenotime miscibility gap thermometry. I. An empirical calibration. *J. Metamorph. Geol.* **15**, 3–16.
- Holmes A. (1913) *The Age of the Earth.*, Harper & Brothers.
- Kirkland C.L., Fougereuse D., Reddy S. M., Hollis J. and Saxey D. W. (2018) Assessing the mechanisms of common Pb incorporation into titanite. *Chem. Geol.* **483**, 558–566.
- La Fontaine A., Piazzolo S., Trimby P., Yang L. and Cairney J. M. (2017) Laser-Assisted Atom Probe Tomography of Deformed Minerals: A Zircon Case Study. *Microsc. Microanal.* **23**, 404–413.
- Larson D. J., Prosa T. J., Ulfig R. M., Geiser B. P. and Kelly T. F. (2013) *Local Electrode Atom Probe Tomography.*
- Lenz C., Thorogood G., Aughterson R., Ionescu M., Gregg D. J., Davis J. and Lumpkin G. R. (2019) The Quantification of Radiation Damage in Orthophosphates Using Confocal μ -Luminescence Spectroscopy of Nd³⁺. *Front. Chem.* **7**, 1–13.
- Li Q. L., Li X. H., Lan Z. W., Guo C. L., Yang Y. N., Liu Y. and Tang G. Q. (2013) Monazite and xenotime U-Th-Pb geochronology by ion microprobe: Dating highly fractionated granites at Xihuashan tungsten mine, SE China. *Contrib. to Mineral. Petrol.* **166**, 65–80.
- Liu Z. C., Wu F. Y., Guo C. L., Zhao Z. F., Yang J. H. and Sun J. F. (2011) In situ U-Pb dating of xenotime by laser ablation (LA)-ICP-MS. *Chinese Sci. Bull.* **56**, 2948–2956.
- McNaughton N. J., Rasmussen B. and Fletcher I. R. (1999) SHRIMP uranium-lead dating of diagenetic xenotime in siliciclastic sedimentary rocks. *Science* (80-.). **285**, 78–80.

- McNaughton Neal J and Rasmussen B. (2018) Geochemical characterisation of xenotime formation environments using U-Th. *Chem. Geol.* **484**, 109–119.
- Moser D. E., Arcuri G. A., Reinhard D. A., White L. F., Darling J. R., Barker I. R., Larson D. J., Irving A. J., McCubbin F. M., Tait K. T., Roszjar J., Wittmann A. and Davis C. (2019) Decline of giant impacts on Mars by 4.48 billion years ago and an early opportunity for habitability. *Nat. Geosci.* **12**, 522–527.
- Muhling J. R., Fletcher I. R. and Rasmussen B. (2012) Dating fluid flow and Mississippi Valley type base-metal mineralization in the Paleoproterozoic Earraheedy Basin, Western Australia. *Precambrian Res.* **212–213**, 75–90.
- Ni Y., Hughes J. M. and Mariano A. N. (1995) Crystal chemistry of the monazite and xenotime structures. *Am. Mineral.* **80**, 21–26
- Peterman E. M., Reddy S. M., Saxey D. W., Fougereuse D., Snoeyenbos D. R. and Rickard W. D. A. (2019) Nanoscale processes of trace element mobility in metamorphosed zircon. *Contrib. to Mineral. Petrol.* **174**.
- Peterman E. M., Reddy S. M., Saxey D. W., Snoeyenbos D. R., Rickard W. D. A., Fougereuse D. and Kylander-Clark A. R. C. (2016) Nanogeochronology of discordant zircon measured by atom probe microscopy of Pb-enriched dislocation loops. *Sci. Adv.* **2**.
- Piazolo S., Belousova E., La Fontaine A., Corcoran C. and Cairney J. M. (2017) Trace element homogeneity from micron- to atomic scale: Implication for the suitability of the zircon GJ-1 as a trace element reference material. *Chem. Geol.* **456**, 10–18.
- Piazolo S., La Fontaine A., Trimby P., Harley S., Yang L., Armstrong R. and Cairney J. M. (2016) Deformation-induced trace element redistribution in zircon revealed using atom probe tomography. *Nat. Commun.* **7**, 10490.
- Pyle J. M. and Spear F. S. (2000) An empirical garnet (YAG) - xenotime thermometer. *Contrib. to Mineral. Petrol.* **138**, 51–58.
- Pyle J. M. and Spear F. S. (2003) Yttrium zoning in garnet: Coupling of major and accessory phases during metamorphic reactions. *Am. Mineral.* **88**, 708.
- Rasmussen B. (2005) Radiometric dating of sedimentary rocks: The application of diagenetic xenotime geochronology. *Earth-Science Rev.* **68**, 197–243.
- Rasmussen B., Fletcher I. R. and Muhling J. R. (2011) Response of xenotime to prograde

- metamorphism. *Contrib. to Mineral. Petrol.* **162**, 1259–1277.
- Rasmussen B., Fletcher I. R., Bengtson S. and McNaughton N. J. (2004) SHRIMP U-Pb dating of diagenetic xenotime in the Stirling Range Formation, Western Australia: 1.8 Billion year minimum age for the Stirling biota. *Precambrian Res.* **133**, 329–337.
- Rasmussen B., Fletcher I. R., Muhling J. R. and Wilde S. A. (2010) In situ U-Th-Pb geochronology of monazite and xenotime from the Jack Hills belt: Implications for the age of deposition and metamorphism of Hadean zircons. *Precambrian Res.* **180**, 26–46.
- Reddy S. M., Saxey D. W., Rickard W. D. A., Fougereuse D., Montalvo S. D., Verberne R. and van Riessen A. (2020) Atom Probe Tomography: Development and Application to the Geosciences. *Geostand. Geoanalytical Res.* **44**, 5–50.
- Reddy S. M., van Riessen A., Saxey D. W., Johnson T. E., Rickard W. D. A., Fougereuse D., Fischer S., Prosa T. J., Rice K. P., Reinhard D. A., Chen Y. and Olson D. (2016) Mechanisms of deformation-induced trace element migration in zircon resolved by atom probe and correlative microscopy. *Geochim. Cosmochim. Acta* **195**, 158–170.
- Schaltegger U., Pettke T., Audétat A., Reusser E. and Heinrich C. A. (2005) Magmatic-to-hydrothermal crystallization in the W–Sn mineralized Mole Granite (NSW, Australia). *Chem. Geol.* **220**, 215–235.
- Seydoux-Guillaume A. M., Fougereuse D., Laurent A. T., Gardés E., Reddy S. M. and Saxey D. W. (2019) Nanoscale resetting of the Th/Pb system in an isotopically-closed monazite grain: A combined atom probe and transmission electron microscopy study. *Geosci. Front.* **10**, 65–76.
- Soddy F. (1913) Intra-atomic Charge. *Nature* **92**, 399–400.
- Spear F. S. and Pyle J. M. (2002) Apatite, monazite, and xenotime in metamorphic rocks (in Phosphates; geochemical, geobiological, and materials importance) Reviews in Mineralogy and Geochemistry. *Rev. Mineral. Geochemistry* **48**, 293–335.
- Stern R. A. and Rayner N. (2003) Ages of several xenotime megacrysts by ID-TIMS: potential reference materials for ion microprobe U-Pb geochronology.,
- Suzuki K. and Kato T. (2008) CHIME dating of monazite, xenotime, zircon and polycrase: Protocol, pitfalls and chemical criterion of possibly discordant age data. *Gondwana Res.* **14**, 569–586.

- Turuani M. J., Laurent A. T., Seydoux-Guillaume A.-M., Fougereuse D., Saxey D., Reddy S. M., Harley S. L., Reynaud S. and Rickard W. D. A. (2022) Partial retention of radiogenic Pb in galena nanocrystals explains discordance in monazite from Napier Complex (Antarctica). *Earth Planet. Sci. Lett.* **588**, 117567.
- Valley J. W., Cavosie A. J., Ushikubo T., Reinhard D. A., Lawrence D. F., Larson D. J., Clifton P. H., Kelly T. F., Wilde S. A., Moser D. E. and Spicuzza M. J. (2014) Hadean age for a post-magma-ocean zircon confirmed by atom-probe tomography. *Nat. Geosci.* **7**, 219–223.
- Valley J. W., Reinhard D. A., Cavosie A. J., Ushikubo T., Lawrence D. F., Larson D. J., Kelly T. F., Snoeyenbos D. R. and Strickland A. (2015) Presidential Address. Nano- and micro-geochronology in Hadean and Archean zircons by atom-probe tomography and SIMS: New tools for old minerals. *Am. Mineral.* **100**, 1355–1377.
- Vallini D. A., Groves D. I., McNaughton N. J. and Fletcher I. R. (2007) Uraniferous diagenetic xenotime in northern Australia and its relationship to unconformity-associated uranium mineralisation. *Miner. Depos.* **42**, 51–64.
- Vallini D., Rasmussen B., Krapež B., Fletcher I. R. and McNaughton N. J. (2002) Obtaining diagenetic ages from metamorphosed sedimentary rocks: U-Pb dating of unusually coarse xenotime cement in phosphatic sandstone. *Geology* **30**, 1083–1086.
- Van Emden B., Thornber M. R., Graham J. and Lincoln F. J. (1997) The incorporation of actinides in monazite and xenotime from placer deposits in Western Australia. *Can. Mineral.* **35**, 95–104.
- Verberne R., Reddy S. M., Saxey D. W., Fougereuse D., Rickard W. D. A., Plavsa D., Agangi A. and Kylander-Clark A. R. C. (2020) The geochemical and geochronological implications of nanoscale trace-element clusters in rutile. *Geology* **XX**, 1–5.
- White L. F., Darling J. R., Moser D. E., Cayron C., Barker I., Dunlop J. and Tait K. T. (2018) Baddeleyite as a widespread and sensitive indicator of meteorite bombardment in planetary crusts. *Geology* **46**, 719–722.
- White L. F., Darling J. R., Moser D. E., Reinhard D. A., Dunlop J., Larson D. J., Lawrence D. and Martin I. (2017) Complex Nanostructures in Shocked, Annealed, and Metamorphosed Baddeleyite Defined by Atom Probe Tomography. In *Microstructural Geochronology: Planetary Records Down to Atom Scale* pp. 351–367.

White L. F., Moser D. E., Tait K. T., Langelier B., Barker I. and Darling J. R. (2019)
Crystallization and impact history of a meteoritic sample of early lunar crust (NWA 3163)
refined by atom probe geochronology. *Geosci. Front.* **10**, 1841–1848.

**Xenotime at the Nanoscale: U-Pb Geochronology and
Optimisation of Analyses by Atom Probe Tomography**

This chapter is published as

Joseph C., Fougrouse D., Saxey D. W., Verberne R., Reddy S. M. and Rickard W. D. A.
(2021) Xenotime at the Nanoscale: U-Pb Geochronology and Optimisation of Analyses by
Atom Probe Tomography. *Geostandards and Geoanalytical Research*. 45, 443–456.

<https://doi.org/10.1111/ggr.12398>

Abstract

Xenotime (YPO_4) is an accessory phase common in low to high-temperature geological environments. Xenotime is an established geochronometer, though its small size, low modal abundance and textural complexity make it more difficult to analyse with traditional techniques but makes a prime candidate for nanoscale analysis. In this study, we develop an atom probe tomography (APT) protocol to determine the $^{206}\text{Pb}/^{238}\text{U}$ and $^{207}\text{Pb}/^{206}\text{Pb}$ ages of micro-scale xenotime crystals with analytical volumes four to six orders of magnitude smaller than typical geochronology techniques. A linear correlation between the $^{206}\text{Pb}/^{238}\text{U}$ fractionation and $^{238}\text{UO}_2^{2+}/^{238}\text{UO}^{2+}$ was used to correct for the atom probe instrument parameters variability between specimens. For $^{207}\text{Pb}/^{206}\text{Pb}$ ages, we employed two methods of background correction owing to the $^{206}\text{Pb}^{2+}$ thermal tail contribution to the $^{207}\text{Pb}^{2+}$ counts: A constant background correction for the younger (~ 1000 Ma) Y1 reference material and a variable correction of background for Archaean age reference material xtc to correct for the thermal tail influence. This contribution also proposes strategies for optimisation of xenotime analysis using APT and permits us to explore the various geological problems in the nanoscale realm. This methodology potentially allows determining the age of small xenotime crystals in sedimentary rocks, low metamorphic grade settings and deformation microstructures.

2.1 Introduction

Xenotime (YPO₄) is an accessory mineral commonly found in pegmatites, peraluminous granites, migmatites, pelitic schists, gneisses, siliciclastic sedimentary rocks, hydrothermal ore deposits and as a constituent in heavy mineral placers (Spear and Pyle, 2002; Rasmussen, 2005). It is an established U-Th-Pb geochronometer on account of its high U and Th content (up to several tens and thousands $\mu\text{g g}^{-1}$ U and Th), low common Pb concentration, high resistance to radiation damage and slower Pb diffusion parameters compared with zircon and monazite (Rasmussen 2005; Cherniak, 2006). Xenotime is notable for recording the timing of diagenesis of sedimentary strata in Precambrian basins where fossils are absent (McNaughton et al., 1999; Rasmussen, 2005). In the absence or in conjunction with other geochronometers such as zircon and monazite, it is used to date igneous processes (Li et al., 2013), low- to high-grade metamorphism (Rasmussen et al. 2005; Sheppard et al., 2007) and hydrothermal mineralisation (Brown et al., 2002; Schaltegger et al., 2005b; Rasmussen et al., 2009; Zi et al., 2015; Li et al., 2020).

The age of xenotime is conventionally measured by secondary ion microprobe (SIMS; McNaughton et al., 1999; Vallini et al., 2002; Rasmussen et al., 2007; Aleinikoff et al., 2012b, a), laser ablation-inductively coupled plasma-mass spectrometry (LA-ICP-MS; Beccaletto et al., 2007; Liu et al., 2011; Budzyń et al., 2018) and electron probe microanalysis (EPMA; Suzuki and Adachi, 1991; Salier et al., 2005; Cocherie and Legendre, 2007; Hetherington et al., 2008; Suzuki and Kato, 2008). Despite its common occurrence, xenotime is volumetrically minor and typically has a small grain size, often less than 10 μm in diameter (Rasmussen 2005). In addition, xenotime commonly preserves its growth and hydrothermal history in fine-scale zones (<5 μm ; Rasmussen et al., 2011) and can record minute secondary textures such as deformation microstructures (<1 μm ; Cavosie et al., 2016). Targeting such features with conventional techniques is challenging because the analytical volume is commonly larger than the grains or their textures and may yield geologically meaningless ages (Rasmussen 2005, Vallini et al., 2005). The petrological effort of finding sufficiently large crystals in siliciclastic sedimentary rocks suitable for the above-mentioned techniques is time-consuming and often not practical.

Atom probe tomography (APT) is a time-of-flight mass spectrometry technique that can provide quantitative, compositional and spatial information in three dimensions with sub-nanometre resolution (Gault et al., 2012) across a broad spectrum of geoscience materials (Reddy et al., 2020). The analytical volume of APT is < 0.008 μm^3 , which is four to six orders

of magnitude smaller than other isotopic capable techniques (Fougerouse et al., 2020). Nanogeochronology by APT has been successfully applied to several accessory phases including zircon using $^{207}\text{Pb}/^{206}\text{Pb}$ or $^{206}\text{Pb}/^{238}\text{U}$ systems (Valley et al., 2014, 2015; Peterman et al., 2016; Arcuri et al., 2020), baddeleyite with the $^{206}\text{Pb}/^{238}\text{U}$ or $^{208}\text{Pb}/^{232}\text{Th}$ systems (White et al., 2017, 2019) and monazite using the $^{208}\text{Pb}/^{232}\text{Th}$ system (Fougerouse et al., 2020, 2021).

In this contribution, we use four reference materials of different compositions and ages for optimising xenotime analysis in APT and used two reference materials to develop a new methodology for age determination of xenotime using APT. This methodology provides the opportunity to date small (<1 μm) xenotime crystals and their microstructural features, which have been previously inaccessible using conventional techniques. This work is the first APT study on the mineral xenotime and lays the foundation for further nanoscale investigations.

2.2 Samples and methodology

2.2.1 Samples

The four xenotime reference materials (MG-1, BS-1, xtc and Y1) used in this study come from different geological settings and have different ages and compositions (Table 2.1). Xtc and Y1 are igneous xenotime crystals, whereas MG-1 and BS-1 are metamorphic in origin (Fletcher et al., 2000, 2004). Concordant ages of these reference materials have been previously obtained from thermal ionisation mass spectrometry (TIMS) and/or SIMS analyses. Xtc was sourced from an Archaean pegmatite in the Yilgarn craton, Western Australia. TIMS analyses of xtc revealed a high actinide composition with U mass fractions of 5000–20000 $\mu\text{g g}^{-1}$ and Th of 3000–12000 $\mu\text{g g}^{-1}$. The grains are slightly discordant (0–3%) with TIMS $^{207}\text{Pb}/^{206}\text{Pb}$ age of 2632 ± 2 Ma and $^{206}\text{Pb}/^{238}\text{U}$ age of 2580 ± 52 Ma (2s). Y1 xenotime reference material is from the Proterozoic Yinnietharra pegmatite (Western Australia), with a U mass fraction of 8000–25000 and 3500–10000 $\mu\text{g g}^{-1}$ Th. The sample is concordant with a SIMS $^{207}\text{Pb}/^{206}\text{Pb}$ age of 949 ± 4.3 Ma (2s; Fletcher et al. 2000). The MG-1 and BS-1 are centimetre-scale euhedral xenotime crystals sampled from metamorphosed host rocks in the Brazilian state of Minas Gerais (Fletcher et al. 2004). Reference material MG-1 has a U mass fraction varying between 500 and 2000 $\mu\text{g g}^{-1}$ and a Th mass fraction spanning 300–1500 $\mu\text{g g}^{-1}$ with a $^{206}\text{Pb}/^{238}\text{U}$ age of 490.0 ± 0.6 Ma (2s, Fletcher et al. 2004). Concordant TIMS analyses of BS-1 yielded a $^{206}\text{Pb}/^{238}\text{U}$ age of 508.9 ± 0.6 Ma with 200–1200 $\mu\text{g g}^{-1}$ U and 2500–6000 $\mu\text{g g}^{-1}$ Th composition (2s).

Table 2.1: Composition and age of reference materials

Sample	U ($\mu\text{g g}^{-1}$)	Th ($\mu\text{g g}^{-1}$)	Pb ($\mu\text{g g}^{-1}$)	Age (Ma)
MG-1	500–2000	300–1500	63	490 ± 0.6
BS-1	200–1200	2500–6000	98	508.9 ± 0.6
Y1	8000–25000	3500–10000	1500–4500 ^a	949 ± 4.1
xtc	5000–20000	3000–12000	2800–11500 ^b	2580 ± 52

^a Calculated from Fletcher et al. (2000).

^b Calculated from Fletcher et al. (2004).

2.2.2 FIB-SEM

A TESCAN Lyra 3 Ga⁺ focussed ion beam coupled with a scanning electron microscope (FIB-SEM) housed at Curtin University was used to prepare the needle-shaped specimens for APT. The FIB was operated at 30 kV accelerating voltage during the preparation of the specimens followed by a 2 kV routine to remove the surface layer affected by the high-energy Ga beam. The location of the specimens was targeted using electron-beam deposited Pt buttons following the methodology detailed elsewhere (Rickard et al., 2020). The final specimen shape differed for each specimen due to the manual FIB preparation; however, the precise tip shape could not be accurately quantified as a consequence of the limited imaging spatial resolution. The specimen apex diameters ranged from approximately 100 to 150 nm and the shank angle between 5° and 7°. No systematic shape variations were introduced between specimens extracted from different xenotime crystals.

2.2.3 APT

A total of nineteen specimens from the four reference materials were analysed at the Geoscience Atom Probe facility, Curtin University. The instrument (CAMECA LEAP 4000X HR) was operated in laser-assisted mode using a UV laser ($\lambda = 355$ nm). The laser pulse energy for analyses was varied between 50 and 450 pJ in order to evaluate its effect on data quality (Table 2.2). The pulse frequency (125 kHz), detection rate (1%) and base temperature (60 K) were kept constant in every analysis except for one MG-1 specimen where the base temperature

was reduced to 30 K. The mass-to-charge spectrum data (Figure 2.1a) was reconstructed and analysed with the IVAS 3.8.2 software. Peaks twice higher than the background were ranged and used for the 3D spatial reconstruction.

Table 2.2: Reference material description, analytical parameters and measurement results for U-Pb geochronology

Age (Ma)	Laser energy (pJ)	$\text{UO}_2^{2+} / \text{UO}^{2+}$	$^{206}\text{Pb}^{2+} / \text{UO}_2^{2+}$	2s	F	2s	Corrected $^{206}\text{Pb}/^{238}\text{U}$	2s	Corrected age	2s
949 ± 4.1	200	1.667	0.329	0.009	46.492	1.193	0.1551	0.025	929.627	78.758
	400	0.783	0.426	0.014	35.848	1.177	0.1565	0.031	937.172	93.480
	450	0.781	0.416	0.018	36.713	1.542	0.1524	0.034	914.524	102.864
2580 ± 52	100	2.255	0.906	0.026	54.622	1.557	0.4856	0.096	2551.956	251.057
	200	1.234	1.145	0.027	43.216	1.015	0.4802	0.081	2528.633	196.439
	200	1.237	1.142	0.028	43.337	1.051	0.4791	0.082	2523.872	199.155
	300	1.093	1.208	0.035	40.987	1.181	0.4855	0.091	2551.767	218.964
400	0.902	1.291	0.047	38.34	1.358	0.4894	0.103	2568.346	245.945	

Sample	Y1			xtc				
Specimen	M10	M7	M8	M20	M18	M19	M19	M19

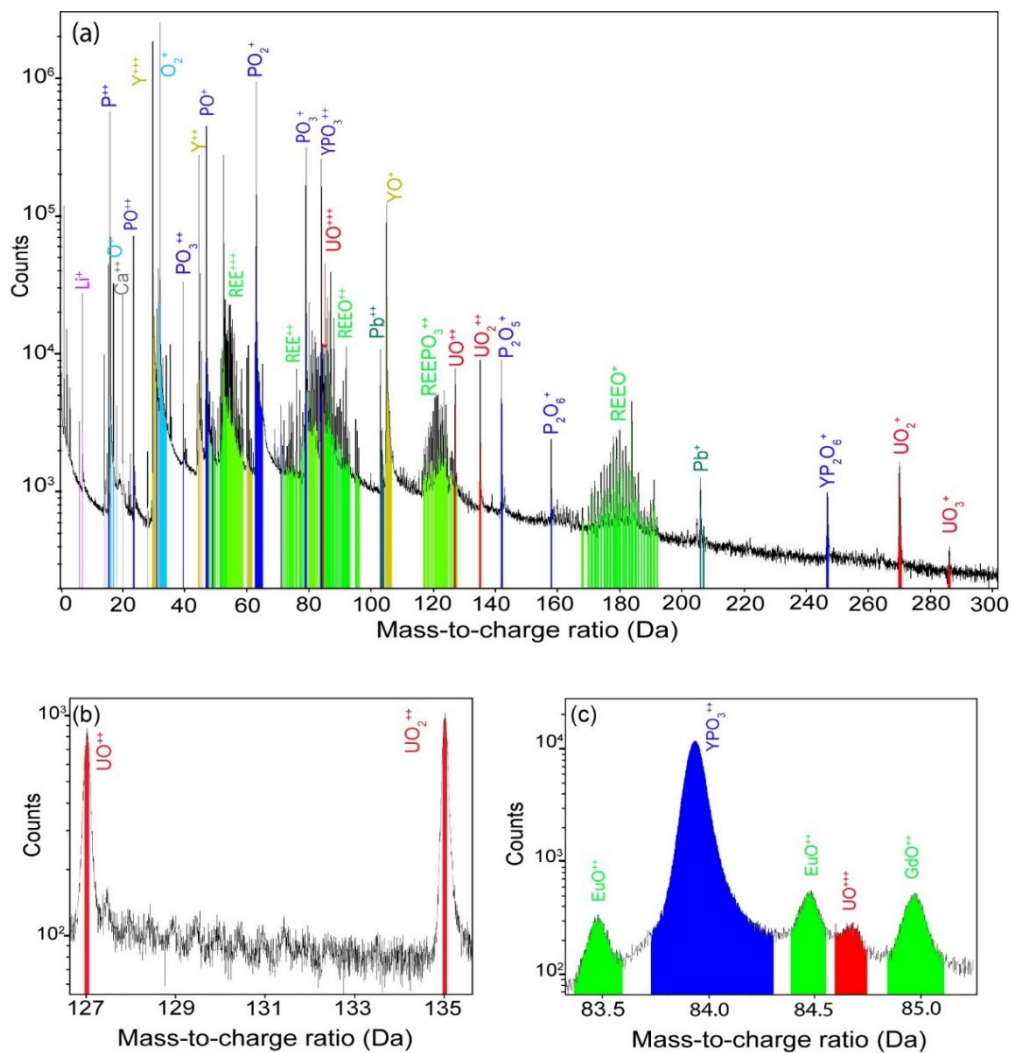


Figure 2.1: (a) Atom probe mass spectra of xenotime (sample – xtc). Peaks are colour-coded by atomic/molecular species. (b) UO_2^{2+} and UO^{2+} molecular peaks used for fractionation correction. (c) Location of major U peak (UO^{3+}) at the tail of YPO_3^{2+} peak.

2.2.4 Isotope quantification

For ^{238}U and ^{206}Pb isotopic quantification, the width of the peak range was fixed to 0.1 Da. A similar approach has been taken for monazite (Fougerouse et al., 2018, 2020), Os alloys (Daly et al., 2018), zircon (Peterman et al., 2016) and pyrite (Fougerouse et al., 2019) and is advantageous to avoid the possible interferences from neighbouring peaks and to compare the peak heights consistently across various data sets and different users. As the background counts in the mass spectrum vary in a single data set and between data sets, the background-corrected counts for each peak were calculated by subtracting the background from the raw counts measured. The local background was estimated with a 1 Da range from an adjacent peak free zone in the mass spectrum. The uncertainties associated with each peak were estimated from counting statistics and background correction.

For ^{207}Pb isotopic measurements, the 0.1 Da range width was applied, and two background correction approaches were tested depending on the quality of mass spectra. In addition to the constant background correction (Figure 2.2a) described above, a method was developed to estimate the noise level in the eventuality of a variable background between the $^{206}\text{Pb}^{2+}$ and $^{207}\text{Pb}^{2+}$ peaks. When the background signal between the $^{206}\text{Pb}^{2+}$ and $^{207}\text{Pb}^{2+}$ was elevated compared with the background before the $^{206}\text{Pb}^{2+}$ peak (Figure 2.2b), the tail of the $^{206}\text{Pb}^{2+}$ peak is assumed to elevate the background beneath the $^{207}\text{Pb}^{2+}$ peak. A variable approximation method (Figure 2.2b) is then employed to estimate the background below the $^{207}\text{Pb}^{2+}$ peak, by defining a straight line through two points from lower and higher Dalton values than the $^{207}\text{Pb}^{2+}$ peak. The two points were taken from the point of minimum background between the $^{206}\text{Pb}^{2+}$ and $^{207}\text{Pb}^{2+}$ peaks and ThPO_3^{3+} and $^{208}\text{Pb}^{2+}$ peaks.

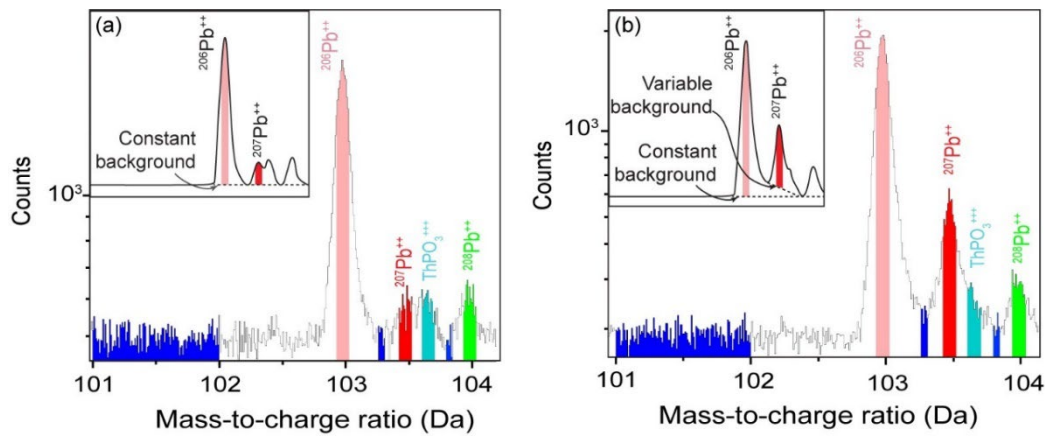


Figure 2.2: (a) Atom probe mass spectrum showing Pb^{2+} peaks of reference material Y1. Shows the constant background before and after $^{206}\text{Pb}^{2+}$ is comparable/consistent, which is illustrated in the inset. Negligible thermal peak tail influence. (b) Atom probe mass spectrum showing Pb^{2+} peaks of reference material xtc. Blue indicates the background. The figure shows the elevated background in between $^{206}\text{Pb}^{2+}$ and $^{207}\text{Pb}^{2+}$ peaks due to the influence of the thermal peak tail of $^{206}\text{Pb}^{2+}$ compared with the constant background (101–102 Da). An illustration of the background correction technique is shown in the inset.

2.3 Results

2.3.1 Characteristics of xenotime APT analysis

The mass spectrum of xenotime obtained by APT is complex with the presence of singly to triply charged major species, including various REE (rare earth elements), REEO and REEPO₃ molecular species (Figure 2.1a) and mass peaks up to 300 Da are obtained. Major elements (Y, P) in the mass spectra are present as elemental forms in different charge states (Y – 2+, 3+ and P – 1+, 2+) and oxygen in its elemental (O^+) and molecular (O_2^+) form. These major elements are combined to form oxides and phosphorus-bearing molecules and are distributed throughout the mass spectra in different charge states. MG-1, BS-1 and xtc are homogenous for every ionic species (Figure 2.3). Y1 contained numerous Ca-rich clusters, whereas all the other ions were found to be homogenous, including Pb and U. The clusters are ~ 5–10 nm in diameter, spaced ~ < 50 nm apart and are marked by an increase in Ca (from ~ 1.5 to 8.5 at. %). These clusters may represent a separate phase such as nano-inclusions observed in monazite (Fougerouse et al., 2018; Seydoux-Guillaume et al., 2019) rather than a xenotime domain enriched in impurities similar to Pb-rich clusters observed in zircon and rutile (Valley et al., 2014; Peterman et al., 2016a; Verberne et al., 2020). In the xenotime mass spectrum (Figure 2.1a), there are U and Pb peaks in xtc and Y1; however, due to the low

concentration of U-Th and Pb in MG-1 and BS-1 (Table 2.1), the Pb peaks are barely above the background level and challenging to quantify. Therefore, the Pb-Pb and U-Pb isotope systematics are focussed on the high U-Th-Pb samples Y1 and xtc. No major peaks could be attributed to Th in xenotime. There is isobaric interference between the major Th species observed in xenotime (ThO^{2+}) and TmPO_3^{2+} (~ 124 Da) rendering impossible its quantification. The only Th species peak observed in the mass spectrum is the minor ThPO_3^{3+} molecule. Therefore, only U-Pb systematics are considered in this study.

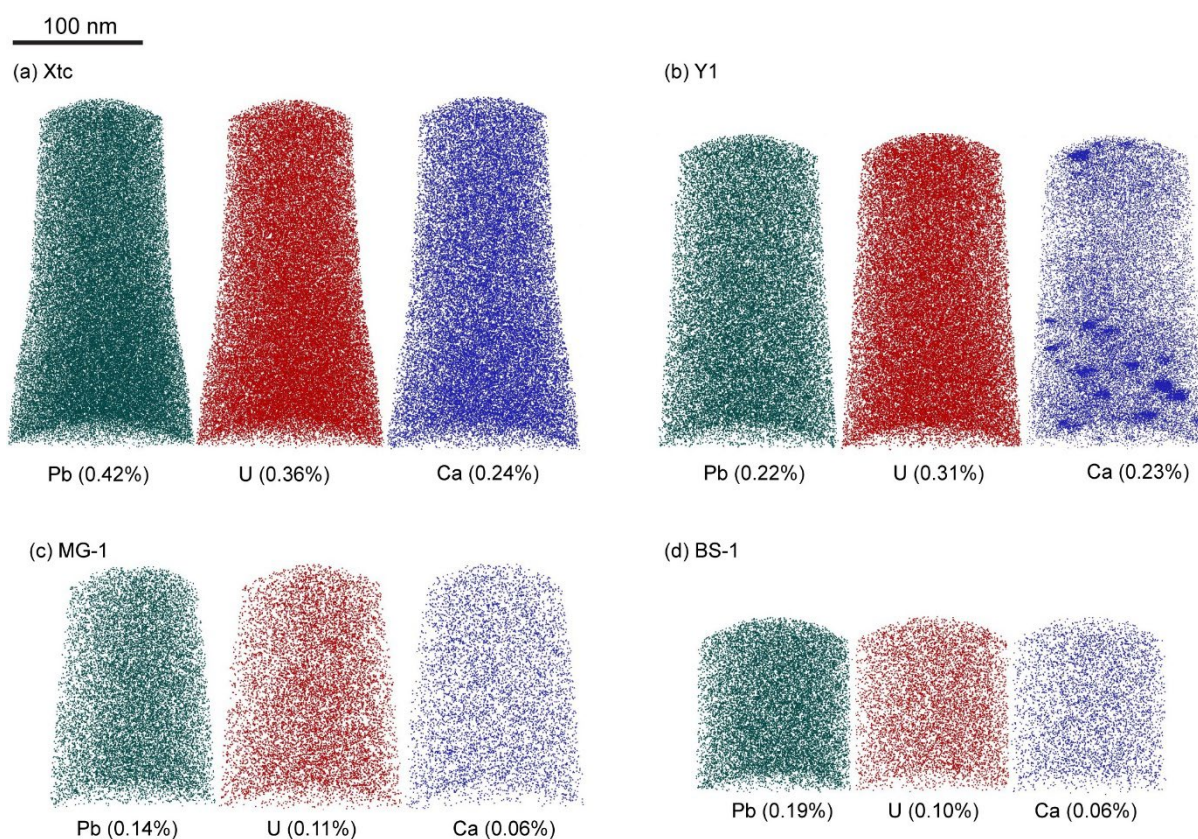


Figure 2.3: Three-dimensional reconstructed atom probe maps of Pb ($^{206}\text{Pb} + ^{207}\text{Pb} + ^{208}\text{Pb}$), U (UO_2) and Ca of four reference materials xtc (a), Y1 (b), MG-1 (c), BS-1 (d). One sphere represents one atom. (b) Y1 shows the presence of Ca-rich clusters in the specimen. Concentration showed in atomic percentage.

The effect of laser pulse energy on different variables in APT analysis on samples BS-1, MG-1, Y1 and xtc is shown in Figure 2.4 (Bachhav et al., 2011; Saxey et al., 2017). The ratio between two charge states of a given ionic species can provide an estimation of the electric field behaviour during the analysis. The $^{206}\text{Pb}^{2+}/^{206}\text{Pb}^+$ ratio follows a negative trend with laser energy (Figure 2.4a). Sample (xtc) at particular laser energy (200 pJ) was found to be similar.

In the IVAS software package, the global background noise of mass spectra is measured in ppm ns⁻¹. The overall background noise decreases with increasing laser pulse energy (Figure 2.4b) with up to 50% noise decrease from 50 to 400 pJ. The specimen base temperature also has a significant effect on the background decreasing from ~40 ppm ns⁻¹ at 60 K to ~20 ppm ns⁻¹ at 30 K for 300 pJ laser pulse energy.

The percentage of single hits indicates the proportion of detection events in which only a single ion hits the detector, compared with two or more ions reaching the detector within the same time-of-flight window. Multiple hit events can lead to a preferential loss of specific ions (Thuvander et al., 2013). The laser pulse energy is positively correlated with the single hit events proportion (Figure 2.4c). From 100 to 400 pJ, the single hit percentage increases by ~9% for the sample xtc.

The ThPO₃³⁺ peak (103.7 Da) is located in the close vicinity of the ²⁰⁷Pb²⁺ (103.49 Da), and its influence on the ²⁰⁷Pb²⁺ quantification should be assessed (Figure 2.2). For xtc, the ThPO₃³⁺ counts per million atoms increases as laser pulse energy increased. For Y1, the counts show an increase from 200 to 400 pJ and fall at 450 pJ (Figure 2.4d).

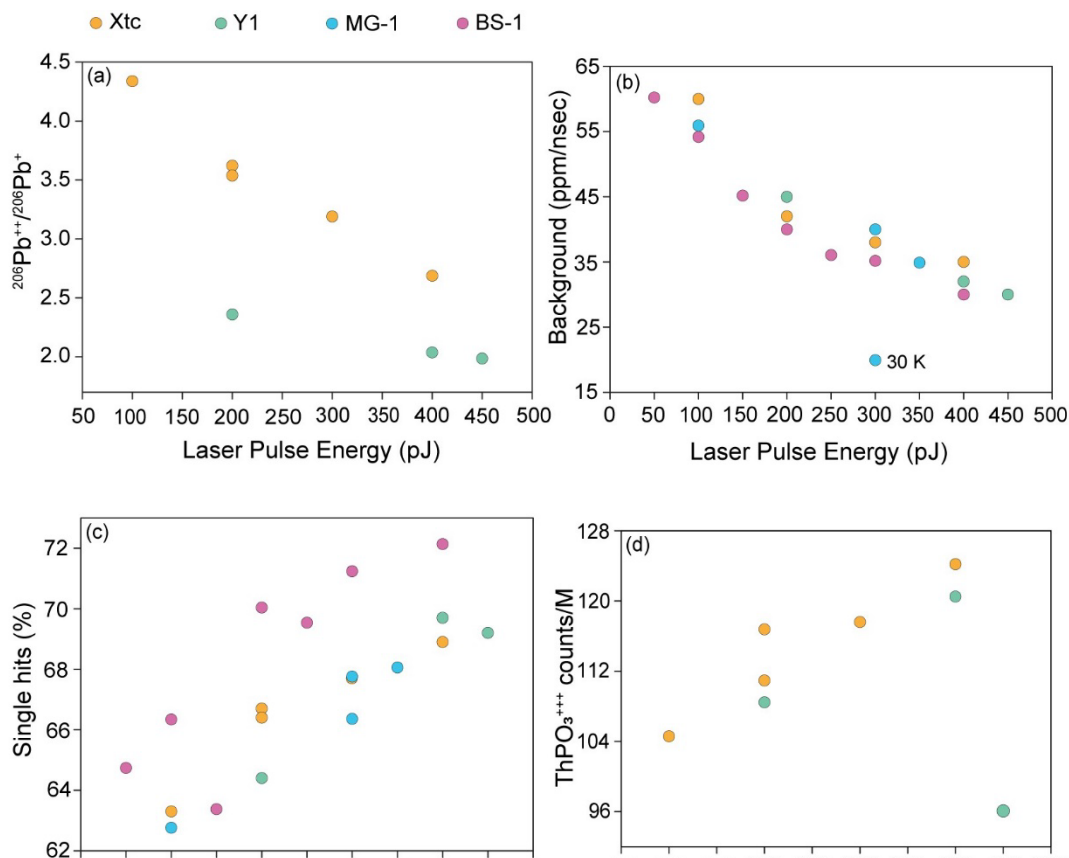


Figure 2.4: All parameters are plotted against laser pulse energy. Specimens are colour coded. (a) ^{206}Pb charge state ratio of xtc and Y1. (b) Background counts measured in ppm ns^{-1} . (c) Percentage of single hits for every analysis. (d) ThPO_3^{3+} counts per million ions.

2.3.2 Pb-Pb systematics

In xenotime, we identify doubly ionised $^{206}\text{Pb}^{2+}$ (102.9), $^{207}\text{Pb}^{2+}$ (103.49), $^{208}\text{Pb}^{2+}$ (103.99) and singly ionised $^{206}\text{Pb}^+$ (205.9) and $^{207}\text{Pb}^+$ (206.9). The ^{204}Pb peaks are not distinguishable from the background in the mass spectra. The doubly charged Pb peaks represent the majority of the Pb signal with $> 75\%$ of the total Pb counts as Pb^{2+} (Figure 2.4a). The $^{207}\text{Pb}^+$ was not always well resolved above the background, and its quantification resulted in large uncertainties compared with the quantification of $^{207}\text{Pb}^{2+}$ only. Therefore, Pb^{2+} was solely used for the calculation of the $^{207}\text{Pb}/^{206}\text{Pb}$ ratio.

Using an adjacent peak free region of the mass spectra (between 101 and 102 Da) and a constant background estimation (same background values for $^{206}\text{Pb}^{2+}$ and $^{207}\text{Pb}^{2+}$), the $^{207}\text{Pb}/^{206}\text{Pb}$ ratio of xtc was determined to range from 0.190 ± 0.010 to 0.203 ± 0.012 (2s; Table 2.3; Figure 2.5a) and differs significantly from the published value of 0.177 ± 0.000105

(Fletcher et al. 2004). The $^{207}\text{Pb}/^{206}\text{Pb}$ ratios of Y1 yielded values between 0.071 ± 0.016 and 0.073 ± 0.025 (2s, Figure 2.5a) in agreement with the published value of 0.070 ± 0.0003 (Fletcher et al. 2000).

Table 2.3: $^{207}\text{Pb}/^{206}\text{Pb}$ geochronology measurement results using constant and variable background estimation.

Specimen	Sample	Age (Ma)	Laser energy (pJ)	Normal constant background correction				Variable approximation background correction					
				$^{207}\text{Pb}^{2+}/^{206}\text{Pb}^{2+}$	2s	Age (Ma)	2s	$^{207}\text{Pb}^{2+}/^{206}\text{Pb}^{2+}$	2s	Age (Ma)	2s		
M10	Y1	949 ± 4.1	200	0.071	0.017	966	480.999						
M7			400	0.072	0.021	987	588.887						
M8			450	0.073	0.026	1015	713.111						
M20	xtc	2632 ± 2	100	0.196	0.013	2794	112.018	0.1778	0.013	2632	122.16		
M18			200	0.192	0.010	2762	87.079	0.1792	0.010	2645	95.533		
M19			200	0.190	0.010	2744	89.403	0.1758	0.010	2613	98.858		
M19			300	0.203	0.012	2852	98.939	0.1921	0.012	2760	106.24		
M19			400	0.198	0.015	2812	123.69	0.1788	0.015	2642	140.76		

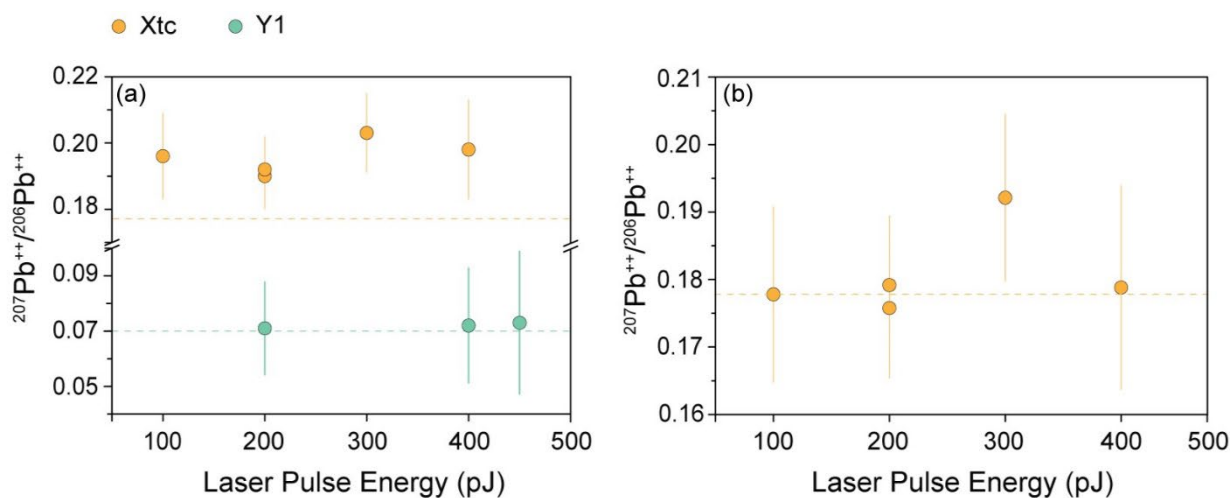


Figure 2.5: $^{207}\text{Pb}/^{206}\text{Pb}$ ratios of xtc and Y1 plotted against laser pulse energy. Errors plotted in $2s$. (a) Graph showing the results of $^{207}\text{Pb}/^{206}\text{Pb}$ ages of xtc and Y1 using constant background correction. (b) $^{207}\text{Pb}/^{206}\text{Pb}$ ratios of xtc using a variable approximation method.

For Y1, the background level between the Pb^{2+} peak was constant, whereas the noise before the $^{207}\text{Pb}^{2+}$ peak was higher than the background level before the $^{206}\text{Pb}^{2+}$ peak for xtc (Figure 2.2a,b). Using the variable background approximation method, the $^{207}\text{Pb}/^{206}\text{Pb}$ ratio of xtc and its uncertainty at $2s$ ranged from 0.176 ± 0.010 (200 pJ) to 0.179 ± 0.010 (200 pJ), which corresponds to an age range of 2613 ± 98 to 2645 ± 95 Ma (Figure 2.5b). One outlier specimen analysed at 300 pJ yielded a ratio of 0.192 ± 0.012 (2760 ± 106 Ma; Table 2.3). Regardless of the background correction method used, the uncertainty of the $^{207}\text{Pb}/^{206}\text{Pb}$ ratio increases with a higher laser pulse energy.

2.3.3 U-Pb systematics

Uranium peaks present in the mass spectrum include $^{238}\text{UO}_2^{2+}$ (135.02 Da), $^{238}\text{UO}^{2+}$ (127.02 Da; Figure 2.1b), $^{238}\text{UO}^{3+}$ (84.68 Da), $^{238}\text{UO}_2^+$ (270.04 Da) and $^{238}\text{UO}_3^+$ (286.04 Da; Figure 2.1a, b). No peaks were present above the background for ^{235}U species. Given the spread of the U signal in numerous peaks, the quantification of the total U is challenging and the background correction on the minor U peaks ($^{238}\text{UO}_3^+$ and $^{238}\text{UO}^{3+}$) increases significantly the overall uncertainty on the ^{238}U quantification. Moreover, the $^{238}\text{UO}^{3+}$ peak (84.68 Da) is strongly affected by the YPO_3^{2+} (89.93 Da) thermal peak tail (Figure 2.1c) and is in close proximity to the EuO^{2+} and GdO^{2+} peaks, making the $^{238}\text{UO}^{3+}$ quantification and background estimation difficult.

A more robust approach to age determination by APT is to determine a fractionation correction (Fougerouse et al. 2020). We used the two major U (UO_2^{2+}) and Pb ($^{206}\text{Pb}^{2+}$) species measured by APT to define the fractionation factor F from the published $^{206}\text{Pb}/^{238}\text{U}$ ratio following Equation (1).

$$F = \left(\frac{\left(\frac{^{206}\text{Pb}}{^{238}\text{U}} \right)_{\text{True}}}{\left(\frac{^{206}\text{Pb}^{++}}{^{238}\text{UO}_2^{++}} \right)_{\text{Measured}}} \right) * 100 \quad (1)$$

The $^{206}\text{Pb}^{2+}/^{238}\text{UO}_2^{2+}$ ratio of both Y1 and xtc obtained from APT analyses shows a positive correlation with the laser pulse energy (Figure 2.6a). $\text{UO}_2^{2+}/\text{UO}^{2+}$ ratio decreased as laser pulse energy increased for both reference materials (Figure 2.6b) suggesting a relationship between U molecular formation and laser pulse energy. Using xtc and Y1, a correlation is apparent between the $^{206}\text{Pb}/^{238}\text{U}$ fractionation and the $\text{UO}_2^{2+}/\text{UO}^{2+}$ ratio (Figure 2.7). Other ionic species defining an apparent correlation with the $^{206}\text{Pb}/^{238}\text{U}$ fractionation coefficient were tested including $\text{PO}^{2+}/\text{PO}^+$, $\text{YO}^{2+}/\text{YO}^+$ and $\text{UO}_2^{2+}/\text{UO}_2^+$; however, the $\text{UO}_2^{2+}/\text{UO}^{2+}$ ratio defined the best correlation with a linear regression yielding a coefficient of determination (R^2) of 0.9843 and an equation $y = 12.06 (\pm 0.621) x + 27.442 (\pm 0.827)$. A prediction interval can be defined using Equation (2) (Geisser, 1993). For any value within the range of $\text{UO}_2^{2+}/\text{UO}^{2+}$ measured, the 95% probability prediction interval for the mean value of y (\hat{y}) is defined by the following expression (Equation (2)):

$$\hat{y} \pm t_{\alpha/2} \cdot \text{SE} \cdot \sqrt{1 + \frac{1}{n} + \frac{(x - \bar{x})^2}{(n-1) \cdot S_x^2}} \quad (2)$$

where $t_{\alpha/2}$ is the t -statistic parameter for 95% confidence, SE the standard error, n the number of observations, \bar{x} and s_x^2 the mean and sample variance of all reference materials $\text{UO}_2^{2+}/\text{UO}^{2+}$ values, respectively.

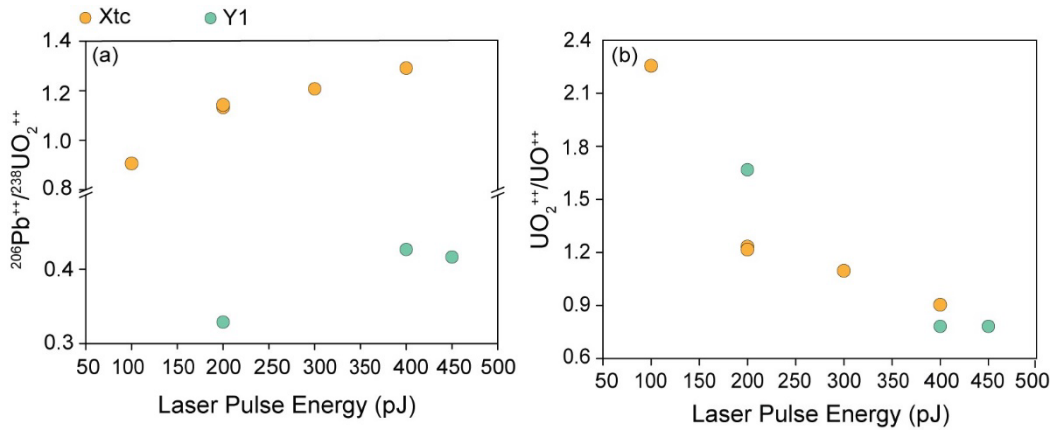


Figure 2.6: (a) $^{206}\text{Pb}^{2+}/^{238}\text{UO}_2^{2+}$ ratio plotted against laser pulse energy. (b) $\text{UO}_2^{2+}/\text{UO}^{2+}$ ratio against laser pulse energy. Uncertainties at $2s$ are smaller than the symbols.

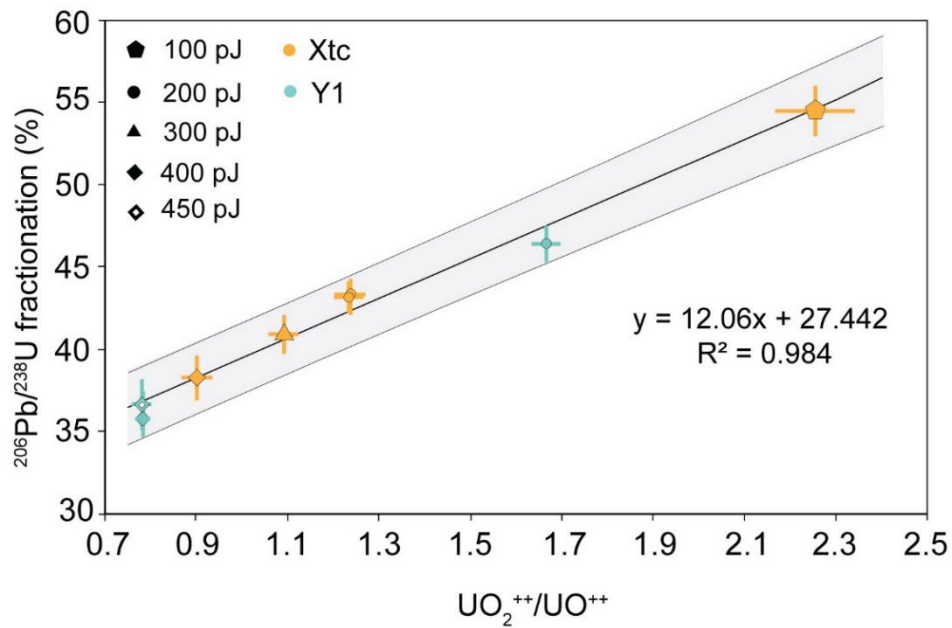


Figure 2.7: The $\text{UO}_2^{2+}/\text{UO}^{2+}$ ratio correlated with $^{206}\text{Pb}/^{238}\text{U}$ fractionation (%) for xtc and Y1 samples. Linear regression through all data points gives an R^2 value of 0.984 and is defined by the equation $y = 12.06(\pm 0.621)x + 27.442(\pm 0.826)$. The grey band represents the 95% prediction band.

2.4 Discussion

2.4.1 Xenotime analysis in APT

No APT studies of xenotime are available in the literature, and therefore, the instrumental running conditions need to be investigated to assess their influence on data quality and accuracy. Laser pulse energy is the prime factor controlling the data quality in laser-assisted atom probe analyses (Kirchhofer et al., 2014; Santhanagopalan et al., 2015).

The charge state ratio of an ionic species provides a qualitative assessment of the electric field strength (Kingham, 1982; Schreiber et al., 2014). In xenotime, the $^{206}\text{Pb}^{2+}/^{206}\text{Pb}^+$ shows a negative trend (Figure 2.4a) indicating a weaker electric field at higher laser pulse energy. The high temperature from the laser pulse to the specimen apex lowers the electric field required to evaporate the sample and thereby reducing the stress on the specimen, which increases the specimen yield. A similar trend has also been observed in zircon (La Fontaine et al., 2017; Saxey et al., 2017) and monazite (Fougerouse et al., 2020).

The background noise is a direct metric of data quality for every mass spectrometry technique and the chemical and isotopic quantification largely depends on this measurement. The background in the APT data arises from several factors such as (a) evaporation events that are out-of- synchronisation with the laser pulse, (b) residual gas molecules in the chamber that become ionised and detected and (c) local elevation of the background due to the thermal tail of a major peak (d) surface diffusion of ions from the needle due to high thermal energy from high laser pulse energies and subsequent ionisation (Larson et al., 2013; Meisenkothen et al., 2020). The overall background level is significantly lower at higher laser pulse energy (Figure 2.4b). As the higher laser pulse energy can contribute to the thermal peak tails due to the slow cooling of the tip, the low background observed at higher laser pulse energy is primarily due to fewer out-of-synchronisation events. A low base temperature has the same effect, with lower background noise at 30 K. This effect is expected because a low base temperature augments the mass resolving power by facilitating high heat flow rates in the tip apex, which also helps to improve vacuum levels in the analysis chamber resulting in a low background (Larson et al. 2013). However, low base temperature was found to reduce the specimen yield during APT analysis (Saxey et al. 2017).

Multi-hit ions are often closely spaced in space and time, and hence, deconvolution of the signals is difficult and reduces detector efficiency (Williams et al., 2013). Single hit events

have been found to increase in proportion at higher laser energies (Figure 2.4c). This trend can be attributed to the weaker field originating from high laser pulse energy.

The plausible influence of a minor ionic species of Th, ThPO_3^{3+} (103.7 Da) on $^{207}\text{Pb}^{2+}$ (103.49 Da) counts were also considered. From the data, it is apparent that the ThPO_3^{3+} counts increased with higher laser pulse energy, except for one point from Y1 (Figure 2.4d). This can be attributed to the combined effect of high laser pulse energy and low field strength, which in turn favours the formation of complex molecules (Kirchhofer et al., 2013; Larson et al., 2013; Saxey et al., 2017).

2.4.2 $^{207}\text{Pb}/^{206}\text{Pb}$ age

Considerable research has been done on the spectral analysis of Pb isotopes on zircon and baddeleyite using APT (Blum et al., 2017; Reinhard et al., 2017; Saxey et al., 2017). $^{207}\text{Pb}/^{206}\text{Pb}$ ages from nanoscale domains and clusters have been used to derive critical information on geological history using zircons (Valley et al., 2014, 2015; Peterman et al., 2016; Piazzolo et al., 2016; Arcuri et al., 2020), baddeleyite (White et al., 2017, 2019) and pyrite (Fougerouse et al., 2019).

Using a constant background estimation, (i.e., subtracting the background signal estimated from a peak free region with a 1 Da range (101–102 Da) from the $^{206}\text{Pb}^{2+}$ and $^{207}\text{Pb}^{2+}$ peaks), the $^{207}\text{Pb}/^{206}\text{Pb}$ ratio is higher than the true value for xtc, whereas the $^{207}\text{Pb}/^{206}\text{Pb}$ ratio for Y1 is in agreement with the published value (Figure 2.5a). The high $^{207}\text{Pb}/^{206}\text{Pb}$ ratio of xtc is attributed to the $^{206}\text{Pb}^{2+}$ thermal peak tail influencing the background counts below the $^{207}\text{Pb}^{2+}$ peak resulting in the overestimation of the $^{207}\text{Pb}^{2+}$ signal (Figure 2.2b).

To calculate the compositional data from the complex APT mass spectra, several methods are in practice, including deconvolution of peak overlaps and peak fitting using Gaussian or exponentially modified Gaussian function (Vella et al., 2011; Johnson et al., 2013; Cairney et al., 2015; London et al., 2017) and filter the multiple hits from the data (Meisenkothen et al., 2020). For zircon and rutile, these tails were modelled using an exponential function (Blum et al. 2017, Verberne et al. 2020). However, there is no commonly accepted method for modelling the ^{206}Pb peak shape and the xenotime data show that the $^{206}\text{Pb}^{2+}$ peak tail has a flat profile in proximity to the $^{207}\text{Pb}^{2+}$ peak, making it difficult to confidently model an exponential function over a range of bin sizes. Being able to quantify the

background level consistently is important as it has been demonstrated that these user-dependent choices can affect the results within the same data set (Exertier et al., 2018). Instead, the background was estimated by a linear approximation of the background by defining a straight line using the background level before the $^{207}\text{Pb}^{2+}$ peak from a range of 103.24 to 103.34 Da and after the $^{207}\text{Pb}^{2+}$ peak from 103.775 to 103.875 Da range. The background level after the $^{207}\text{Pb}^{2+}$ peak comes back to the normal background level (i.e., background before the $^{206}\text{Pb}^{2+}$ peak). This approach drew more accurate results, for xtc. Using a variable approximation of the background, for sample xtc (Figure 2.5b) the results ranged from 0.176 ± 0.010 (200 pJ) to 0.179 ± 0.010 (200 pJ; 2s) which is consistent with the published value of 0.177 ± 0.000105 (Fletcher et al. 2004). The 300 pJ run for unknown reasons gives a higher value of 0.192 ± 0.012 .

The laser pulse energy has a strong influence on the thermal tail formation which also has been observed in oxide materials (Kirchhofer et al., 2013; La Fontaine et al., 2015; Verberne et al., 2019). Higher laser pulse energy leads to severe thermal tail formation which results from the excess heating of the specimen tip, which in turn retards the cooling time and spans out the ion departure time (Saxey et al. 2017). This trend is not so pronounced in the younger sample Y1 with the negligible influence of the $^{206}\text{Pb}^{2+}$ thermal peak tail. This is probably due to a smaller abundance of Pb in the sample.

The uncertainty associated with the $^{207}\text{Pb}^{2+}/^{206}\text{Pb}^{2+}$ ratio of both samples increases with the increase in laser energy, and this can be explained by the decrease of the Pb^{2+} abundance compared with the Pb^+ counts (Figure 2.4a) due to the lower electric field conditions.

2.4.3 U-Pb age

A linear correlation is apparent between the $\text{UO}_2^{2+}/\text{UO}^{2+}$ ratio and $^{206}\text{Pb}^{2+}/^{238}\text{UO}_2^{2+}$ fractionation coefficient, from 100 to 450 pJ laser energy, resulting an equation of $y = 12.06(\pm 0.621)x + 27.442(\pm 0.826)$. Similar approaches [$\ln(\text{Pb}^+/\text{U}^+); \ln(\text{UO}^+/\text{U}^+)$] have been used in SHRIMP data reduction to correct for associated U-Pb fractionation (Fletcher et al. 2000, 2004; Ireland et al., 2008).

Using this correlation, it is possible to correct the $^{206}\text{Pb}^{2+}/^{238}\text{UO}_2^{2+}$ ratio and provide $^{206}\text{Pb}/^{238}\text{U}$ ages for a volume of $< 0.008 \mu\text{m}^3$, and also to propagate the uncertainties resulting from counting statistics, background and fractionation correction. To test the level of uncertainties using this protocol, we corrected the same xtc and Y1 whole data sets used to define the

fractionation correction. For xtc, the APT $^{206}\text{Pb}/^{238}\text{U}$ ages ranged from 2523 ± 199 to 2568 ± 245 Ma with a weighted mean age of 2542 ± 96 Ma ($2s$, $n=5$, $\text{MSWD}=0.028$, probability=0.998; Figure 2.8a). For Y1, the APT individual analyses range from 914 ± 102 to 937 ± 93 Ma with a weighted mean age of 928 ± 51 Ma ($2s$, $n=3$, $\text{MSWD}=0.054$, probability=0.95 (Figure 2.8b). For individual analyses, the uncertainties were in the range of 7–11% ($2s$) and decreases to $\sim 5.5\%$ for weighted mean ages (xtc, $n = 5$).

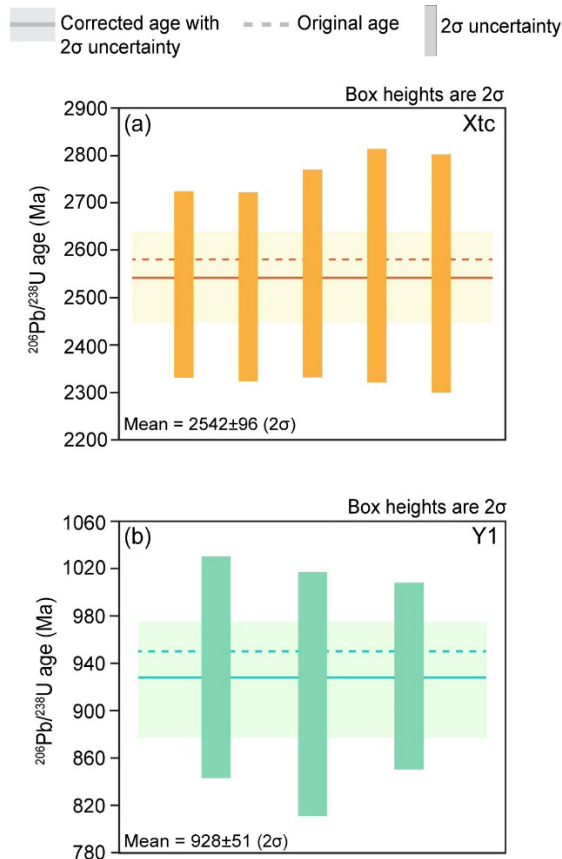


Figure 2.8: Weighted mean data of (a) xtc (orange) and (b) Y1 (green). The solid line represents the weighted mean age obtained from the data and the dotted lines represent the actual age of the specimens. The square band represents the uncertainties plotted ($2s$).

2.5 Recommendations and conclusions

Nanogeochronology of xenotime using APT requires instrumental parameters to be optimised for acquiring reliable data and to improve associated uncertainties. Concerning $^{207}\text{Pb}/^{206}\text{Pb}$ ages, the prominent charge state in which Pb is found in APT mass spectra is as doubly charged ($^{206}\text{Pb}^{2+}$ at 102.9 Da and $^{207}\text{Pb}^{2+}$ at 103.49 Da). Therefore, the accuracy and precision of Pb-Pb dates using APT from xenotime depend on how well we

characterise these peaks. It was found that the $^{206}\text{Pb}^{2+}$ peak tail can lead to overestimating ^{207}Pb counts for high Pb containing crystals. The laser pulse energy has a distinctive influence on the thermal peak tail formation, as the thermal tails increase in proportion to the laser pulse energy. In addition, at higher laser energy the proportion of Pb^+ ions is higher and degrades the Pb^{2+} counting statistics (Figure 2.4a). Furthermore, higher laser energy favours ThPO_3^{3+} molecular formation and plausibly contributes to the overestimation of $^{207}\text{Pb}^{2+}$ counts. However, very low laser energy may lead to reduced specimen yield and increased background noise (Figure 2.4b). Therefore, we suggest an optimal range of laser pulse energy between 100 and 200 pJ. Furthermore, for samples with lower Pb concentration (negligible thermal peak tail from $^{206}\text{Pb}^{2+}$), it is suggested that the constant background correction is used, and for samples with high Pb concentration, the variable approximation of the background should be employed to correct for the overestimation of $^{207}\text{Pb}^{2+}$ counts.

The method developed in this study allows correction of the $^{206}\text{Pb}/^{238}\text{UO}_2$ fractionation for xenotime samples of different compositions and age, extrinsic instrumental parameters such as laser energy but also intrinsic parameters such as specimen geometry and voltage range. The optimum pulse rate for xenotime analysis is determined to be 125 kHz in order to acquire all mass peaks, especially U peaks at high masses (UO_2^+ at 270.04 Da and UO_3^+ at 286.04 Da). The associated uncertainties can be reduced by using weighted mean ages from several analyses.

In conclusion, $^{207}\text{Pb}/^{206}\text{Pb}$ and $^{206}\text{Pb}/^{238}\text{U}$ ages can be obtained from xenotime for volume 4 to 6 orders of magnitude smaller than previous methods using APT. However, the actinide composition of the xenotime has a critical impact on the data, and crystals containing low U (for example of diagenetic or hydrothermal origin) or young samples may not be suitable for the current sensitivity of the available APT instrumentation. The uncertainties obtained were <11% for individual analyses and can be reduced by calculation of weighted mean ages. Although less precise than other methods, APT can date xenotime grains smaller than 1 μm as well as nano-inclusions/altered sub-domains with geologically meaningful uncertainties.

2.6 Acknowledgements

Mounts UWA A-13 and 05-12 used in this project are part of the McNaughton Legacy Collection, which was created by the John de Laeter Centre (Brent McInnes – 0000-0002-2776-0574, Eleanore Blereau – 0000-0001-8850-397X and Neal McNaughton), Curtin University Library (Amanda Bellenger, David Lewis, John Brown, and Colin Meikle) and the Geological

Survey of Western Australia (Michael Wingate – 0000-0003-2528-417X). The project was jointly enabled by NCRIS via AuScope, GSWA and Curtin University. This study was supported by the Australian Science and Industry Endowment Fund (grant SIEF RI13-01) and the Discovery Early Career Research Award from the Australian Research Council to D. Fougere (DE190101307).

2.7 References

- Aleinikoff J. N., Hayes T. S., Evans K. V., Mazdab F. K., Pillers R. M. and Fanning C. M. (2012a) SHRIMP U-Pb Ages of Xenotime and Monazite from the Spar Lake Red Bed-Associated Cu-Ag Deposit, Western Montana: Implications for Ore Genesis. *Econ. Geol.* **107**, 1251–1274.
- Aleinikoff J. N., Lack J. F. S., Lund K., Evans K. V., Fanning C. M., Mazdab F. K., Wooden J. L. and Pillers R. M. (2012b) Constraints on the timing of Co-Cu ± Au mineralization in the Blackbird district, Idaho, using SHRIMP U-Pb ages of monazite and xenotime plus zircon ages of related Mesoproterozoic orthogneisses and metasedimentary rocks. *Econ. Geol.* **107**, 1143–1175.
- Arcuri G. A., Moser D. E., Reinhard D. A., Langelier B. and Larson D. J. (2020) Impact-triggered nanoscale Pb clustering and Pb loss domains in Archean zircon. *Contrib. to Mineral. Petrol.* **175**, 59.
- Bachhav M., Danoix R., Danoix F., Hannoyer B., Ogale S. and Vurpillot F. (2011) Investigation of wustite (Fe_{1-x}O) by femtosecond laser assisted atom probe tomography. *Ultramicroscopy* **111**, 584–588.
- Beccaletto L., Bonev N., Bosch D. and Bruguier O. (2007) Record of a Palaeogene syn-collisional extension in the north Aegean region: Evidence from the Kemer micaschists (NW Turkey). *Geol. Mag.* **144**, 393–400.
- Blum T. B., Reinhard D. A., Chen Y., Prosa T. J., Larson D. J. and Valley J. W. (2017) Uncertainty and sensitivity analysis for spatial and spectral processing of Pb isotopes in zircon by atom probe tomography. *Geophys. Monogr. Ser.* **232**, 327–350.
- Brown S. M., Fletcher I. R., Stein H. J., Snee L. W. and Groves D. I. (2002) Geochronological Constraints on Pre-, Syn-, and Postmineralization Events at the World-Class Cleo Gold Deposit, Eastern Goldfields Province, Western Australia. *Econ. Geol.* **97**, 541–559.

- Budzyń B., Sláma J., Kozub-Budzyń G. A., Konečný P., Holický I., Rzepa G. and Jastrzębski M. (2018) Constraints on the timing of multiple thermal events and re-equilibration recorded by high-U zircon and xenotime: Case study of pegmatite from Piława Górna (Góry Sowie Block, SW Poland). *Lithos* **310**–311, 65–85.
- Cairney J. M., Rajan K., Haley D., Gault B., Bagot P. A. J., Choi P.-P., Felfer P. J., Ringer S. P., Marceau R. K. W. and Moody M. P. (2015) Mining information from atom probe data. *Ultramicroscopy* **159**, 324–337.
- Cavosie A. J., Montalvo P. E., Timms N. E. and Reddy S. M. (2016) Nanoscale deformation twinning in xenotime, a new shocked mineral, from the Santa Fe impact structure (New Mexico, USA). *Geology* **44**, 803–806.
- Cherniak D. J. (2006) Pb and rare earth element diffusion in xenotime. *Lithos* **88**, 1–14.
- Cocherie A. and Legendre O. (2007) Potential minerals for determining U-Th-Pb chemical age using electron microprobe. *Lithos* **93**, 288–309.
- Daly L., Bland P. A., Tessalina S., Saxey D. W., Reddy S. M., Fougereuse D., Rickard W. D. A., Forman L. V., La Fontaine A., Cairney J. M., Ringer S. P., Schaefer B. F. and Schwander D. (2018) Defining the Potential of Nanoscale Re-Os Isotope Systematics Using Atom Probe Microscopy. *Geostand. Geoanalytical Res.* **42**, 279–299.
- Exertier F., La Fontaine A., Corcoran C., Piazzolo S., Belousova E., Peng Z., Gault B., Saxey D. W., Fougereuse D., Reddy S. M., Pedrazzini S., Bagot P. A. J., Moody M. P., Langelier B., Moser D. E., Botton G. A., Vogel F., Thompson G. B., Blanchard P. T., Chiaramonti A. N., Reinhard D. A., Rice K. P., Schreiber D. K., Kruska K., Wang J. and Cairney J. M. (2018) Atom probe tomography analysis of the reference zircon gJ-1: An interlaboratory study. *Chem. Geol.* **495**, 27–35.
- Fletcher I. R., McNaughton N. J., Aleinikoff J. A., Rasmussen B. and Kamo S. L. (2004) Improved calibration procedures and new standards for U - Pb and Th - Pb dating of Phanerozoic xenotime by ion microprobe. *Chem. Geol.* **209**, 295–314.
- Fletcher I. R., Rasmussen B. and McNaughton N. J. (2000) SHRIMP U-Pb geochronology of authigenic xenotime and its potential for dating sedimentary basins. *Aust. J. Earth Sci.* **47**, 845–859.
- Fougereuse D., Kirkland C. L., Saxey D. W., Seydoux-Guillaume A. M., Rowles M. R., Rickard W. D. A. and Reddy S. M. (2020) Nanoscale Isotopic Dating of Monazite.

Geostand. Geoanalytical Res. **44**, 637–652.

Fougerouse D., Reddy S. M., Kirkland C. L., Saxey D. W., Rickard W. D. and Hough R. M. (2019) Time-resolved, defect-hosted, trace element mobility in deformed Witwatersrand pyrite. *Geosci. Front.* **10**, 55–63.

Fougerouse D., Reddy S. M., Saxey D. W., Erickson T. M., Kirkland C. L., Rickard W. D. A., Seydoux-Guillaume A.-M., Clark C. and Buick I. S. (2018) Nanoscale distribution of Pb in monazite revealed by atom probe microscopy. *Chem. Geol.* **479**, 251–258.

Fougerouse D., Reddy S. M., Seydoux-Guillaume A.-M., Kirkland C. L., Erickson T. M., Saxey D. W., Rickard W. D. A., Jacob D., Leroux H. and Clark C. (2021) Mechanical twinning of monazite expels radiogenic lead. *Geology* **49**, 417–421.

Gault B., Moody M. P., Cairney J. M. and Ringer S. P. (2012) *Atom Probe Microscopy*, Springer New York, New York, NY. **160**, 396

Geisser S. (1993) *Predictive inference: an introduction*, Chapman and Hall, New York, NY, 240.

Hetherington C. J., Jercinovic M. J., Williams M. L. and Mahan K. (2008) Understanding geologic processes with xenotime: Composition, chronology, and a protocol for electron probe microanalysis. *Chem. Geol.* **254**, 133–147.

Ireland T. R., Clement S., Compston W., Foster J. J., Holden P., Jenkins B., Lanc P., Schram N. and Williams I. S. (2008) Development of SHRIMP. *Aust. J. Earth Sci.* **55**, 937–954.

Johnson L. J. S., Thuvander M., Stiller K., Odén M. and Hultman L. (2013) Blind deconvolution of time-of-flight mass spectra from atom probe tomography. *Ultramicroscopy* **132**, 60–64.

Kingham D. R. (1982) The post-ionization of field evaporated ions: A theoretical explanation of multiple charge states. *Surf. Sci.* **116**, 273–301.

Kirchhofer R., Diercks D. R., Gorman B. P., Ihlefeld J. F., Kotula P. G., Shelton C. T. and Brennecke G. L. (2014) Quantifying Compositional Homogeneity in Pb(Zr,Ti)O₃ Using Atom Probe Tomography. *J. Am. Ceram. Soc.* **97**, 2677–2697.

Kirchhofer R., Teague M. C. and Gorman B. P. (2013) Thermal effects on mass and spatial resolution during laser pulse atom probe tomography of cerium oxide. *J. Nucl. Mater.*

- La Fontaine A., Gault B., Breen A., Stephenson L., Ceguerra A. V., Yang L., Dinh Nguyen T., Zhang J., Young D. J. and Cairney J. M. (2015) Interpreting atom probe data from chromium oxide scales. *Ultramicroscopy* **159**, 354–359.
- La Fontaine A., Piazzolo S., Trimby P., Yang L. and Cairney J. M. (2017) Laser-Assisted Atom Probe Tomography of Deformed Minerals: A Zircon Case Study. *Microsc. Microanal.* **23**, 404–413.
- Larson D. J., Prosa T. J., Ulfing R. M., Geiser B. P. and Kelly T. F. (2013) Local Electrode Atom Probe Tomography.,318
- Li L. X., Zi J. W., Meng J., Li H. M., Rasmussen B., Sheppard S., Wilde S. A. and Li Y. H. (2020) Using in situ monazite and xenotime U-Pb geochronology to resolve the fate of the “missing” banded iron formation-hosted high-grade hematite ores of the North China craton. *Econ. Geol.* **115**, 189–204.
- Li Q. L., Li X. H., Lan Z. W., Guo C. L., Yang Y. N., Liu Y. and Tang G. Q. (2013) Monazite and xenotime U-Th-Pb geochronology by ion microprobe: Dating highly fractionated granites at Xihuashan tungsten mine, SE China. *Contrib. to Mineral. Petrol.* **166**, 65–80.
- Liu Z. C., Wu F. Y., Guo C. L., Zhao Z. F., Yang J. H. and Sun J. F. (2011) In situ U-Pb dating of xenotime by laser ablation (LA)-ICP-MS. *Chinese Sci. Bull.* **56**, 2948–2956.
- London A. J., Haley D. and Moody M. P. (2017) Single-Ion Deconvolution of Mass Peak Overlaps for Atom Probe Microscopy. *Microsc. Microanal.* **23**, 300–306.
- McNaughton N. J., Rasmussen B. and Fletcher I. R. (1999) SHRIMP uranium-lead dating of diagenetic xenotime in siliciclastic sedimentary rocks. *Science*, **285**, 78–80.
- Meisenkothen F., Samarov D. V., Kalish I. and Steel E. B. (2020) Exploring the accuracy of isotopic analyses in atom probe mass spectrometry. *Ultramicroscopy* **216**, 113018.
- Peterman E. M., Reddy S. M., Saxey D. W., Snoeyenbos D. R., Rickard W. D. A., Fougereuse D. and Kylander-Clark A. R. C. (2016) Nanogeochronology of discordant zircon measured by atom probe microscopy of Pb-enriched dislocation loops. *Sci. Adv.* **2**.
- Piazzolo S., La Fontaine A., Trimby P., Harley S., Yang L., Armstrong R. and Cairney J. M. (2016) Deformation-induced trace element redistribution in zircon revealed using atom

- probe tomography. *Nat. Commun.* **7**, 10490.
- Rasmussen B. (2005) Radiometric dating of sedimentary rocks: The application of diagenetic xenotime geochronology. *Earth-Science Rev.* **68**, 197–243.
- Rasmussen B., Fletcher I. R. and Muhling J. R. (2011) Response of xenotime to prograde metamorphism. *Contrib. to Mineral. Petrol.* **162**, 1259–1277.
- Rasmussen B., Fletcher I. R., Muhling J. R., Thorne W. S. and Broadbent G. C. (2007) Prolonged history of episodic fluid flow in giant hematite ore bodies: Evidence from in situ U-Pb geochronology of hydrothermal xenotime. *Earth Planet. Sci. Lett.* **258**, 249–259.
- Rasmussen B., Mueller A. G. and Fletcher I. R. (2009) Zirconolite and xenotime U-Pb age constraints on the emplacement of the golden mile dolerite sill and gold mineralization at the Mt charlotte mine, Eastern Goldfields Province, Yilgarn Craton, Western Australia. *Contrib. to Mineral. Petrol.* **157**, 559–572.
- Reddy S. M., Saxey D. W., Rickard W. D. A., Fougereuse D., Montalvo S. D., Verberne R. and van Riessen A. (2020) Atom Probe Tomography: Development and Application to the Geosciences. *Geostand. Geoanalytical Res.* **44**, 5–50.
- Reinhard D. A., Moser D. E., Martin I., Rice K. P., Chen Y., Olson D., Lawrence D., Prosa T. J. and Larson D. J. (2017) Atom probe tomography of phalaborwa baddeleyite and reference zircon BR266. *Microstruct. Geochronol. Planet. Rec. Down to Atom Scale*, 315–326.
- Rickard W. D. A., Reddy S. M., Saxey D. W., Fougereuse D., Timms N. E., Daly L., Peterman E., Cavosie A. J. and Jourdan F. (2020) Novel Applications of FIB-SEM-Based ToF-SIMS in Atom Probe Tomography Workflows. *Microsc. Microanal.* **26**, 750–757.
- Salier B. P., Groves D. I., McNaughton N. J. and Fletcher I. R. (2005) Geochronological and stable isotope evidence for widespread orogenic gold mineralization from a deep-seated fluid source at ca 2.65 Ga in the Laverton Gold Province, Western Australia. *Econ. Geol.* **100**, 1363–1388.
- Santhanagopalan D., Schreiber D. K., Perea D. E., Martens R. L., Janssen Y., Khalifah P. and Meng Y. S. (2015) Effects of laser energy and wavelength on the analysis of LiFePO₄ using laser assisted atom probe tomography. *Ultramicroscopy* **148**, 57–66.

- Saxey D. W., Reddy S. M., Fougereuse D. and Rickard W. D. A. (2017) The Optimization of Zircon Analyses by Laser-Assisted Atom Probe Microscopy. *In Microstructural Geochronology: Planetary Records Down to Atom Scale* pp. 293–313.
- Schaltegger U., Pettke T., Audétat A., Reusser E. and Heinrich C. A. (2005) Magmatic-to-hydrothermal crystallization in the W–Sn mineralized Mole Granite (NSW, Australia). *Chem. Geol.* **220**, 215–235.
- Schreiber D. K., Chiaramonti A. N., Gordon L. M. and Kruska K. (2014) Applicability of post-ionization theory to laser-assisted field evaporation of magnetite. *Appl. Phys. Lett.* **105**, 18–23.
- Seydoux-Guillaume A.-M., Fougereuse D., Laurent A. T., Gardés E., Reddy S. M. and Saxey D. W. (2019) Nanoscale resetting of the Th/Pb system in an isotopically-closed monazite grain: A combined atom probe and transmission electron microscopy study. *Geosci. Front.* **10**, 65–76.
- Sheppard S., Rasmussen B., Muhling J. R., Farrell T. R. and Fletcher I. R. (2007) Grenvillian-aged orogenesis in the Palaeoproterozoic Gascoyne complex, Western Australia: 1030–950Ma reworking of the Proterozoic Capricorn Orogen. *J. Metamorph. Geol.* **25**, 477–494.
- Spear F. S. and Pyle J. M. (2002) Apatite, monazite, and xenotime in metamorphic rocks (in Phosphates; geochemical, geobiological, and materials importance) Reviews in Mineralogy and Geochemistry. *Rev. Mineral. Geochemistry* **48**, 293–335.
- Suzuki K. and Adachi I. M. (1991) Precambrian provenance and Silurian metamorphism of the Tsubonosawa paragneiss in the South Kitakami terrane, Northeast Japan, revealed by the chemical Th-U-total Pb isochron ages of monazite, zircon and xenotime. *Geochem. J.* **25**, 357–376.
- Suzuki K. and Kato T. (2008) CHIME dating of monazite, xenotime, zircon and polycrase: Protocol, pitfalls and chemical criterion of possibly discordant age data. *Gondwana Res.* **14**, 569–586.
- Thuvander M., Kvist A., Johnson L. J. S., Weidow J. and Andréén H.-O. (2013) Reduction of multiple hits in atom probe tomography. *Ultramicroscopy* **132**, 81–85.
- Valley J. W., Cavosie A. J., Ushikubo T., Reinhard D. A., Lawrence D. F., Larson D. J., Clifton P. H., Kelly T. F., Wilde S. A., Moser D. E. and Spicuzza M. J. (2014) Hadean age for

- a post-magma-ocean zircon confirmed by atom-probe tomography. *Nat. Geosci.* **7**, 219–223.
- Valley J. W., Reinhard D. A., Cavosie A. J., Ushikubo T., Lawrence D. F., Larson D. J., Kelly T. F., Snoeyenbos D. R. and Strickland A. (2015) Presidential Address. Nano-and micro-geochronology in Hadean and Archean zircons by atom-probe tomography and SIMS: New tools for old minerals. *Am. Mineral.* **100**, 1355–1377.
- Vallini D. A., Rasmussen B., Krapež B., Fletcher I. R. and McNaughton N. J. (2005) Microtextures, geochemistry and geochronology of authigenic xenotime: Constraining the cementation history of a Palaeoproterozoic metasedimentary sequence. *Sedimentology* **52**, 101–122.
- Vallini D., Rasmussen B., Krapež B., Fletcher I. R. and McNaughton N. J. (2002) Obtaining diagenetic ages from metamorphosed sedimentary rocks: U-Pb dating of unusually coarse xenotime cement in phosphatic sandstone. *Geology* **30**, 1083–1086.
- Vella A., Mazumder B., Da Costa G. and Deconihout B. (2011) Field evaporation mechanism of bulk oxides under ultra-fast laser illumination. *J. Appl. Phys.* **110**, 044321.
- Verberne R., Reddy S. M., Saxey D. W., Fougereuse D., Rickard W. D. A., Plavsa D., Agangi A. and Kylander-Clark A. R. C. (2020) The geochemical and geochronological implications of nanoscale trace-element clusters in rutile. *Geology* **XX**, 1–5.
- Verberne R., Saxey D. W., Reddy S. M., Rickard W. D. A., Fougereuse D. and Clark C. (2019) Analysis of Natural Rutile (TiO₂) by Laser-assisted Atom Probe Tomography. *Microsc. Microanal.* **25**, 539–546.
- White L. F., Darling J. R., Moser D. E., Reinhard D. A., Dunlop J., Larson D. J., Lawrence D. and Martin I. (2017) Complex Nanostructures in Shocked, Annealed, and Metamorphosed Baddeleyite Defined by Atom Probe Tomography. In *Microstructural Geochronology: Planetary Records Down to Atom Scale* pp. 351–367.
- White L. F., Moser D. E., Tait K. T., Langelier B., Barker I. and Darling J. R. (2019) Crystallization and impact history of a meteoritic sample of early lunar crust (NWA 3163) refined by atom probe geochronology. *Geosci. Front.* **10**, 1841–1848.
- Williams C. A., Smith G. D. W. and Marquis E. A. (2013) Quantifying the composition of yttrium and oxygen rich nanoparticles in oxide dispersion strengthened steels. *Ultramicroscopy* **125**, 10–17.

Zi J. W., Rasmussen B., Muhling J. R., Fletcher I. R., Thorne A. M., Johnson S. P., Cutten H. N., Dunkley D. J. and Korhonen F. J. (2015) In situ U-Pb geochronology of xenotime and monazite from the Abra polymetallic deposit in the Capricorn Orogen, Australia: Dating hydrothermal mineralization and fluid flow in a long-lived crustal structure. *Precambrian Res.* **260**, 91–112.

**Radiogenic Pb In Xenotime Trapped In Nanoscale
Inclusions Of Apatite During Fluid Alteration**

This chapter is published as

Joseph C., Fougereuse D., Reddy S. M., Olierook H. K. H., Tacchetto T., Kennedy A., Saxey D. W., Rickard W. D. A., Denyszyn S. and Dodd A. (2023) Radiogenic Pb in xenotime trapped in nanoscale inclusions of apatite during fluid alteration. *Chemical Geology*, 121444.

<https://doi.org/10.1016/j.chemgeo.2023.121444>

Abstract

This study focuses on the low-temperature mineralogical response of xenotime, a phosphate mineral routinely used as a geochronometer, to fluid-assisted alteration. The studied xenotime grain (z6413) comes from a ~1000 Ma pegmatite from the Grenville Province, Canada, and is commonly used as reference material for U-Pb analyses. At the microscale, the grain has a mottled texture, sub-micrometer porosity, and small domains dark in backscattered electron (BSE) images that are characterised by curvilinear, sharp boundaries. The small dark BSE domains are associated with Th-U-rich inclusions and larger porosity (2–3 μm) and are interpreted to result from localised fluid-assisted coupled dissolution-reprecipitation. Sensitive high-resolution ion microprobe (SHRIMP) U-Pb analyses of unaltered and fluid-affected domains yield concordant crystallisation dates, irrespective of the textural domains. The apparently unaltered xenotime domain was characterised at the nanoscale to determine if the grain was affected by fluids beyond the altered domains defined by BSE imaging. Transmission electron microscopy (TEM) imaging results indicate the presence of randomly distributed Ca + Pb nanoscale precipitates. Atom probe tomography (APT) reveals the presence of spherical clusters (4 to 18 nm in size) enriched in radiogenic Pb, Ca, and Si atoms, which, combined with TEM observations, are interpreted as nanoscale inclusions of apatite. In addition to the inclusions, a dislocation enriched in Ca and fluid mobile elements such as Cl, Li, Na, and Mn was imaged from APT data indicating percolating of fluids further than the reaction front. APT $^{206}\text{Pb}/^{238}\text{U}$ nanogeochronology indicates that the nanoscale inclusions of apatite formed at 863 ± 28 Ma, 100–150 Ma after crystallisation of the host xenotime, with its formation attributed to fluid metasomatism. This study shows that fluid-xenotime reaction caused Pb* to be redistributed at the nanoscale, recording the timing of metasomatism. However, at the scale of SHRIMP analytical spot (10 μm), xenotime is concordant, indicating that Pb was not mobile at the microscale and fluid-altered xenotime can preserve its crystallisation age. Although the studied grain shows a limited amount of altered domains in BSE imaging, nanoscale analyses reveal a more pervasive re-equilibration of the minerals through the percolation of fluids along dislocations.

3.1 Introduction

The interaction between fluids and rocks within crustal lithologies (i.e., fluid–rock interactions) represents a fundamental aspect of the geological processes of mineral transformation. Fluid-assisted mineral alteration reactions include processes such as dissolution, precipitation, and recrystallization, to which each rock constituent responds distinctively (Putnis, 2002). These processes have the potential to partially or entirely reset mineral-specific parent-daughter isotopic pairs, thereby providing the opportunity to determine the timing of fluid events in the crust (e.g., Villa and Williams, 2013). Although the mechanistic processes occurring at the fluid-mineral interface and the behaviour of U-Th-Pb during fluid alteration have been studied in detail (Seydoux-Guillaume et al., 2002a; Williams et al., 2011; Didier et al., 2013), the longer range effect of fluid alteration beyond the recrystallisation front has not received a lot of attention. It is assumed that apparently unaltered grain domains are not affected by fluid alteration; however, it was suggested that elements could diffuse further than dissolution-reprecipitation recrystallisation fronts (Lenting et al., 2018; Geisler et al., 2019) and that fluids can percolate along dislocation networks (Tacchetto et al., 2021, 2022b). The effects of these processes at scales spanning tens of micrometres from the recrystallisation front on the U-Pb geochronometers remain untested.

Phosphate minerals are particularly reactive to fluid alteration, and their geochemical behaviour is relatively well understood from experimental and nanoscale studies (Harlov et al., 2005; Williams et al., 2011; Grand’Homme et al., 2016; Turuani et al., 2022). For example, experimental studies have shown that monazite undergoes partial to complete resetting of the U-Pb chronometer during alteration at 450 °C (Williams et al., 2011; Budzyń and Kozub-Budzyń, 2015; Grand’Homme et al., 2016). Similarly, apatite is also highly susceptible to fluid-induced chemical and textural changes that may reset isotope systematics, thereby enabling the dating of fluid-rock interactions from the deep crust to the near-surface (Harlov, 2015; Kirkland et al., 2018a). In contrast, xenotime (Y,HREE)PO₄ is comparatively stable in fluid-mediated settings (Budzyń and Sláma, 2019). Experimental studies have shown that xenotime is stable in the low-temperature window (~250 °C) and resets partially at amphibolite facies conditions (550 °C and 650 °C), mostly by coupled dissolution–reprecipitation (Budzyń and Sláma, 2019). However, compared to other phosphates, the resilience of xenotime to fluid interaction is poorly understood, especially in low-temperature settings.

Xenotime is a common accessory mineral found in a range of rock types, including felsic intrusive rocks (Amli, 1975; Li et al., 2013; Schaltegger et al., 2015), metasedimentary metamorphic rocks (Rasmussen et al., 2011), Sn-W, gold, base metal, iron, and uranium

hydrothermal deposits (Rasmussen et al., 2009, 2016; Aleinikoff et al., 2012b), and sedimentary rocks, as either a detrital phase or diagenetic overgrowths on zircon (McNaughton et al., 1999; Rasmussen, 2005). The high actinide concentration, low common Pb incorporation during the growth, high closure temperature, and resistance to radiation damage make xenotime an ideal geochronometer for these geological settings (Fletcher et al., 2004; Rasmussen, 2005). Mineral-fluid interaction processes operating at the nanoscale, however, can affect the parent-daughter isotopic pair of a mineral at the scale of common geochronological techniques. In this study, we investigate the low-temperature, fluid-present alteration behaviour of xenotime, including the effects of alteration in apparently unaltered domains, using sensitive high-resolution ion microprobe (SHRIMP), transmission electron microscopy (TEM), and atom probe tomography (APT).

3.2 Sample and geological background

Xenotime sample z6413 (also referred to as XENO-1) comes from a granitic pegmatite from the Mesoproterozoic Grenville province of Ontario, Canada (Stern and Rayner, 2003) (Figure 3.1). This sample is commonly used as a reference material for U-Pb analyses of high-U xenotime (Fletcher et al., 2004). The pegmatite is located in the ~1.6 to 1.0 Ga Central Gneiss belt (CGB) of the Grenville province, an area that dominantly comprises upper amphibolite to granulite facies orthogneiss and supracrustal units. Structurally, the Central Gneiss Belt underlies the Composite Arc Belt and overlies the Allochthon Boundary Thrust (ABT) (Ketchum and Davidson, 2000; Rivers et al., 2012). These rocks were involved in two orogenic phases. The protracted metamorphism of the Ottavan phase at ~1090–1040 Ma and the thrusting and metamorphism Rigolet phase (1020–980 Ma) (Timmermann et al., 1997; Slagstad et al., 2004; Culshaw et al., 2016). After the Grenville orogeny, no significant high-temperature metamorphic event has been reported to affect the region since the 1.0 Ga Grenville orogeny (Stott, et., 1991; Carr et al., 2000). At c. 590 Ma, the emplacement of mafic dyke swarms is associated with the opening of the Iapetus Ocean and the breakup of Rodinia (Kamo et al., 1995; Spencer et al., 2015).

Original isotope dilution thermal ionisation mass spectrometry (ID-TIMS) from xenotime z6413 yielded $^{207}\text{Pb}^*/^{206}\text{Pb}^*$ and $^{206}\text{Pb}^*/^{238}\text{U}$ ages of 996.7 ± 0.8 Ma and 993.8 ± 0.7 Ma, respectively (Stern and Rayner, 2003). Reassessing the U decay constants, Schoene et al., (2006) re-analysed z6413 and obtained slightly older $^{207}\text{Pb}^*/^{206}\text{Pb}^*$ and $^{206}\text{Pb}^*/^{238}\text{U}$ ages of 999.7 ± 0.3 Ma and 997.9 ± 0.3 Ma, respectively.

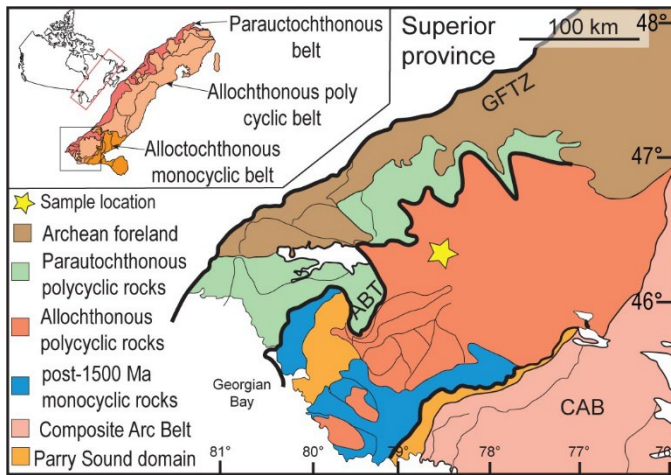


Figure 3.1: Lithotectonic map of the Central Gneiss Belt, Grenville province, Ontario. The location of the sample studied is indicated with a star symbol. Inset showing first-order subdivisions of Grenville province in Canada. GFTZ – Grenville Front Tectonic Zone, ABT – Allochthon Boundary Thrust, CAB – Composite Arc Belt. Modified from Culshaw et al., 2016; Kerckhove, 2016).

3.3 Methods

3.3.1 Scanning electron microscopy (SEM)

Secondary electron (SE) and backscattered electron (BSE) images were collected using a TESCAN MIRA3 field emission scanning electron microscope (FEG-SEM) at the Microscopy and Microanalysis Facility, Curtin University.

3.3.2 Sensitive high-resolution ion micro-probe (SHRIMP)

U-Th-Pb analyses were conducted in two sessions on a SHRIMP II at the John de Laeter Centre, Curtin University. MG-1 was selected as the primary standard (Fletcher et al., 2004). The primary O_2^- ion beam diameter was put through a $\sim 30 \mu m$ Kohler aperture to produce elliptical spots of $\sim 10 \times 7 \mu m$ with a beam current of $\sim 0.2-0.3$ nA. Six scans of the mass spectrum were recorded for each analysis, using a 9-peak run table comprising $^{194}Y_2O^+$, $^{204}Pb^+$, background ($^{204}Pb^+ + 0.0145$ AMU offset), $^{206}Pb^+$, $^{207}Pb^+$, $^{208}Pb^+$, $^{238}U^+$, $^{248}ThO^+$ and $^{254}UO^+$ (Fletcher et al., 2004). A retardation lens in front of the secondary ion collector was active to maximize abundance sensitivity.

U-Pb ratios and absolute abundances were determined relative to the MG-1 reference xenotime [$^{206}Pb^*/^{238}U$ age = 489.9 ± 0.5 Ma; $^{207}Pb^*/^{206}Pb^*$ age = 491.8 ± 1.2 Ma; U = ~ 900 ppm; Th = ~ 800 ppm]. SQUID3 software was used to calibrate Pb/U and Th/U

using floating robust regressions through $\ln(^{206}\text{Pb}^+ / ^{238}\text{U}^+)$ vs $\ln(^{254}\text{UO}^+ / ^{238}\text{U}^+)$ for MG-1 (Bodorkos et al., 2020). Sessions 1 and 2 yielded calibration constants of $0.0052 \pm 1.1\%$ (1σ , MSWD=1.4, $p=0.11$) and $0.0076 \pm 0.9\%$ (1σ , MSWD=1.3, $p=0.17$), respectively. Common Pb was corrected using contemporaneous Pb compositions by Stacey and Kramers, (1975).

Xenotime may have a wide range of possible compositions in both actinides (e.g., U=0–6 wt%) and rare earth elements ($\Sigma\text{REE}=12\text{--}22\%$ wt%), a correction of $^{206}\text{Pb}/^{238}\text{U}$ ratios is required to account for matrix differences between the reference material and unknowns. For $\ln(^{206}\text{Pb}^+ / ^{238}\text{U}^+)$ vs $\ln(^{254}\text{UO}^+ / ^{238}\text{U}^+)$, correction coefficients of $f\text{U}=6.93\%$, $f\text{Th}=3.23\%$, $f\Sigma\text{REE}=0.7\%$ were used (Fletcher et al., 2004). U and Th concentrations were determined via SHRIMP, using calibrations from Fletcher et al., (2000). As the primary reference material MG-1 is not homogeneous in U and Th, a ± 500 ppm uncertainty on both elements was incorporated, as in Fletcher et al. (2004), typical of the variation on primary reference material MG-1.

The ΣREE required for the matrix correction on $^{206}\text{Pb}^* / ^{238}\text{U}$ ratio was determined using a JEOL JXA-8530F Electron Probe Micro analyser (EPMA) housed at the Centre for Microscopy, Characterisation, and Analysis at the University of Western Australia, Western Australia. The operating conditions used were a 40° take-off angle, 25 keV beam energy, and 100 nA beam current. The electron beam diameter was set to $3 \times 3 \mu\text{m}$ spot size. Drake and Weill glasses and USNM phosphates from the Smithsonian institute were used as standards for instrumental calibration. The unknown values are produced using the Probe for EPMA© software package (Probe Software®). The elements were acquired using analysing crystals LiFH for Ho $\text{l}\beta$, Yb $\text{l}\alpha$, Lu $\text{l}\beta$, Eu $\text{l}\alpha$, Tb $\text{l}\alpha$, Tm $\text{l}\alpha$, LiF for Er $\text{l}\alpha$, Nd $\text{l}\alpha$, Sm $\text{l}\alpha$, Gd $\text{l}\alpha$, Dy $\text{l}\alpha$, PETJ for U $\text{m}\beta$, Zr $\text{l}\alpha$, Y $\text{l}\alpha$, P $\text{k}\alpha$, Ca $\text{k}\alpha$, Th $\text{m}\alpha$, and TAP for Si $\text{k}\alpha$. For Y $\text{l}\alpha$, P $\text{k}\alpha$, Ca $\text{k}\alpha$, Lu $\text{l}\beta$, Eu $\text{l}\alpha$, Tb $\text{l}\alpha$, Tm $\text{l}\alpha$, Nd $\text{l}\alpha$, Sm $\text{l}\alpha$, Gd $\text{l}\alpha$ the on-peak count times were 20 s. For Er $\text{l}\alpha$, Yb $\text{l}\alpha$, Ho $\text{l}\beta$, Dy $\text{l}\alpha$ on-peak count times were 30 s, U $\text{m}\beta$, Th $\text{m}\alpha$ - 60 s, Zr $\text{l}\alpha$ - 80 s and Si $\text{k}\alpha$ - 150 s. The off-peak counting time is maintained to be the same as the on-peak time. The off-peak correction method was exponential for Ca $\text{k}\alpha$ and U $\text{m}\beta$, slope for Tb $\text{l}\alpha$, and linear for all other elements. Unknown and standard intensities were corrected for dead time, and the latter were corrected for standard drift over time. Oxygen was calculated by cation stoichiometry and included in the matrix correction (Donovan et al., 1993). The Phi-Rho-Z algorithm utilized was Armstrong/Love Scott (Armstrong, 1988). The uncertainties on U, Th, and ΣREE are propagated in quadrature to the measured internal error on $^{206}\text{Pb}^* / ^{238}\text{U}$.

3.3.3 Focused ion beam (FIB)

Samples for APT and TEM were prepared using a TESCAN Lyra3 Ga⁺ focused ion beam coupled with a scanning electron microscope (FIB-SEM) at the John the Laeter Centre, Curtin University. Both APT specimens and TEM lamellae were prepared by using the Ga⁺ ion beam operated at 30 kV accelerating voltage. Final polishing was done with a 2 kV accelerating voltage to remove the damaged layer affected by high-energy Ga⁺ ions. Seven needle-shaped APT specimens were prepared from one lift-out, and only one textural domain was targeted as described elsewhere (Rickard et al., 2020).

3.3.4 Transmission electron microscopy (TEM)

TEM analyses were conducted on a ≤ 100 nm thick section mounted into a copper half grid using the FEI Talos FS200X FEG TEM housed at the Microscopy and Microanalysis Facility, Curtin University. The electron beam was operated at 200 kV accelerating voltage. High-angle annular dark-field (HAADF), scanning transmission electron microscopy (STEM) images, fast Fourier transform (FFT) images, and EDS x-ray elemental maps of selected areas of the foil were collected using a double-tilted specimen holder.

3.3.5 Atom probe tomography (APT)

Atom probe tomography (APT) is an analytical technique that determines the distribution of major and trace elements of minerals at the sub-nanometre scale (Reddy et al., 2020). APT utilises the high field-induced evaporation of ionic species from the crystal lattice of the sample, triggered by a laser pulse applied to the apex of a needle-shaped sample. The samples used in APT are needle-shaped to meet the requirements for field evaporation and to maintain an adequate uniform field during the analysis (Gault et al., 2012). The evaporated atoms are ionised and accelerated towards the position-sensitive detector, which records the time between the laser pulse and the collision with the detector yielding time-of-flight mass spectrometry. The resultant data are in the form of a mass-to-charge spectrum and a 3D point cloud of the detected ionic species. The peaks in the mass spectrum are identified by the mass, charge state (1+ to 3+), and relative isotopic abundances of the species. For reconstruction, the lateral coordinates (x, y) of the species are obtained from the impact location on the detector and the depth (z) is determined from the sequence of evaporation of atoms.

Seven needle-shaped specimens from sample z6413 were analysed at the Geoscience Atom Probe Facility, Curtin University. The instrument (CAMECA LEAP 4000 \times HR) was operated

in laser-assisted mode using a UV laser ($\lambda=355$ nm). Temperature and detection rate was kept constant at 60 K and 1%, respectively, for every analysis. The laser pulse frequency was maintained at 125 kHz except for one specimen (z6413–M2), which ran at a pulse frequency of 200 kHz. The laser pulse energy changed from 200 to 450 pJ with different analyses. The mass-to-charge spectrum was reconstructed to 3D data using the AP suite 6 software. Peaks that have intensities twice as high as background were identified and included in the 3D reconstruction. For the 3D reconstruction, voltage-based models were applied. The detector efficiency was set at 36%, k-factor at 3.3, image compression factor at 1.65, atomic volume computed at $0.01190 \text{ nm}^3/\text{atom}$ for xenotime, and the field evaporation estimated at 28.98 V/nm as determined empirically (Fougerouse et al., 2021c).

The maximum separation method (MSM; Williams et al., 2013) was used to identify clusters in the 3D reconstructions with the following parameters: d_{max} (maximum cluster ion separation) – 1.5 nm, O (order) – 1, N (number of chemical species) – 30, L (cluster detection envelope parameter) and E (cluster detection erosion distance) both – 0.75 nm. Proximity histogram analysis was performed to determine the composition of linear features based on a 0.4 at. % Ca isoconcentration surface (above a limit of Ca concentration of 0.4 at. %) (Hellman et al., 2000) (Figure 3.6).

The isotopic composition of U and Pb is measured from a narrow 0.1 Da (Dalton) range on the $^{206}\text{Pb}^{++}$ and $^{238}\text{UO}_2^{++}$ peaks and corrected for background. The background was estimated using a peak-free region (1 Da) adjacent to each peak (constant background estimation method, Joseph et al., 2021). Only U-Pb systematics were considered in this study because of the interference of the major ThO^{++} molecule with TmPO_3^{++} . For U–Pb systematics, the $^{206}\text{Pb}/^{238}\text{U}$ ratio is calculated using the fractionation correction method between the ratio of $\text{UO}_2^{++}/\text{UO}^{++}$ and $^{206}\text{Pb}^{++}/^{238}\text{UO}_2^{++}$ for each analysis (Joseph et al., 2021). $^{206}\text{Pb}/^{238}\text{U}$ dates were calculated from the whole specimen and the matrix (whole specimen without clusters) using the molecular fractionation correction method (Joseph et al., 2021).

3.4 Results

3.4.1 Scanning electron microscopy

BSE imaging of the grain showed variations in grey scale density throughout the grain with a mottled appearance. Throughout the grain, thin ($<1 \mu\text{m}$) and discontinuous (10–20 μm in length), planar features can be observed on the grain surface, with a higher density of features in the central portion of the grain (Figure 3.2a,b). These planar features have a preferred orientation, extending parallel to the long axis of the grain. Sub-micrometer porosity is

associated with these features. Domains defined by sharp curvilinear boundaries are characterised by a dark BSE signal that can be observed trending subparallel to the long axis of the grain (Figure 3.2a,c). The BSE dark domains are seen chiefly associated with the edges of the grain, although they are also present closer to the centre of the grain (Figure 3.2a). The BSE dark domains are often associated with larger pores ($\sim 2\text{--}3\ \mu\text{m}$) compared to the minute pores ($< 1\ \mu\text{m}$) in other areas of the grain. Small ($\sim 1\text{--}2\ \mu\text{m}$) Th-U rich inclusions are associated with the BSE dark domains. The SHRIMP analyses targeted both textural domains. The TEM and APT samples were prepared from a domain of grain devoid of BSE dark domains, and a low density of planar features in order to test the presence of alteration features away from the BSE dark domains.

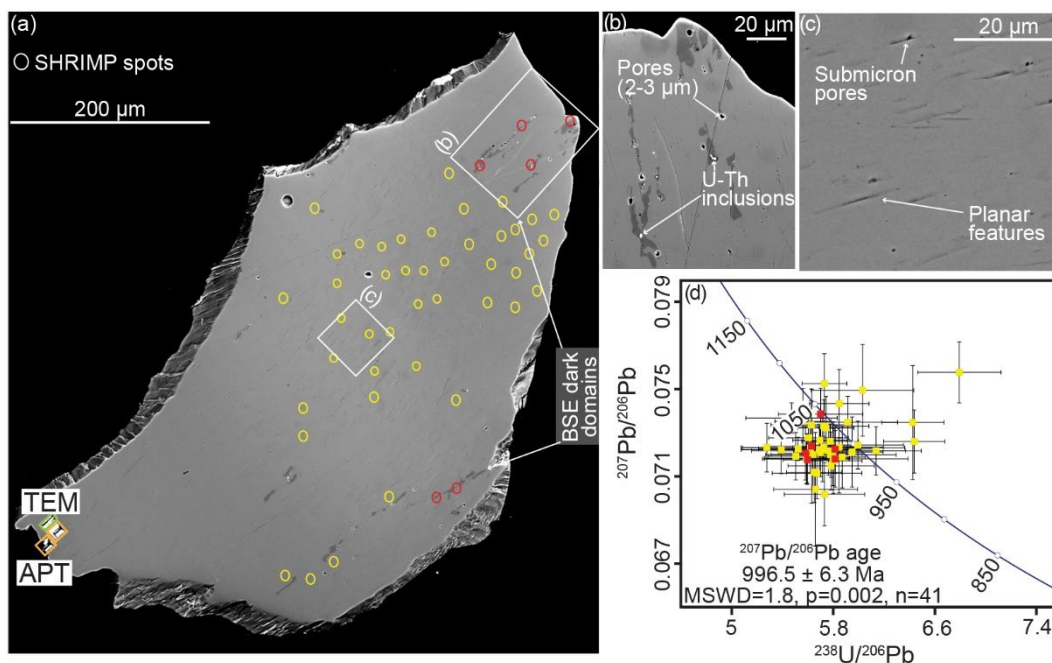


Figure 3.2: (a) Backscattered electron (BSE) image of grain z6413 showing altered and unaltered regions in xenotime. SHRIMP, TEM and APT sample locations are shown in the sample. SHRIMP spots colour code: yellow - unaltered region, Red - dark altered domains. (b) The grain shows altered mottled texture with planar features and submicron porosity. (c) Showing BSE dark domains of altered xenotime, mostly seen in the outer portions of the grain with U-Th rich inclusions precipitated in the boundary of altered and unaltered domains and larger pores ($2\text{--}3\ \mu\text{m}$). (d) Tera-Wasserburg diagram SHRIMP results with weighted mean $^{207}\text{Pb}/^{206}\text{Pb}$ age. The error bars are 2σ , with the point matches to the colour-coded of grain textural domains.

3.4.2 Sensitive high-resolution ion micro-probe

SHRIMP analyses from the mottled zone with planar features have an average U and Th concentration of $\sim 13,800$ ppm and ~ 2400 ppm respectively, with Th/U ratio of ~ 0.18 to 0.19 (Appendix 3.1, Appendix 3.2). The spot analyses targeting the BSE dark domains represent a mixture of BSE dark and mottled texture xenotime as the size of SHRIMP pits is larger than the BSE dark domains. These spots have significantly lower U and Th concentrations of $\sim 10,870$ ppm and 2030 ppm, respectively, and slightly higher and more variable Th/U ratios of ~ 0.18 – 0.22 than the rest of the grain. Regardless of the texture, common ^{204}Pb signal was below detection limit in the majority of the SHRIMP analyses. The lower concentrations of actinides with decreasing brightness in BSE are consistent with U and Th content, at least partially controlling the BSE signal.

Despite the textural variation in z6413, there does not appear to be a clear link to geochronological results. From 47 analyses, six are discordant, and they are obtained from the mottled domain. The concordant analyses from mottled ($n = 35$) and mixed mottled–BSE dark regions ($n = 6$) yield weighted mean $^{207}\text{Pb}^*/^{206}\text{Pb}^*$ ages of 996.6 ± 6.7 Ma (all 2σ , MSWD = 1.8, $p = 0.002$ [slightly over dispersed]), 996 ± 25 Ma (MSWD = 1.7, $p = 0.12$) respectively (Figure 3.2d; Appendix 3.1). Note that most analyses are slightly reversely discordant, with apparently older $^{206}\text{Pb}^*/^{238}\text{U}$ dates. Such discrepancies are a function of using a linear correction to adjust the matrix mismatch between reference material MG-1 and z6413 (with significantly different actinide concentrations), a correction that in reality, is non-linear but difficult to model (see Fletcher et al., 2004 and Cross and Williams, 2018, for discussion). A combined weighted mean $^{207}\text{Pb}^*/^{206}\text{Pb}^*$ age of 996.5 ± 6.3 Ma (MSWD = 1.8, $p = 0.002$) is slightly over-dispersed but within error of the published ID-TIMS analyses (Stern and Rayner, 2003; Schoene et al., 2006). The slight over dispersion implies that there may be cryptic mobility of Pb, but this is not correlated with textures.

3.4.3 Transmission electron microscopy

TEM lamellae from the sample z6413 appeared mostly homogenous at low magnification. The high-angle annular dark field (HAADF) images from TEM shows the atomic number contrast in the sample, in which atoms with high atomic number will appear bright. HAADF images generated from the sample showed different grey contrasts with dark spots and bright spherical domains, ~ 10 nm in size (Figure 3.3a). The STEM-EDS data indicate that the bright domains show enrichment in Ca and Pb, and depleted in Y, P, and O

compared to the surrounding xenotime (Figure 3.3 c and d). High-resolution images show the mottled appearance of the xenotime host. The diffraction data from these images show the crystalline order of the sample analysed is consistent with the xenotime crystal structure. Diffraction data collected from the region of interest with bright spherical domains showed xenotime diffraction patterns along with distinctive ring patterns (Figure 3.3b).

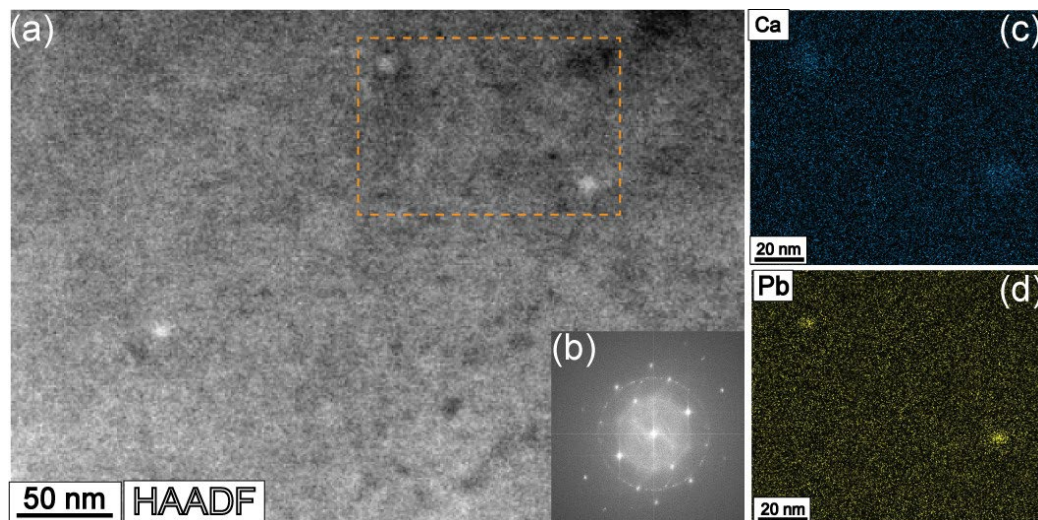


Figure 3.3: (a) High Angle Annular Dark Field (HAADF) image of sample z6413 showing bright spherical domains distributed in the xenotime matrix. The location of c and d is indicated with a dashed orange area. (b) Diffraction pattern obtained from the same region in higher resolution (HR) mode showing circular rings along with the xenotime crystal diffraction pattern. (c) and (d) EDS X-ray element maps collected with the scanning transmission electron microscope (STEM).

3.4.4 Atom probe tomography

The APT mass spectra of z6413 are consistent with the analysis of xenotime reference materials (Joseph et al., 2021) (Appendix 3.3a). Mass peaks up to 300 Da are obtained in which the major elements (Y, P) are present in elemental forms in various charge states and oxygen in elemental (O^+) and molecular form (O_2^+). These major Y, P, and O elements can combine to form oxides and P-bearing molecules that are evaporated in different charge states. Peaks for the rare earth elements are present as REE^+ and REE^{++} and as molecular $REEO$ and $REEPO_3$ species. Uranium (^{238}U) was present in five peaks $^{238}UO_2^{++}$ (135.02 Da), $^{238}UO^{++}$ (127.02 Da), $^{238}UO^{+++}$ (84.68 Da), $^{238}UO_2^+$ (270.04 Da), and $^{238}UO_3^+$ (286.035 Da) (Appendix 3.3a). No peaks in the mass spectra could be attributed to ^{235}U . ^{206}Pb and ^{207}Pb were present as doubly charged and singly charged species, with the

double-charged species more dominant. No ^{204}Pb was detected above the background. The ThPO_3^{+++} (103.7 Da) peak, which is close to the $^{207}\text{Pb}^{++}$ (103.49 Da) peak, was prominent and could not be deconvolved from the $^{207}\text{Pb}^{++}$ peak (Appendix 3.3b). Therefore, $^{207}\text{Pb}/^{206}\text{Pb}$ ratios were not determined for this sample.

The total amount of Ca, Pb, and U within all APT specimens is ~ 0.01 at. %, ~ 0.04 at. % and ~ 0.22 at. %, respectively. However, these elements are not homogeneously distributed. The presence of spherical and linear features enriched in trace elements was identified. Numerous Ca-Pb-rich clusters (Figure 3.4a) were found, except in one specimen (M2) where Ca and Pb were distributed homogeneously. A total of 23 clusters from the six specimens were detected. Thirteen of the 23 clusters are located on the edge of the analytical volume (partial), so their full size cannot be determined. The other ten clusters have a diameter ranging from ~ 4 to 18 nm (Figure 3.4a). The clusters are notably enriched in Ca (up to $500\times$ greater than in the matrix, ~ 0.01 to 5.45 at. %) and Pb (up to $70\times$, 0.10 to 6.70 at. %) (Figure 3.4b). Other than Ca and Pb, Si was also found enriched in most of the clusters compared to the matrix (up to $5\times$, 0.20 to 2.36 at. %). (Figure 3.4). A positive trend was observed between the size of the cluster and the Ca+Pb concentration inside the clusters (Figure 3.5) and can be explained by the local magnification effect and ion trajectory aberrations during atom probe analyses (Vurpillot et al., 2000; Fougerouse et al., 2016; Reddy et al., 2020). U and Th are homogeneously distributed and showed no change in concentration between the clusters and the xenotime matrix. Conversely, the clusters were depleted in Y, P, and O, the three main mineral-forming elements of xenotime, but no minor elements were significantly depleted.

In one of the APT specimens (M1), a linear feature (Figure 3.6) extending at a high angle to the specimen edge is defined by enrichment of Ca ($380\times$, ~ 0.01 at. % to 2.22 at. %), Cl ($210\times$, 0.01 at. % to 0.91 at. %), Na ($65\times$ 0.002 to 0.14 at. %), Li ($8\times$, 0.02 at. % to 0.13 at. %), and U ($4\times$, 0.23 at. % to 0.95 at. %) (Figure 3.6b). Ca-Pb-rich clusters are also observed in the same specimen.

Using the MSM method, clusters are isolated from the whole specimen to compute U-Pb ratios. The $^{206}\text{Pb}/^{238}\text{U}$ dates of the whole specimen including the clusters, ranged from 857 ± 43 Ma to 971 ± 52 Ma with a weighted mean date of 912 ± 39 Ma (2σ ; MSWD=2.9, probability=0.013 (Figure 3.7). The matrix, excluding clusters, yielded even younger $^{206}\text{Pb}/^{238}\text{U}$ dates of 830 ± 42 Ma to 937 ± 51 Ma with a weighted mean age of 863 ± 28 Ma (2σ ; MSWD=2.1, probability=0.047. (Appendix 3.4) Weighted means for both the whole specimens and matrix show excess scatter for a single population (MSWD=2.7, $p=0.014$ and MSWD=2.1, $p=0.047$, respectively), indicative of nanoscale variability in age across z6413.

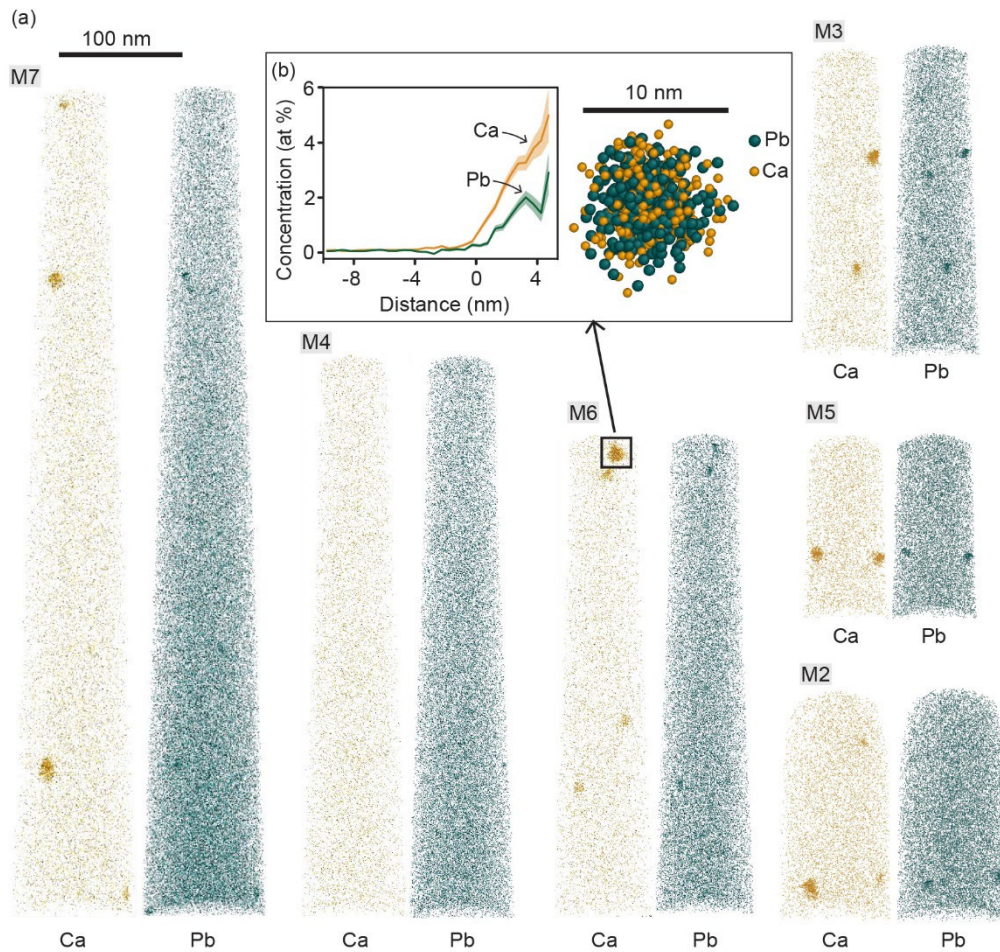


Figure 3.4: (a) APT 3d reconstruction of specimens from sample z6413. Each sphere represents an atom of Ca (orange) and Pb (teal). Ca-Pb* apatite inclusions are distributed heterogeneously in the xenotime matrix. (b) close up of apatite inclusion and proximity histogram showing the concentration Ca and Pb in the cluster. Error 1σ .

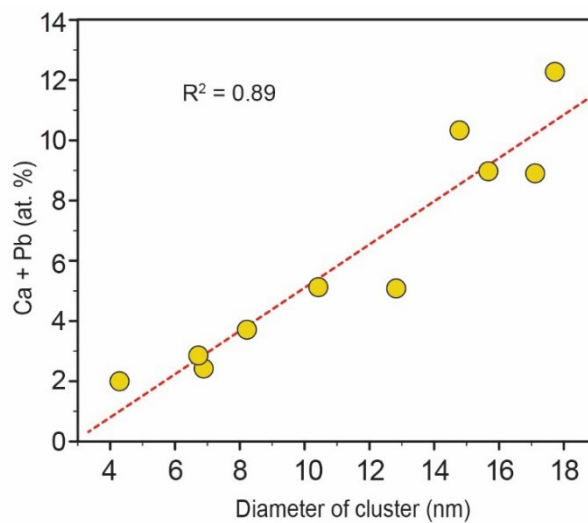


Figure 3.5: Diameter of the apatite inclusions versus Ca+Pb concentration. The composition of the smaller clusters is affected by local magnification effect during atom probe analysis leading underestimation of the composition of the clusters. Local magnification is resultant of evaporation difference between the host and the precipitate (cluster).

(a) 100 nm

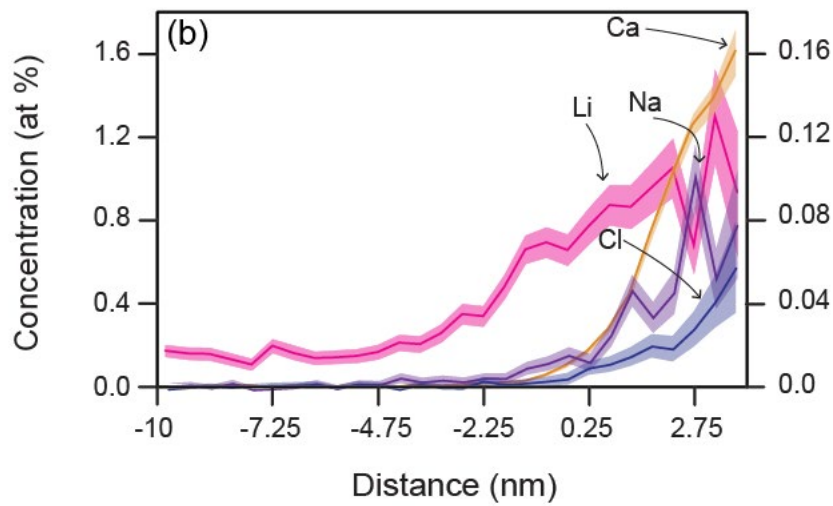
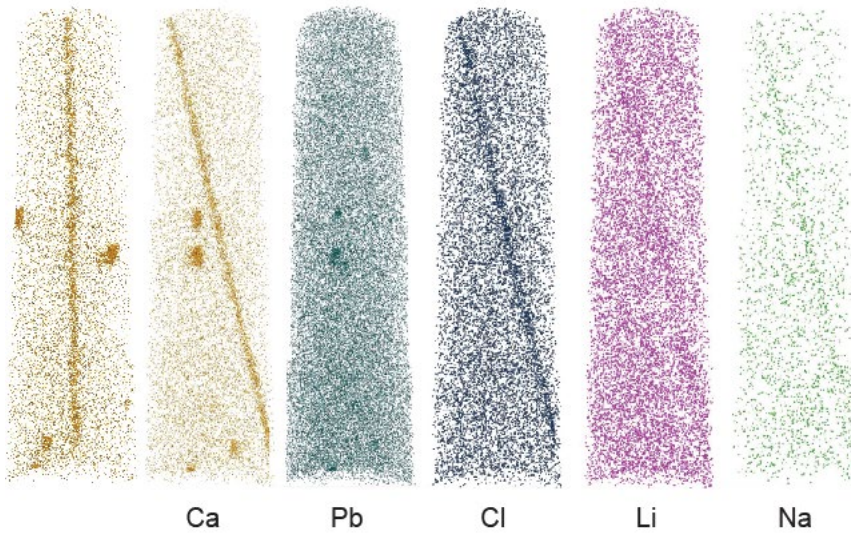


Figure 3.6: (a) M1 specimen showing distribution of Ca, Pb, Cl, Li, and Na in the dislocation; (b) Proximity histogram of elements in the dislocation, errors are 1σ . Values of Li and Na plotted in the secondary axis.

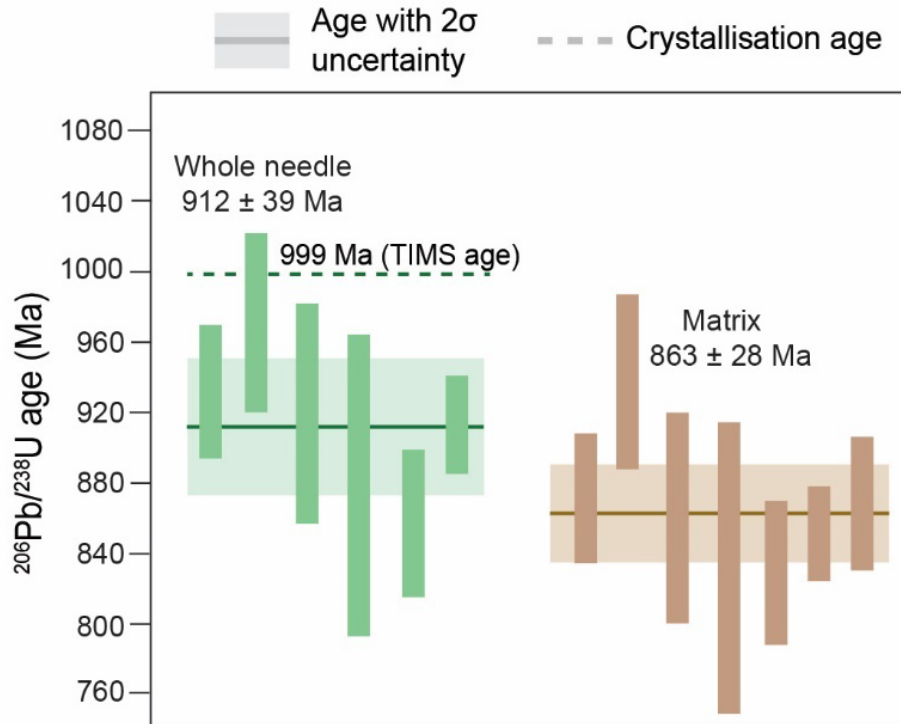


Figure 3.7: APT $^{206}\text{Pb}/^{238}\text{U}$ weighted mean data of sample z6413. Green colour represents the data from whole specimen and brown represents age of the matrix, excluding the clusters. The solid line denotes the weighted mean age obtained from the data and the dotted line represent the crystallisation age determined by TIMS. The coloured bands represent the uncertainties plotted at 2σ .

3.5 Discussion

3.5.1 Fluid alteration microstructures and geochronology

The grain is characterised by two textural domains, as the BSE image shows. Primarily the grain shows planar features, extending parallel to the long axis of the grain. These features are discontinuous, associated with sub-micron porosity, and widely distributed in the grain (Figure 3.2b). The planar features which have a preferred orientation, are conceived to be representing the cleavage planes of the crystal. This domain is considered unaltered based on textures and the tight range of U/Th ratio obtained from SHRIMP analyses. The dark BSE domains, coincide with a change in U and Th composition from the SHRIMP analysis. Lower actinide concentrations characterise the BSE dark domains in the grain compared to the mottled domain, which constitutes the rest of the grain. These domains have sharp boundaries with the

original xenotime and are also characterised by the presence of Th-U-rich inclusions and are associated with large-scale porosity (2–3 μm ; Figure 3.2a,c). The depletion of U and Th from the BSE dark zones and the presence of U-Th rich inclusions are attributed to the process of fluid-assisted coupled dissolution-reprecipitation (Putnis, 2009). Based on the above observations, these BSE dark domains represent fluid-altered domains. Dissolution-reprecipitation is the process in which, in the presence of a reactive fluid, a mineral phase is replaced by an altered composition of the same phase or replaced by an entirely new phase in order to minimise Gibbs free energy (Putnis, 2002). U and Th were likely dissolved from the xenotime by the fluid and simultaneously precipitated in the form of U+Th-rich minerals such as coffinite, thorite, or uraninite in the pores, cracks, and along grain boundaries (Hetherington et al., 2008; Ondrejka et al., 2016; Budzyń et al., 2018b).

Results from SHRIMP analysis obtained from both altered and unaltered (mottled domain) regions of the investigated grain show no correlation of alteration with age and broadly yield the same ages as previous studies (Stern and Rayner, 2003; Rasmussen et al., 2004; Schoene et al., 2006). As a first interpretation, this suggests that the interaction of the grain with the metasomatic fluid does not affect the U-Pb system to an extent detectable by SHRIMP analysis. Alternatively, the alteration occurred in a short time after crystallisation which is not resolvable from the data. Whichever scenario is correct, it seemingly justifies the use of z6413 as reference material for U-Pb analyses. However, there is a slight excess scatter amongst concordant analyses (MSWD=1.8, $p=0.002$) and some discordant analyses from the unaltered domain are indicative of Pb mobility within this xenotime crystal (Figure 3.2d)(Villa and Hanchar, 2017).

Xenotime is well known for its stability in an active fluid environment compared to other phosphates such as monazite and apatite (Budzyń and Kozub-Budzyń, 2015; Budzyń and Sláma, 2019; Hetherington et al., 2010). Dissolution-reprecipitation processes have been shown to partially or fully reset the U-Th-Pb isotopic systematics in high-temperature environments (Rasmussen et al., 2011; Budzyń and Sláma, 2019). However, xenotime is stable below ~ 450 °C in some fluid-present metamorphic and late-granitic environments (Broska et al., 2005; Janots et al., 2008; Rasmussen et al., 2011). The SHRIMP results from this study is consistent and supports the attribute of xenotime to be stable in fluid active settings. However, the data obtained from the SHRIMP is slightly over dispersed and six analyses are discordant in which the spots were from the apparently homogeneous zone of the grain.

The APT nanogeochronology results from mottled domain of the xenotime give a weighted mean $^{206}\text{Pb}/^{238}\text{U}$ date from the whole specimen 912 ± 39 Ma and the matrix 863 ± 28

Ma. The APT results suggest Pb mobility in the form of radiogenic Pb-enriched clusters and younger dates. With the exception of one specimen, all APT-determined whole specimen $^{206}\text{Pb}/^{238}\text{U}$ dates do not overlap at 2σ with the SHRIMP (996.5 ± 6.3 Ma) (Figure 3.2d) and previously published ID-TIMS ages (999.7 ± 0.3 Ma) (Figure 3.7). The heterogeneous distribution of Pb at the nanoscale can affect the isotopic composition measured by APT. As demonstrated in monazite, a low density of Pb clusters similar to the cluster distribution in our sample can bias nanogeochronology results (Fougerouse et al., 2018). Although the dates obtained from the whole specimen are younger than the TIMS/SHRIMP age, these younger dates are likely the results of the heterogeneous distribution of Pb clusters. Such effect is negligible in TIMS/SHRIMP data because specimen enough clusters are homogenised in the analytical volume unless Pb is diffused outside the crystal. The younger ages from the matrix, 863 ± 28 Ma compared to the crystallisation age of 999.7 ± 0.3 Ma, represents the maximum age of the event responsible for the Pb mobility into the clusters, which can also potentially lead to Pb loss out of the grain resulting in this minor discordancy. The age of 863 ± 28 Ma does not correlate with a known event in the terrain and could indicate an unidentified event or a localised event in the region.

3.5.2 Nanoscale compositional heterogeneities in xenotime

Based on BSE and SHRIMP results of the sample, it is established that some parts of the grain have undergone fluid alteration and present a clear example of fluid-present coupled dissolution-reprecipitation. There are numerous studies on the response of dissolution-reprecipitation reactions in minerals and also on the behaviour of the U-Th-Pb system, mainly focusing re-equilibrated grain domains and on the reaction front (Seydoux-Guillaume et al., 2002a; Williams et al., 2011; Didier et al., 2013; Ruiz-Agudo et al., 2014; Moser et al., 2022). However, whether the effect of fluids can be observed beyond the re-equilibrated domains has not received much scrutiny. In turn, the potential effect of alteration features not recognisable through petrography using classic electron microscopy techniques has not been tested.

SHRIMP analyses on the grain from this study displayed the dispersion of the Pb-Pb ages, and the discordant analyses from the apparently unaltered domain of the grain, forcing the idea that minor changes in isotopic distribution in the unaltered domain are present. The discordance is minor, but it is essential to understand these processes which are possibly operating at the nanoscale, for a better understanding of xenotime as a geochronometer and its response to fluid. Therefore, this study it is aimed to analyse a region beyond the altered domains using TEM and APT, testing the long-range effect of fluid alteration.

The TEM HAADF maps showed dark patches and bright spherical domains in the grey matrix xenotime. The dark patches giving the mottled appearance are interpreted to have resulted from the annealing of radiation damage, similar to monazite and zircon (Seydoux-Guillaume et al., 2002b; Drost et al., 2013; Nasdala et al., 2020). This is explainable based on the high actinide concentration of the sample. HAADF and EDS STEM results also show bright spherical domains enriched in Ca and Pb (Figure 3.3). High concentration of Pb with a higher atomic number in the spherical domains results in bright reflection signals than Y, P and O (lower atomic number than Pb) which constitutes the xenotime matrix. The diffraction data from the TEM high-resolution image shows the well-ordered xenotime structure as well as a ring pattern (Figure 3.3b). The ring patterns form when electron diffraction occurs simultaneously from many different grains with different crystallographic orientations (polycrystalline nature), and as the number of crystals and randomness increase, they result in partial to complete diffraction rings (Lind, 1983). Therefore, the ring pattern indicates the presence of ultrafine (10–100 nm) polycrystalline grains with a random distribution within an otherwise ordered xenotime matrix (Lind, 1983; Asadi Asadabad and Jafari Eskandari, 2015; Asadabad and Eskandari, 2016).

Given the scale of the nanocrystalline precipitates found in TEM, it is most likely that these Ca + Pb-rich domains are the same Ca+Pb that are observed within APT specimens (Figure 3.4a). Clusters in minerals have been shown to be enriched domains likely representing crystal defects (Valley et al., 2014; Peterman et al., 2016a; Fougrouse et al., 2019; Verberne et al., 2020a) or separate phases (Fougrouse et al., 2016, 2018, 2021a; 2021b); Seydoux-Guillaume et al., 2019). In z6413, clusters have combined Ca and Pb enrichments up to 12 at. %, two to three orders of magnitude higher than the surrounding matrix. The compositional range of the clusters is correlated with their size, with the smaller clusters comprising less Ca and Pb (Figure 3.5), this compositional range is likely an analytical artefact. The analyses of multiphased materials with APT commonly suffer from local magnification effects. The local magnification effect in the atom probe analysis is due to the difference in the evaporation field for different phases (e.g., precipitate vs host), which causes ion trajectory aberrations during evaporation. This leads to defocussing effects resulting in lower or higher apparent atomic density in the 3d reconstruction profile depending on the evaporation field of the analysed precipitate (Philippe et al., 2010). It has been demonstrated that due to this artefact, smaller clusters would proportionally be more affected, leading to compositional underestimation (Vurpillot et al., 2000; Devaraj et al., 2014; Tacchetto et al., 2021; Fougrouse et al., 2016; Reddy et al., 2020). Thus, all the Ca - Pb clusters observed in the studied xenotime grain might

therefore represent the same mineralogical feature but with a different size distribution.

Xenotime has a tetragonal crystal structure with PO_4 tetrahedra and REO_8 (Rare earth) polyhedra, in which the RE site is occupied by Y^{3+} and HREE^{3+} ions which have similar ionic radii (Y^{3+} 1.02 Å). In xenotime, Ca is incorporated into the crystal structure by $2(\text{REE}^{3+}, \text{Y}^{3+}) \leftrightarrow (\text{Th}, \text{U})^{4+} + \text{Ca}^{2+}$ (cheralite substitution). And in the case of Pb, only a negligible amount of Pb is incorporated into the xenotime structure during its growth. Both Ca^{2+} and Pb^{2+} with ionic radii 1.29 Å and 1.12 Å, respectively are larger cations compared to the small Y^{3+} ion (1.02 Å) (Shannon, 1976; Ni et al., 1995). The Pb in the xenotime is primarily radiogenic and no signal of common Pb was detected by APT. Combining APT and TEM results from this study, it is likely these combined Ca+Pb rich are separate phases within the xenotime formed later crystallisation. Based on the composition of the clusters the phase likely to represent the mineral apatite [$\text{Ca}_5(\text{PO}_4)_3(\text{F}, \text{Cl}, \text{OH})$] in which Pb can substitute for Ca and Si for P (Harrison et al., 2002; Pan and Fleet, 2002). Hence from here on we treat these clusters as apatite nanoscale inclusions in xenotime and the possible causes of formation are described in the next section.

One APT specimen (M1) is characterised by the presence of a linear feature primarily delineated by enrichments in Ca and Cl, but also Na, Li, Mn and U (Figure 3.6). These features show similarities with fission tracks commonly observed in apatite (Donelick et al., 2005). However, xenotime has the property to rapidly self-anneal the radiation damage created by alpha recoil during radionuclide fission (Harrison et al., 2002; Rasmussen, 2005). Therefore, it is unlikely that such a feature is the result of radiation damage. Alternatively, this geometry could be representative of a linear defect of the crystal lattice (i.e., dislocation). This consideration arises from the fact that a growing number of APT studies on minerals show the local enrichment of particular elements along dislocations (Dubosq et al., 2019; Piazzolo et al., 2016; Kirkland et al., 2018; Fougereuse et al., 2019, 2021a; Schipper et al., 2020; Tacchetto et al., 2021, 2022a; Verberne et al., 2023). Within minerals, dislocations are defects produced abundantly by plastic deformation of the host crystal in response to stress (Hirth and Pond, 1996; Hull and Bacon, 2001; Barber et al., 2010). The enrichment of elements along these interfaces can include mechanisms of interface diffusion and/or segregation by defect impurity pair (Reddy et al., 2016b; Verberne et al., 2022). In addition, dislocations can be formed during crystal growth in super cooled melts (Klapper, 2010; Klapper and Rudolph, 2015). Considering the above observations and the similarities with previous APT studies on mineral interfaces, the linear feature captured in the APT dataset likely represents an isolated dislocation.

Unfortunately, because of the isolated character of this dislocation, its origin, deformation or growth remains unclear.

Together with Ca, the dislocation in APT specimen, M6 is enriched in exotic, fluid-mobile elements such as Cl and Na that are most notably found in saline fluids. The presence of such fluid-mobile elements along the dislocation likely represents the input from an external source. The role of dislocations as pathways for the diffusion of externally derived trace elements has been previously described in pyrite (Fougerouse et al., 2019), titanite (Kirkland et al., 2018b), olivine (Tacchetto et al., 2021a), and garnet (Tacchetto et al., 2022b). In particular, the association of Na and Cl has been attributed to the presence of a fluid infiltrating along the dislocations (Tacchetto et al., 2021). With the available dataset, we interpret the enrichment of Cl, Na, and Li to represent the signature of an externally derived fluid present during the alteration of the grain. There is a marginal increase of U in the dislocation. It is unclear whether the enrichment of U is derived from the fluid or diffused into the dislocation from the grain itself. The U^{6+} ion is highly mobile in the fluid environment. In a recent publication based on TEM observations from an unaltered zone of altered xenotime, dislocations were found to be enriched in U, Th and Si and interpreted to be responsible for age discordance (Budzyń et al., 2023). Contrary to what is expected in an apparently homogenous BSE domain, nanoscale analysis shows evidence of fluid activity in grain areas beyond the altered domains from the chemistry of the dislocation.

Therefore, considering the composition of the dislocation and the sampling location of this specimen which is beyond the range of the fluid-altered domains, there is clear evidence of fluid activity inside the crystal even though it is not noticeable in textural analysis using BSE.

3.5.3 Formation mechanism of apatite nanoscale inclusions

Previous studies proposed different mechanisms for the formation of clusters and the mobility of Pb in minerals. For example, in zircon, a mineral that is susceptible to radiation damage, Pb-enriched clusters were formed during the thermal annealing of radiation damage during high-temperature metamorphism (Valley et al., 2014; Peterman et al., 2016a, 2019a, 2021a). The radiation damage in zircon accumulates with time and reaches a percolation point where which the damaged sites create a network in the crystal facilitating faster diffusion of trace elements (Utsunomiya et al., 2004a; Geisler et al., 2007; Pidgeon, 2014; Kusiak et al., 2015). In zircon during high temperature metamorphism, radiation damage anneals and trap Pb along with other trace elements in the damaged sites (Valley et al., 2014; Peterman et al., 2016a,

2019a, 2021a). Similar to zircon, in rutile it is thought to be transient radiation damaged sites facilitates Pb and other trace element mobility. During high temperature metamorphism the trace elements gets trapped in the core of the damaged site of the crystal lattice which has not undergone annealing (Verberne et al., 2020a). In the case of xenotime, no metamict xenotime has been observed in nature (Harrison et al., 2002). Experimental studies have proven that a phosphate phase such as xenotime have lower critical amorphisation temperature and lower activation energy for recrystallisation compared to zircon (A. Meldrum et al., 1997; Lenz et al., 2019a; Rafiuddin et al., 2020). Xenotime recovers rapidly from radiation damage, the percolation point is never reached and Pb cannot diffuse efficiently through that process (Rasmussen, 2005; Harrison et al., 2002). In addition, the xenotime sample studied is sourced from an igneous pegmatite from a geologically stable terrain from which no significant high-temperature event ($T \sim > 300 \text{ }^\circ\text{C}$) has been documented since the crystallisation of the pegmatite. The diffusion of Pb in xenotime is slower than other accessory minerals such as zircon and monazite and is negligible at upper crustal conditions (Cherniak, 2006, 2010). The absence of significant metamorphism also rules out the possibility for Pb volume diffusion, such that even the transient damage sites would not have attracted the impurities due to the low diffusion rates at low temperatures to form the apatite nanoscale inclusions. This feature of xenotime renders unlikely the possibility of the formation of apatite inclusions by the process of annealing of radiation damage during metamorphism, although this process cannot be excluded.

Another model to form Pb-rich clusters has been proposed for pyrite, by means of entanglement of dislocations forming energetically favourable nanoscale domains to host Pb that diffuse along dislocation cores (Fougerouse et al., 2019). The clusters observed in the data are not spatially associated with the dislocation and therefore it is unlikely that the cluster formed due to the interaction of dislocations.

Nanoscale apatite inclusions have been explained to be formed by the process of phase immiscibility, during rapid cooling in monazite from the granulite facies Sandmata complex, India (Fougerouse et al., 2018). The phase immiscibility model suggests that during rapid crystal growth excess impurities such as Ca be assimilated into the crystal structure and favours the unmixing during the cooling of the crystal (Putnis, 1992; Watson, 1996; Ferraris et al., 2005). In the APT monazite case study from the Sandmata complex, the Pb concentration in inclusions found in monazite was only up an order magnitude higher than that of the matrix (Fougerouse et al., 2018). In sample z6413, the Pb concentration in the inclusions is up to 6.7 at. % from a 0.1 at. % concentration in the matrix. The phase immiscibility model

predicates that the excess Ca incorporated during rapid growth exsolved from the xenotime during cooling shortly after crystallisation. The xenotime grain studied here originated from a pegmatite (Stern and Rayner, 2003). Pegmatites crystallise at relatively low temperatures ($\sim 100\text{--}525\text{ }^{\circ}\text{C}$) and undergo relatively fast cooling (Kozłowski, 1978; Kozłowski and Marcinowska, 2007; London and Kontak, 2012; Phelps et al., 2020). Pb diffusion distance during cooling from the crystallisation temperature of the pegmatite is therefore insignificant and cannot explain up to ~ 7 at. % enrichment in the inclusions. Furthermore, from the nanogeochronology $^{206}\text{Pb}/^{238}\text{U}$ data of the matrix, excluding Ca-Pb-rich clusters, is 863 ± 28 Ma, which is younger than the TIMS-derived crystallisation age (Figure 3.7). Therefore, the apatite nanoscale inclusions formed $\sim 100\text{--}150$ Ma after the crystallisation of the xenotime, representing a timeframe incompatible with the slow cooling model for the formation of the inclusions. Microscale observation of xenotime grain z6413 showed fluid assisted coupled dissolution reprecipitation process which is shown as BSE dark zones, depleted in actinide concentration and concomitant precipitation of U-Th rich inclusions in the proximity of the depleted zones. This alteration is not recorded in the SHRIMP analyses from the altered domains. In nanoscale analysis, there is evidence of fluid activity based on the presence of fluid-associated elements in the dislocation. Previous studies in monazite have shown the formation of mineral inclusions due to the dissolution reprecipitation process (Harlov et al., 2011). The action of fluids provides a faster way of mass transfer with activation energy many times faster than the solid-state diffusion and it operates at low temperatures (Putnis and Austrheim, 2010). A recent study on monazite postulates that nanoscale radiogenic Pb-rich galena formed by the redistribution of radiogenic Pb during fluid dissolution-reprecipitation (Turuani et al., 2022). Our results, therefore, suggest that the apatite inclusions seen in this xenotime sample are likely be the result of a mineral-fluid reaction, 100–150 Ma after crystallisation. It is important to note that, the small field of view of nanoscale analyses limits the confidence of our interpretations and alternative models for the formation of Ca-Pb-rich nanoscale inclusions should not be discarded. However, if the clusters formed through a fluid-present alteration process, the observation of clusters in the apparently unaltered domains of the xenotime indicate that the entire grain studied here may have undergone alteration. Such features may only be observed at the nanoscale but may be pervasive at the grain scale.

3.5.4 Summary and geochronological implications

The xenotime grain studied in this study is affected by fluid alteration based on textural and nanoscale observations. Geochronological SHRIMP U-Pb analyses showed little or no

correlation between altered and unaltered textures, indicating that the parent-daughter pair was not decoupled at the microscale, in agreement with previous studies highlighting the stability of xenotime in fluid active settings (Budzyń and Sláma, 2019). However, SHRIMP analyses recorded slight over dispersion of the data and discordant analyses which are obtained from the presumably unaltered domain. Nanoscale analyses on the unaltered domain of the sample revealed the presence of a dislocation decorated with fluid-related elements such as Cl, Na, Li, and U and apatite inclusions containing radiogenic Pb. These apatite inclusions are interpreted to form by the activity of fluid 100–150 Ma after crystallisation, pervasively throughout the studied xenotime. The fluid is responsible for radiogenic Pb redistribution at the nanoscale only and is not recorded by conventional microscale textural analyses. APT is capable of revealing fluid-rock interactions previously not recognized in microscale investigations. However, these inclusions witness a Pb mobility event that may cause minor changes in the U-Pb results from conventional analyses. The distribution of apatite inclusions in the grain could be responsible for the slight over dispersion of the SHRIMP ages. It is argued that the apatite inclusions can be the primary targets of later, more recent radiogenic Pb loss which give rise to discordant analyses. The combined micro-to-nanoscale data from this study highlights the role of apatite nanoscale inclusions to protect and retain radiogenic Pb during metasomatism. This may explain why fluid-altered xenotime geochronology yields unaffected to partially reset results, leading to the biased assumption that xenotime is more stable in fluid active settings. Instead, our results suggest that xenotime re-equilibrates extensively during metasomatism but that the U-Pb systematics are largely preserved by nanoscale heterogeneities.

3.6 Acknowledgments

Mount 05-12 used in this project are part of the McNaughton Legacy Collection which was created by the John de Laeter Centre (JdLC). This study was supported by the Australian Science and Industry Endowment Fund (grant SIEF RI13-01) and the Discovery Early Career Research Award from the Australian Research Council to Denis Fougere (DE190101307). The author acknowledges the support of Microscopy and Microscopy Facility and JdLC, Curtin University whose instrumentation has been supported by University, State and Commonwealth Government funding. We are grateful for the feedback and helpful comments from the two reviewers Bernard Bingen, and Callum J. Hetherington.

3.7 References

- Aleinikoff J. N., Lack J. F. S., Lund K., Evans K. V., Fanning C. M., Mazdab F. K., Wooden J. L. and Pillers R. M. (2012) Constraints on the timing of Co-Cu ± Au mineralization in the Blackbird district, Idaho, using SHRIMP U-Pb ages of monazite and xenotime plus zircon ages of related Mesoproterozoic orthogneisses and metasedimentary rocks. *Econ. Geol.* **107**, 1143–1175.
- Amlı R. (1975) Mineralogy and Rare Earth Geochemistry of Apatite and Xenotime from the Gloserheia Granite Pegmatite, Froland, Southern Norway. *Am. Mineral.* **60**, 607–620.
- Armstrong J. T. (1988) Quantitative analysis of silicates and oxide minerals comparison of Monte-Carlo, ZAF and procedures. *Microbeam Anal.*, 239–246.
- Asadabad M. A. and Eskandari M. J. (2016) Electron Diffraction. In *Modern Electron Microscopy in Physical and Life Sciences* (ed. M. J. E. E.-M. J. E.-R. Kral). InTech, Rijeka. p. Ch. 1.
- Asadi Asadabad M. and Jafari Eskandari M. (2015) Transmission Electron Microscopy as Best Technique for Characterization in Nanotechnology. *Synth. React. Inorganic, Met. Nano-Metal Chem.* **45**, 323–326.
- Barber D. J., Wenk H.-R., Hirth G. and Kohlstedt D. L. (2010) Chapter 95 Dislocations in Minerals. In (eds. J. P. Hirth and L. B. T.-D. in S. Kubin). Elsevier. pp. 171–232.
- Bodorkos S., Bowring J. F. and Rayner N. M. (2020) *Squid3: next-generation data processing software for sensitive high-resolution ion microprobe (SHRIMP).*,
- Broska I., Williams C. T., Janák M. and Nagy G. (2005) Alteration and breakdown of xenotime-(Y) and monazite-(Ce) in granitic rocks of the Western Carpathians, Slovakia. *Lithos* **82**, 71–83.
- Budzyń B. and Kozub-Budzyń G. (2015) The stability of xenotime in high Ca and Ca-Na systems, under experimental conditions of 250-350°C and 200-400 MPa: the implications for fluid-mediated low-temperature processes in granitic rocks. *Geol. Q.* **59**, 316–324.
- Budzyń B. and Sláma J. (2019) Partial resetting of U–Pb ages during experimental fluid-induced re-equilibration of xenotime. *Lithos* **346–347**, 105163.
- Budzyń B., Sláma J., Kozub-Budzyń G. A., Konečný P., Holický I., Rzepa G. and Jastrzębski M. (2018) Constraints on the timing of multiple thermal events and re-equilibration recorded by high-U zircon and xenotime: Case study of pegmatite from Piława Górna (Góry Sowie Block, SW Poland). *Lithos* **310–311**, 65–85.
- Budzyń B., Wirth R., Sláma J., Kozub-Budzyń G. A. and Schreiber A. (2023) Atomic-scale Th and U segregation into dislocation cores and U-Pb age discordance in xenotime. *Lithos*,

107105.

- Carr S. D., Easton R. M., Jamieson R. A. and Culshaw N. G. (2000) Geologic transect across the Grenville orogen of Ontario and New York. *Can. J. Earth Sci.* **37**, 193–216.
- Cherniak D. J. (2010) Diffusion in accessory minerals: Zircon, titanite, apatite, monazite and xenotime. *Rev. Mineral. Geochemistry* **72**, 827–869.
- Cherniak D. J. (2006) Pb and rare earth element diffusion in xenotime. *Lithos* **88**, 1–14.
- Cross A. J. and Williams I. S. (2018) SHRIMP U–Pb–Th xenotime (YPO₄) geochronology: A novel approach for the correction of SIMS matrix effects. *Chem. Geol.* **484**, 81–108.
- Culshaw N., Foster J., Marsh J., Slagstad T. and Gerbi C. (2016) Kiosk domain, Central Gneiss Belt, Grenville Province, Ontario: A Labradorian palimpsest preserved in the ductile deep crust. *Precambrian Res.* **280**, 249–278.
- Devaraj A., Colby R., Vurpillot F. and Thevuthasan S. (2014) Understanding Atom Probe Tomography of Oxide-Supported Metal Nanoparticles by Correlation with Atomic-Resolution Electron Microscopy and Field Evaporation Simulation. *J. Phys. Chem. Lett.* **5**, 1361–1367.
- Didier A., Bosse V., Boulvais P., Bouloton J., Paquette J.-L., Montel J.-M. and Devidal J.-L. (2013) Disturbance versus preservation of U–Th–Pb ages in monazite during fluid–rock interaction: textural, chemical and isotopic in situ study in microgranites (Velay Dome, France). *Contrib. to Mineral. Petrol.* **165**, 1051–1072.
- Donelick R. A., O’Sullivan P. B. and Ketcham R. A. (2005) Apatite Fission-Track Analysis. *Rev. Mineral. Geochemistry* **58**, 49–94.
- Donovan J. J., Snyder D. A. and Rivers M. L. (1993) An improved interference correction for trace element analysis.
- Drost K., Wirth R., Košler J., Fonneland Jørgensen H. and Ntaflos T. (2013) Chemical and structural relations of epitaxial xenotime and zircon substratum in sedimentary and hydrothermal environments: a TEM study. *Contrib. to Mineral. Petrol.* **165**, 737–756.
- Dubosq R., Rogowitz A., Schweinar K., Gault B. and Schneider D. A. (2019) A 2D and 3D nanostructural study of naturally deformed pyrite: assessing the links between trace element mobility and defect structures. *Contrib. to Mineral. Petrol.* **174**, 72.
- Ferraris C., White T. J., Plévert J. and Wegner R. (2005) Nanometric modulation in apatite. *Phys. Chem. Miner.* **32**, 485–492.
- Fletcher I. R., McNaughton N. J., Aleinikoff J. A., Rasmussen B. and Kamo S. L. (2004) Improved calibration procedures and new standards for U - Pb and Th - Pb dating of Phanerozoic xenotime by ion microprobe. *Chem. Geol.* **209**, 295–314.

- Fletcher I. R., Rasmussen B. and McNaughton N. J. (2000) SHRIMP U-Pb geochronology of authigenic xenotime and its potential for dating sedimentary basins. *Aust. J. Earth Sci.* **47**, 845–859.
- Fougerouse D, Cavosie A. J., Erickson T., Reddy S. M., Cox M. A., Saxey D. W., Rickard W. D. A. and Wingate M. T. D. (2021a) A new method for dating impact events – Thermal dependency on nanoscale Pb mobility in monazite shock twins. *Geochim. Cosmochim. Acta* **314**, 381–396.
- Fougerouse D., Reddy S. M., Kirkland C. L., Saxey D. W., Rickard W. D. and Hough R. M. (2019) Time-resolved, defect-hosted, trace element mobility in deformed Witwatersrand pyrite. *Geosci. Front.* **10**, 55–63.
- Fougerouse D., Reddy S. M., Saxey D. W., Erickson T. M., Kirkland C. L., Rickard W. D. A., Seydoux-Guillaume A.-M., Clark C. and Buick I. S. (2018) Nanoscale distribution of Pb in monazite revealed by atom probe microscopy. *Chem. Geol.* **479**, 251–258.
- Fougerouse D., Reddy S. M., Saxey D. W., Rickard W. D. A., van Riessen A. and Micklethwaite S. (2016) Nanoscale gold clusters in arsenopyrite controlled by growth rate not concentration: Evidence from atom probe microscopy. *Am. Mineral.* **101**, 1916–1919.
- Fougerouse D, Reddy S. M., Seydoux-Guillaume A.-M., Kirkland C. L., Erickson T. M., Saxey D. W., Rickard W. D. A., Jacob D., Leroux H. and Clark C. (2021b) Mechanical twinning of monazite expels radiogenic lead. *Geology* **49**, 417–421.
- Fougerouse D, Saxey D. W., Rickard W. D. A., Reddy S. M. and Verberne R. (2021c) Standardizing Spatial Reconstruction Parameters for the Atom Probe Analysis of Common Minerals. *Microsc. Microanal.*, 1–10.
- Gault B., Moody M. P., Cairney J. M. and Ringer S. P. (2012) *Atom Probe Microscopy*., Springer New York, New York, NY.
- Geisler T., Dohmen L., Lenting C. and Fritzsche M. B. K. (2019) Real-time in situ observations of reaction and transport phenomena during silicate glass corrosion by fluid-cell Raman spectroscopy. *Nat. Mater.* **18**, 342–348.
- Geisler T., Schaltegger U. and Tomaschek F. (2007) Re-equilibration of zircon in aqueous fluids and melts. *Elements* **3**, 43–50.
- Grand’Homme A., Janots E., Seydoux-Guillaume A.-M., Guillaume D., Bosse V. and Magnin V. (2016) Partial resetting of the U-Th-Pb systems in experimentally altered monazite: Nanoscale evidence of incomplete replacement. *Geology* **44**, 431–434.
- Harlov D. E. (2015) Apatite: A fingerprint for metasomatic processes. *Elements* **11**, 171–176.
- Harlov D. E., Wirth R. and Förster H.-J. (2005) An experimental study of dissolution–

- reprecipitation in fluorapatite: fluid infiltration and the formation of monazite. *Contrib. to Mineral. Petrol.* **150**, 268–286.
- Harlov D. E., Wirth R. and Hetherington C. J. (2011) Fluid-mediated partial alteration in monazite: the role of coupled dissolution–reprecipitation in element redistribution and mass transfer. *Contrib. to Mineral. Petrol.* **162**, 329–348.
- Harrison T. M., Catlos E. J. and Montel J.-M. (2002) U-Th-Pb Dating of Phosphate Minerals. *Rev. Mineral. Geochemistry* **48**, 524–558.
- Hellman O. C., Vandenbroucke J. A., Rüsing J., Isheim D. and Seidman D. N. (2000) Analysis of Three-dimensional Atom-probe Data by the Proximity Histogram. *Microsc. Microanal.* **6**, 437–444.
- Hetherington C. J., Harlov D. E. and Budzyń B. (2010) Experimental metasomatism of monazite and xenotime: Mineral stability, REE mobility and fluid composition. *Mineral. Petrol.* **99**, 165–184.
- Hetherington C. J., Jercinovic M. J., Williams M. L. and Mahan K. (2008) Understanding geologic processes with xenotime: Composition, chronology, and a protocol for electron probe microanalysis. *Chem. Geol.* **254**, 133–147.
- Hirth J. P. and Pond R. C. (1996) Steps, dislocations and disconnections as interface defects relating to structure and phase transformations. *Acta Mater.* **44**, 4749–4763.
- Hull D. and Bacon D. J. (2001) Origin and Multiplication of Dislocations. In *Introduction to Dislocations* (eds. D. Hull and D. J. Bacon). Elsevier, Oxford. pp. 145–156.
- Janots E., Engi M., Berger A., Allaz J., Schwarz J. O. and Spandler C. (2008) Prograde metamorphic sequence of REE minerals in pelitic rocks of the Central Alps: Implications for allanite-monazite-xenotime phase relations from 250 to 610°C. *J. Metamorph. Geol.* **26**, 509–526.
- Joseph C., Fougereuse D., Saxey D. W., Verberne R., Reddy S. M. and Rickard W. D. A. (2021) Xenotime at the Nanoscale: U-Pb Geochronology and Optimisation of Analyses by Atom Probe Tomography. *Geostand. Geoanalytical Res.* **45**, 443–456.
- Kamo S. L., Krogh T. E. and Kumarapeli P. S. (1995) Age of the Grenville dyke swarm, Ontario - Quebec: implications for the timing of Iapetan rifting. *Can. J. Earth Sci.* **32**, 273–280.
- Kerckhove S. R. Van De (2016) Tectonic history of the Nepewassi domain, Central Gneiss Belt, Grenville Province, Ontario: A lithological, structural, metamorphic and geochronological study.

- Ketchum J. W. F. and Davidson A. (2000) Crustal architecture and tectonic assembly of the Central Gneiss Belt, southwestern Grenville Province, Canada: A new interpretation. *Can. J. Earth Sci.* **37**, 217–234.
- Kirkland C.L., Fougereuse D., Reddy S. M., Hollis J. and Saxey D. W. (2018a) Assessing the mechanisms of common Pb incorporation into titanite. *Chem. Geol.* **483**, 558–566.
- Kirkland C L, Yakymchuk C., Szilas K., Evans N., Hollis J., McDonald B. and Gardiner N. J. (2018b) Apatite: a U-Pb thermochronometer or geochronometer? *Lithos* **318–319**, 143–157.
- Klapper H. (2010) Generation and Propagation of Defects During Crystal Growth. In *Springer Handbook of Crystal Growth* (eds. G. Dhanaraj, K. Byrappa, V. Prasad, and M. Dudley). Springer Berlin Heidelberg, Berlin, Heidelberg. pp. 93–132.
- Klapper H. and Rudolph P. (2015) Defect Generation and Interaction during Crystal Growth. In *Handbook of Crystal Growth* Elsevier. pp. 1093–1141.
- Kozłowski A. (1978) Pneumatolytic and hydrothermal activity in the Karkonosze-Izera block. *Acta Geol. Pol.* **28**, 171–222.
- Kozłowski A. and Marcinowska A. (2007) Hydrothermal activity in the Karkonosze, Strzegom and Strzelin massifs—a fluid inclusion study. *Granitoids Poland. AM Monogr.* **1**, 243–252.
- Kusiak M. A., Dunkley D. J., Wirth R., Whitehouse M. J., Wilde S. A. and Marquardt K. (2015) Metallic lead nanospheres discovered in ancient zircons. *Proc. Natl. Acad. Sci.* **112**, 4958–4963.
- Lenting C., Plümper O., Kilburn M., Guagliardo P., Klinkenberg M. and Geisler T. (2018) Towards a unifying mechanistic model for silicate glass corrosion. *npj Mater. Degrad.* **2**, 28.
- Lenz C., Thorogood G., Aughterson R., Ionescu M., Gregg D. J., Davis J. and Lumpkin G. R. (2019) The Quantification of Radiation Damage in Orthophosphates Using Confocal μ -Luminescence Spectroscopy of Nd³⁺. *Front. Chem.* **7**, 1–13.
- Li Q. L., Li X. H., Lan Z. W., Guo C. L., Yang Y. N., Liu Y. and Tang G. Q. (2013) Monazite and xenotime U-Th-Pb geochronology by ion microprobe: Dating highly fractionated granites at Xihuashan tungsten mine, SE China. *Contrib. to Mineral. Petrol.* **166**, 65–80.
- Lind C. J. (1983) *Characterization of mineral precipitates by electron microscope photographs and electron diffraction patterns.*
- London D. and Kontak D. J. (2012) Granitic Pegmatites: Scientific Wonders and Economic Bonanzas. *Elements* **8**, 257–261.
- McNaughton N. J., Rasmussen B. and Fletcher I. R. (1999) SHRIMP uranium-lead dating of

- diagenetic xenotime in siliciclastic sedimentary rocks. *Science* (80-.). **285**, 78–80.
- Meldrum A., Boatner L. A. and Ewing R. C. (1997) Displacive radiation effects in the monazite- and zircon-structure orthophosphates. *Phys. Rev. B* **56**, 13805–13814.
- Moser A. C., Hacker B. R., Gehrels G. E., Seward G. G. E., Kylander-Clark A. R. C. and Garber J. M. (2022) Linking titanite U–Pb dates to coupled deformation and dissolution–reprecipitation. *Contrib. to Mineral. Petrol.* **177**, 42.
- Nasdala L., Akhmadaliev S., Burakov B. E., Chanmuang N C. and Škoda R. (2020) The absence of metamictisation in natural monazite. *Sci. Rep.* **10**, 14676.
- Ni Y., Hughes J. M. and Mariano A. N. (1995) Crystal chemistry of the monazite and xenotime structures. *Am. Mineral.* **80**, 21–26
- Ondrejka M., Putiš M., Uher P., Schmiedt I., Pukančík L. and Konečný P. (2016) Fluid-driven destabilization of REE-bearing accessory minerals in the granitic orthogneisses of North Veporic basement (Western Carpathians, Slovakia). *Mineral. Petrol.* **110**, 561–580.
- Pan Y. and Fleet M. E. (2002) Compositions of the Apatite-Group Minerals: Substitution Mechanisms and Controlling Factors. *Rev. Mineral. Geochemistry* **48**, 13–49.
- Peterman E. M., Reddy S. M., Saxey D. W., Fougereuse D., Quadir M. Z. and Jercinovic M. J. (2021) Trace-element segregation to dislocation loops in experimentally heated zircon. *Am. Mineral.* **106**, 1971–1979.
- Peterman E. M., Reddy S. M., Saxey D. W., Fougereuse D., Snoeyenbos D. R. and Rickard W. D. A. (2019) Nanoscale processes of trace element mobility in metamorphosed zircon. *Contrib. to Mineral. Petrol.* **174**.
- Peterman E. M., Reddy S. M., Saxey D. W., Snoeyenbos D. R., Rickard W. D. A., Fougereuse D. and Kylander-Clark A. R. C. (2016) Nanogeochronology of discordant zircon measured by atom probe microscopy of Pb-enriched dislocation loops. *Sci. Adv.* **2**.
- Phelps P. R., Lee C.-T. A. and Morton D. M. (2020) Episodes of fast crystal growth in pegmatites. *Nat. Commun.* **11**, 4986.
- Philippe T., Gruber M., Vurpillot F. and Blavette D. (2010) Clustering and Local Magnification Effects in Atom Probe Tomography: A Statistical Approach. *Microsc. Microanal.* **16**, 643–648.
- Piazolo S., La Fontaine A., Trimby P., Harley S., Yang L., Armstrong R. and Cairney J. M. (2016) Deformation-induced trace element redistribution in zircon revealed using atom probe tomography. *Nat. Commun.* **7**, 10490.
- Pidgeon R. T. (2014) Zircon radiation damage ages. *Chem. Geol.* **367**, 13–22.
- Putnis A. (1992) *An Introduction to Mineral Sciences.*, Cambridge University Press.

- Putnis A. (2002) Mineral replacement reactions: from macroscopic observations to microscopic mechanisms. *Mineral. Mag.* **66**, 689–708.
- Putnis A. (2009) Mineral replacement reactions. *Rev. Mineral. Geochemistry* **70**, 87–124.
- Putnis A. and Austrheim H. (2010) Fluid-induced processes: metasomatism and metamorphism. *Geofluids* **10**, 254–269.
- Rafiuddin M. R., Seydoux-Guillaume A.-M., Deschanel X., Mesbah A., Baumier C., Szenknect S. and Dacheux N. (2020) An in-situ electron microscopy study of dual ion-beam irradiated xenotime-type ErPO₄. *J. Nucl. Mater.* **539**, 152265.
- Rasmussen B., Fletcher I. R., Bengtson S. and McNaughton N. J. (2004) SHRIMP U-Pb dating of diagenetic xenotime in the Stirling Range Formation, Western Australia: 1.8 Billion year minimum age for the Stirling biota. *Precambrian Res.* **133**, 329–337.
- Rasmussen B. (2005) Radiometric dating of sedimentary rocks: The application of diagenetic xenotime geochronology. *Earth-Science Rev.* **68**, 197–243.
- Rasmussen B., Fletcher I. R. and Muhling J. R. (2011) Response of xenotime to prograde metamorphism. *Contrib. to Mineral. Petrol.* **162**, 1259–1277.
- Rasmussen B., Mueller A. G. and Fletcher I. R. (2009) Zirconolite and xenotime U-Pb age constraints on the emplacement of the golden mile dolerite sill and gold mineralization at the Mt charlotte mine, Eastern Goldfields Province, Yilgarn Craton, Western Australia. *Contrib. to Mineral. Petrol.* **157**, 559–572.
- Rasmussen B., Zi J. W., Sheppard S., Krapež B. and Muhling J. R. (2016) Multiple episodes of hematite mineralization indicated by U-Pb dating of iron-ore deposits, Marquette Range, Michigan, USA. *Geology* **44**, 547–550.
- Reddy S. M., van Riessen A., Saxey D. W., Johnson T. E., Rickard W. D. A., Fougereuse D., Fischer S., Prosa T. J., Rice K. P., Reinhard D. A., Chen Y. and Olson D. (2016) Mechanisms of deformation-induced trace element migration in zircon resolved by atom probe and correlative microscopy. *Geochim. Cosmochim. Acta* **195**, 158–170.
- Reddy S. M., Saxey D. W., Rickard W. D. A., Fougereuse D., Montalvo S. D., Verberne R. and van Riessen A. (2020) Atom Probe Tomography: Development and Application to the Geosciences. *Geostand. Geoanalytical Res.* **44**, 5–50.
- Rickard W. D. A., Reddy S. M., Saxey D. W., Fougereuse D., Timms N. E., Daly L., Peterman E., Cavosie A. J. and Jourdan F. (2020) Novel Applications of FIB-SEM-Based ToF-SIMS in Atom Probe Tomography Workflows. *Microsc. Microanal.* **26**, 750–757.
- Rivers T., Culshaw N., Hynes A., Indares A., Jamieson R. and Martignole J. (2012) The Grenville Orogen - A post-Lithoprobe perspective. *Tecton. Styles Canada Lithoprobe*

Perspect. **49**, 97–236.

- Ruiz-Agudo E., Putnis C. V and Putnis A. (2014) Coupled dissolution and precipitation at mineral–fluid interfaces. *Chem. Geol.* **383**, 132–146.
- Schaltegger U., Schmitt A. K. and Horstwood M. S. A. (2015) U–Th–Pb zircon geochronology by ID-TIMS, SIMS, and laser ablation ICP-MS: Recipes, interpretations, and opportunities. *Chem. Geol.* **402**, 89–110.
- Schipper C. I., Rickard W. D. A., Reddy S. M., Saxey D. W., Castro J. M., Fougereuse D., Quadir Z., Conway C., Prior D. J. and Lilly K. (2020) Volcanic SiO₂-cristobalite: A natural product of chemical vapor deposition. *Am. Mineral.* **105**, 510–524.
- Schoene B., Crowley J. L., Condon D. J., Schmitz M. D. and Bowring S. A. (2006) Reassessing the uranium decay constants for geochronology using ID-TIMS U-Pb data. *Geochim. Cosmochim. Acta* **70**, 426–445.
- Seydoux-Guillaume A.-M., Fougereuse D., Laurent A. T., Gardés E., Reddy S. M. and Saxey D. W. (2019) Nanoscale resetting of the Th/Pb system in an isotopically-closed monazite grain: A combined atom probe and transmission electron microscopy study. *Geosci. Front.* **10**, 65–76.
- Seydoux-Guillaume A.-M., Paquette J.-L., Wiedenbeck M., Montel J.-M. and Heinrich W. (2002a) Experimental resetting of the U–Th–Pb systems in monazite. *Chem. Geol.* **191**, 165–181.
- Seydoux-Guillaume A.-M., Wirth R., Heinrich W. and Montel J.-M. (2002b) Experimental determination of Thorium partitioning between monazite and xenotime using analytical electron microscopy and X-ray diffraction Rietveld analysis. *Eur. J. Mineral.* **14**, 869–878.
- Shannon R. D. (1976) Revised effective ionic radii and systematic studies of interatomic distances in halides and chalcogenides. *Acta Crystallogr. Sect. A* **32**, 751–767.
- Slagstad T., Hamilton M. A., Jamieson R. A. and Culshaw N. G. (2004) Timing and duration of melting in the mid orogenic crust: Constraints from U-Pb (SHRIMP) data, Muskoka and Shawanaga domains, Grenville Province, Ontario. *Can. J. Earth Sci.* **41**, 1339–1365.
- Spencer C. J., Cawood P. A., Hawkesworth C. J., Prave A. R., Roberts N. M. W., Horstwood M. S. A. and Whitehouse M. J. (2015) Generation and preservation of continental crust in the Grenville Orogeny. *Geosci. Front.* **6**, 357–372.
- Stacey J. S. and Kramers J. D. (1975) Approximation of terrestrial lead isotope evolution by a two-stage model. *Earth Planet. Sci. Lett.* **26**, 207–221.
- Stern R. A. and Rayner N. (2003) *Ages of several xenotime megacrysts by ID-TIMS: potential*

reference materials for ion microprobe U-Pb geochronology.

- Stott, G.M., Sutcliffe, R.H., Thurston, P.C., Williams H. R. (1991) *The Grenville Province and the Proterozoic history of central and southern Ontario.*
- Tacchetto T., Clark C., Erickson T., Reddy S. M., Bhowany K. and Hand M. (2022a) Weakening the lower crust: conditions, reactions and deformation. *Lithos* **422–423**, 106738.
- Tacchetto T., Reddy S. M., Fougereuse D., Clark C., Saxey D. W. and Rickard W. D. A. (2022b) Crystal plasticity enhances trace element mobility in garnet. *Geology* **50**, 1387–1392.
- Tacchetto T., Reddy S. M., Saxey D. W., Fougereuse D., Rickard W. D. A. and Clark C. (2021) Disorientation control on trace element segregation in fluid-affected low-angle boundaries in olivine. *Contrib. to Mineral. Petrol.* **176**, 59.
- Timmermann H., Jamieson R. A., Culshaw N. G. and Parrish R. R. (1997) Time of metamorphism beneath the Central Metasedimentary Belt boundary thrust zone, Grenville Orogen, Ontario: accretion at 1080 Ma? *Can. J. Earth Sci.* **34**, 1023–1029.
- Turuani M. J., Laurent A. T., Seydoux-Guillaume A.-M., Fougereuse D., Saxey D., Reddy S. M., Harley S. L., Reynaud S. and Rickard W. D. A. (2022) Partial retention of radiogenic Pb in galena nanocrystals explains discordance in monazite from Napier Complex (Antarctica). *Earth Planet. Sci. Lett.* **588**, 117567.
- Utsunomiya S., Palenik C. S., Valley J. W., Cavosie A. J., Wilde S. A. and Ewing R. C. (2004) Nanoscale occurrence of Pb in an Archean zircon. *Geochim. Cosmochim. Acta* **68**, 4679–4686.
- Valley J. W., Cavosie A. J., Ushikubo T., Reinhard D. A., Lawrence D. F., Larson D. J., Clifton P. H., Kelly T. F., Wilde S. A., Moser D. E. and Spicuzza M. J. (2014) Hadean age for a post-magma-ocean zircon confirmed by atom-probe tomography. *Nat. Geosci.* **7**, 219–223.
- Verberne R., Reddy S. M., Saxey D. W., Fougereuse D., Rickard W. D. A., Plavsa D., Agangi A. and Kylander-Clark A. R. C. (2020) The geochemical and geochronological implications of nanoscale trace-element clusters in rutile. *Geology* **XX**, 1–5.
- Verberne R., Reddy S. M., Saxey D. W., Fougereuse D., Rickard W. D. A., Quadir Z., Evans N. J. and Clark C. (2022) Dislocations in minerals: Fast-diffusion pathways or trace-element traps? *Earth Planet. Sci. Lett.* **584**, 117517.
- Verberne R., van Schrojenstein Lantman H. W., Reddy S. M., Alvaro M., Wallis D., Fougereuse D., Langone A., Saxey D. W. and Rickard W. D. A. (2023) Trace-element

- heterogeneity in rutile linked to dislocation structures: Implications for Zr-in-rutile geothermometry. *J. Metamorph. Geol.* **41**, 3–24.
- Villa I. M. and Hanchar J. M. (2017) Age discordance and mineralogy. *Am. Mineral.* **102**, 2422–2439.
- Villa I. M. and Williams M. L. (2013) Geochronology of Metasomatic Events. In *Lecture Notes in Earth System Sciences* pp. 171–202.
- Vurpillot F., Bostel A. and Blavette D. (2000) Trajectory overlaps and local magnification in three-dimensional atom probe. *Appl. Phys. Lett.* **76**, 3127–3129.
- Watson E. B. (1996) Surface enrichment and trace-element uptake during crystal growth. *Geochim. Cosmochim. Acta* **60**, 5013–5020.
- Williams C. A., Haley D., Marquis E. A., Smith G. D. W. and Moody M. P. (2013) Defining clusters in APT reconstructions of ODS steels. *Ultramicroscopy* **132**, 271–278.
- Williams M. L., Jercinovic M. J., Harlov D. E., Budzyń B. and Hetherington C. J. (2011) Resetting monazite ages during fluid-related alteration. *Chem. Geol.* **283**, 218–225.

**Fluid Alteration And Ca Composition Control The
Formation Of Nanoscale Ca-Pb Clusters In Xenotime, Not
High-Temperature Metamorphism**

Abstract

Previous atom probe tomography (APT) and other correlative microscopic analyses on geochronometers such as zircon, rutile, and monazite have identified redistribution of radiogenic Pb, as a consequence of different processes; in which radiation damage and high-temperature metamorphism thought to be dominant. The redistribution of radiogenic Pb* and formation of nanoscale inclusions affects the isotopic daughter-parent pair in geochronometers and the mechanism, responsible for Pb* mobility, in turn influences the interpretation of geochronological data. This study investigates the formation mechanisms of nanoscale inclusions of apatite in xenotime and tests in particular the effects of high-temperature metamorphism and mineral composition. Sample Y1 is from an igneous pegmatite of the Gascoyne Province (Western Australia), has a high Ca content (0.13 wt. %) and has not undergone high-temperature metamorphism post crystallisation. Textural analysis of sample Y1 shows evidence of a fluid-assisted dissolution-precipitation process and concordant sensitive high resolution ion microprobe (SHRIMP) U-Pb analyses result in the sample's crystallisation age. These findings indicate that the fluid alteration did not affect the U-Pb system at the scale of SHRIMP analysis. Atom probe analysis of Y1 revealed two generations of apatite nanoscale inclusions, numerous Pb* depleted, and few Pb* enriched Ca-Pb* inclusions. The Pb* depleted apatite inclusions are proposed to form by phase immiscibility during cooling of the crystal whereas the Pb* enriched inclusions are likely formed by fluid alteration. The second case study is a suite of metapelite samples from the Fanad contact aureole (Glinsk, Ireland) that has experienced different metamorphic grades. The Fanad xenotime grains are characterised by a low Ca content and show two generations of xenotime. In the distal samples, fine-grained xenotime is related to the breakdown of regional garnet. In proximal samples, larger xenotime crystals are related to contact metamorphism and are chemically zoned with core characterised by high Y and P, and rims by low Y and P with antithetic Ca and U distribution. From chemical analysis the core of the zoned xenotime is ascertained to be regional metamorphic retrograde xenotime with low Ca and U, surrounded by new contact metamorphic xenotime with high Ca and U. Atom probe analysis of samples from Fanad showed no heterogeneity in either Ca or Pb distribution. The absence of apatite inclusions in metamorphic xenotime undergone high-temperature contact metamorphism (700-800 °C) can be explained by the slow Pb diffusion and resistant to radiation damage property of xenotime. Comparing both samples studied the presence and absence of apatite inclusions in Y1 and Fanad samples respectively, the level of impurity (Ca content) of the sample is one of the crucial factors facilitating the formation of apatite inclusions in xenotime.

4.1 Introduction

Nanoscale studies of minerals using atom probe tomography and other correlative microscopic techniques have revealed compositional and structural heterogeneities in minerals (Reddy et al., 2020). These nanoscale variations in the minerals are of particular importance in the case of geochronometers for a better understanding and interpretation of geochronological data. APT and transmission electron microscopy (TEM) studies of geochronometers such as zircon, monazite, and rutile have found radiogenic Pb enriched clusters along with other trace elements in varied concentrations, which can be representing different phase or trace element enriched crystal defects (Valley et al., 2014, 2015; Piazzolo et al., 2016; Peterman et al., 2016, 2019; Fougrouse et al., 2018; Seydoux-Guillaume et al., 2019; Verberne et al., 2020). The Pb isotopic composition of the clusters Pb (e.g., $^{207}\text{Pb}/^{206}\text{Pb}$ ratio) or the isotopic composition of the matrix surrounding the clusters can be used to constrain the age of the geological events causing their formation.

Various mechanisms have been proposed to form radiogenic Pb (Pb*) enriched clusters in minerals. However, high-temperature metamorphism at any stage in the mineral's history appears to be one of the most influential factors facilitating cluster formation. Radiation damage in crystals from radioactive decay is also critical in forming Pb* clusters. In the case of zircon, it was suggested that volume diffusion of Pb into radiation-damaged nanoscale domains during high-temperature metamorphism as the mechanism for Pb* clusters formation (Valley et al., 2014, 2015). Natural and experimental observations of toroidal-shaped clusters in zircon indicate that Pb* is entrapped during thermally driven annealing of radiation damage in dislocation loops (Peterman et al., 2016, 2021). Studies on high-temperature monazite grains have proposed the Pb mobility associated with younger high T metamorphism into clusters (Laurent et al., 2016; Seydoux-Guillaume et al., 2019). In rutile, Pb* clusters were interpreted to form in transient radiation damage cores of the crystal lattice during metamorphism. Other mechanisms have also been proposed for the Pb mobility and formation of clusters, such as fluid-assisted dissolution reprecipitation processes (Fougrouse et al., 2021a; Turuani et al., 2022; Joseph et al., 2023), phase immiscibility (Fougrouse et al., 2018), intersection of deformation related dislocations (Fougrouse et al., 2019). Multiple factors seem to influence the formation process of clusters with both the intrinsic mineral properties and extrinsic geologic factors such as metamorphism, fluid activity and deformation (Reddy et al., 2020). In this study, we study the effect of high temperature metamorphism and initial mineral geochemistry on the formation of clusters on xenotime, a widely used geochronometer.

Xenotime is a geochronometer owing to its high concentration of actinides, incorporation of low common Pb during growth, high closure temperature and resistance to radiation damage (Rasmussen, 2005; Cherniak, 2006; Harrison et al., 2002). Xenotime is especially used to constrain accurate ages of diagenesis of sedimentary rocks (Rasmussen, 2005), along with dating igneous, metamorphic and hydrothermal processes (Spear and Pyle, 2002; Rasmussen et al., 2011; Aleinikoff et al., 2012; Li et al., 2013). Xenotime is resistant to radiation damage, due to its lower activation energy for annealing. These properties make xenotime less complex to study compared to other radiation-prone minerals such as zircon and thereby providing an opportunity to study the effect of isolated geological processes for the nanoscale mobility of Pb* (Meldrum et al., 1997; Lenz et al., 2019). In xenotime, Ca and Pb* enriched nanoscale apatite inclusions have been proposed to form due to fluid alteration and have implications on the stability of xenotime during fluid alteration processes (Joseph et al., 2023). In this study, we study two xenotime samples, including a sample affected by high-temperature metamorphism and another not affected by high-temperature metamorphism but with a high-Ca content, to decipher the role of temperature and composition in nanoscale Pb* mobility in xenotime.

4.2 Samples and geological history

4.2.1 Y1 – Yinnietharra pegmatite, Gascoyne province

The xenotime sample is Y1, sourced from a Proterozoic Yinnietharra pegmatite Gascoyne province, Western Australia (Figure 4.1a). The pegmatite is hosted in the Paleoproterozoic Davey Well granite dated between 1670 and 1648 Ma (Johnson and Sheppard, 2015). The Yinnietharra pegmatite is a part of the Thirty-Three Supersuite of 1030 – 955 Ma Edmondian orogeny which comprises leucocratic tourmaline granites and Rare Earth Elements (REE) bearing pegmatites (muscovite tourmaline pegmatite; Johnson and Sheppard, 2015). Yinnietharra pegmatite xenotime geochronology indicates a $^{207}\text{Pb}/^{206}\text{Pb}$ 948±5 Ma crystallisation age (Fletcher et al. 2000) with 0.8–3.3 % discordance and is associated with the final stages of the Edmondian orogeny. A ~955–830 Ma Kuparr event of very low to low temperature metamorphism (<300°C), profuse metasomatism and minor pegmatitic and leucocratic magmatism with NW-SE fault reactivation has reported recently (Piechocka et al. 2017; Olierook et al., 2019), which is interpreted to be the result of Rodinia supercontinent assembly and breakup stages. The hydrothermal activity associated with this event was reportedly localised to the faults and fractures. The Mulka tectonic event was the last event that occurred ca. 570 Ma, associated with intracontinental reactivation along with the Gondwana

supercontinent formation, and no significant metamorphism was recorded in the region at that time (Johnson et al. 2013).

4.2.2 Fanad contact aureole, Ireland.

Xenotime grains are sourced from the Fanad contact aureole, Ireland, which is a part of the granites of Donegal in the North of Ireland (Figure 4.1b). The Fanad granodiorite is the northernmost of the Donegal group of granites. The study area is near the town of Glinsk. A well-marked pelitic horizon strikes towards north to the granite contact (Pitcher and Read, 1963). The pluton emplaced into the Dalradian Supergroup (Sessiagh-Clonmass formation) of the Neoproterozoic age and underwent regional metamorphism during the Grampian Phase of the Caledonian orogeny to greenschist facies, and then later retrogressed (Lambert and McKerrow, 1976; Kerrick, 1987). The host pelitic rock is quartz-chlorite-muscovite-garnet schist and metamorphosed into coarse biotite-rich hornfels towards the contact (Naggar and Atherton, 1970; Pitcher and Read, 1963; Edmunds and Atherton, 1971; Howie, 1974). The Fanad pluton emplaced into the pelitic schist, c. 400 [(402±10 Ma - Rb-Sr whole rock isochron ; O'Connor et al., (1987), 420±60 Ma - Th-Pb on monazite Fougereuse et al., (2020)], developing a well-delineated contact aureole with a succession of minerals from biotite, garnet, staurolite, andalusite, cordierite, K-feldspar and fibrolite, and finally sillimanite (Naggar and Atherton, 1970; Kerrick, 1987). Thin sections were selected from four locations, from distal to the contact of the granite 1606 (2000 m), 1621 (1520 m), 1630 (990 m) and 1642 (0 m) (Figure 4.1b). The xenotime grains were then selected for further analyses. Sample description is given in the next section.

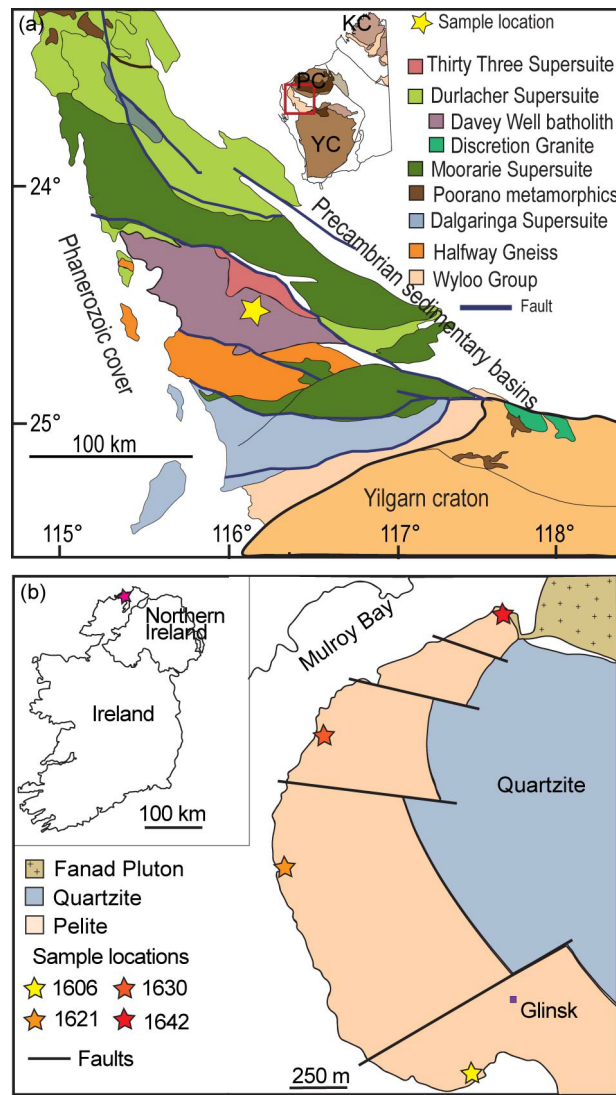


Figure 4.1: (a) Simplified regional geology of the Gascoyne Province bounded by E-W trending faults. Inset showing tectonic divisions of Western Australia. PC: Pilbara Craton, YC: Yilgarn Craton, KC: Kimberly Craton. Modified from Piechocka et al. (2017). (b) Geological map of the area around Glinsk, Fanad, County Donegal showing sample locations. Inset showing the sample location in Ireland modified after Kerrick (1987).

4.3 Methods

4.3.1 Xenotime imaging

Secondary electron (SE), and backscatter electron (BSE) images from samples Y1 (mount UWA A-13), thin sections from Fanad xenotime were collected using TESCAN MIRA3 field emission scanning electron microscope (FEG-SEM) at the Microscopy and Microanalysis Facility, John de Laeter centre, Curtin University. For samples from Fanad aureole, basic petrographical observations were done using optical microscopy prior to SEM

imaging. Xenotime grains from the thin sections were identified using the energy dispersive spectroscopy (EDS) technique, and representative grains were selected for further analysis.

4.3.2 Xenotime compositions

Geochemistry data from selected xenotime grains from three metamorphic grades of Fanad aureole (1606–2000 m, 1630–990 m, 1642–0 m) were acquired using JEOL JXA-8230 Superprobe equipped with 5 Wavelength-Dispersive spectrometers, housed at Electron probe microanalysis facility of University of Wellington, New Zealand. Four semi-quantitative X-ray maps were acquired from four xenotime grains from 1642 samples (1642-1, 1642-2, 1642-3, 1642-4). Ten elemental maps were made on Ca, Y, Gd, Yb, P, Th, U, Pb, and Dy. Analyses were performed using a 15 kV accelerating voltage, a 15 nA beam current and a dwell time of 10 ms. Elements Ca, Y, Gd, Yb, P, Th, U, Pb measured on PETL crystal, Si on TAP crystal and Dy on LIF crystal. A total of 73 spot analyses were conducted on selected xenotime grains using 15 kv accelerating voltage and 20 nA beam current and a 1 μm spot size. A 30 s count time and 15 s background time were used for all elements. For spot analysis, the standards used are - Ca, P - Durango apatite (Jarosewich et al., 1980), REE – four REE-bearing synthetic glasses (Drake and Weill, 1972), Si – plagioclase, Pb – galena. No standards were available for U-Th and hence the data is semi-quantitative. Elements are reported as molecular oxides and as elemental abundances. The resulted oxide totals from the samples are high, probably because of the semi-quantitative nature of U-Th values which might have skewed the data to higher totals (Appendix 4.1).

4.3.3 U-Pb geochronology using SHRIMP.

U-Th-Pb analyses on sample Y1 were conducted in March 2022, on a SHRIMP II at the John de Laeter Centre, Curtin University. MG-1 [$^{206}\text{Pb}/^{238}\text{U}$ age = 489.9 ± 0.5 Ma; $^{207}\text{Pb}/^{206}\text{Pb}$ age = 491.8 ± 1.2 Ma; U = ~ 900 ppm; Th = ~ 800 ppm], was selected as the primary standard. A ~ 30 μm Kohler aperture produced elliptical spots of $\sim 10 \times 7$ μm with a beam current of ~ 0.2 – 0.3 nA. Each analysis included six scans of the mass spectrum, using a 9-peak run table comprising $^{194}\text{Y}_2\text{O}^+$, $^{204}\text{Pb}^+$, background ($^{204}\text{Pb}^+$ + 0.0145 AMU offset), $^{206}\text{Pb}^+$, $^{207}\text{Pb}^+$, $^{208}\text{Pb}^+$, $^{238}\text{U}^+$, $^{248}\text{ThO}^+$ and $^{254}\text{UO}^+$ (Fletcher et al., 2004).

Pb/U and Th/U ratio calculated using floating robust regressions through $\ln(^{206}\text{Pb}^+/^{238}\text{U}^+)$ vs $\ln(^{254}\text{UO}^+/^{238}\text{U}^+)$ for MG-1 using SQUID3 software (Bodorkos et al., 2020). The session yielded a calibration constant of $0.0076 \pm 0.9\%$ (1σ , MSWD=1.3, $p=0.17$).

Common Pb was corrected using contemporaneous Pb compositions by Stacey and Kramers (1975).

Xenotime can be highly heterogeneous in terms of both actinide and REE concentration. Therefore, matrix correction is required to account for differences between reference material and unknown. U and Th concentrations were determined via SHRIMP, using calibrations from Fletcher et al. (2000). For $\ln(^{206}\text{Pb}+^{238}\text{U})$ vs $\ln(^{254}\text{UO}+^{238}\text{U})$, correction coefficients of $f\text{U}=6.93\%$, $f\text{Th}=3.23\%$, $f\Sigma\text{REE} = 0.7\%$ were used (Fletcher et al., 2004). As the primary reference material MG-1 is not homogeneous in U and Th, a ± 500 ppm uncertainty on both elements was incorporated, as in Fletcher et al. (2004), typical of the variation on primary reference material MG-1. The ΣREE required for the matrix correction on $^{206}\text{Pb}*/^{238}\text{U}$ ratio was determined using a JEOL JXA-8530F Electron Probe Micro analyser (EPMA) at the Centre for Microscopy, Characterisation, and Analysis at the University of Western Australia, Western Australia. A 40° take-off angle, 25 keV beam energy, and 100 nA beam current were the operating conditions used with a 3×3 μm spot size. Drake and Weill glasses and USNM phosphates from the Smithsonian institute were used as standards for instrumental calibration. The unknown values are produced using the Probe for EPMA© software package (Probe Software®). The analysing crystals used are Ho $l\beta$, Yb $l\alpha$, Lu $l\beta$, Eu $l\alpha$, Tb $l\alpha$, Tm $l\alpha$, LiF for Er $l\alpha$, Nd $l\alpha$, Sm $l\alpha$, Gd $l\alpha$, Dy $l\alpha$ – LiFH, U $m\beta$, Zr $l\alpha$, Y $l\alpha$, P $k\alpha$, Ca $k\alpha$, Th $m\alpha$ – PETJ, Si $k\alpha$ – TAP. The off-peak counting time is maintained to be the same as the on-peak time, in which Y $l\alpha$, P $k\alpha$, Ca $k\alpha$, Lu $l\beta$, Eu $l\alpha$, Tb $l\alpha$, Tm $l\alpha$, Nd $l\alpha$, Sm $l\alpha$, Gd $l\alpha$ the on-peak count times were 20 s. For Er $l\alpha$, Yb $l\alpha$, Ho $l\beta$, Dy $l\alpha$ on-peak count times were 30 s, U $m\beta$, Th $m\alpha$ - 60 s, Zr $l\alpha$ – 80 s and Si $k\alpha$ – 150 s.

4.3.4 Nanoscale geochemistry – sample preparation and analysis

Needle shaped specimens for atom probe tomography analysis were made using a TESCAN Lyra3 Ga^+ focused ion beam coupled with a scanning electron microscope (FIB-SEM) at the John the Laeter Centre, Curtin University. The needles prepared using Ga^+ ion with an accelerating voltage of 30 kV, followed by a 2 kV final polishing. The procedure followed the protocol by (Rickard et al., 2020). A total of 5 needle specimens from Y1 and 21 specimens from Fanad sample were prepared.

3 specimens from Y1 and 13 specimens from Fanad xenotime sample successfully analysed in the instrument CAMECA local electrode atom probe (LEAP) 4000 \times HR operated in laser-assisted mode using a UV laser ($\lambda=355$ nm) housed at Geoscience Atom

Probe Facility, Curtin University. Y1 specimens analysed M7, M8 and M10 in laser pulse energies of 400 pJ, 450 pJ and 200 pJ respectively. All specimens from Fanad analysed in a constant laser pulse energy of 200 pJ. All the other instrumental parameters for both Y1 and Fanad analyses, detection rate, base temperature, laser pulse frequency was kept constant at 1 %, 60 K and 125 kHz respectively. AP suite 6 software was used to construct the 3D reconstruction of the sample using mass to charge spectrum. The detector efficiency was set at 36%, k-factor at 3.3, image compression factor at 1.65, atomic volume computed at 0.01190 nm³/atom for xenotime, and the field evaporation estimated at 28.98 V/nm as determined empirically (Fougerouse et al., 2021b). The mass-to-charge spectrum was reconstructed to 3D data using the AP suite 6 software. Peaks that have intensities twice as high as the background were identified and included in the 3D reconstruction.

4.4 Results

4.4.1 Y1 - Textural, geochemical, and geochronological characterisation

Y1, a $\sim 550 \times 300 \mu\text{m}$ xenotime grain, was separated from the host rock and mounted in epoxy. The petrological context, therefore, could not be studied. The grain shows complex texture in the high-contrast BSE images through the entire grain (Figure 4.2). The xenotime shows three levels of intensity in BSE images as well as inclusions rich in U and Th. The BSE-bright domain occupies the top portion of the grain as well as the core of the grain and the bottom portion of the grain. A BSE-intermediate domain surrounds the BSE-bright domain in the bottom part of the grain. The boundary between the BSE-intermediate and BSE-bright is convoluted to straight indicating a possible resorption event between the precipitation of the core and the rim. Both domains are dissected by numerous BSE-dark and U-Th inclusions. The BSE-dark xenotime is characterised by $<10 \mu\text{m}$ finger-like, convoluted domains distributed mainly surrounding small cracks and pores.

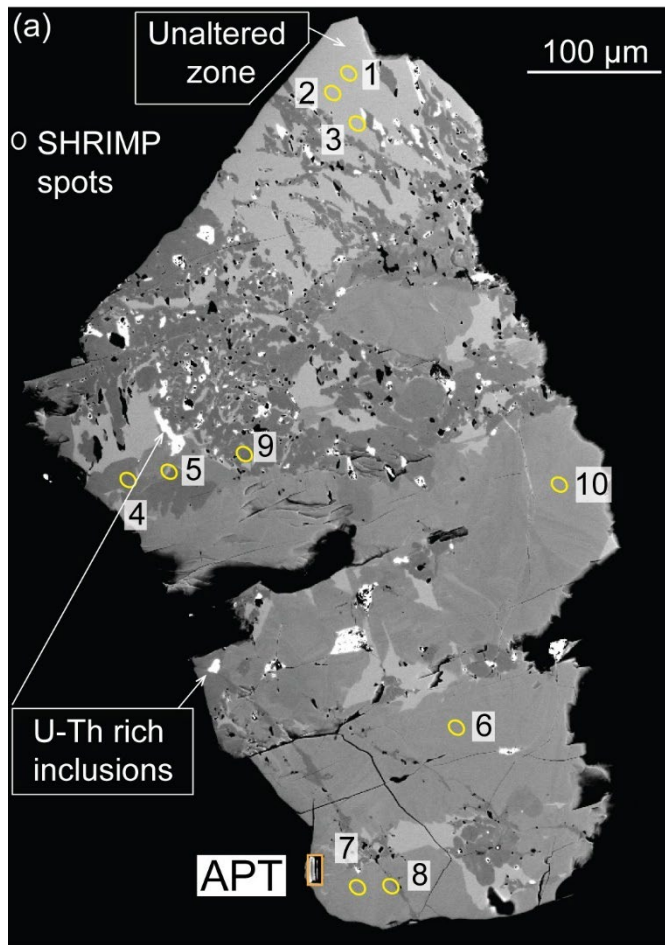


Figure 4.2: Backscattered electron (BSE) image of grain Y1. BSE image showing BSE bright, BSE dark and BSE intermediate zones in the grain. BSE dark domains are associated with U-Th rich inclusions. SHRIMP and APT locations are marked.

To understand the complex texture of the pegmatite xenotime sample U-Pb geochronological analysis has been done using ion microprobe. The BSE-bright domain has a U/Th ratio of 2.4 with a U concentration of ~25000 ppm and Th ~10000 ppm. The BSE-intermediate domain has a consistent U/Th ratio across the spots, 3.04 (U ~12500 ppm, Th ~4200 ppm). The BSE-dark domain associated with U-Th-rich phases, has a low U/Th ratio from 1.2–2.0. Both U and Th are depleted in these domains (U ~6000 ppm, Th ~4000 ppm). The Ca concentration of this grain from 10 spot analysis using electron microprobe is 0.06 to 0.18 with an average of 0.13 wt. %.

SHRIMP U-Pb analysis on the grain over 10 spots resulted in a concordant $^{207}\text{Pb}/^{206}\text{Pb}$ age of 949 ± 21 Ma (2σ , MSWD=1.5, $p=0.16$) (Figure 4.3) consistent with published age of 948 ± 5 Ma age (Fletcher et al., 2000). There is no correlation between the texture and the geochronological results, and no disturbance in the U-Pb system can be observed in the scale

of analysis except for one spot (Y1.4; Appendix 4.2) in the BSE-dark domain showing minor Pb loss. The age of disturbance cannot be determined confidently with the available results.

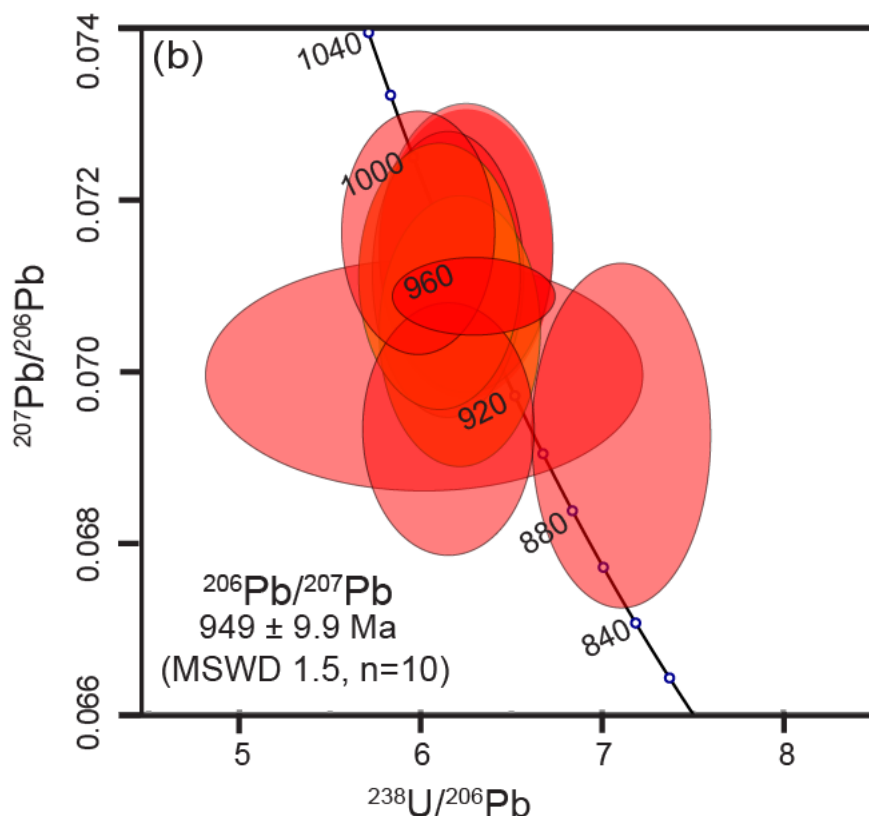


Figure 4.3: Tera-Wasserburg diagram plotting results from the Y1 SHRIMP data with weighted mean $^{207}\text{Pb}/^{206}\text{Pb}$ age.

4.4.2 Fanad contact aureole - Petrological, textural, and geochemical characterisation.

4.4.2.1 Sample 1606

Sample 1606 represents the country rock collected 2000 m away from the contact zone. The sample is a chlorite, muscovite, quartz schist. Chlorite porphyroblasts are embedded in the quartz-muscovite fabric, some of which preserves remnants of garnet in the core. Common accessory minerals found are monazite, zircon, xenotime, rutile, and ilmenite. More than 90 percent of the xenotime in the rock is found inside the chlorite porphyroblasts. Xenotime in the rock is anhedral to subhedral with pitted appearance, small size (<5–30 μm), and has lower modal abundance than other accessory phases (Figure 4.4 a-d). Some xenotime grains are overgrowing on zircon crystals.

A total of 18 EPMA spot analyses combined matrix xenotime (4 spots) and xenotime inside the chlorite porphyroblasts (14 spots), and 15 analyses yielded good data (Appendix

4.1). The major element chemistry average values both P and Y are higher in the xenotime inclusions in chlorite (P-15.2 wt. %, Y-38.6 wt. %) compared with the xenotime from the matrix (P-13.7 wt. %, Y-36.89 wt. %). In contrast, U and Th concentration is significantly higher in the matrix xenotime, with a 6.8 average U/Th ratio compared to an average of 0.73 for xenotime in chlorite inclusions (range from 0.11 to 2.03 and excluding an outlier with a single spot at 14.5; Figure 4.5). The average Ca content of both matrix and xenotime inclusions is 0.01 wt. %.

4.4.2.2 Sample 1621

Sample 1621 was collected 1520 m from the contact zone, within the aureole extend. New biotite-garnet and andalusite growth in the rock, whereas chlorite and muscovite is less abundant. Similar to sample 1606, xenotime occurrence is concentrated inside the chlorite-biotite assemblage. The grains are anhedral to subhedral with 5–20 μm in size (Figure 4.4 e-h). The modal abundance of xenotime is lower than sample 1606 from the host rock. No microprobe analysis was made on the xenotime grains from sample 1621.

4.4.2.3 Sample 1630

Sample 1630 is located 990 m from the contact zone. Muscovite almost disappears at this stage, biotite nearly entirely replacing the chlorite knots, where the biotite flakes are seen within the schistosity. The proportion of quartz and K-feldspar increase compared to the distal samples, and garnet is present. Xenotime is seen as subhedral, fewer and larger grains ($\sim \geq 10 \mu\text{m}$) than the lower grade samples 1606 and 1621 (Figure 4.4 i-l). Xenotime is also found to be associated with zircon and monazite.

Eight EPMA spot analyses targeted four xenotime grains identified from the thin section. The composition of P and Y is 15.4 wt. % and 38.1 wt. % respectively. The U/Th ratio is 4.6 to 12.2, with an average of 6.8. The average U/Th ratio of xenotime grains from this sample and the U/Th ratio of the matrix xenotime in the host rock (sample 1606) are comparable (Figure 4.5). The average Ca concentration from the grains is 0.06 wt. % (Appendix 4.1).

4.4.2.4 Sample 1642

Sample 1642 is from the contact zone between the metapelite and Fanad granite. The sample consists of coarse biotite-rich hornfels with quartz, K-feldspar and plagioclase with former schistosity obliterated. The modal abundance and grain size of xenotime has increased in this sample. Xenotime is seen as subhedral to euhedral grains, with grain size ~5-50 μm . Xenotime is found associated with zircon and rarely with monazite. Several xenotime grains from the thin sections studied showed zoning in BSE imaging, with a dark core and bright rim (Figure 4.4 m-t).

From sample 1642, microprobe compositional maps on four xenotime grains were done. These four grains (1642-1, 1642-2, 1642-3, 1642-4) showed mild to conspicuous zoning in BSE imaging (Figure 4.4 o, p, s, t). 29 spot analyses were also performed on these grains. Euhedral xenotime grains with no compositional zoning were also analysed (9 spots) for comparison. Major element chemistry from the unzoned xenotime grains yields an average P ~15.5 wt. % and Y 37.6 wt. %. The major element chemistry from the core of the zoned xenotime grains yields an average of P ~15.2 and Y ~38.0 wt. %, whereas the rim composition is P ~ 14.82 wt. % and Y ~ 36.1 wt. %. From x-ray compositional maps, the dark core of the grains coincides with high Y, Dy and bright rim corresponds to mainly U and a high concentration of Ca. Y and Yb zoning is antithetical to each other (Figure 4.6-4.7). The U/Th ratio from the core of the four xenotime grains ranges from 0.88 to 4.4, with an anomalously high value of 10.6 and an average U/Th ratio yielding 3.6. Whereas the U/Th ratio from the rim ranges from 7.5 to 17.7, with an average ratio of 9.0. Similar tightly clustered values (U/Th 5.4–10.6) have been obtained from unzoned euhedral xenotime grains, with an average of 7.7 (Figure 4.5). In this case, it is observed that the actinide content is mainly responsible for the zoning observed; however, the changes in major element chemistry must also have contributed. The Ca zoning in the grains is similar to the U, low Ca core and high Ca rim. The Ca content from the core of the grains has an average of 0.02 wt. %, whereas the rim and euhedral grains combined have 0.09 wt. % (Appendix 4.1).

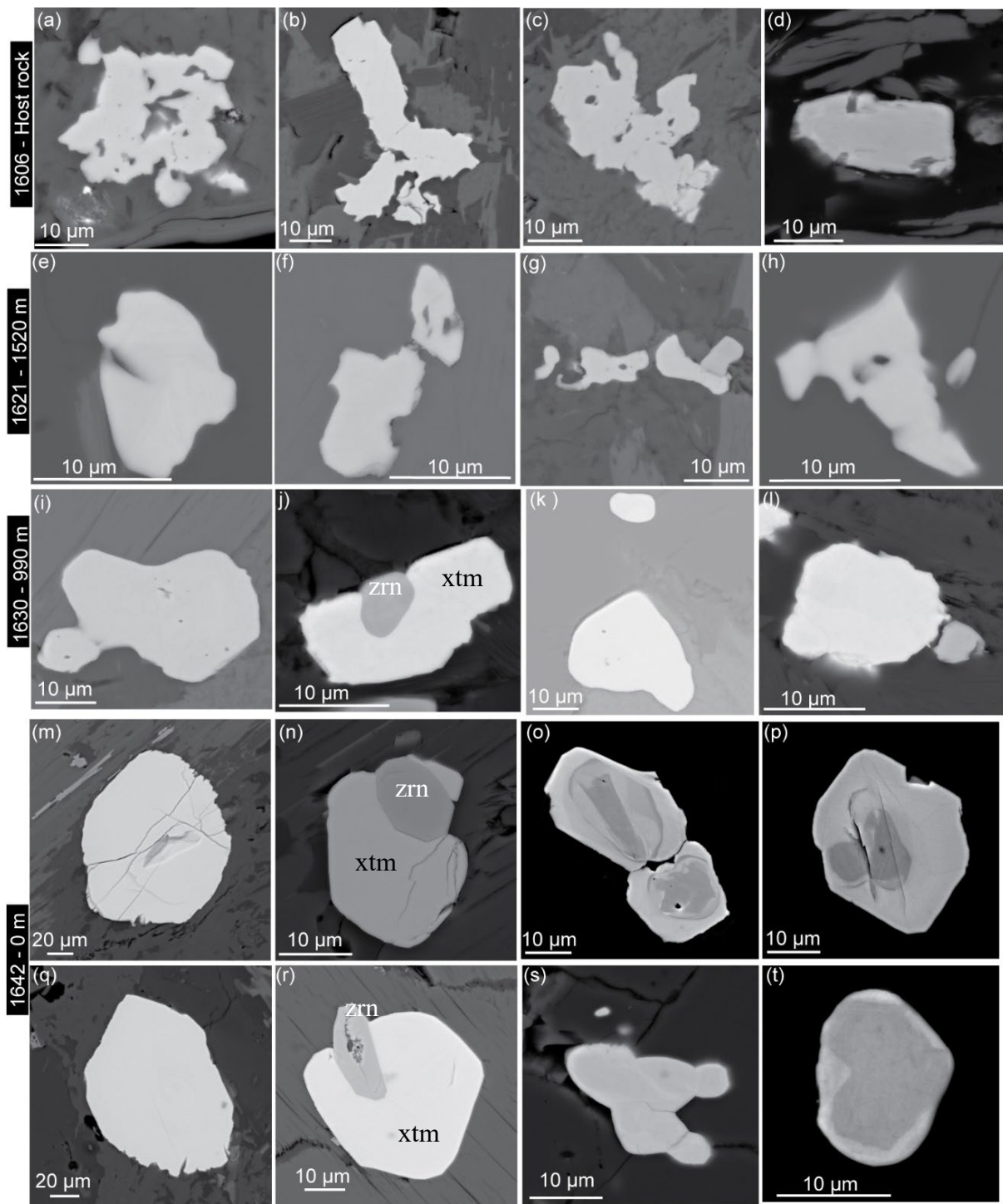


Figure 4.4: BSE images of representative xenotime grains from each metamorphic grade from Fanad contact aureole.

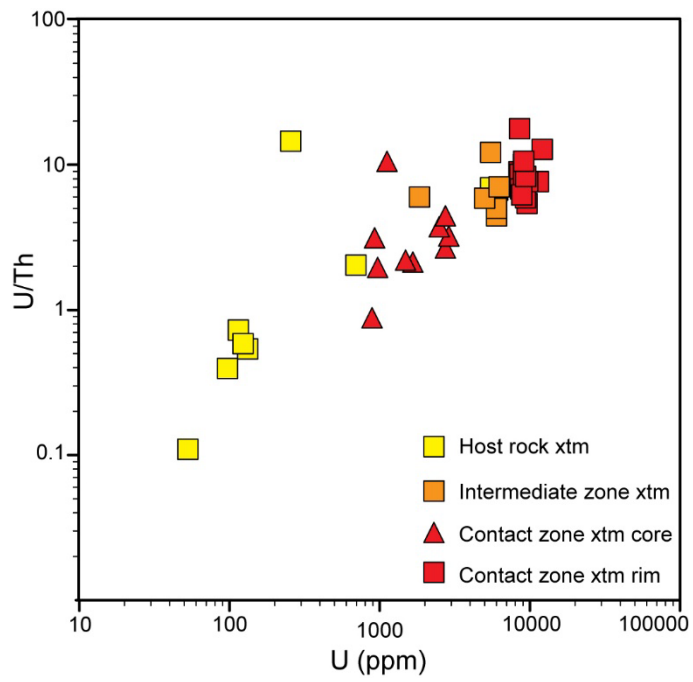


Figure 4.5: Graph plotting U concentration vs U/Th ratio from the samples, distinguishing xenotime from different metamorphic grades.

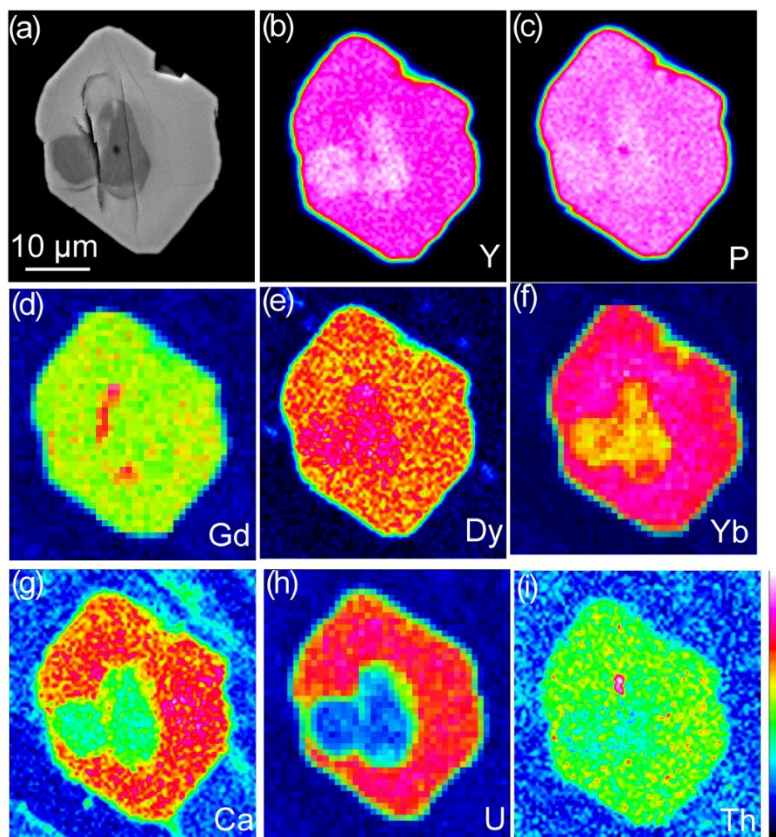


Figure 4.6: EPMA x-ray compositional maps of grain 1642-1

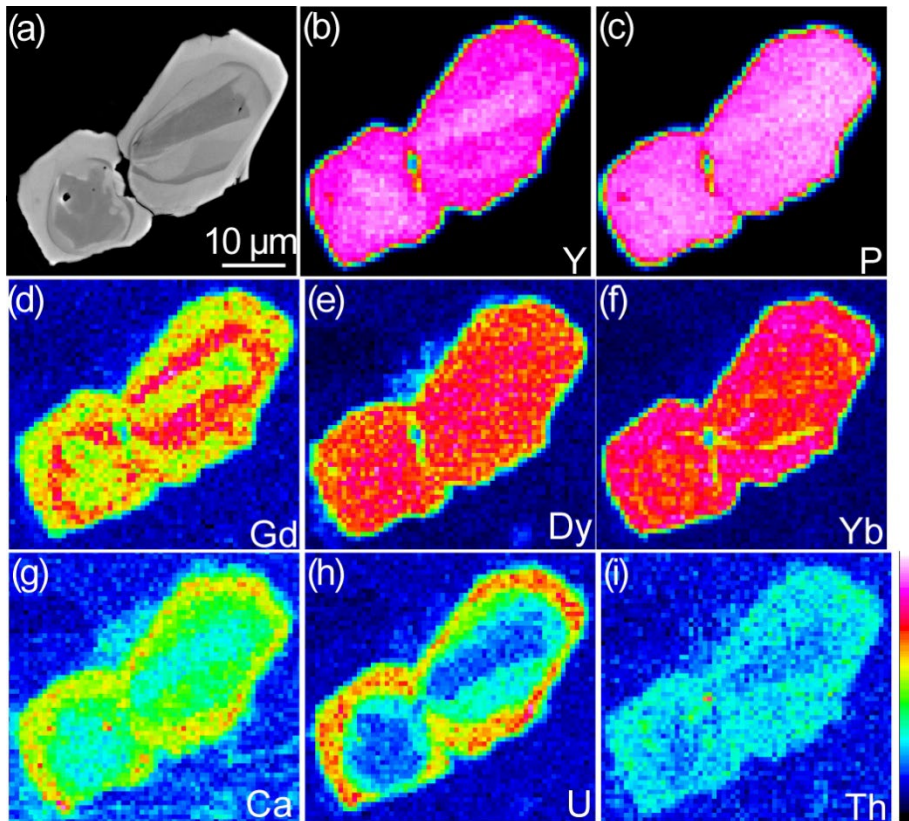


Figure 4.7: EPMA x-ray compositional maps of grain 1642-2.

4.4.3 Insights from atom probe tomography analyses

4.4.3.1 Y1 - Gascoyne Province

Three specimens were analysed from the BSE-intermediate domain of the Y1 grain. The SHRIMP U-Pb geochronology results from the grain showed no disturbance in the scale of analysis, except for one spot from the dark BSE domain. Therefore, the location of the atom probe specimen is isotopically undisturbed at the scale of SHRIMP analysis (Figure 4.2). The mass spectrum obtained from the specimens was consistent with typical xenotime analysis, with a complex mass spectrum consisting of major element peaks (Y, P, O) and rare earth element peaks (HREE) and combined species in different charge states. At the nanoscale, all major elements are distributed homogeneously. However, all three analysed specimens, display a high density of 5-12 nm Ca-rich clusters throughout the analytical volume (Figure 4.8a). The clusters are marked by an increase in Ca (from ~ 0.1 in the matrix to ~ 13 at. % in clusters), and Pb is enriched in low concentration (mostly ~ 0.1 in the matrix to < 1 at. % in clusters) in clusters (Figure 4.8b). However, a small number of clusters ($n=3$), which are comparatively bigger in size, are enriched with up to ~ 4 at. % Pb (Figure 4.8c). In summary, sample Y1 includes two

types of nanoscale clusters, based on their radiogenic Pb concentration, thereafter, named as Ca-rich and Ca-Pb*-rich clusters. The Y, P, and O composition in the clusters is lower than the xenotime matrix and radioactive elements such as U and Th atoms are not enriched in the clusters. Age data for second generation of clusters were not acquired, since there are only a few clusters, the ages of whole specimen and clusters overlapped, and no statistically meaningful data could be derived.

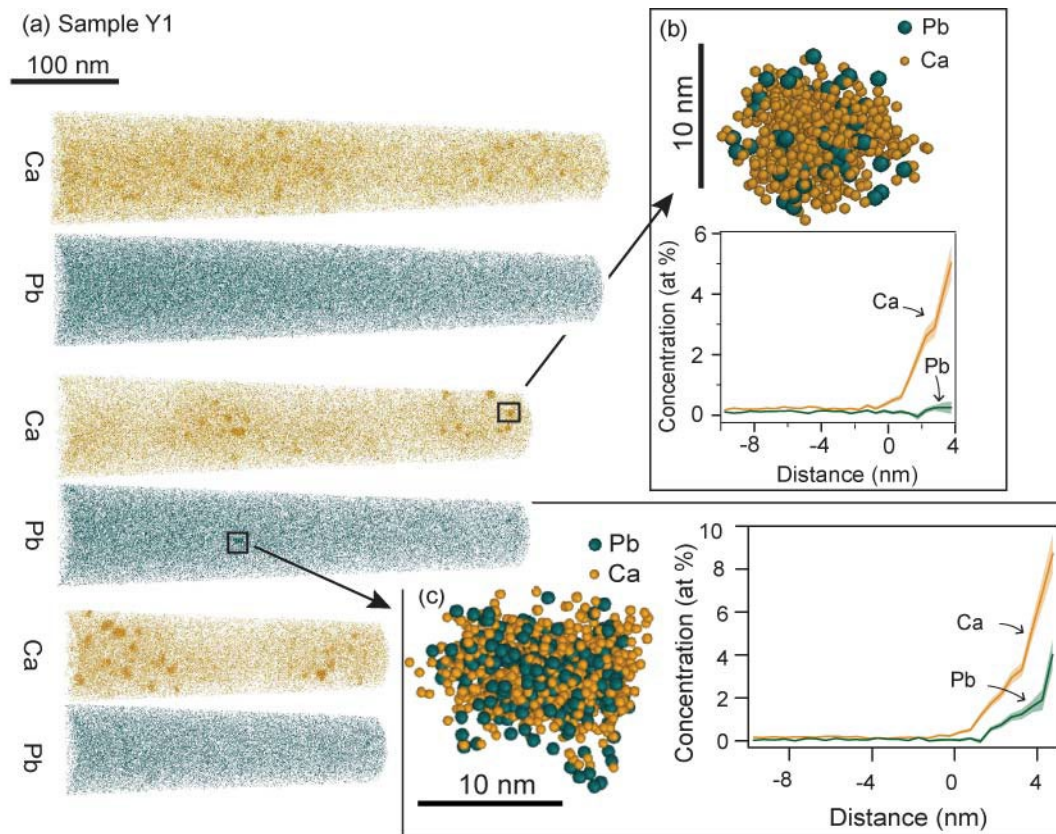


Figure 4.8: (a) APT 3D reconstruction profile showing distributions of Ca and Pb from sample Y1. The needle contains numerous Ca-rich clusters and few Ca-Pb* rich clusters. (b) Closer look of Ca-rich clusters with proximity histogram showing Ca and Pb concentration. Error 1σ . (c) Closer look of Ca-Pb* rich cluster with proximity histogram showing Ca and Pb concentration in Pb* rich clusters.

4.4.3.2 Fanad contact aureole.

A total of 21 specimens were prepared from Fanad xenotime grains, with four specimens from the distal host rock sample 1606 and 17 specimens from the contact zone sample 1642 (Figure 4.9 a,c,d, Appendix 4.4). Out of 22 specimens, 13 specimens were analysed successfully by APT.

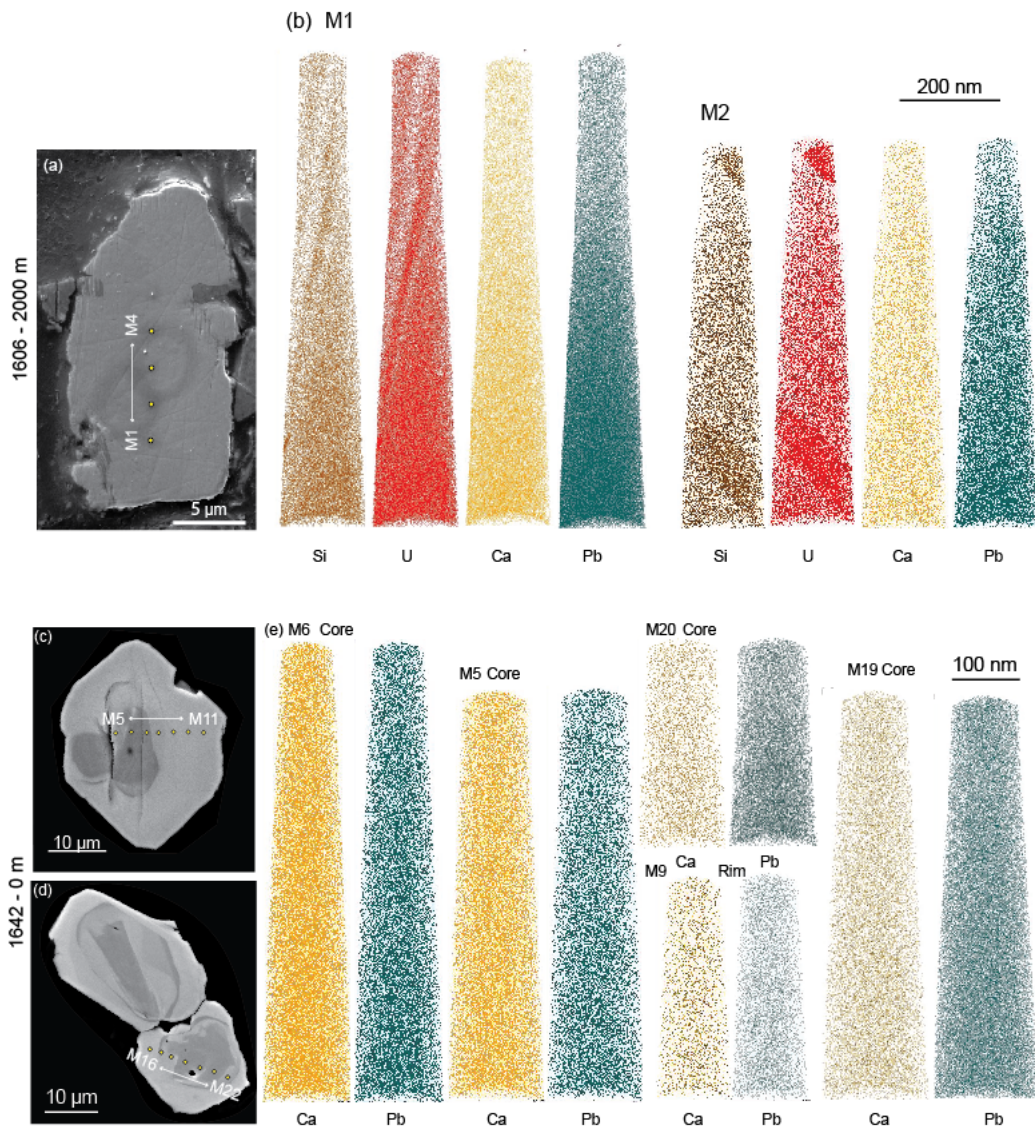


Figure 4.9: (a) Location of APT specimens from xenotime grain from sample 1606 corresponding to host xenotime grain. (b) APT 3D reconstruction profile showing distributions of Si, U, Ca and Pb from specimens M1 and M2. (c) and (d) Xenotime grains showing APT sample locations, sourced from contact zone. (e) APT 3D reconstruction profile showing distributions of Ca and Pb from both core and rim of the grains.

Three out of five needles targeted a matrix xenotime grain from the host rock sample 1606. No heterogeneity in the distribution of trace elements such as Pb* and Ca is observed. However, planar domains (~10 nm, ~100 nm, and ~200 nm in width) rich in Si and U transect the specimens at various orientations (M1 and M2; Figure 4.9b). The increase of Si and U is compensated by a lower major elements concentration (Y, P).

Ten specimens were analysed from two xenotime grains in contact zone sample 1642 with specimens from both the core and the rim of the two zoned xenotime grains (Figure 4.9

c,d). The 3d reconstructions of the major (Y, P and O) and trace (U, Si, Ca and Pb) elements are homogenous at the nanoscale, except for one specimen characterised by the presence of a dislocation enriched in Si (Appendix 4.4).

No nanogeochronology data could not be performed using APT from Fanad xenotime specimens due to low concentrations of U-Pb in the samples (particularly in host xenotime grains) and consequently high uncertainties obtained overlapped between regional metamorphism (xenotime core - ~ 460 Ma) and contact metamorphism (xenotime rim - ~ 420 Ma) events.

4.5 Discussion

4.5.1 Microscale texture and geochemistry of xenotime

4.5.1.1 Y1 - Gascoyne Province, Western Australia

Xenotime sample from pegmatite Y1 shows a complex texture in the BSE image, showing three domains (Figure 4.2). The BSE-bright domain, distributed mainly at the top and in the core of the grain, has the highest U, Th content, with a U/Th ratio of 2.4 considered as the unaltered original part of the grain. The BSE-intermediate domain, which constitutes most of the grain, has a U/Th ratio of ~ 3. The BSE-dark domain is characterised by sharp boundaries and associated with the presence of numerous U-Th inclusions linked with porosity. This domain has the lowest U/Th ratio of ~1.6. Depletion of actinides from the BSE-dark domain concurrent with the presence of U-Th inclusions and associated porosity advises the mechanism of the fluid-mediated dissolution-precipitation process (Putnis, 2009; Joseph et al., 2023). In the case of the BSE-intermediate domain, the U/Th ratio is close to the original (BSE-bright) xenotime; therefore, this domain is likely an igneous overgrowth on the BSE-bright core. The contact between BSE-bright and BSE-intermediate domains indicates some amount of grain edge dissolution between the two episodes of xenotime growth. The geochronology results, which targeted all the domains yield concordant results except for one point from the BSE-dark domain showing Pb loss trend (Figure 4.4). The concordant results from the U-Pb analysis show that the fluid alteration has no or limited impact on the resetting of the U-Pb system and preserves the crystallisation of the sample at the scale of SHRIMP analysis.

4.5.1.2 Fanad contact aureole, Ireland.

Xenotime is a common accessory phase in a pelitic metamorphic assemblage. The growth and consumption of xenotime are tightly linked to the stability of garnet as both

minerals incorporate heavy rare earth elements (Gd – Lu + Y) in their structure (Pyle and Spear, 2000, 2003; Spear and Pyle, 2002). The small grain size and mostly anhedral shape of the xenotime grains, especially xenotime grains seen as inclusions in chlorite knots, suggests that the xenotime grains are either remnant after garnet growth or these grains are formed as the result of garnet retrogression to chlorite. The latter may be the most favourable, as reflected in the geochemistry, in which the xenotime inclusions in the chlorite show higher Y content (Y - 38.6 wt. %) compared to the matrix xenotime (Y - 36.89 wt. %). The slightly higher Y content in the xenotime inclusions in the chlorite is probably the result of Y released from garnet during retrogression to chlorite. The dissimilarity between xenotime inclusions and matrix xenotime also reflects in different U/Th ratios, 0.73 and 6.8, respectively. The higher U/Th ratio of matrix xenotime could suggest a detrital origin. However, further evidence is needed to support the argument, such as rare earth element behaviour; for example, a strong negative Eu anomaly from xenotime indicates igneous origin (Kositcin et al., 2003; Aleinikoff et al., 2015). Nevertheless, for the samples, the Eu signal was below the EPMA detection limit; therefore, no conclusions were made on the origin of the xenotime in the matrix. The xenotime grains from the intermediate zones of the contact aureole, sample 1621 – 1520 m from the contact zone, still showcase small, anhedral xenotime grains, which indicates that there is only limited impact of metamorphism in this zone and is likely to represent the regional metamorphic xenotime. In sample 1630 (990 m from the contact zone), the xenotime grains change into larger subhedral to sub-euhedral grain shapes and are associated with other major accessory phases such as zircon and monazite (Figure 4.4). The association with other accessory phases and larger grains could suggest new contact metamorphic xenotime growth. The EPMA spot analysis from the sample shows no noticeable changes in the major element chemistry. However, the U/Th ratio of the sample is in the range of ~ 6.8, which is significantly higher than the U/Th ratio from xenotime inclusions from the host rock. The high ratio is possibly due to the co-precipitation of monazite, in which Th gets incorporated into monazite (Spear and Pyle, 2002; Rasmussen et al., 2011).

Xenotime grains observed in the contact zone sample 1642 are subhedral to euhedral shape with an increased grain size of up to 50 μm , as shown in previous studies (Franz et al., 1996; Rubatto et al., 2001). The major element chemistry of both unzoned xenotime grains (P ~15.5 wt. % and Y 37. 6 wt. %) and the rim of the zoned xenotime (P ~14.82 wt. % and Y ~ 36.1 wt. %) from this high-temperature metamorphic realm, is slightly lower than the major element chemistry from the core of the zoned grains (P ~ 15.2 and Y ~ 38.0 wt. %). The decrease of Y content in xenotime at higher temperatures is consistent with previous studies on

metamorphic xenotime (Pyle et al., 2001; Spear and Pyle, 2002; Pyle and Spear, 2003). The systematic decrease in Y in xenotime and increase of Y in monazite towards higher metamorphic grade is used as a geothermometer in metamorphic terranes (Gratz and Heinrich, 1998). The rim of the zoned grains shows higher actinide content and higher Ca. This sympathetic relationship of U, Th and Ca supports the brabantite substitution reaction $(U/Th)^{4+} + Ca^{2+} = 2REE^{3+}$ (Spear and Pyle, 2002). The difference in U/Th ratio of the samples, unzoned xenotime grains, and core and rim composition of the zoned xenotime grains clearly indicate that the two generations of xenotime are of different origins. The core represents xenotime precipitating from the regional breakdown of garnet, whereas the rim and the unzoned grains represent new xenotime growth during contact metamorphism (Figure 4.5). Therefore, it is clear that the core of the zoned xenotime grains was exposed to contact metamorphism (650 – 700 °C, Tuttle and Bowen, 1958) during the granite emplacement.

4.5.2 Influence of composition and cooling rate in the formation of nanoscale clusters

Nanoscale analyses on phosphates have shown the presence of Pb* enriched clusters, which have been proposed to form by the processes such as dissolution-reprecipitation (Fougerouse et al., 2021a; Turuani et al., 2022; Joseph et al., 2023), phase immiscibility (Fougerouse et al., 2018; Seydoux-Guillaume et al., 2019). In monazite, Pb* enriched galena nanocrystals have been shown to form by fluid-mediated dissolution-reprecipitation processes (Turuani et al., 2022) and, in another instance, formation of nanoscale britholite inclusions due to fluid alteration (Fougerouse et al., 2021a). Phase immiscibility coupled with continuous diffusion of Pb* to form Pb* enriched clusters has been shown in monazite, which had undergone high-temperature metamorphism (Seydoux-Guillaume et al., 2019). Phase immiscibility associated with the cooling of the monazite crystal has also been proposed in the formation of apatite inclusions (Fougerouse et al., 2018). In recent studies on xenotime, fluid-mediated dissolution reprecipitation has been purported to form nanoscale apatite inclusions from a fluid-altered pegmatite xenotime sample (Joseph et al., 2023). The redistribution of Pb* in the nanoscale is significant as the distribution of these Pb* enriched phases can attribute to a mechanism of resetting the geochronometer. This can also explain the variability in the geochronology results obtained from conventional analytical techniques, and the time constrain can be availed from these nanoscale phases using nanogeochronology methods (Seydoux-Guillaume et al., 2019; Fougerouse et al., 2021a; Joseph et al., 2023)

In the case of pegmatite xenotime sample Y1, two types of clusters can be seen; the numerous Ca rich, Ca clusters and the rare Pb enriched (up to ~4 at. % Pb) Ca-Pb* clusters.

Clusters in minerals represent either crystal defects (Peterman et al., 2016) or a separate phase (Fougerouse et al., 2016, 2018; Seydoux-Guillaume et al., 2019). Here, in this case, the Ca+Pb concentration in the clusters is up to ~14 at. % and both types of clusters likely represent a different phase. Clusters of equivalent compositions in xenotime from Ontario, Canada, were determined to represent a separate phase using APT and diffraction data from transmitted electron microscopy (Joseph et al., 2023). The composition of the nanoscale inclusions is consistent with apatite $[\text{Ca}_5(\text{PO}_4)_3(\text{F},\text{Cl},\text{OH})]$, in which Ca can substitute for Pb and exists as a complete solid solution (Harrison et al., 2002; Pan and Fleet, 2002).

The concentration of Pb* in the Ca rich apatite inclusions is less than 1 at. %, indicating a short time frame between crystallisation and the formation of the inclusions. Calcium is incorporated into the xenotime structure by coupled substitution with U/Th, where Ca replaces P in the structure ($\text{U/Th}^{4+} + \text{Ca}^{2+} = 2\text{REE}^{3+}$) (Spear and Pyle, 2002). However, the ionic radius of both Ca and Pb with +2 charge is larger compared to the small $(\text{Y/REE})^{3+}$ (Shannon, 1976; Van Emden et al., 1997). The larger radius of the Ca and Pb causes strain in the crystal lattice, therefore, it is proposed that the apatite inclusions are formed due to phase immiscibility and exsolved during the cooling of the crystal. Phase immiscibility has been proposed to form mineral inclusions in other minerals and also in monazite, as mentioned before (Putnis, 2002; Ferraris et al., 2005; Harlov, 2011; Fougerouse et al., 2018). The Pb* enriched apatite inclusions, in which the Pb* concentration is up to ~4 at. %, must be a different generation of apatite inclusion formation later in the history of the grain. Provided the grain has not undergone any high-temperature metamorphism post-crystallisation, the apatite inclusions are likely to be formed by fluid activity. A recent study in fluid-altered xenotime has proposed pervasive fluid activity to be responsible for the formation of apatite nanoscale inclusion (Joseph et al., 2023). The mechanism is highly favourable because the Y1 grain is characterised by fluid alteration microscale texture. However, the limited number of Pb* enriched inclusions (4 from 3 APT specimens) may indicate that the alteration was selective and not pervasive enough to affect the SHRIMP geochronology results.

In the Fanad contact metamorphic xenotime samples, sample 1606, a matrix xenotime grain from the host rock, shows homogeneity in Pb* and Ca distribution. However, trace elements such as Si and U are enriched in planar domains (5 – up to 200 nm thick) in two specimens (Figure 4.9b). The coupling of Si and U in xenotime points towards the substitution mechanism in which actinides get into the xenotime structure, $(\text{Th/U})^{4+} + \text{Si}^{4+} = \text{REE}^{3+} + \text{P}^{5+}$, where Si replacing P and Th/U replacing the Y/REE (Spear and Pyle, 2002).

In zoned xenotime grains analysed from the contact zone, the U/Th ratio from the sample shows that the core of the xenotime grain is likely to represent xenotime from the host rock and the rim newly formed xenotime from contact metamorphism (Figure 4.5). Therefore, it is apparent that the core has undergone high-temperature metamorphism during granite emplacement. Fanad contact aureole is considered one of the high-temperature contact aureoles in the Donegal group of granites with the presence of pristine sillimanite growth, ranging up to 700–800 °C and mineral texture suggests a long period of static crystallization (Pitcher and Read, 1963; Naggar and Atherton, 1970). The exposure to high temperature for an extended period seemingly does not affect the xenotime crystal, as observed from the atom probe results, where the Pb* and Ca nanoscale distribution is homogeneous (Figure 4.9). Observations from nanoscale analysis of other geochronometers exposed to high-temperature metamorphism have shown heterogeneities in Pb* distribution in previous cases studies (Peterman et al., 2016, 2019; Verberne et al., 2020), which is contrary to what has been observed in the xenotime samples from the Fanad case study.

From all the previous studies on minerals, one common influencing factor can be identified is the radiation damage affecting the minerals and later facilitating the redistribution of Pb* during the annealing of the crystal (Utsunomiya et al., 2004; Valley et al., 2014, 2015; Peterman et al., 2016; Verberne et al., 2020). For e.g., in zircon, often the diffusivity of trace elements including Pb* is enhanced when percolation point is achieved due to a high dose of radiation damage, in which the amorphous domains make an interconnected network serving as fast diffusion pathways (Salje et al., 1999; Ríos et al., 2000; Trachenko et al., 2003; Utsunomiya et al., 2004). In the case of xenotime, primarily, the Pb diffusion is found to be slower than other accessory phases, such as monazite and zircon (Cherniak, 2006, 2010). Furthermore, xenotime is resistant to radiation damage, and no metamict xenotime has been found in nature (Harrison et al., 2002; Lenz et al., 2019). This resistance to radiation damage is attributed to lower activation energy to anneal the radiation damage in xenotime (Lenz et al., 2019). Therefore, a condition even close to the percolation point, like in zircon, must have never been achieved in the Fanad xenotime sample due to the annealing of radiation damage. Along with the slow Pb diffusion in xenotime, conditions to form Pb* enriched phases have never been attained.

When the metamorphic xenotime sample is compared to the Y1 pegmatite sample, a distinction can be found in the Ca composition of the samples. The Ca composition of host rock xenotime, which has undergone high-temperature metamorphism, is in the range of ~0.01

wt. %. Whereas for igneous pegmatite sample Y1, the average Ca concentration is ~ 0.13 wt. %, which is around 12 times higher than the metamorphic xenotime (Figure 4.10).

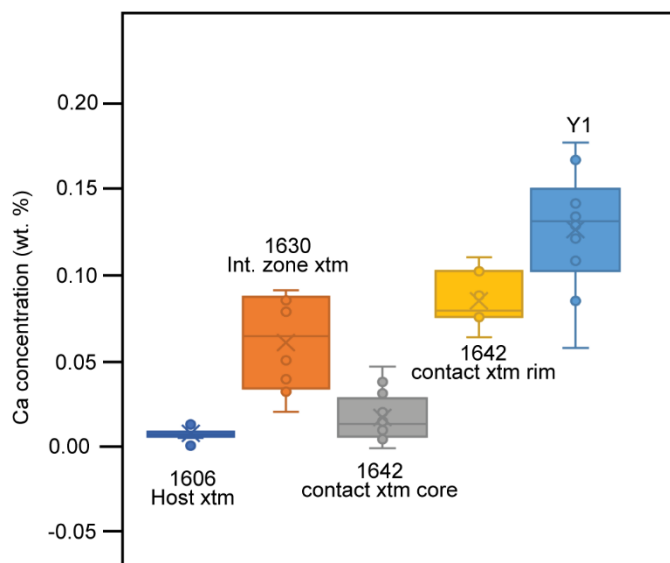


Figure 4.10: Box and whisker graph showing the Ca concentration of samples studied.

Ca in xenotime structure bigger (Ca^{2+} 1.12 Å) than Y^{3+} (1.019 Å) ion (Shannon, 1976). Fanad xenotime samples were heated up to ~700–800 °C (Pitcher and Read, 1963; Kerrick, 1987), whereas the crystallisation temperature of a pegmatite (Y1) is < 500 °C (Kozłowski, 1978; Kozłowski and Marcinowska, 2007; London and Kontak, 2012); when both these samples underwent cooling with different levels of Ca in their structure, apatite inclusions formed in the sample with high Ca content (Figure 4.11). Therefore, Ca concentration in xenotime may control the formation of apatite inclusions thereby, redistribution in Pb^* . Possibly the cooling rate of the sample also has an influence in which faster cooling directly affects the formation of apatite inclusions. In this case, the cooling rate is faster for the pegmatite sample than a slowly cooling metamorphic contact aureole in which the system can homogenise. Therefore in the case of xenotime, it appears that major factors contributing to the redistribution of Pb^* are its primary composition and fluid activity (Joseph et al., 2023). The observation of high Ca xenotime facilitating apatite inclusion formation, which can act as a sink for Pb^* in later geological events, possibly helps xenotime to retain the Pb^* formed in the crystal structure itself. The retainment of Pb^* in such a way could imply that the high Ca xenotime is more resilient to age resetting due to limited Pb^* mobility.

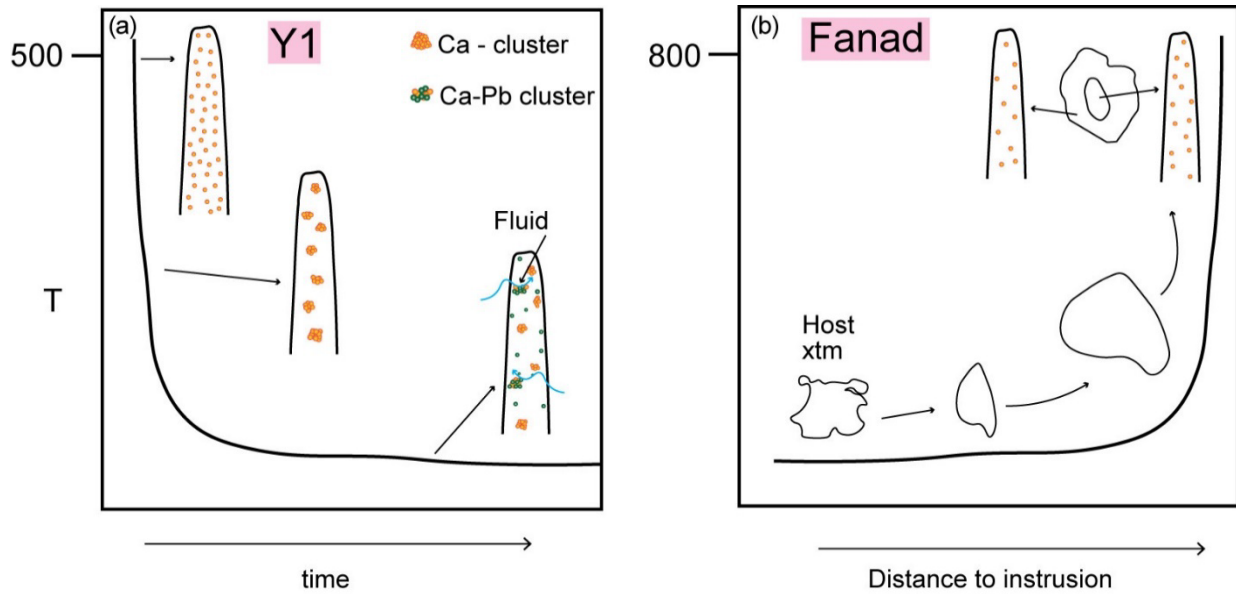


Figure 4.11: Summary diagram illustrating processes that affected the samples. (a) Crystallisation of high Ca pegmatite xenotime. Exsolution of Ca rich apatite inclusions during cooling of the crystal with minor Pb*. Later fluid alteration causing selective Pb* mobility into the previously formed apatite inclusions, forming of Ca-Pb* rich apatite inclusions. (b) Crystallisation of xenotime from garnet breakdown (xtm host) in the host metapelite. Coarsening of xenotime grains by increasing metamorphic grade and forming new xenotime rims due to contact metamorphism. Host xenotime exists as core, having low Ca concentration is affected by high-temperature metamorphism. However, no formation of apatite inclusions at this high temperature. (Colour code: orange – Ca atom, green – Pb atom).

4.6 Conclusion

Formation of Pb* enriched clusters is rather a common observation in nanoscale analysis of geochronometers. The processes of radiation damage and high-temperature metamorphism found to be the controlling factors for the formation of Pb* heterogeneities from previous studies of the minerals. However, the results obtained from two different samples, having different geological histories and compositions have shown that, in xenotime the composition and fluid activity are possibly the main decisive factors in the redistribution of Pb* and formation of clusters. The behaviour of Pb* is tightly linked to Ca, owing to the similarity in ionic sizes.

4.7 Acknowledgements

Mount A-13 (Y1) and mount 05-12 (MG-1) used for xenotime standard in this project is part of the McNaughton Legacy Collection, by John de Laeter Centre (JdLC). This study supported by the Australian Science and Industry Endowment Fund (grant SIEF RI13-01) and the Discovery Early Career Research Award from the Australian Research Council to Denis Fougere (DE190101307). The author acknowledges the support of Microscopy and Microscopy Facility and JdLC, Curtin University, whose instrumentation has been supported by University, State and Commonwealth Government funding.

4.8 References

- Aleinikoff J. N., Lack J. F. S., Lund K., Evans K. V., Fanning C. M., Mazdab F. K., Wooden J. L. and Pillers R. M. (2012) Constraints on the timing of Co-Cu \pm Au mineralization in the Blackbird district, Idaho, using SHRIMP U-Pb ages of monazite and xenotime plus zircon ages of related Mesoproterozoic orthogneisses and metasedimentary rocks. *Econ. Geol.* **107**, 1143–1175.
- Aleinikoff J. N., Lund K. and Fanning C. M. (2015) SHRIMP U-Pb and REE data pertaining to the origins of xenotime in belt supergroup rocks: Evidence for ages of deposition, hydrothermal alteration, and metamorphism. *Can. J. Earth Sci.* **52**, 722–745.
- Bodorkos S., Bowring J. F. and Rayner N. M. (2020) Squid3: next-generation data processing software for sensitive high-resolution ion microprobe (SHRIMP).
- Cherniak D. J. (2010) Diffusion in accessory minerals: Zircon, titanite, apatite, monazite and xenotime. *Rev. Mineral. Geochemistry* **72**, 827–869.
- Cherniak D. J. (2006) Pb and rare earth element diffusion in xenotime. *Lithos* **88**, 1–14.
- Drake M. J. and Weill D. F. (1972) New rare earth element standards for electron microprobe analysis. *Chem. Geol.* **10**, 179–181.
- Edmunds W. M. and Atherton M. P. (1971) Polymetamorphic evolution of garnet in the Fanad aureole, Donegal, eire. *Lithos* **4**, 147–161.
- Ferraris C., White T. J., Plévert J. and Wegner R. (2005) Nanometric modulation in apatite. *Phys. Chem. Miner.* **32**, 485–492.
- Fletcher I. R., McNaughton N. J., Aleinikoff J. A., Rasmussen B. and Kamo S. L. (2004) Improved calibration procedures and new standards for U-Pb and Th-Pb dating of Phanerozoic xenotime by ion microprobe. *Chem. Geol.* **209**, 295–314.

- Fletcher I. R., Rasmussen B. and McNaughton N. J. (2000) SHRIMP U-Pb geochronology of authigenic xenotime and its potential for dating sedimentary basins. *Aust. J. Earth Sci.* **47**, 845–859.
- Fougerouse D, Cavosie A. J., Erickson T., Reddy S. M., Cox M. A., Saxey D. W., Rickard W. D. A. and Wingate M. T. D. (2021a) A new method for dating impact events – Thermal dependency on nanoscale Pb mobility in monazite shock twins. *Geochim. Cosmochim. Acta* **314**, 381–396.
- Fougerouse D., Kirkland C. L., Saxey D. W., Seydoux-Guillaume A. M., Rowles M. R., Rickard W. D. A. and Reddy S. M. (2020) Nanoscale Isotopic Dating of Monazite. *Geostand. Geoanalytical Res.* **44**, 637–652.
- Fougerouse D., Reddy S. M., Kirkland C. L., Saxey D. W., Rickard W. D. and Hough R. M. (2019) Time-resolved, defect-hosted, trace element mobility in deformed Witwatersrand pyrite. *Geosci. Front.* **10**, 55–63.
- Fougerouse D., Reddy S. M., Saxey D. W., Erickson T. M., Kirkland C. L., Rickard W. D. A., Seydoux-Guillaume A.-M., Clark C. and Buick I. S. (2018) Nanoscale distribution of Pb in monazite revealed by atom probe microscopy. *Chem. Geol.* **479**, 251–258.
- Fougerouse D., Reddy S. M., Saxey D. W., Rickard W. D. A., van Riessen A. and Micklethwaite S. (2016) Nanoscale gold clusters in arsenopyrite controlled by growth rate not concentration: Evidence from atom probe microscopy. *Am. Mineral.* **101**, 1916–1919.
- Fougerouse D, Saxey D. W., Rickard W. D. A., Reddy S. M. and Verberne R. (2021b) Standardizing Spatial Reconstruction Parameters for the Atom Probe Analysis of Common Minerals. *Microsc. Microanal.*, 1–10.
- Franz G., Andrehs G. and Rhede D. (1996) Crystal chemistry of monazite and xenotime from Saxothuringian-Moldanubian metapelites, NE Bavaria, Germany. *Eur. J. Mineral.* **8**, 1097–1118.
- Gratz R. and Heinrich W. (1998) Monazite-xenotime thermometry. III. Experimental calibration of the partitioning of gadolinium between monazite and xenotime. *Eur. J. Mineral.* **10**, 579–588.
- Harrison T. M., Catlos E. J. and Montel J.-M. (2002) U-Th-Pb Dating of Phosphate Minerals. *Rev. Mineral. Geochemistry* **48**, 524–558.

- Harlov D. E., Wirth R. and Hetherington C. J. (2011) Fluid-mediated partial alteration in monazite: the role of coupled dissolution–reprecipitation in element redistribution and mass transfer. *Contrib. to Mineral. Petrol.* **162**, 329–348.
- Howie R. A. (1974) W. S. Pitcher and A. R. Berger. The geology of Donegal: a study of granite emplacement and unroofing (with a coloured r : 63 360 geol. map compiled by Margaret O. Spencer). New York and London (Wiley-Interscience), 1972. xii+435 pp., 150 figs., 2 maps. *Mineral. Mag.* **39**, 614–616.
- Jarosewich e., Nelen J. A. and Norberg J. A. (1980) Reference Samples for Electron Microprobe Analysis*. *Geostand. Geoanalytical Res.* **4**, 43–47.
- Johnson S.P., Sheppard S. (2015) Davey Well Granite (P _ -DUda-mgmu). *WA Geol. Online, Explan. Notes Extr.*, 4–8.
- Johnson S.P., Sheppard S., and Korhonen F.J., (2013) Mulka Tectonic Event (MK): Geological Survey of Western Australia, WA Geology Online, *Explanatory Notes extract* <www.dmp.wa.gov.au/ens>
- Joseph C., Fougereuse D., Reddy S. M., Olierook H. K. H., Tacchetto T., Kennedy A., Saxey D. W., Rickard W. D. A., Denyszyn S. and Dodd A. (2023) Radiogenic Pb in xenotime trapped in nanoscale inclusions of apatite during fluid alteration. *Chem. Geol.*, 121444.
- Kerrick D. M. (1987) Fibrolite in contact aureoles of Donegal, Ireland. *Am. Mineral.* **72**, 240–254.
- Kositcin N., McNaughton N. J., Griffin B. J., Fletcher I. R., Groves D. I. and Rasmussen B. (2003) Textural and geochemical discrimination between xenotime of different origin in the Archaean Witwatersrand Basin, South Africa. *Geochim. Cosmochim. Acta* **67**, 709–731.
- Kozłowski A. (1978) Pneumatolytic and hydrothermal activity in the Karkonosze-Izera block. *Acta Geol. Pol.* **28**, 171–222.
- Kozłowski A. and Marcinowska A. (2007) Hydrothermal activity in the Karkonosze, Strzegom and Strzelin massifs—a fluid inclusion study. *Granitoids Poland. AM Monogr.* **1**, 243–252.
- Lambert R. S. J. and McKerrow W. S. (1976) The Grampian Orogeny. *Scottish J. Geol.* **12**, 271–292.
- Laurent A. T., Seydoux-Guillaume A.-M., Duchene S., Bingen B., Bosse V. and Datas L. (2016) Sulphate incorporation in monazite lattice and dating the cycle of sulphur in

- metamorphic belts. *Contrib. to Mineral. Petrol.* **171**, 94.
- Lenz C., Thorogood G., Aughterson R., Ionescu M., Gregg D. J., Davis J. and Lumpkin G. R. (2019) The Quantification of Radiation Damage in Orthophosphates Using Confocal μ -Luminescence Spectroscopy of Nd³⁺. *Front. Chem.* **7**, 1–13.
- Li Q. L., Li X. H., Lan Z. W., Guo C. L., Yang Y. N., Liu Y. and Tang G. Q. (2013) Monazite and xenotime U-Th-Pb geochronology by ion microprobe: Dating highly fractionated granites at Xihuashan tungsten mine, SE China. *Contrib. to Mineral. Petrol.* **166**, 65–80.
- London D. and Kontak D. J. (2012) Granitic Pegmatites: Scientific Wonders and Economic Bonanzas. *Elements* **8**, 257–261.
- Meldrum A, Boatner L. A. and Ewing R. C. (1997) Displacive radiation effects in the monazite- and zircon-structure orthophosphates. *Phys. Rev. B* **56**, 13805–13814.
- Naggar M. H. and Atherton M. P. (1970) The composition and metamorphic history of some aluminium silicate-bearing rocks from the aureoles of the Donegal granites. *J. Petrol.* **11**, 549–589.
- O'Connor P. J., Long C. B. and Evans J. A. (1987) Rb-Sr whole-rock isochron studies of the Barnesmore and Fanad plutons, Donegal, Ireland. *Geol. J.* **22**, 11–23.
- Olierook H. K. H., Agangi A., Plavsa D., Reddy S. M., Yao W., Clark C., Occhipinti S. A. and Kylander-Clark A. R. C. (2019) Neoproterozoic hydrothermal activity in the West Australian Craton related to Rodinia assembly or breakup? *Gondwana Res.* **68**, 1–12.
- Pan Y. and Fleet M. E. (2002) Compositions of the Apatite-Group Minerals: Substitution Mechanisms and Controlling Factors. *Rev. Mineral. Geochemistry* **48**, 13–49.
- Peterman E. M., Reddy S. M., Saxey D. W., Fougereuse D., Quadir M. Z. and Jercinovic M. J. (2021) Trace-element segregation to dislocation loops in experimentally heated zircon. *Am. Mineral.* **106**, 1971–1979.
- Peterman E. M., Reddy S. M., Saxey D. W., Fougereuse D., Snoeyenbos D. R. and Rickard W. D. A. (2019) Nanoscale processes of trace element mobility in metamorphosed zircon. *Contrib. to Mineral. Petrol.* **174**.
- Peterman E. M., Reddy S. M., Saxey D. W., Snoeyenbos D. R., Rickard W. D. A., Fougereuse D. and Kylander-Clark A. R. C. (2016) Nanogeochronology of discordant zircon measured by atom probe microscopy of Pb-enriched dislocation loops. *Sci. Adv.* **2**.

- Piazolo S., La Fontaine A., Trimby P., Harley S., Yang L., Armstrong R. and Cairney J. M. (2016) Deformation-induced trace element redistribution in zircon revealed using atom probe tomography. *Nat. Commun.* **7**, 10490.
- Piechocka A. M., Gregory C. J., Zi J. W., Sheppard S., Wingate M. T. D. and Rasmussen B. (2017) Monazite trumps zircon: applying SHRIMP U–Pb geochronology to systematically evaluate emplacement ages of leucocratic, low-temperature granites in a complex Precambrian orogen. *Contrib. to Mineral. Petrol.* **172**, 1–17.
- Pitcher W. S. and Read H. H. (1963) Contact Metamorphism in Relation to Manner of Emplacement of the Granites of Donegal, Ireland. *J. Geol.* **71**, 261–296.
- Putnis A. (2002) Mineral replacement reactions: from macroscopic observations to microscopic mechanisms. *Mineral. Mag.* **66**, 689–708.
- Putnis A. (2009) Mineral replacement reactions. *Rev. Mineral. Geochemistry* **70**, 87–124.
- Pyle J. M. and Spear F. S. (2000) An empirical garnet (YAG) - xenotime thermometer. *Contrib. to Mineral. Petrol.* **138**, 51–58.
- Pyle J. M. and Spear F. S. (2003) Yttrium zoning in garnet: Coupling of major and accessory phases during metamorphic reactions. *Am. Mineral.* **88**, 708.
- Pyle J. M., Spear F. S., Rudnick R. L. and McDonough W. F. (2001) Monazite-xenotime-garnet equilibrium in metapelites and a new monazite-garnet thermometer. *J. Petrol.* **42**, 2083–2107.
- Rasmussen B. (2005) Radiometric dating of sedimentary rocks: The application of diagenetic xenotime geochronology. *Earth-Science Rev.* **68**, 197–243.
- Rasmussen B., Fletcher I. R. and Muhling J. R. (2011) Response of xenotime to prograde metamorphism. *Contrib. to Mineral. Petrol.* **162**, 1259–1277.
- Reddy S. M., Saxey D. W., Rickard W. D. A., Fougereuse D., Montalvo S. D., Verberne R. and van Riessen A. (2020) Atom Probe Tomography: Development and Application to the Geosciences. *Geostand. Geoanalytical Res.* **44**, 5–50.
- Rickard W. D. A., Reddy S. M., Saxey D. W., Fougereuse D., Timms N. E., Daly L., Peterman E., Cavosie A. J. and Jourdan F. (2020) Novel Applications of FIB-SEM-Based ToF-SIMS in Atom Probe Tomography Workflows. *Microsc. Microanal.* **26**, 750–757.
- Ríos S., Salje E. K. H., Zhang M. and Ewing R. C. (2000) Amorphization in zircon: evidence

- for direct impact damage. *J. Phys. Condens. Matter* **12**, 2401.
- Rubatto D., Williams I. S. and Buick I. S. (2001) Zircon and monazite response to prograde metamorphism in the Reynolds Range, central Australia. *Contrib. to Mineral. Petrol.* **140**, 458–468.
- Salje E. K. H., Chrosch J. and Ewing R. C. (1999) Is “metamictization” of zircon a phase transition? *Am. Mineral.* **84**, 1107–1116.
- Seydoux-Guillaume A. M., Fougrouse D., Laurent A. T., Gardés E., Reddy S. M. and Saxey D. W. (2019) Nanoscale resetting of the Th/Pb system in an isotopically-closed monazite grain: A combined atom probe and transmission electron microscopy study. *Geosci. Front.* **10**, 65–76.
- Shannon R. D. (1976) Revised effective ionic radii and systematic studies of interatomic distances in halides and chalcogenides. *Acta Crystallogr. Sect. A* **32**, 751–767.
- Spear F. S. and Pyle J. M. (2002) Apatite, monazite, and xenotime in metamorphic rocks (in Phosphates; geochemical, geobiological, and materials importance) *Reviews in Mineralogy and Geochemistry. Rev. Mineral. Geochemistry* **48**, 293–335.
- Stacey J. S. and Kramers J. D. (1975) Approximation of terrestrial lead isotope evolution by a two-stage model. *Earth Planet. Sci. Lett.* **26**, 207–221.
- Trachenko K., Dove M. T. and Salje E. K. H. (2003) Large swelling and percolation in irradiated zircon. *J. Phys. Condens. Matter* **15**, L1–L7.
- Turuani M. J., Laurent A. T., Seydoux-Guillaume A.-M., Fougrouse D., Saxey D., Reddy S. M., Harley S. L., Reynaud S. and Rickard W. D. A. (2022) Partial retention of radiogenic Pb in galena nanocrystals explains discordance in monazite from Napier Complex (Antarctica). *Earth Planet. Sci. Lett.* **588**, 117567.
- Tuttle O. F. and Bowen N. L. (1958) Origin of granite in the light of experimental studies in the system NaAlSi₃O₈–KAlSi₃O₈–SiO₂–H₂O.
- Utsunomiya S., Palenik C. S., Valley J. W., Cavosie A. J., Wilde S. A. and Ewing R. C. (2004) Nanoscale occurrence of Pb in an Archean zircon. *Geochim. Cosmochim. Acta* **68**, 4679–4686.
- Valley J. W., Cavosie A. J., Ushikubo T., Reinhard D. A., Lawrence D. F., Larson D. J., Clifton P. H., Kelly T. F., Wilde S. A., Moser D. E. and Spicuzza M. J. (2014) Hadean age for a

- post-magma-ocean zircon confirmed by atom-probe tomography. *Nat. Geosci.* **7**, 219–223.
- Valley J. W., Reinhard D. A., Cavosie A. J., Ushikubo T., Lawrence D. F., Larson D. J., Kelly T. F., Snoeyenbos D. R. and Strickland A. (2015) Presidential Address. Nano- and micro-geochronology in Hadean and Archean zircons by atom-probe tomography and SIMS: New tools for old minerals. *Am. Mineral.* **100**, 1355–1377.
- Van Emden B., Thornber M. R., Graham J. and Lincoln F. J. (1997) The incorporation of actinides in monazite and xenotime from placer deposits in Western Australia. *Can. Mineral.* **35**, 95–104.
- Verberne R., Reddy S. M., Saxey D. W., Fougereuse D., Rickard W. D. A., Plavsa D., Agangi A. and Kylander-Clark A. R. C. (2020) The geochemical and geochronological implications of nanoscale trace-element clusters in rutile. *Geology* **48**, 1126–1130.

**Towards a new impact geochronometer:
Deformation microstructures and U-Pb systematics
of shocked xenotime**

Abstract

Shock-deformation microstructures in xenotime have been proposed to record diagnostic evidence for meteorite impacts. Evaluating the potential for impact-induced U-Pb age resetting of the various microstructures that form in shocked xenotime remains largely unexplored. In this study, we investigate the U-Pb systematics of shocked xenotime from three impact structures, including Vredefort (South Africa), Santa Fe (New Mexico, USA), and Araguainha (Brazil). Xenotime at these sites is found in shocked granite, impact melt rock, and as detrital grains, and preserves a range of impact-induced microstructures, including planar fractures, planar deformation bands, deformation twins, and polycrystalline neoblastic grains. Microstructures in xenotime characterised by electron backscatter diffraction and then targeted for U-Pb geochronology by secondary ion mass spectrometry (SIMS) and atom probe tomography (APT) to determine element mobility mechanisms at micrometer- to nanometer-scale. At the precision level of SIMS spots, no resetting of the U-Pb system was observed in areas with lattice deformation, planar deformation bands, and twinning. However, some grains with neoblastic textures were found to yield impact ages, with U-Pb disturbance correlating to the degree of recrystallisation. APT data showed nanoscale compositional heterogeneities in the form of Pb*-Ca enriched clusters, dislocations, and grain boundaries with higher concentration of trace elements such as Si, Mg, Ca, Na, Cl, and Al. Combining microstructural, geochronological and nanoscale characterisation, this study demonstrates that only the neoblastic microstructure can yield accurate impact ages. Shocked xenotime with neoblastic texture thus appears to represent a new impact geochronometer that can be used, in some cases, to directly constrain the age of impact events.

5.1 Introduction

Impact events are important in Earth's dynamic history, from possibly triggering plate tectonics and crust formation to the evolution of life (Schulte et al., 2010; O'Neill et al., 2017; Osinski et al., 2020). There are currently ~200 confirmed terrestrial impact structures (Earth Impact Database; Kenkmann, 2021; Osinski et al., 2022), but less than 10% have been accurately dated with a precision better than $\pm 2\%$ (Jourdan et al., 2009, 2012; Schmieder and Kring, 2020). Dating an impact event is challenging, as there are few geochronometers capable of providing precise impact ages (McGregor et al., 2021a). In addition, appropriate material for accurate dating is not always readily available because of erosion and/or post-impact processes which can reset geochronometers (e.g., Kamo et al., 1996). A common method for precisely dating impact events is through application of the U-Pb system in accessory minerals such as zircon, monazite, apatite, titanite, and baddeleyite in targeted microstructural domains (Hodych and Dunning, 1992; Darling et al., 2016; Erickson et al., 2017; Papapavlou et al., 2018; McGregor et al., 2018, 2019, 2020; Erickson et al., 2020; Timms et al., 2020; Kenny et al., 2021).

Shock metamorphism involves a short pulse of high dynamic pressure which generates high temperature that collectively cause an instantaneous breakdown of mineral structure; this process produces deformation microstructures that are diagnostic of impact processes (Langenhorst and Deutsch, 2012). For example, planar deformation features (PDF) in quartz, high pressure phases (e.g., coesite, stishovite, reidite), and deformation twins (e.g., {112} twins in zircon) are some manifestations of shock metamorphism (Langenhorst and Deutsch, 2012; Timms et al., 2017; Cavosie et al., 2021a). The formation of certain microstructures has been shown to reset U-Pb geochronometers; for example, recrystallised granular zircon from impact sites can provide precise impact ages (Gibson et al., 1997; Moser, 1997; Cavosie et al., 2015; Kenny et al., 2021). However, granular zircon is susceptible to partial resetting during the impact, post-impact Pb-loss, as well as radiation damage, which can result in ages that are either older or younger than the impact event (Kamo et al., 1996, 2011; Tohver et al., 2012; Schmieder et al., 2015, 2019; McGregor et al., 2019, 2020). In monazite, neoblastic domains and deformation twins have also been shown to yield impact ages (Erickson et al., 2017, 2020; Fougereuse et al., 2021a). However, monazite is susceptible to age resetting associated with fluid alteration (Williams et al., 2011). Apatite can also yield impact ages, but typically has low actinide concentrations (<100 ppm U), and a high proportion of common Pb (from a few

% to nearly 100%; Chew et al., 2014; Kirkland et al., 2018). The U-Pb response of apatite to impact modification appears to be less controlled by microstructures compared to other accessory minerals, and more dependent on the textural setting of the grain (McGregor et al., 2018, 2020, 2021a). Recrystallised neoblastic titanite grains have been reported from several impact environments (e.g., Timms et al., 2020); however to date, they have not been shown to record unambiguous impact age resetting (Cavosie et al., 2022, and references within).

Xenotime ($[Y, \text{HREE}]PO_4$) is a promising and relatively understudied impact geochronometer. Xenotime is a common accessory mineral in igneous rocks, in low- to high-grade metamorphic rocks, as a product of hydrothermal mineralisation, and as both a detrital and diagenetic phase in sedimentary rocks (Van Emden et al., 1997; McNaughton et al., 1999; Brown et al., 2002; Rasmussen, 2005; Vallini et al., 2005; Aleinikoff et al., 2012; Li et al., 2013; Spear and Pyle, 2002). Even though xenotime contains significant U and Th (up to 1000s ppm), it is resistant to radiation damage and metamictisation is rare (Harrison et al., 2002). During growth, xenotime incorporates negligible amounts of common Pb, and Pb diffusion is slower in xenotime than in other accessory phases such as monazite and zircon (Cherniak, 2006, 2010). Therefore, xenotime is considered to be a robust U-Pb geochronometer (Rasmussen, 2005; Hetherington et al., 2008; McNaughton and Rasmussen, 2018).

Xenotime has been shown to form similar shock deformation microstructures to those found in zircon, including, planar fractures (PF), planar deformation bands (PDB), $\{112\}$ deformation twin lamellae, recrystallisation to neoblastic domains, and broad regions of crystal-plastic deformation (Cavosie et al. 2016a, 2021b; Cox et al., 2021). The only published U-Pb data for shocked xenotime is SHRIMP data for a PDB- and shock-twin-bearing xenotime grain from the Vredefort impact structure; no impact-age resetting was detected associated with either the $\{112\}$ twins or PDB, but evidence for a younger (post-impact) thermal event that caused Pb-loss was identified from a lower Concordia intercept (Cavosie et al., 2021b).

In order to determine if any of the different shock microstructures in xenotime can be utilized as chronometers for dating impact events, shocked xenotime samples from three impact structures, including Vredefort (South Africa), Santa Fe (New Mexico, USA), and Araguainha (Brazil) were analysed. This study aims to 1) characterise shock deformation microstructures in xenotime from different crater environments (where known), 2) evaluate the U-Pb response of the different shock microstructures in xenotime, and 3) determine mechanisms responsible for trace element mobility during shock-induced crystal-plastic deformation.

5.2 Samples

5.2.1 Vredefort impact structure, South Africa

The Vredefort impact structure is located on the Kaapvaal Craton in South Africa and has been dated at 2020 ± 3 Ma using both zircon and monazite U-Pb geochronology (Kamo et al., 1996; Gibson et al., 1997; Moser, 1997; Erickson et al., 2017). With an original estimated diameter of ~ 300 km, the Vredefort impact structure is the largest recognised impact structure on Earth and is exposed as a ~ 90 km wide structure which represents the eroded central uplift (Grieve and Theriault, 2000) (Figure 5.1a). The core comprises ca. 3.1 Ga Archean granitoid gneissic rocks (~ 45 km wide) subdivided into an inner core of granulite facies leucogranitic gneiss (Inlandsee leucogranofels) and an outer core of amphibolite grade granodioritic to tonalitic gneiss (Outer granite gneiss). The core is surrounded by a 15–20 km collar of overturned strata comprising 3.07–2.02 Ga supracrustal sequences of the Dominion Group and the Witwatersrand, Ventersdorp, and Transvaal supergroups, with metamorphic grade transitioning from mid-amphibolite facies in the inner collar to greenschist facies in the outer collar (Kamo et al., 1996; Gibson et al., 1997, 1998; Moser, 1997).

The Vredefort shocked xenotime grain studied here is a detrital grain collected from a pavement of Permian tillite (sample 14DG14, $26^{\circ}53'23.1''$ S $27^{\circ}24'23.0''$ E) exposed in the outer core (Figure 1a). The sampling site is located between the 10 and 15 GPa isobars defined by planar deformation features (PDF) in quartz (Gibson and Reimold, 2005). Bedrock at this location is dominated by shocked granitoid and pseudotachylitic breccia, however the host rock of the detrital shocked xenotime grain is not known; it is assumed to have an igneous origin.

5.2.2 Santa Fe impact structure, USA

The Santa Fe impact structure is located in the southern Sangre de Cristo Mountains, ~ 8 km northeast of Santa Fe, New Mexico, USA (Fackelman et al., 2008; Montalvo et al., 2019). Shatter cones and shocked quartz provided the initial evidence of an impact event (Fackelman et al., 2008, Figure 5.1b). The shocked rocks that define the Santa Fe structure comprise a km-sized block that is fault-bound to the east and west (Montalvo et al., 2019). Rocks in the area are regionally metamorphosed gneissic granitoids and biotite granite, which are interlayered with amphibolite and metasedimentary rocks (Bauer and Ralser, 1995; Read et al., 2000; Bauer et al., 1996). There is no geomorphological or geophysical expression of an impact structure; it has been proposed that the area experienced post-impact tectonic activity and is likely to have been deeply eroded (Fackelman et al., 2008; Cavosie et al., 2016a;

Montalvo et al., 2019). Estimates of crater diameter range from ~6 to 13 km based on shatter cone distribution and extent of detrital shocked zircon in local drainages (Fackelman et al., 2008; Montalvo et al., 2019). The age of the Santa Fe impact is poorly constrained. A detrital shock-twinned zircon yielded a SIMS U-Pb age of 1472 ± 35 Ma that was interpreted to record crystallization, which provides a maximum age for the impact event (Montalvo et al., 2019). A minimum impact age of c. 350 Ma is based on undeformed Madera group Palaeozoic sedimentary rocks overlying the basement granitoids (Fackelman et al., 2008; Montalvo et al., 2019). Pressure estimates for exposed rocks in the area are up to 20 GPa, based on PDF in quartz, shock-twinned zircon, and the abundance of shatter cones (Fackelman et al., 2008; Cavosie et al., 2016a; Montalvo et al., 2019).

The three Santa Fe shocked xenotime grains studied here are in a thin section from a shatter cone of granitoid (sample 14NM10A, $35^{\circ}43'35.6''\text{N}$ $105^{\circ}51'26.9''\text{W}$) that contains alkali feldspar with minor quartz, plagioclase, muscovite, chlorite, biotite, and opaque minerals. Shock microstructures and the petrographic context of these grains were previously described; their igneous origin is thus well-established (see Cavosie et al., 2016a) (Figure 5.1b).

5.2.3 Araguainha impact structure, Brazil

The Araguainha impact structure is located in the northern Paraná Basin of central Brazil, and is the best-exposed complex impact structure in South America (Tohver et al., 2012). The structure is ~40 km in diameter, with a 10 km wide central uplift, annular ring features, and a rim defined by radial and concentric faults (Lana et al., 2007). The central uplift comprises Cambrian alkali granite basement, which is crosscut by pseudotachylitic breccia and it is surrounded by thick (~1500–1800 m) Devonian to Permian sedimentary rocks in the collar (Lana et al., 2007; Lana et al., 2008; Tohver et al., 2012). The impact exposed the Araguainha basement granitoid, a pink coarse-grained monzo- to syenogranite, with a crystallization age of 512 ± 11 Ma (Tohver et al., 2012). Shatter cones, melt rocks, and breccias are preserved in the central uplift, even though erosion has removed much of the crater fill (Engelhardt et al., 1992; Lana et al., 2008). Multiple studies have reported ages ranging from 260–250 Ma for the Araguainha impact event. A study of several different impactites combined the results of U-Pb and Th-Pb dating of zircon and monazite, and $^{40}\text{Ar}/^{39}\text{Ar}$ of melt inclusions, to yield an impact age of 254.7 ± 2.5 Ma (Tohver et al., 2012). Granular monazite from a sedimentary rock-derived impact melt rock yielded an impact age of ~260 Ma (Erickson et al., 2017). Granular zircon from a different sedimentary rock-derived impact melt rock yielded an impact age of 251.5 ± 2.9 Ma (Hauser et al., 2019).

The three Araguainha shocked xenotime grains studied here are from an impact melt rock (sample SF20) derived from a sedimentary rock located in the core of the impact structure (16°49'45.3"S 52°59'16.8"W, Figure 5.1c). The grains were identified in a heavy mineral concentrate, so their petrographic context is unknown. Given the protolith of the impact melt rock, the xenotime grains are assumed to be detrital grains that likely have an igneous origin.

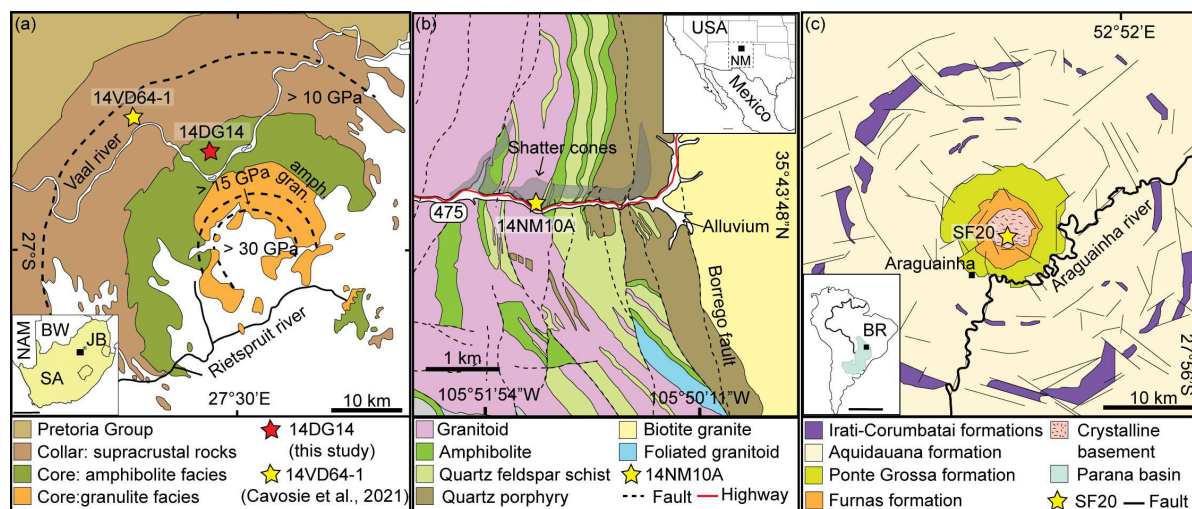


Figure 5.1: Simplified geological maps of the three impact structures with sample locations. (a) The central uplift of the Vredefort dome, South Africa (modified after (Cavosie et al., 2010) with inset showing the location in South Africa (SA – South Africa, JB – Johannesburg, NAM – Namibia, BW – Botswana). (b) Map showing shocked rocks that define the Santa Fe impact structure (modified after Bauer et al., 1996; Montalvo et al., 2019) with inset showing the location of Santa Fe impact structure in New Mexico (NM – New Mexico). (c) Map of the Araguainha impact crater (modified after (Lana et al., 2008)) with inset showing location of Araguainha impact structure in Brazil.

5.3 Methods

5.3.1 Sample mounting

The Vredefort xenotime 14DG14 was mounted in epoxy. The three xenotime grains from the Santa Fe impact structure were identified in thin section; three millimetre-sized slices containing each xenotime grain and surrounding grains were removed from the thin section and re-mounted in epoxy. The three Araguainha xenotime grains were mounted in epoxy.

5.3.2 Scanning electron microscope-electron backscatter diffraction (SEM-EBSD)

Secondary electron (SE), backscattered electron (BSE) images, and EBSD analyses were acquired using TESCAN Clara and Mira3 field emission gun scanning electron microscopes (FEG-SEM) housed in the John de Laeter Centre (JdLC) at Curtin University. For the Vredefort and Araguinha samples, EBSD analyses were done using a TESCAN Mira3 SEM, and the Santa Fe grains were analysed with a TESCAN Clara SEM; both instruments are equipped with Oxford Instruments Symmetry EBSD cameras. The EBSD analyses were similar for all samples, and generally follow methods described in Cavosie et al. 2016a and 2021b (Appendix 5.1). In brief, all measurements used a 20 kV accelerating voltage, ~20-25 mm working distance, a 1-2 nA beam current, and a 70° specimen tilt, with pixel sizes for maps ranging from 60 to 100 nm. EBSD maps were collected with the xenotime (Y) match unit from the Inorganic Crystal Structure Database (ICSD) based on structural data from Ni et al. (1995). The EBSD data were collected with the Oxford Instruments acquisition program AZtec, and post-processed using the software AZtecCrystal (v. 2.1). EBSD maps used include band contrast (BC), which shows the quality of diffraction pattern; bright areas can be considered as more crystalline than dark areas. Orientation maps with an inverse pole figure (IPF) color scheme show variations in crystallographic orientation, and are useful for resolving crystal-plastic deformation, twin lamellae, and neoblasts. Pole figures are all equal area lower hemisphere projections in the sample reference frame. The Grain Reference Orientation Deviation (GROD) angle map shows the misorientation at any given point with respect to the average orientation of the grain. Texture component (TC) maps show the relative misorientation across a grain relative to a user-specified reference point.

5.3.3 Sensitive high resolution ion microprobe (SHRIMP) and Electron micro probe analyser (EMPA)

The U-Pb geochronology data from the xenotime grains were acquired in two sessions in January (Santa Fe and Araguinha) and March 2022 (Vredefort) at the JdLC using a SHRIMP II secondary ion mass spectrometer (SIMS). Xenotime standard MG-1 ($^{206}\text{Pb}^*/^{238}\text{U}$ age = 489.96 ± 0.54 Ma; $^{207}\text{Pb}^*/^{206}\text{Pb}^*$ age = 491.8 ± 1.2 Ma; U = ~900 ppm; Th = ~800 ppm) was used as the primary reference material. The standards z6413 ($^{206}\text{Pb}^*/^{238}\text{U}$ age = 993.83 ± 0.74 Ma; $^{207}\text{Pb}^*/^{206}\text{Pb}^*$ age = 996.64 ± 0.82 Ma; U = ~10,000–20,000 ppm; Th = 1500–4000 ppm) and Y1 ($^{207}\text{Pb}^*/^{206}\text{Pb}^*$ age = 948 ± 5 Ma; U = ~8,000–25,000; Th = 3,500–10,000) were used as secondary reference materials (Fletcher et al., 2000, 2004). The reference materials were located on an adjacent mount to the unknowns in the SHRIMP, and both mounts were cleaned

and gold-coated prior to each session. A spot size of $\sim 10 \times 7 \mu\text{m}$ was produced by passing the primary O^{2-} ion beam through a $\sim 30 \mu\text{m}$ Kohler aperture. Each analysis consisted of six scans, including a nine peak run table of $^{194}\text{Y}_2\text{O}^+$, $^{204}\text{Pb}^+$, background ($^{204}\text{Pb}^+ + 0.0145 \text{ AMU offset}$), $^{206}\text{Pb}^+$, $^{207}\text{Pb}^{2+}$, $^{208}\text{Pb}^+$, $^{238}\text{U}^+$, $^{248}\text{ThO}^+$ and $^{254}\text{UO}^+$ (Fletcher et al., 2004). A retardation lens was used in front of the secondary ion collector to maximise the abundance sensitivity and eliminate scattered ions (Fletcher et al., 2000).

Calibrating Pb/U and Th/U ratios was done using SQUID3 software, using fixed (slope =2) robust regressions through $\ln(^{206}\text{Pb}^+/^{238}\text{U}^+)$ vs $\ln(^{254}\text{UO}^+/^{238}\text{U}^+)$ for MG-1 (Bodorkos et al., 2020). The calibration constants obtained for the January and March sessions were $0.0052 \pm 1.1\%$ (1σ , MSWD =1.4, $p = 0.11$) and $0.0076 \pm 0.9\%$ (1σ , MSWD =1.3, $p = 0.17$), respectively. A common Pb correction was determined using contemporaneous Pb compositions of Stacey and Kramers (1975). For matrix corrections, U and Th values were used from the SHRIMP session.

The ΣREE values for a matrix correction of SIMS data (cf. Fletcher et al., 2004) were determined using a JEOL JXA-8530F Electron Probe Microanalyser (EPMA) (Appendix 5.2) at the Centre for Microscopy, Characterisation and Analysis at the University of Western Australia. A take-off angle of 40° and beam energy of 25 keV were used during analysis. The EMPA beam current was 100 nA for both calibration and unknown sample measurements. The unknowns were acquired using the Probe for EPMA© 257 software package (Probe Software®). A selection of in-house silicates, Drake and Weill glasses, and USNM REE phosphates from the Smithsonian Institute were used as standards for instrumental calibration. During the analytical sessions, when matrix-corrected using U, Th and ΣREE concentrations, z6413 and Y1 yield $^{206}\text{Pb}^*/^{238}\text{U}$ and $^{207}\text{Pb}^*/^{206}\text{Pb}^*$ weighted mean ages within 2 s.d. of published values. Age calculations and plots were made with Isoplot 4.15 (Ludwig, 2012) and IsoplotR (Vermeesch, 2018).

5.3.4 Atom probe tomography (APT)

Needle-shaped specimens for atom probe tomography were prepared using a TESCAN Lyra3 Ga⁺ focused ion beam with SEM (FIB-SEM) at the JdLC, Curtin University, and were accurately targeted using Pt fiducials (Rickard et al., 2020). For milling and shaping of the specimens the FIB was operated at a 30 kV accelerating voltage, followed by a 2 kV cleaning procedure for final polishing of the specimen. A total of 22 xenotime APT specimens were extracted from grains representative of each impact structure.

The specimens were analysed using a CAMECA local electrode atom probe (LEAP) 4000X HR at the Geoscience Atom Probe Facility, JdLC, Curtin University. The instrument was operated in laser-assisted mode using a UV laser ($\lambda=355$ nm). For each analysis, analytical parameters such as temperature, detection rate, laser pulse energy and laser pulse frequency were kept constant at 60K, 1%, 200 pJ and 125 kHz respectively. The mass-to-charge spectrum was reconstructed to 3D data using AP Suite 6 software. For the 3D reconstruction, voltage-based models were applied. The detector efficiency was set at 36%, k-factor at 3.3, image compression factor at 1.65, atomic volume computed at 0.01190 nm³/atom for xenotime, and the field evaporation estimated at 28.98 V/nm as determined empirically (Fougerouse et al., 2021c)

In the 3D reconstruction, cluster identification was obtained by the maximum separation method (MSM; Williams et al., 2013) with the following parameters: dmax (maximum cluster ion separation) – 1.5 nm, O (order) – 1, N (number of chemical species) – 30, L (cluster detection envelope parameter) and E (cluster detection erosion distance) both – 0.75 nm.

The isotopic composition of U and Pb is measured from a narrow 0.1 Da range on the ²⁰⁶Pb⁺⁺, ²⁰⁷Pb⁺⁺, and ²³⁸UO₂⁺⁺ peaks and corrected for background. The background was estimated using a peak-free region (1 Da) adjacent to each peak (constant background estimation method, Joseph et al., 2021). For U-Pb dates, the ²⁰⁶Pb/²³⁸U ratio is calculated using the fractionation correction method, between the ratio of UO₂⁺⁺/UO⁺⁺ and ²⁰⁶Pb⁺⁺/²³⁸UO₂⁺⁺ for each analysis (Joseph et al., 2021). The ²⁰⁷Pb-²⁰⁶Pb dates were calculated using a variable background correction method (Joseph et al., 2021).

5.4 Results

Results of BSE, EBSD, SHRIMP and APT analyses of shocked xenotime are summarised below for the Vredefort grain, and three grains each from the Santa Fe and Araguainha impact structures.

5.4.1 Microstructural characterisation of shocked xenotime

5.4.1.1 Vredefort impact structure

Xenotime grain 14DG14 from Vredefort is a rounded 300×170 μm grain. Four apparent directions of planar fractures (PF) are visible in BSE images (Figure 5.2a). Backscattered electron imaging reveals lower intensity, slightly dark patches distributed

unevenly through the grain. Analysis by EBSD shows several microstructures, including low angle boundaries ($<10^\circ$ misorientation), planar deformation bands (PDB), deformation twins, and localised neoblastic textures (Figure 5.2b-d). Three different sets of deformation twin lamellae along $\{112\}$ were identified (t1, t2, t3), all defined by a 65° disorientation about the host $<110>$ (Figure 5.2b) and a shared $\{112\}$ direction between host and twin. The t1 twin set is the most dominant in the grain, consisting of 11 discrete lamellae; the t2 and t3 twins contain fewer lamellae. Twin lamellae are generally $<1\ \mu\text{m}$ in width, except for some t1 twin lamellae, which have apparent widths up to $\sim 1.6\ \mu\text{m}$. The three twin directions coincide with the directions of planar fractures (PF2-4) in the grain (Figure 5.2a,b). Individual twin lamellae occur in segments as long as $\sim 30\ \mu\text{m}$ but are otherwise generally discontinuous. The $\{112\}$ twin in t3 orientation consists of a single lamella that is segmented into a series of 2 to $3\ \mu\text{m}$ long lamellae, some of which deviate from the canonical $65^\circ/<110>$ orientation (Figure 5.2e). The individual segments define misorientations close to, but different from, the $\{112\}$ twin, including $72^\circ/<342>$, $68^\circ/<232>$, $70^\circ/<341>$, and $70^\circ/<340>$ (Figure 5.2e,f).

A set of low angle boundaries is observed parallel to the t1 and t2 twin directions (Figure 5.2b,c), and cumulative strain up to 12° is present across the grain. Maximum degrees of local misorientation occur along the edges of the grain and along PF2 and PF3 (Figure 5.2c). PDB are present, and dominantly parallel to the t1 and t2 $\{112\}$ twins, with relatively sharp boundaries and typically $<3^\circ$ of misorientation from the host. Broader PDB with diffuse boundaries are found sub-parallel to the t2 and t3 twins, and preserve cumulative misorientations up to $\sim 12^\circ$ from the host (Figure 5.2c). Small isolated neoblasts (up to $5\ \mu\text{m}$ in diameter) are present along PF1 and some have an orientation similar to the t1 twin, whereas others appear randomly oriented (Figure 5.2d,f).

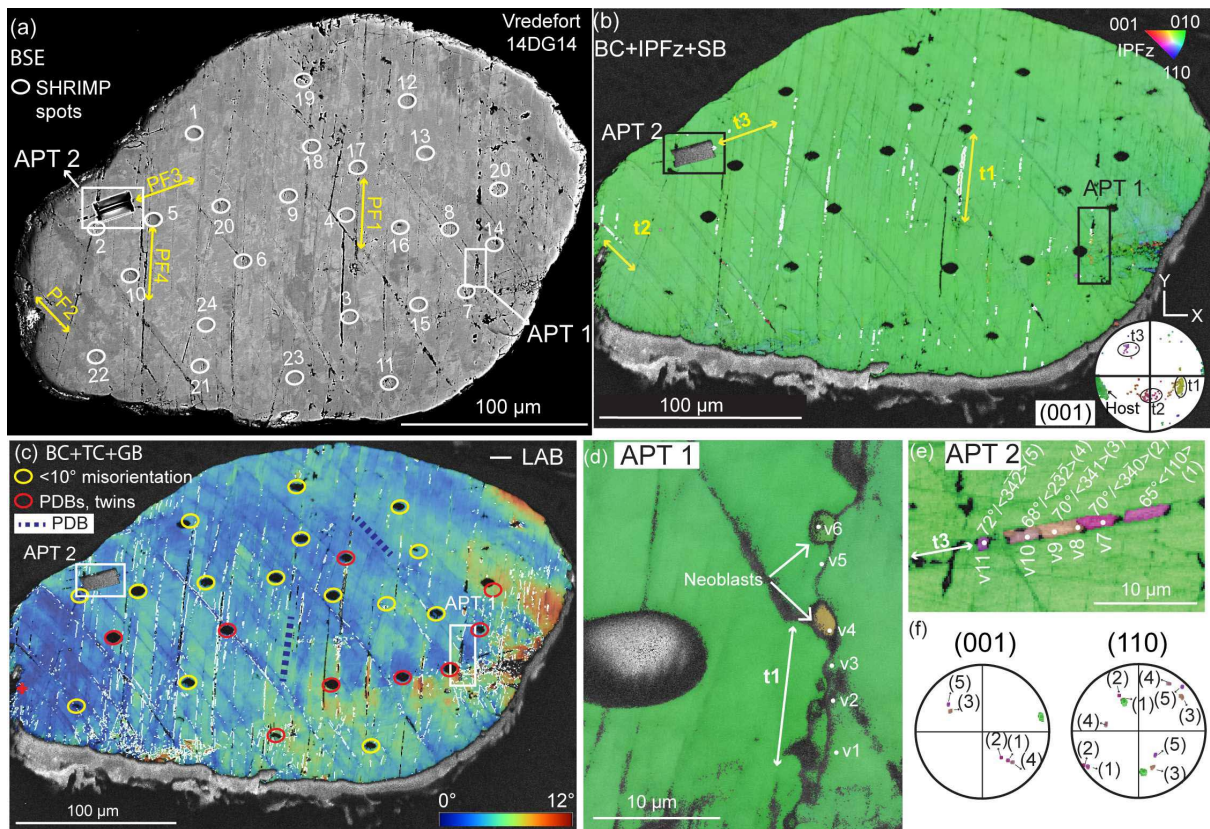


Figure 5.2: Microstructures of Vredefort xenotime grain 14DG14. (a) Backscattered electron (BSE) image. Four orientations of planar fractures (PF1 – PF4) are visible. SHRIMP spots and atom probe sample locations are indicated. (b) Electron backscatter diffraction (EBSD) grain orientation map (inverse pole figure, z projection [IPFz]). Deformation features are indicated, deformation twin lamellae (t) parallel to PF. Inset pole figure showing 3 sets of $\{112\}$ twins (t1, t2, t3) and the host (lower-hemisphere, equal-area projection). (c) Texture component map showing low angle boundaries ($< 10^\circ$ in white color), planar deformation bands (PDB) oriented mostly parallel to the t2 twin direction, and also parallel to t1 twin direction (dark blue dashed line). The grain shows up to 12° of misorientation from the reference point (red cross left side). SHRIMP spots targeting PDB and twins are shown in red and yellow ellipses shows SHRIMP spots targeted the areas in the grain with $< 10^\circ$ of misorientation. (d) Inverse pole figure (IPFz) map showing location of atom probe sample APT 1, where the grain showing recrystallised neoblasts. (e) Inverse pole figure map showing location of atom probe sample APT 2, which targeted the segmented twin lamellae (t3). Four segments define disorientations close to, but different from, the $\{112\}$ twin orientation, including $72^\circ/\langle 342 \rangle$, $68^\circ/\langle 232 \rangle$, $70^\circ/\langle 341 \rangle$, and $70^\circ/\langle 340 \rangle$; one segment records the $\{112\}$ twin direction ($65^\circ/\langle 110 \rangle$). (f) Pole figures showing the twin and host relations from E.

5.4.1.2 Santa Fe impact structure

Microstructures in the three analysed xenotime grains from the Santa Fe impact structure (SFx3, SFx4, SFx5) are similar to those previously described by Cavosie et al. (2016a). All of the grains contain planar fractures, broad areas with conspicuous lattice misorientation, planar deformation bands, and two of the grains contain $\{112\}$ twins. Planar fractures occur in one orientation in grain SFx4, and three orientations in grains SFx3 and SFx5 (Figure 5.3a,b,c). Grain SFx4 contains a single $\{112\}$ twin lamella, whereas SFx5 contains three sets of twins (Figure 5.3e,f); in all cases, the twin orientations coincide with the traces of PF on the polished surface. In grain SFx5 the t1 twins are the dominant set, with apparent lamellae widths up to 270 nm. Twins in sets t2 (subparallel to t1) and t3 consist of thin lamellae that are generally only ~ 50 nm (one pixel) in apparent width.

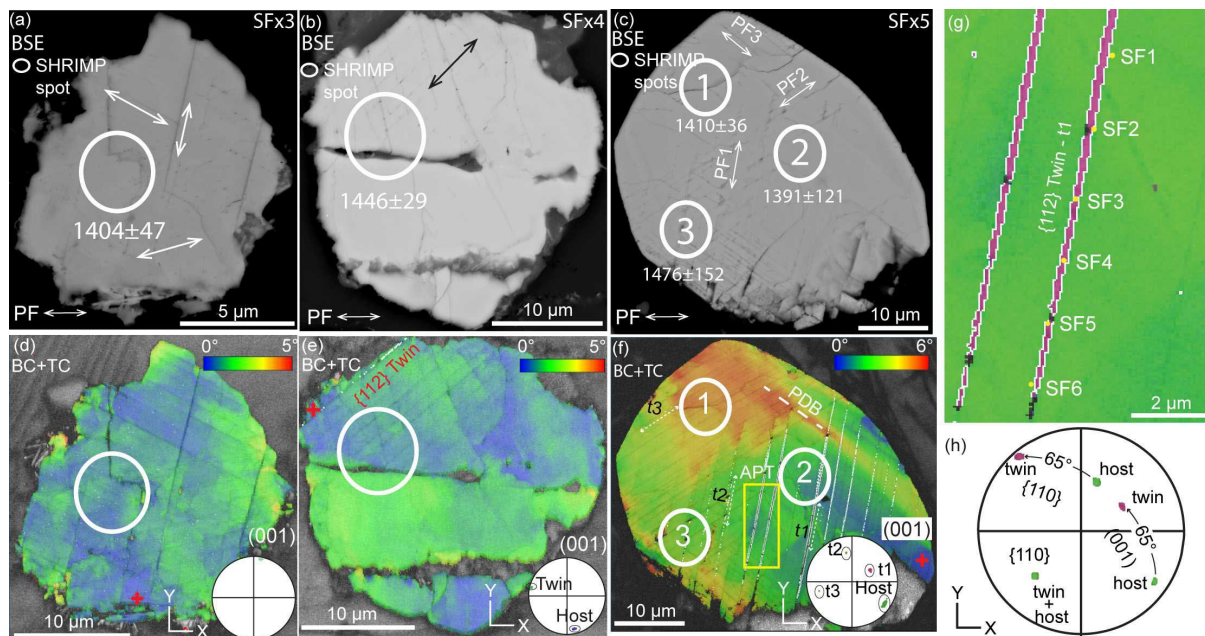


Figure 5.3: Microstructures of Santa Fe xenotime grains SFx3, SFx4 and SFx5. (a), (b) and (c) Backscattered electron (BSE) images showing directions of planar fractures (indicated by arrows). SHRIMP spots are indicated, along with ages in Ma. (d), (e) and (f) Texture component maps showing relative misorientation from a reference point (red cross) with inset pole figures of (001) (lower-hemisphere, equal-area projection). (d) Grain SFx3 showing up to 5° misorientation (e) Grain SFx4 showing one $\{112\}$ twin lamella and up to 5° misorientation (f) Grain SFx5 showing three sets of $\{112\}$ twin lamellae (t1, t2, t3), up to 6° of misorientation, and planar deformation band (PDB). (g) Location of atom probe samples in grain SFx5 (h) Pole figure of G, recording the $\{112\}$ twin and host relationship.

5.4.1.3 Araguainha impact structure

Xenotime grains X1, X2 and X3 from Araguainha are subhedral to anhedral rounded grains that range from 50 to 200 μm in length (Figure 5.4a,bc). The EBSD band contrast (BC) images show that all three are partially to fully polycrystalline. Orientation maps for grain X1 shows a mixture of highly strained host and neoblasts that are mostly equant and range in size from 2 to 15 μm (Figure 5.4d). Neoblasts mostly occur along the margin of the grain, in clusters within the grain, and along fractures, and define two main orientation populations in the pole figure; each cluster shows considerable orientation dispersion (Figure 5.4d, pole figure). A more detailed examination of orientation data for grain X1 reveals that the host domain is largely preserved across the grain and records a cumulative misorientation of $\sim 20^\circ$ (Figure 5.5a). Further, each neoblast orientation clusters preserves a systematic orientation relation with the host domain of $65^\circ/\langle 110 \rangle$ and shares a $\{112\}$ direction (Figure 5.5b,c). The neoblast orientations preserve the same orientations as $\{112\}$ twin lamellae, and are thus interpreted to represent recrystallized $\{112\}$ twins.

Orientation maps for grain X2 show a fully neoblastic aggregate with two main orientation clusters that consist of neoblasts oriented sub-parallel to the c-axis (Figure 5.4e). Orientation maps for grain X3 show a fully neoblastic aggregate of inequigranular grains, most of which preserve high-angle boundaries (Figure 5.4c,f). Although there is considerable dispersion in orientations, the neoblasts appear to define two or three broad orientations, with an inner zone consisting of neoblasts with similar orientations and an outer zone of randomly oriented neoblasts (Figure 5.4f, pole figure). No systematic orientation relations indicative of recrystallized $\{112\}$ twins were detected in grains X2 or X3. A GROD angle map of X3 shows generally no misorientation within most neoblasts, though a limited number of neoblasts shows up to 15° internal misorientation; these are distributed mainly in the central portion of the grain, and may represent less recrystallized relict host domains (Appendix 5.3). In the GROD angle map, a lobate texture is seen generally along grain boundaries, in which a low strain neoblast has grown into a neoblast with high misorientation (Figure 5.4h). This particular type of grain boundary was targeted for nanoscale analysis by APT.

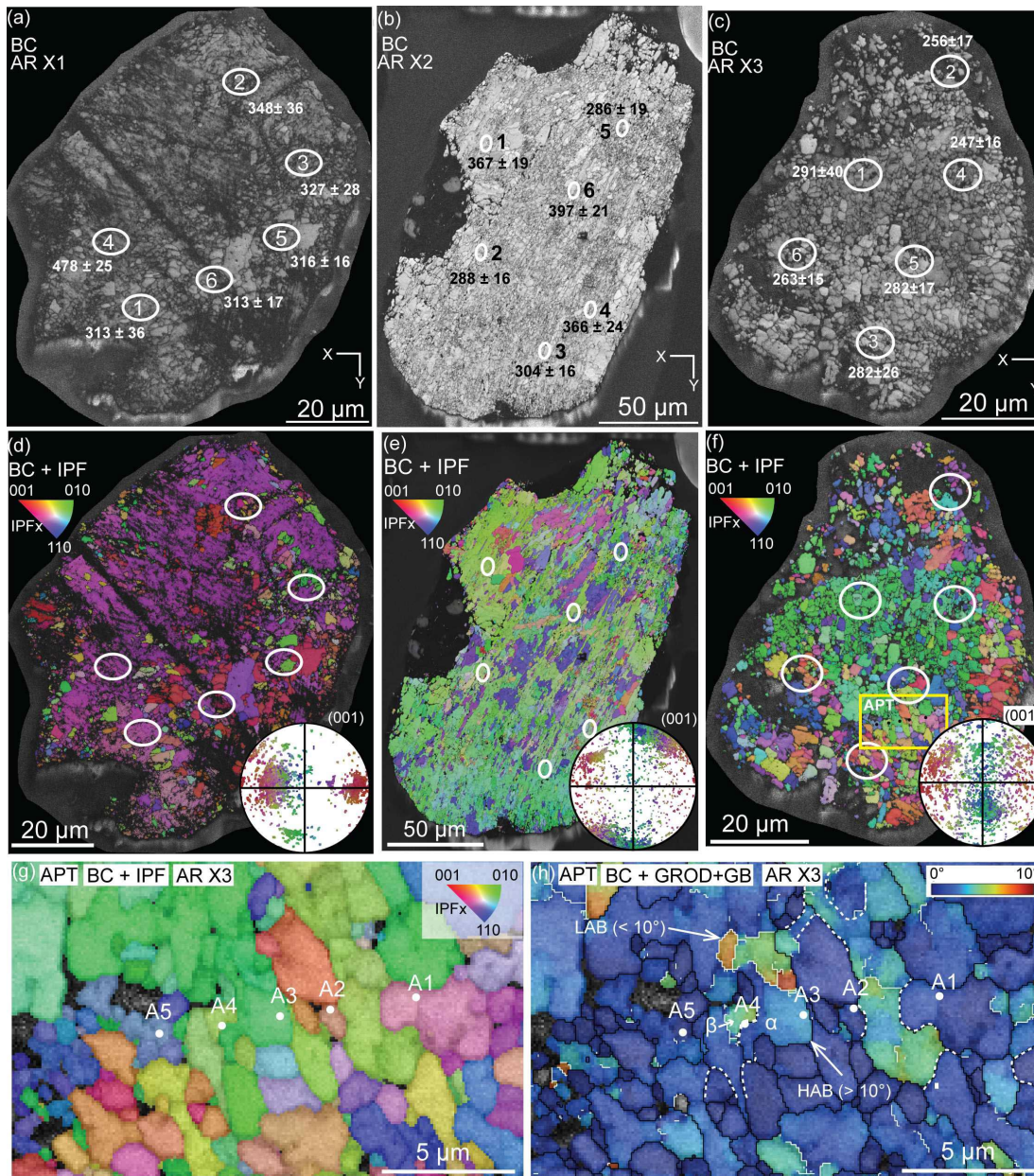


Figure 5.4: Microstructures of three xenotime grains from the Araguainha impact structure. (a), (b) and (c) EBSD band contrast (BC) maps with SHRIMP spots and U-Pb ages in Ma indicated. (d), (e) and (f) EBSD grain orientation maps (inverse pole figure, x projection [IPF_x]) with insets showing orientation distribution of the recrystallised neoblasts from pole figures (lower-hemisphere, equal-area projection). (g) Close-up IPF_x map showing location of atom probe samples from grain X3. (h) Grain reference orientation deviation (GROD) angle map of the area shown in G to up to 10°, showing the deviation of orientation from the average orientation of the grain. Note the lobate texture between neoblasts at the A4 atom probe specimen location, in which the larger grain (α) with no misorientation is grown into grain with higher internal misorientation (β). Dashed lines represent contact between neoblasts showing lobate texture.

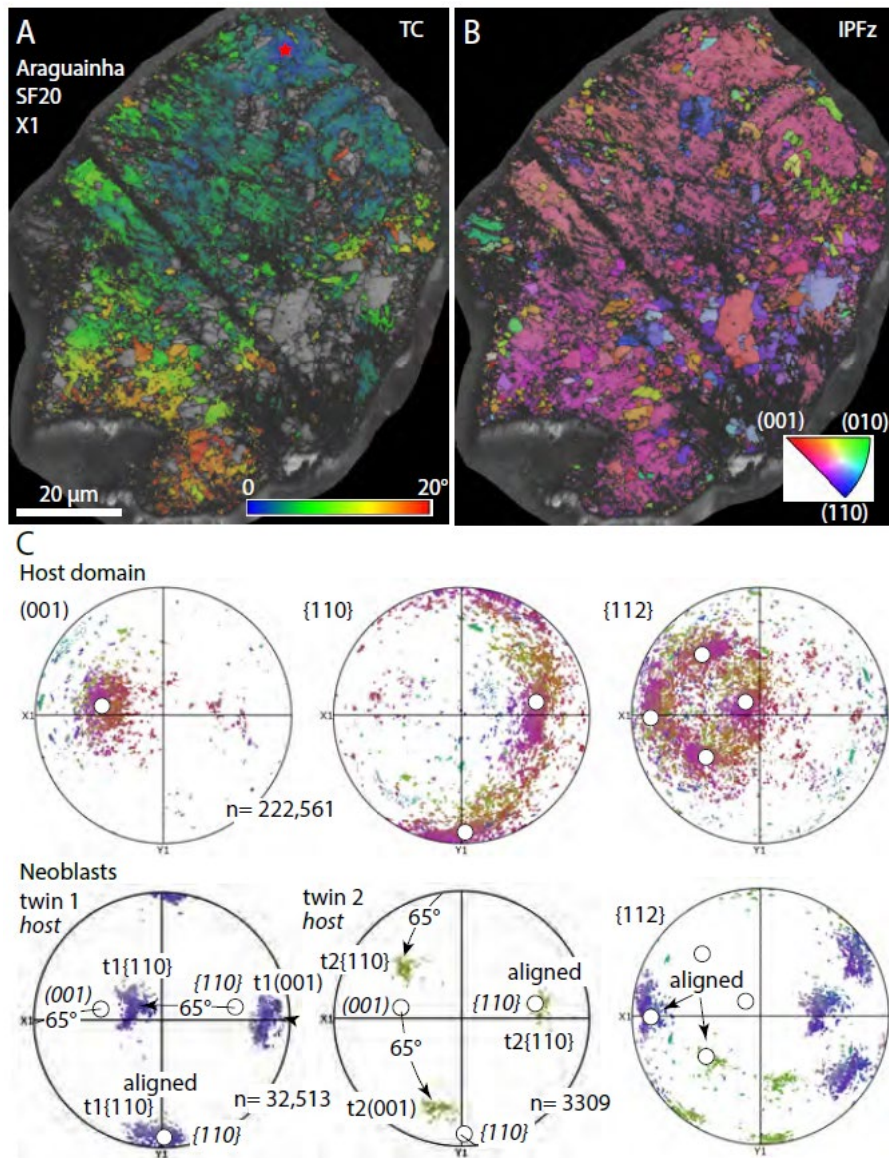


Figure 5.5: EBSD maps of grain X1 from Araguainha. (a) Texture component map of X1 showing up to $\sim 20^\circ$ cumulative misorientation in the host domain of the grain. (b) EBSD grain orientation map of grain X1 (inverse pole figure, z projection [IPFz]). (c) Pole figures (lower-hemisphere, equal area projections) from (b), showing orientation relationship between the host domain with neoblast clusters. The neoblast orientations preserve the same orientations as $\{112\}$ twin lamellae.

5.4.2 SIMS U-Pb geochronology

A total of 24 SHRIMP spots (Figure 5.2a and 6a) were made on Vredefort xenotime 14DG14. The U concentration varies from 1200 to 1900 ppm, with a Th/U ratio from 1.8 to 2.4 (Appendix 5.2). The upper Concordia intercept yields an age of 3136 ± 110 Ma (2σ), and the lower Concordia intercept yields an age of 1803 ± 280 Ma (2σ). No correlation was observed

between actinide concentration and BSE contrast, or between degree of crystal misorientation and U-Pb discordance. Spots that overlapped PDB and/or {112} twins show minor variations in $^{207}\text{Pb}^*/^{206}\text{Pb}^*$ age but do not define unique regions of the Discordia regression (Figure 5.6a). No analyses plot near the 3136 Ma upper intercept; the oldest five concordant analyses (spots: 1, 13, 18, 20, and 24) yield a weighted mean $^{207}\text{Pb}^*/^{206}\text{Pb}^*$ age of 2938 ± 16 Ma (2σ , MSWD = 0.78, $p = 0.53$), and likely represent a minimum crystallization age for the detrital grain. The lower intercept age of 1803 ± 280 is imprecise; it overlaps both the accepted impact age (2020 Ma, Kamo et al., 1996) and also a recently proposed hydrothermal event at ca. 1750 Ma (Cavosie et al., 2021b).

Five SHRIMP spots on three xenotime grains from Santa Fe shocked granite sample 14NM10 yield concordant (or nearly so) analyses (Figure 5.3a,b,c, and 6b). The U concentration varies from 4770 ppm (SFx4), to 5800 ppm (SFx3), to 8000-11,200 ppm (SFx5) (Appendix 5.2). A $^{207}\text{Pb}^*/^{206}\text{Pb}^*$ weighted mean age for all analyses is 1427 ± 20 Ma (2σ , MSWD = 1.10, $p = 0.36$, $n = 5$).

A total of 18 SHRIMP spots were made on the three Araguainha xenotime grains, with six spots on each grain (Figure 5.7). The U concentrations vary from ~3600–7100 ppm (Appendix 5.2), and most analyses yield concordant ages ranging from ca. 475 to 250 Ma. For grain X1, five of six analyses overlap and yield a weighted mean $^{238}\text{U}/^{206}\text{Pb}$ age of 318 ± 10 Ma (2SD, MSWD = 0.92, $X^2 = 0.45$, $n = 5$); the sixth spot is conspicuously older and was not included in the age calculation. For grain X2, the six analyses yielded a bimodal age population. The three youngest analyses yield a weighted mean $^{238}\text{U}/^{206}\text{Pb}$ age of 293 ± 9 Ma (2SD, MSWD = 1.5, $X^2 = 0.22$, $n = 3$), whereas the three older analyses yield a weighted mean $^{238}\text{U}/^{206}\text{Pb}$ age of 378.5 ± 12 Ma (2SD, MSWD = 2.5, $X^2 = 0.085$, $n = 3$). Grain X3 yielded the youngest age population. The six analyses from grain X3 define a Discordia array defined by a mixture of common and radiogenic Pb. A regression through all six analyses yields a lower intercept age of 255 ± 11 Ma (2SD, MSWD = 1.9, $X^2 = 0.11$, $n = 6$) which is interpreted as the time of neoblast formation. The upper Concordia intercept indicates a $^{207}\text{Pb}/^{206}\text{Pb}$ ratio of 0.42 ± 0.32 , which is interpreted to represent the composition of common Pb present when the neoblasts formed.

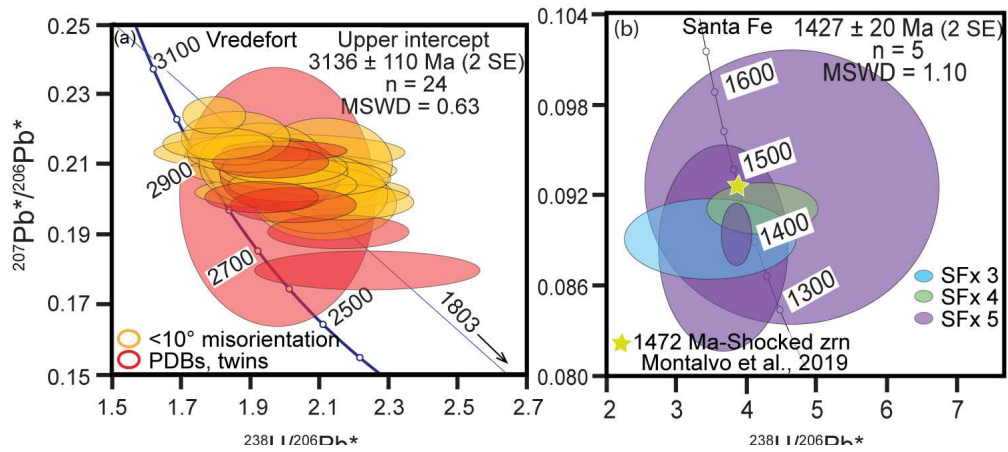


Figure 5.6: SHRIMP U-Pb geochronology results plotted on Tera-Wasserburg diagrams. (a) Results for Vredefort xenotime grain 14DG14. Red ellipses – spots targeting twins and planar deformation bands; yellow ellipses – spots targeting areas with $< 10^\circ$ misorientation. The lower intercept of the discordia is $1803 \pm 270 \text{ Ma}$. (b) Results for Santa Fe xenotime grains.

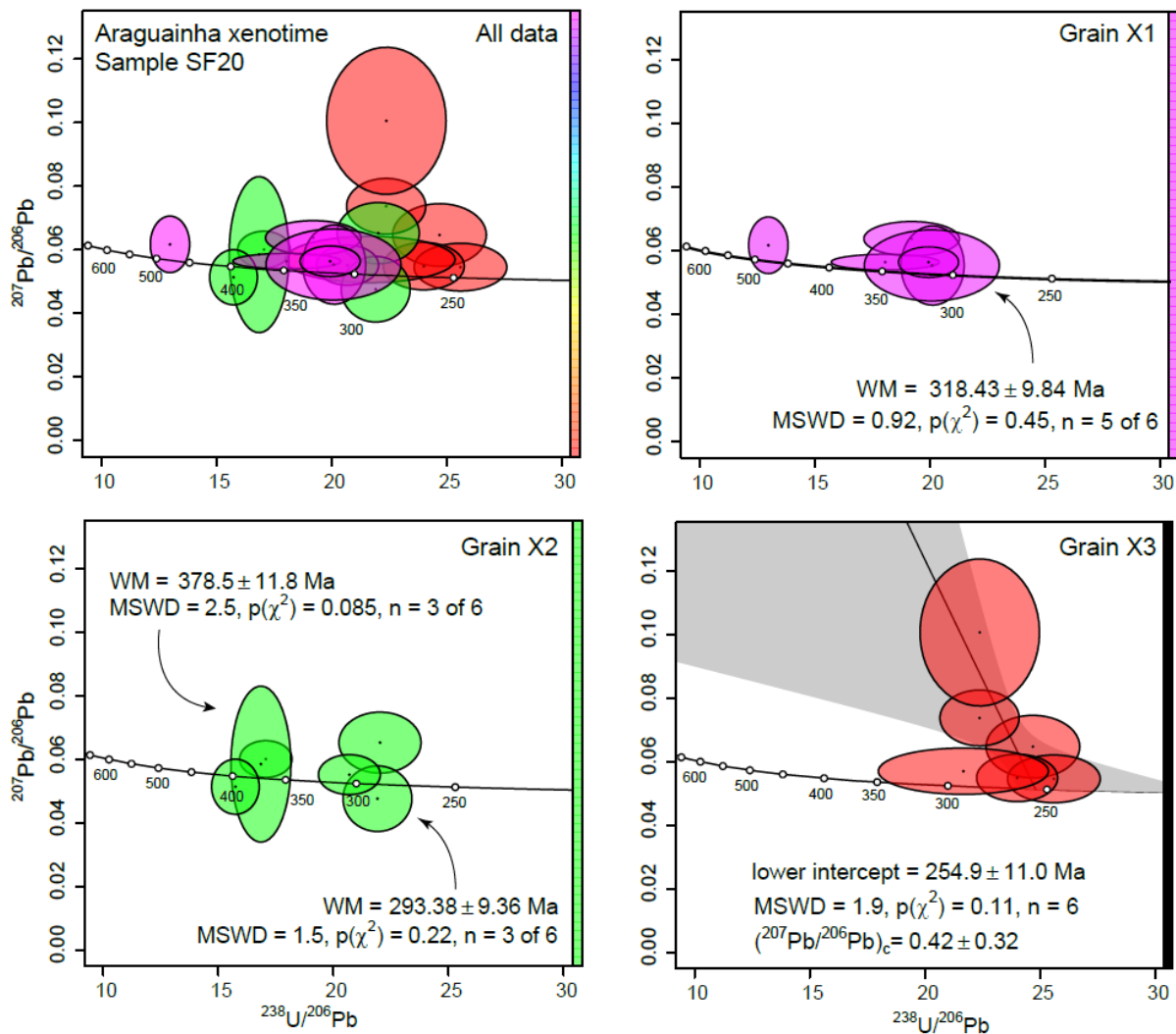


Figure 5.7: SHRIMP U-Pb geochronology results from Araguainha xenotime grains plotted on Tera-Wasserburg diagram. (a) Combined results from grain X1, X2 and X3. (b), (c) and (d) plotting results from grains X1, X2 and X3 respectively.

5.4.3 Nanoscale characterisation

Nanoscale characterisation of deformation microstructures in xenotime was conducted with APT, targeting deformation twins (Vredefort and Santa Fe) and neoblastic domains (Vredefort and Araguainha). A total of 22 APT specimens were prepared and 16 ran successfully (73% success rate). The survivability of APT specimens of shocked xenotime during atom probe analyses was thus higher than that for APT specimens of shocked zircon (12% success rate) (Montalvo et al., 2019; Montalvo, 2020). No ^{204}Pb peak was detected in the mass spectra from any of the xenotime specimens.

5.4.3.1 Vredefort xenotime (grain 14DG14)

Eleven APT specimens were prepared from the Vredefort xenotime grain, including six from individual neoblasts (APT 1 area) and five from the {112} twins (APT 2 area) (Figure 5.2d,e). Seven of the eleven APT specimens ran successfully. Six of the seven APT specimens (2 from neoblasts and 2 from {112} twins) preserve trace element segregations (clusters) at nanoscale (Figure 5.8a, Appendix 5.4).

Five specimens from the highly strained domain of the grain (APT2 area) (yielded more than 10 million ions each. Two specimens (V1 and V4) contain thirteen randomly distributed Ca and Pb*-rich nanoscale clusters that range in size from ~8 to 20 nm (Figure 5.8a). The abundances of Ca, Pb, and Si are lower in the matrix and higher in the clusters (Ca: 0.04 vs. 7 at. %; Pb: 0.09 vs. 3.5 at. %; Si: 0.08 vs. 1.86 at. %). Specimen V4 contains clusters enriched in OH and Na, which defines a discontinuous linear feature diagonal to the long axis of the specimen. There are also clusters enriched in Al distributed randomly through the specimen and also along the linear feature. Cl is heterogeneously distributed, forming clusters and also correlates to Ca distribution in the specimen (Figure 5.8a). In specimen V5, a set of dislocations enriched in Si, Cl, Ca, Na, and Al is present in a planar domain that is nearly perpendicular to the long axis of the specimen (Appendix 5.4). In specimen V3 a dislocation has elevated elements such as Ca and Si, and specimen V2 showed no heterogeneities (Appendix 5.4).

The APT $^{207}\text{Pb}/^{206}\text{Pb}$ dates obtained from the whole specimen with Ca-Pb* clusters are 3005 ± 547 Ma and 3101 ± 674 Ma (2σ) from V1 and V4 specimens respectively. The matrix, which excludes the Ca-Pb* clusters from specimens V1 and V4, yield $^{207}\text{Pb}/^{206}\text{Pb}$ dates of 2859 ± 618 Ma (V1) and 2519 ± 1088 Ma (V4) respectively. Other specimens are homogeneous in Ca and Pb distribution at the nanoscale (no clusters) and yield $^{207}\text{Pb}/^{206}\text{Pb}$ dates of 2411 ± 777 Ma, 2591 ± 968 Ma, 2647 ± 780 Ma (2σ). The combined data from specimens V2, V3, and V5 yield a weighted mean average of 2647 ± 350 Ma (2σ , MSWD=0.23, $p=0.92$). The APT $^{206}\text{Pb}/^{238}\text{U}$ dates from the five whole specimens, including specimens containing Pb*-rich clusters (V1 to V5), range from 1450 ± 187 Ma to 1749 ± 286 Ma (2σ), with a weighted mean average age 1596 ± 93 Ma (MSWD=1.12, $p=0.35$, $n=5$). The matrix $^{206}\text{Pb}/^{238}\text{U}$ dates from specimens with clusters (V1 and V4) yields 1539 ± 184 Ma and 1611 ± 276 Ma. The $^{206}\text{Pb}/^{238}\text{U}$ dates of specimens without clusters range from 1450 ± 187 Ma to 1684 ± 200 Ma (Figure 5.9a, Appendix 5.5).

Out of five specimens analysed from the twin domain, two ran successfully (V7, V9), and showed two different types of clusters (Appendix 5.5). Specimen V9 is characterised by

Pb*-only clusters, with Pb* concentration up to 2.5 at. % (compared to 0.05 at. % in the matrix). In contrast specimen V7 shows Ca-rich clusters but with no Pb. The $^{207}\text{Pb}/^{206}\text{Pb}$ dates obtained are 1967 ± 2769 Ma (V7), and 2333 ± 975 Ma (V9, including Pb clusters). The $^{207}\text{Pb}/^{206}\text{Pb}$ matrix age of specimen V9 is 2186 ± 1092 Ma (Figure 5.9a). Whole specimen $^{206}\text{Pb}/^{238}\text{U}$ dates (matrix + clusters) for V7 and V9 are 1319 ± 322 Ma and 1688 ± 223 Ma, respectively (Appendix 5.5).

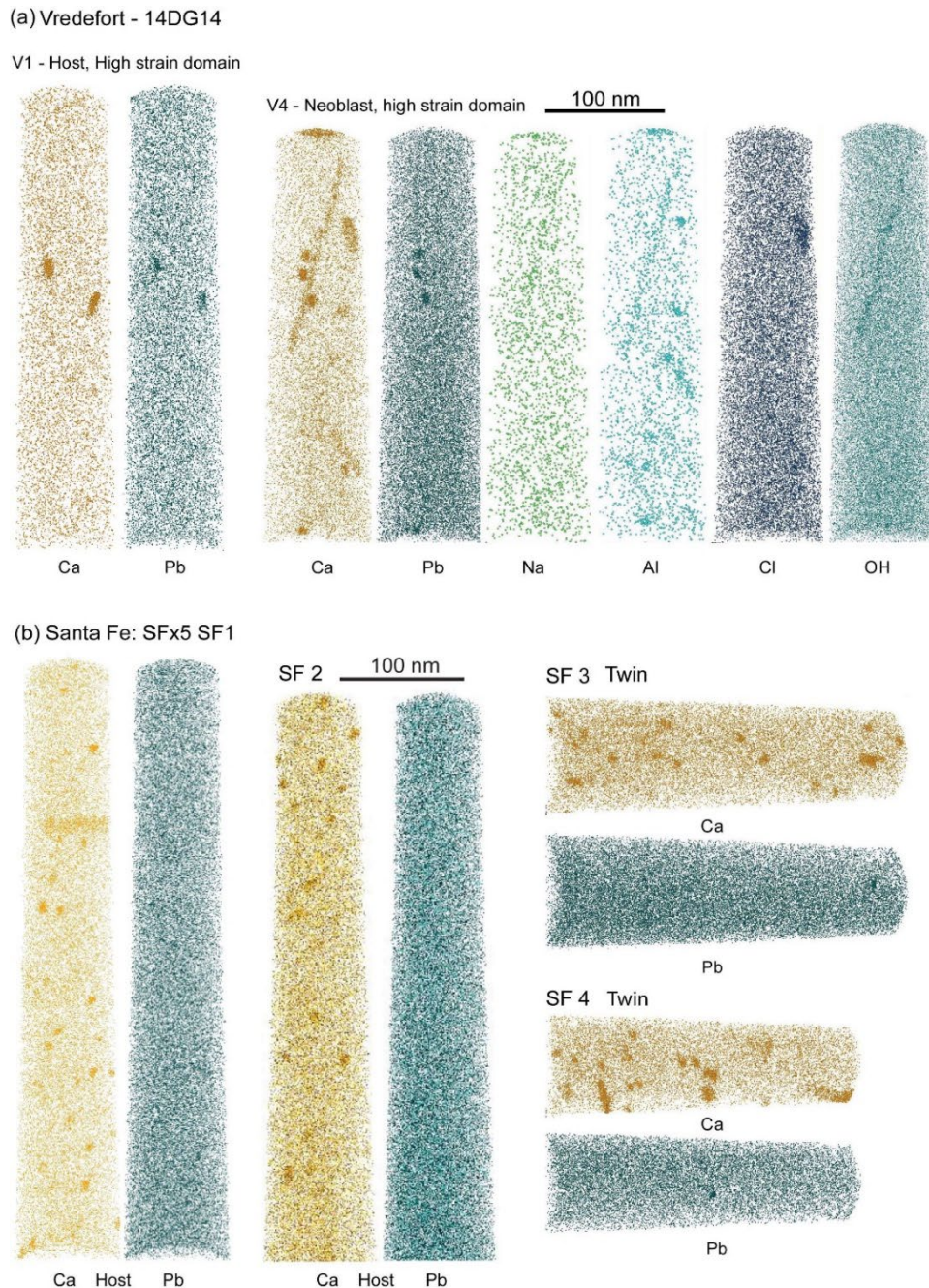


Figure 5.8: Atom probe 3D reconstruction of representative specimens from Vredefort xenotime grain 14DG14 and Santa Fe grain SFx5. Each sphere represents an atom of the indicated element. (a) Specimen V1, host xenotime from the high strain domain of the grain showing Ca and Pb* enriched clusters and a dislocation enriched in Ca, Na, Al, and OH. Cl is also distributed heterogeneously in clusters. Specimen V4 from a neoblast from the recrystallised domain of the grain showing Ca and Pb* enriched clusters. (b) Specimen SF1, SF2 from host and both SF3 and SF4 the twin domains. Host and specimen showing numerous Ca clusters with < 1% Pb* clusters. Note that Pb* enriched Ca clusters is only present in specimen from twin domain.

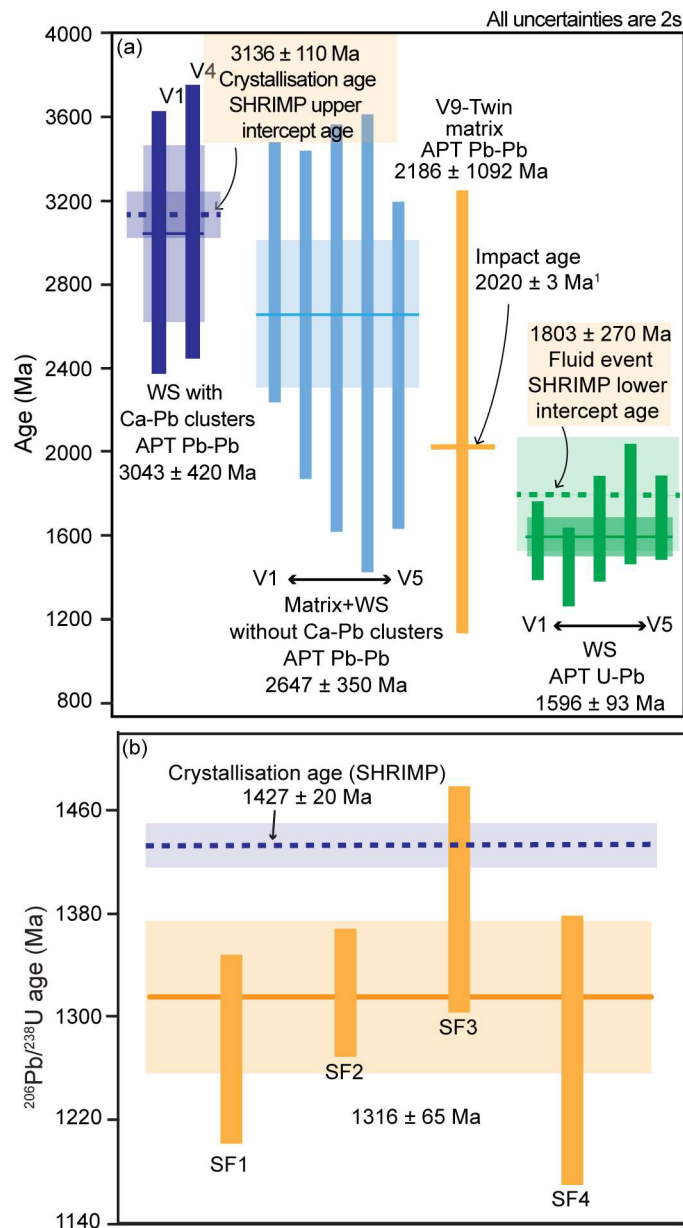


Figure 5.9: (a) Summary of both Pb-Pb and U-Pb nanogeochronology results obtained from the different domains (neoblastic and twin) of the Vredefort grain (¹ - Kamo et al., 1996)(WS – Whole atom probe specimen). (b) U-Pb nanogeochronology results from the four specimens from Santa Fe.

5.4.3.2 Santa Fe xenotime (grain SFx5)

Four of six APT specimens were analysed from xenotime SFx5. Specimen SF1 is from the host, SF2 targeted a host-twin boundary, and specimens SF3 and SF4 are from the same {112} lamellar twin (Figure 5.3g). SF1 and SF2 are characterised by the presence of numerous small (~5 to 20 μm) Ca-Pb* enriched clusters (Figure 5.8b). The Ca concentration is up to 3.6

at. % in clusters, as compared from 0.07 at. % in the matrix; Pb concentration also increases up to 1 at. % from 0.08 at. %. In addition to the small Ca-Pb* clusters, specimen SF3 is characterised by one large (~18 nm) cluster in which the Pb* enrichment is higher (from 0.08 to ~6 at. % Pb), with Ca (0.07 to 2.5 at. %) and Si (0.08 to 1.6 at. %). In specimen SF4, there are numerous Ca-rich clusters with no Pb, and one cluster with Pb* enrichment from 0.08 to ~3.8 at. %, and Si (0.08 to 1.8 at. %) (Figure 5.8b). The $^{206}\text{Pb}/^{238}\text{U}$ dates do not show significant variation between host and twin domains. The $^{206}\text{Pb}/^{238}\text{U}$ dates obtained are 1275 ± 69 Ma, 1319 ± 45 Ma, 1391 ± 83 Ma, 1274 ± 100 Ma (2σ) from SF1, SF2, SF3 and SF4 respectively with a weighted mean date of 1316 ± 69 Ma (2σ , MSWD=1.8, $p=0.14$) (Figure 5.9b). The matrix age from specimens SF3 and SF4 yield a $^{206}\text{Pb}/^{238}\text{U}$ date of 1329 ± 81 Ma and 1213 ± 98 Ma, respectively, which is within uncertainty of the whole specimen date (Appendix 5.5).

5.4.3.3 Araguainha xenotime (grain X3)

Five specimens were prepared from grain X3, and three successfully analysed by APT. One specimen targeted the grain boundary between two neoblasts (A4), one specimen sampled a ~ 3 μm neoblast with no internal misorientation (grain α) and the other a ~1 μm neoblast (grain β) with internal misorientation up to ~7°. In orientation maps, grain α protrudes into grain β , producing a lobate grain boundary (Figure 5.4h); this grain boundary was captured in APT specimen A4. The geometrical orientation of APT specimen A4 relative to the polished surface of the grain was monitored during FIB sample preparation and loading/analysis by APT. The boundary is conspicuously enriched in a range of elements compared to the matrix, including Si =2.67 vs. 0.10 at. %, Mg =1.21 vs. 0.06 at. %, Ca =1.01 vs. 0.15 at. %, Cl =0.72 vs. 0.13 at. %, Na =0.23 vs. 0.01 at. %, and Al =0.26 vs. 0.01 at. % (Figure 5.10). In A4 numerous Si- and Mg-rich clusters (Si up to 7.5 at. %, Mg up to 1.5 at. %) 5 to 20 nm in diameter are present in grain β (small and minor internal misorientation) and whereas only a few Si-Mg clusters are present in the other grain α (large and no misorientation). Other specimens analysed (A2, A5) contain dislocations enriched in Ca, Si, Mg, Na, and Al. None of the Pb isotopes were able to be detected above the background, therefore no age data are available from any of the Araguainha xenotime APT specimens.



Figure 5.10: Specimen A4 from Araguainha showing grain boundary enriched in elements such as Si, Mg, Ca, Cl, Na, Al. The specimen also shows the presence of Si-Mg clusters distributed variably in different grains.

5.5 Discussion

5.5.1 Shock microstructures in xenotime

The xenotime grains investigated in this study originate from different sites and different crater environments (where known). The grains show a variety of crystal-plastic deformation microstructures that were investigated to evaluate the response of the U-Pb system. Microstructures investigated include PF, PDB, deformation twin lamellae, as well as grains that have partially or fully recrystallized to neoblastic domains. The following section

summarizes the microstructures in the grains studied in the context of previously descriptions of shocked xenotime.

5.5.1.1 Planar fractures (PF)

Planar fractures have been documented in xenotime grains from the Santa Fe (Figure 5.3; Cavosie et al., 2016a) and Spider (Cox et al., 2021) impact structures, and here we report an example of PF in xenotime from the Vredefort impact structure. Four orientations of PF were documented in Vredefort xenotime 14DG14 (Figure 5.2). In all cases thus far described, PF consist of multiple sets of closely spaced (1 to 5 μm) penetrative parallel fractures that typically extend fully across grains (or nearly so). In two of the three Santa Fe grains analysed (grains SFx2, SFx4), as well as the Vredefort grain (14DG14), one or more sets of PF were found to contain $\{112\}$ deformation twins (Figure 5.3). However, twins were not identified in Santa Fe grain SFx3, and were also not present in several PF-bearing xenotime grains documented by Cox et al. (2021). This observation demonstrates that deformation twins can not be assumed to be present in xenotime grains that contain PF. In this regard, PF in xenotime appear analogous to those in zircon; they seem to be a common microstructure in shocked grains, but alone they do not provide diagnostic evidence of shock deformation.

5.5.1.2 Planar deformation bands (PDB)

The presence of PDB have been documented in xenotime grains from the Vredefort (Cavosie et al., 2021b), Santa Fe (Cavosie et al., 2016a), and Spider (Cox et al., 2021) impact structures. The PDB described by Cavosie et al. (2021b) in a Vredefort detrital xenotime occurred in three discrete orientations, with individual PDB typically 5 to 10 μm wide, and preserving up to 40° of misorientation relative to the host grain. Significant misorientation across discrete 2-3 μm -wide PDB were also described in xenotime grains from shatter cones in quartzite (Cox et al., 2021). The PDB in Vredefort xenotime 14DG14 described here mostly occur in areas bound by cross-cutting PF sets and near grain margins. They are mostly 10-20 μm wide and are sub-parallel to PF sets, but some are irregular in shape and have diffuse boundaries with up to $\sim 12^\circ$ of misorientation relative to the host grain (Figure 5.2c). The only significant PDB found in the Santa Fe xenotime grains occurs in grain SFx5, and are concentrated near the margin of the grain (some are sub-parallel to PF set 3), and preserve up to 6° of misorientation from the host (Figure 5.3c,f). The above observations highlight the magnitude of variable misorientations across PDB in xenotime grains from different impact structures. Similar to PF, PDB are not regarded as diagnostic evidence of shock deformation in xenotime, as is the case for both zircon (Timms et al., 2017) and apatite (Cox et al., 2020).

5.5.1.3 Deformation twins in {112}

Lamellar deformation twins are commonly found in shocked zircon (see discussion in Cavosie and Folco, 2021a), shocked monazite (Erickson et al., 2016), and shocked titanite (Timms et al., 2019). Deformation twins in shocked xenotime have thus far been reported in grains from the Vredefort, Santa Fe, and Spider impact structures (Cavosie et al., 2021b; Cavosie et al., 2016a; Cox et al., 2021). Here we document {112} twins in Vredefort grain 14DG14 and also in Santa Fe grains SFx4 and SFx5 (the latter two were described previously). Lamellar deformation twins in {112} in xenotime are defined by a 65° misorientation from the <110> of the host grain and a shared {112} direction (Cavosie et al., 2016a, 2021b; Cox et al., 2021). Formation conditions of {112} twins in xenotime have not been calibrated experimentally, however, empirical constraints suggest formation conditions of 5 to 20 GPa based on their occurrence in samples that contain shocked quartz and shocked zircon, as well as their presence in shatter cones (Cavosie et al., 2016a; Montalvo et al., 2019; Cox et al., 2021). A new observation of twin phenomenon here is the discontinuous nature of individual {112} twin lamellae in Vredefort xenotime 14DG14. In that grain, the t3 {112} twin preserves twin segments with different disorientations along the length of a single lamellae, including (72°/<342>, 68°/<232>, 70°/<341>, and 70°/<340>) (Figure 5.2e). The segmented twins could represent a progressive shear transformation to accommodate the geometry of {112} twins, or alternatively, the lamellar twin may have responded in a heterogeneous way to localised stresses that effectively fractured the lamella during twin formation, resulting in multiple orientations of ‘failed twin’ domains along its length. Alternatively post-impact partial annealing could also have modified the lamellar twin, as has been discussed for zircon (Erickson et al., 2013b).

5.5.1.4 Recrystallisation to neoblastic texture

There are few reports of neoblastic textures in xenotime from shocked rocks. Multiple examples of polycrystalline xenotime grains consisting of aggregates of low strain ~1 µm sized neoblasts were reported from the Spider impact structure by Cox et al. (2021), occurring in shatter cone samples of quartzite that contained quartz with PDF and shock-twinned zircon. However, in most cases the polycrystalline xenotime grains occurred in cracks and vugs; it was therefore not clear if the polycrystalline microstructures formed by impact processes, or if they had a diagenetic/secondary origin, as systematic orientation relations among the neoblasts were not observed. Only one xenotime grain described by Cox et al. that consisted of both recrystallized polygonal neoblasts and a strained host domain with PDB had an unambiguous

impact origin. In this study neoblastic microstructures were found in Vredefort grain 14DG14 and in all three Araguainha xenotime grains.

Vredefort grain 14DG14 contains rare localized occurrences of 2-3 μm sized neoblasts along PF planes that also contain $\{112\}$ twins (Figure 5.2d). The neoblasts are generally round and isolated in occurrence and are a very minor microstructural feature of grain 14DG14. Given their location on PF planes that elsewhere contain $\{112\}$ twins, the origin of these neoblasts is likely related to local shear-stress induced recrystallization that was energetically insufficient to form a lamellar twin. The stored strain energy lowered the energy barrier for nucleation, forming neoblasts locally via grain boundary migration (Erickson et al., 2017). Given their rarity in grain 14DG14, it is unlikely that the neoblasts in this grain formed via thermal recrystallization process (Moser et al., 2011; Erickson et al., 2017).

In contrast, EBSD analysis shows that the three Araguainha xenotime grains from impact melt rock sample SF20 reported here contain variable amounts of recrystallized neoblastic domains. Grain X1 consists mostly of a strained host domain ($\sim 86\%$) that preserves up to 20° of accumulated misorientation across the grain. The strained host domain does not contain other discrete microstructures, such as PDB or deformation twins. Two populations of neoblasts comprise 14% of grain X1; each shares a systematic orientation with the host domain of $65^\circ/\langle 110 \rangle$ and a shared $\{112\}$ direction (Figure 5.5). Both populations of neoblasts are thus interpreted to have formed by the recrystallization of former $\{112\}$ deformation twins, similar to that reported in some granular zircon grains (Cavosie et al., 2016b), and also in partially recrystallized monazite (Erickson et al., 2015). Xenotime grains X2 and X3 consist entirely of recrystallized neoblasts, however, no systematic orientation relations indicative of recrystallized twins is present in either grain (Figure 5.4). In grain X2, the majority of neoblasts are dispersed about the c-axis (Figure 5.4b). Grain X3 contains a central area approximately $40 \mu\text{m} \times 20 \mu\text{m}$ that consists of neoblasts that preserve the host grain orientation; neoblasts in different orientations form a wide margin around the central area (Figure 5.4d,f). In general, neoblasts in all Araguainha xenotime grains preserve high angle boundaries ($>10^\circ$) with adjacent neoblasts. The host rock of the Araguainha xenotime grains is an impact melt rock derived from a sedimentary rock, and likely become molten during shock pressures $>20 \text{ GPa}$ and subsequent heating (Stöffler et al., 2018).

5.5.2 SIMS U-Pb geochronology of shock microstructures in xenotime

5.5.2.1 Shocked twins, PDB and PF in xenotime (Vredefort and Santa Fe)

A total of 24 SHRIMP spot analyses made on Vredefort grain 14DG14 yield a discordant array with an upper Concordia intercept of 3136 Ma which is interpreted as the crystallisation age of the grain, as it broadly overlaps ages of basement gneisses exposed at the Vredefort impact structure (3.5 to 3.1 Ga, Hart et al., 1981; Flowers et al., 2003; Moser et al., 2011). The SHRIMP analyses overlapped {112} twins, PDB, and PF, however no correlations between age and microstructure were detected. At the scale of the SIMS analysis, the shock microstructures targeted here do not record Pb-loss related to the impact event, similar to a previously report for a different shocked xenotime grain from the Vredefort structure (Cavosie et al., 2021b).

The five SIMS analyses of three Santa Fe xenotime grains include spots on {112} twins, PDB, and PF. The five analyses are concordant and yield a weighted mean $^{207}\text{Pb}^*/^{206}\text{Pb}^*$ age of 1427 ± 20 Ma. The age of the Santa Fe impact event is not well constrained (see Fackelman et al., 2008; Montalvo et al., 2019), and the granites in the area have not previously been dated. However, the Mesoproterozoic age determined here is best interpreted as the crystallisation age of the host granitoid. Detrital zircon grains throughout the area where shatter cones are exposed mostly range in age from 1.7 to 1.4 Ga, and the 1427 ± 20 Ma age determined here overlaps with the 1472 ± 35 Ma age determined from detrital shocked zircon in the same area (Montalvo et al., 2019).

In summary, no apparent impact age resetting associated with PF, PDB, and deformation twins in xenotime was detected at the scale of SIMS analyses from the Vredefort and Santa Fe impact structures. In this regard, the U-Pb response of these shock microstructures in xenotime are thus similar to those in zircon (Moser et al., 2011; Erickson et al., 2013a; Cavosie et al., 2015, 2018a; Montalvo et al., 2019; McGregor et al., 2021b).

5.5.2.2 Neoblast formation in Araguainha – Pb mobility and age resetting

The three xenotime grains from Araguainha were each analysed in six locations by SIMS. Analysis spots on grain X1 were mostly mixtures of host and neoblasts, whereas all analyses on grain X2 were on neoblasts. Grains X1 and X2 both show coherent clusters on Concordia diagrams, however, none of the age clusters coincides with the known impact age. All spot analyses on grain X3 were on neoblasts, and common Pb was also detected. Grain X3 is the only grain to yield a reset age that coincides with the known impact age (255 ± 11 Ma, MSWD =1.9, n=6). The oldest spot analysis measured on any of the Araguainha xenotime grains is 478 ± 25 Ma (grain X1, host domain). This age overlaps with the crystallisation age of the Araguainha granite (512 ± 11 Ma, Tohver et al., 2012), suggesting that the xenotime grains

analysed from sample SF20 are likely to have been sourced from the Araguainha granite. The SHRIMP U-Pb results indicate that solid-state recrystallisation of xenotime in impact melt rocks leads to the formation of neoblasts with variable U-Pb resetting. The spread of data between the inferred crystallisation age and the impact age represents variable Pb-loss, and such ages likely have no geological significance. The neoblastic microstructure in xenotime is thus the prime candidate microstructure to target for dating impact events, as has been observed in other minerals such as zircon and monazite (Moser et al., 2011; Cavosie et al., 2015; Erickson et al., 2017; Kenny et al., 2017; Erickson et al., 2020; McGregor et al., 2021b).

5.5.2.3 Significance of the Vredefort xenotime lower discordia intercept

The SIMS data for Vredefort xenotime 14DG14 define a Discordia line with an imprecise lower Concordia intercept of 1803 ± 270 Ma. This age is >200 Ma younger than the accepted impact age, although it does overlap given the large uncertainty. However, the lower intercept age is also similar to a lower Concordia intercept age of 1754 ± 150 Ma previously determined on detrital shocked xenotime grain from the Vredefort impact structure (Cavosie et al., 2021b). The 1754 ± 150 Ma age was interpreted to record a unknown alteration event in the Witwatersrand basin (Cavosie et al. 2021b). An age of 1772 ± 150 Ma from a Vredefort shocked monazite grain was determined in an APT study and interpreted to represent an alteration event that formed nanoscale element clusters in monazite (Fougerouse et al., 2021a). To date, Paleoproterozoic ages (1.8–1.7 Ga) in shocked minerals from the Vredefort impact structure have only been reported in monazite (Flowers et al., 2003; Fougerouse et al, 2021a) and xenotime (this study; Cavosie et al., 2021b); they have conspicuously not been reported in U-Pb studies of Vredefort shocked zircon (e.g., Flowers et al., 2003; Armstrong et al., 2006; Moser et al., 2011).

Post-impact age resetting has been reported in other shocked minerals from other impact structures. Shocked baddeleyite from Sudbury impact melt sheet was shown to record post-impact metamorphic signatures (White et al., 2017). The formation of shock deformation microstructures such as fractures and deformation twins can enhance the mobility of elements through fast diffusion pathways. The new pathways formed due to shock deformation may render the mineral susceptible to younger (post-impact) Pb loss events, especially for phases more readily susceptible to fluid alteration, such as phosphates. The above results further demonstrate that impact metamorphism augments the susceptibility of certain minerals to post-impact metamorphic or hydrothermal events.

5.5.3 Nanoscale heterogeneities in shock-deformed xenotime

5.5.3.1 Nanoscale analysis of twins and neoblasts from Vredefort and Santa Fe

APT specimens from areas of high lattice misorientation in the Vredefort xenotime (Figure 5.2d), are characterised by the presence of small, strain-free neoblasts that contain Ca-Pb* rich clusters in two out of five specimens analysed. The largest cluster from specimen V4 (Figure 5.6a) is composed of 7.2 at. % Ca, 2.67 at. % Pb, and 0.8 at. % Si, with a combined Ca+Pb+Si concentration of 10.67 at. %. Such a composition suggests that the cluster is likely a nanoscale inclusion of a different phase (Fougerouse et al., 2016, 2018, 2021a; Seydoux-Guillaume et al., 2019), rather than a trace element enriched domain of xenotime, as has been observed in zircon and rutile (Valley et al., 2014; Peterman et al., 2016, 2019; Verberne et al., 2020). The chemical composition of the clusters is most consistent with the mineral apatite $\text{Ca}_5(\text{PO}_4)_3(\text{OH},\text{F},\text{Cl})$, in which Pb can substitute for Ca (Pan and Fleet, 2002). The $^{207}\text{Pb}/^{206}\text{Pb}$ APT age obtained from the two specimens with Ca-Pb* clusters are 3043 ± 420 Ma, which is consistent with the inferred crystallisation age of the sample (Figure 5.9a). Excluding the clusters, combining the matrix of the same specimens and the specimens devoid of the Ca-Pb* clusters yields a weighted mean $^{207}\text{Pb}/^{206}\text{Pb}$ age of 2647 ± 350 Ma. On the assumption that all Pb* migrated into the clusters during formation, the $^{207}\text{Pb}/^{206}\text{Pb}$ 2647 ± 350 Ma matrix age represents the formation age of the clusters (Figure 5.9a). One specimen (V4) from the high strain domain contains OH-enriched clusters, and a linear feature enriched in Na, Al, and Cl, which is interpreted as a dislocation based on previous APT studies (Piazolo et al., 2016; Fougerouse et al., 2021a; Verberne et al., 2022). Specimen V5 present a set of dislocations in a planar domain Si, Ca, Cl, Na, and Al. The geometry is consistent with that of low angle boundaries in olivine (Tacchetto et al., 2021). All ions present in the dislocations are not part of the mineral xenotime and represent nanoscale evidence of fluid activity in the sample (Tacchetto et al., 2021; Joseph et al., 2023). Therefore, we suggest that the apatite inclusions formed during a post-crystallisation fluid alteration event at 2647 ± 350 Ma. The date of 2647 ± 350 Ma also overlaps with $\sim 2729\text{--}2665$ Ma Ventersdorp volcanism in South Africa (Schneiderhan et al., 2011; Altermann and Lenhardt, 2012; Gumsley et al., 2020). However, the high uncertainty associated with the APT dates preclude a robust determination of causation (V1-V5, Figure 5.9a). Whole sample (matrix+clusters) APT $^{206}\text{Pb}/^{238}\text{U}$ dates from these five specimens yield a weighted mean age of 1596 ± 93 Ma. The younger $^{206}\text{Pb}/^{238}\text{U}$ age obtained from whole specimen data overlaps with the cryptic post-impact alteration event reported previously in both xenotime and monazite (Cavosie et al., 2021b; Fougerouse et al., 2021a). Two APT specimens analysed from $\{112\}$ twin domains (Figure 5.2e) also show a different

type of cluster, one with enrichment of only Ca and one with enrichment of only Pb. The $^{207}\text{Pb}/^{206}\text{Pb}$ dates obtained from the matrix of the specimen with Pb* clusters is 2186 ± 1092 Ma, which broadly coincides with the known impact age of ~ 2020 Ma, however, the high uncertainties do not allow a conclusive interpretation (Figure 5.9a).

In the case of Santa Fe xenotime SFx5, nanoscale analysis of the xenotime host and {112} twin reveals nanoscale Ca-enriched clusters (up to 4 at. % Ca), with varying Pb* concentration (between 1 and 3.8 at. % Pb) between specimens (Figure 5.8b). The low Pb* containing clusters are only seen in specimens from the host (SF1 and SF2), and not from the twin domain (SF3 and SF4). The absence or low concentration (maximum of ~ 1 at. %) of Pb* in the small Ca-enriched clusters suggests the clusters formed in a short time span after crystallisation. The mechanism behind cluster formation in the absence of fluids is presumably the exsolution of apparently bigger Ca^{2+} (1.12 Å) and Pb^{2+} (1.29 Å) ions compared to the Y^{3+} (1.02 Å) ion, due to the size disparity during cooling of the crystal (Shannon, 1976). This phase immiscibility model has been proposed to form nanoscale apatite inclusions in previous xenotime and monazite atom probe studies (Fougerouse et al., 2018; Joseph et al., 2021).

The APT specimens SF3 and SF4, from the twin domain of the Santa Fe grain, contain Ca clusters with higher Pb* enrichment, up to 6 at. % (SF3) compared to other Ca-Pb clusters from the Santa Fe grain, in which the Pb* concentration is less than 1 at. %. The higher Pb* concentration in these clusters indicates formation a considerable period of time after crystallisation. Nanoscale mobility of Pb into clusters during twin formation has been documented during crystal plastic deformation of monazite, both in tectonic and shock settings with apparent temperature control (Fougerouse et al., 2021a, b). It is thus possible that the Pb*-rich clusters formed at the time of twin formation during shock deformation. However, the $^{206}\text{Pb}/^{238}\text{U}$ nanogeochronology dates of SF3 and SF4 from the whole specimen (SF3 - 1391 ± 83 Ma, SF4 - 1274 ± 100 Ma) overlap with the respective dates obtained from the matrix (SF3 - 1329 ± 81 Ma, SF4 - 1213 ± 98 Ma), and it is therefore not possible to confirm if they formed during twinning. Considering the data for xenotime samples from Vredefort and Santa Fe, there is an indication of Pb mobility associated with twin formation, however it is not conclusive based on the available data.

5.5.3.2 Nanoscale analysis of neoblasts from Araguainha

In Araguainha xenotime samples, the Pb signal in the atom probe mass spectra was not significantly above the background, and therefore no APT nanogeochronology data could be extracted for these samples. The grain boundary analysed between two neoblasts and the

dislocations from Araguinha grain X3 (specimen A4) are enriched primarily with Si, followed by Mg, Ca, Cl, Na and Al. In addition, Si-Mg clusters are distributed preferably on one side of the grain boundary in specimen A4. Elements such as Si and Ca can be incorporated into xenotime by cheralite and huttonite substitution (Spear and Pyle, 2002). The rest of the elements found along the grain boundary (Cl, Na and Al) are not commonly present in xenotime, and could have been derived from an external source, such as fluids (e.g., Tacchetto et al., 2021, 2022).

Trace element migration is found to be intimately associated with the defect density in materials (Watanabe, 1985). The segregation of trace elements which are not inherently part of the host mineral to the grain boundary is more energetically favourable to reduce the lattice stress principally caused by the differences in ionic size between the host grain sites and the trace element (Hoskin and Black, 2000; Reddy et al., 2016). The enrichment of trace elements in dislocations and both low and high-angle boundaries has documented in minerals from different geological settings (Suzuki, 1987; Hiraga et al., 2003; Reddy et al., 2016; Dubosq et al., 2018; Fougereuse et al., 2019; Tacchetto et al., 2021, 2022). Shock deformation produces high strain in minerals, resulting in numerous dislocations and low-angle boundaries. During annealing facilitated by high temperatures from the melting of surrounding rocks, neoblasts nucleate from sub grain boundaries through grain boundary migration (Doherty et al., 1997; Piazzolo et al., 2012). Grain boundary migration occurs when a grain with low degree of imperfection grows in to a grain with higher degree of dislocations and low angle boundaries creating a lobate inter-fingering texture (Poirier, 1985; Jessell, 1987; Passchier and Trouw, 2005; Drury and Pennock, 2007). This texture can be seen in the neoblasts selected for nanoscale APT analysis, where a grain with no misorientation is seen growing into a grain with higher misorientation along a lobate texture (Figure 5.4h).

The difference in the degree of internal misorientation in a neoblast is reflected in the composition from APT analysis showing a difference in the density of Si-Mg clusters from one neoblast to another. The orientation of the boundary in the APT specimen coincides with the orientation of the boundary determined by EBSD (Figure 5.4g and 5.10). In the APT specimen, the domain above the grain boundary corresponds to the neoblast with no misorientation identified from EBSD (Figure 5.4h) and has a limited number of Si-Mg clusters (Figure 10). The domain below the grain boundary in the APT specimen corresponds to the neoblast with higher degree of internal misorientation and is characterised by a higher density of Si-Mg clusters (Figure 5.10). These observations suggest that the grain boundary of the neoblasts with no misorientation (grain α , Figure 5.11) displaced Si-Mg clusters during its migration, forming

strain-free neoblasts during the recovery stage of shock deformation, forming the lobate texture (Passchier and Trouw, 2005; Figure 5.11). The formation of defects, grain boundaries and neoblasts is very rapid as inherent to impact metamorphism; further growth of neoblasts can continue if sufficient temperature is provided. The process of grain boundary migration reduces strain in a crystal, and it is here hypothesised that Pb* was collected by the grain boundaries and diffused to the grain edges. As mentioned above, as Pb is a large cation in the xenotime structure it is likely to escape from the crystal lattice during grain boundary migration resulting in resetting the age recorded in the grain. The higher the degree of recrystallisation through this process, the higher will the degree of Pb loss from the grain be, as observed from the grains from X1 to X3.

Alternatively, the trace element enrichment in the grain boundary may represent a melt phase. In granular neoblastic zircon void spaces between neoblasts can contain melt glass, lechatelierite, or other minerals (Cavosie et al., 2016b, 2018b, 2018c). In the Araguainha xenotime, the composition of Si reaches ~2.6 at. %, which is likely not high enough to represent a silicate impact melt composition.

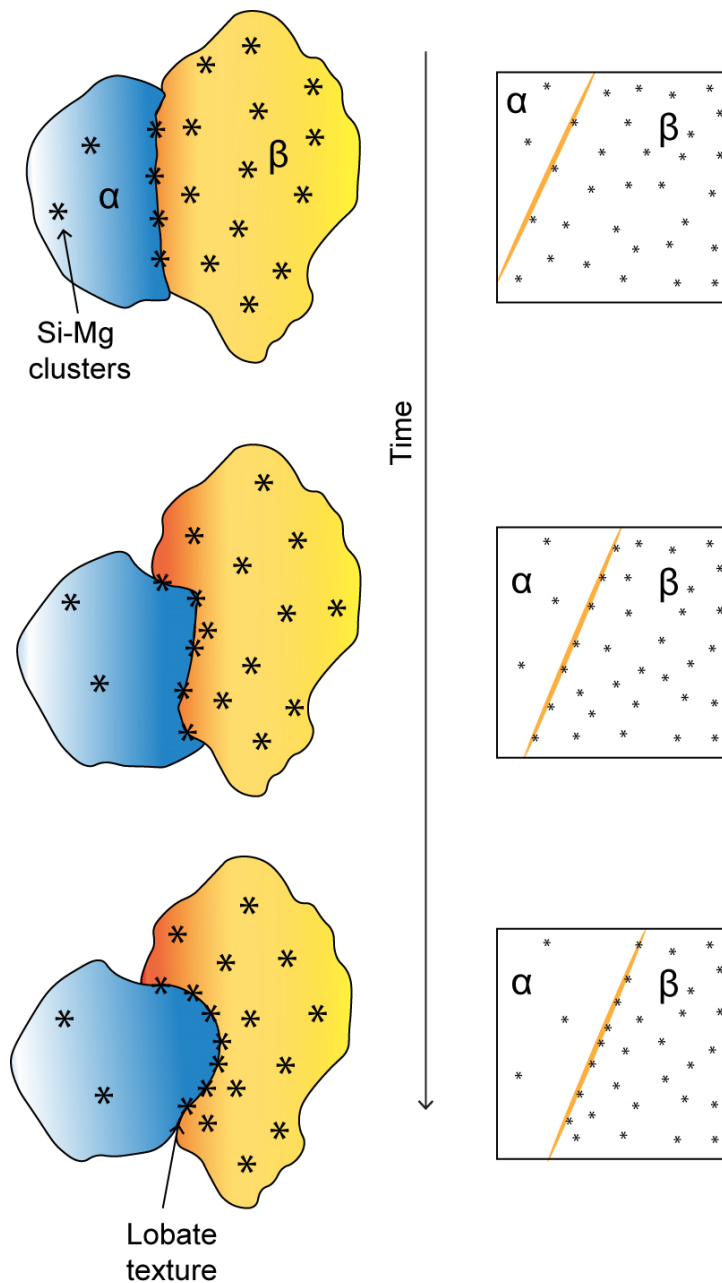


Figure 5.11: Illustration of the grain boundary migration forming the lobate texture between the recrystallised neoblasts at the grain scale (left) and nanoscale (right). Large crystal α has a lower dislocation density, less number of clusters hence less crystal distortion. Crystal β has a higher cluster density, with internal misorientation. With time, more deformed crystal is consumed, by atoms from β reorganise to fit the crystal lattice of α forming a interfingering lobate texture.

5.6 Summary and Concluding remarks

This study attempted to demonstrate response of xenotime to shock metamorphic conditions from samples from different impact structures using multiple techniques including,

EBSD, SIMS and APT, as a potential impact geochronometer. Shock microstructures observed from the samples studied comprises PF, PDB, varying degrees of lattice misorientation, shock deformation {112} twins, and newly identified shock induced neoblastic texture in xenotime. Targeted SIMS U-Pb analyses revealed the microscale U-Pb response of different shock induced microstructures in xenotime. Spot analyses targeted {112} twins, PDBs from Vredefort and Santa Fe samples showed no impact related resetting, which is similar to U-Pb response from zircon from previous studies. Vredefort sample record discordant age array with upper intercept corresponding to the crystallisation age of the sample (~3.1 Ga) and lower intercept to a cryptic fluid alteration event at ~1.8–1.7 Ga which has only recorded in phosphates (monazite - Fougereuse et al., 2021a, xenotime - Cavosie 2021b). Concordant U-Pb analyses from xenotime sourced from the shatter cones of Santa Fe yielded the first direct age determination of the target rock of Santa Fe impact structure, 1427 ± 20 Ma. On the other hand, xenotime grains from Araguainha with varying proportions of recrystallisation between grains (neoblastic texture) showed a correlation between the degree of recrystallisation to the degree of resetting of the U-Pb system. The oldest age determined is from the least recrystallised grain, matches the age of the host granitoid, and the youngest age from the fully recrystallised neoblastic grain yielded the age of Araguainha impact (255 ± 11 Ma). This records the first-time impact age determination of an impact site from xenotime, to our knowledge. APT analyses on different microstructural domains in shocked xenotime such as deformation twins, areas of high lattice misorientation, and neoblasts showed nanoscale compositional heterogeneities in the form of clusters, dislocations, and grain boundaries with higher concentration of trace elements such as Si, Mg, Ca, Na, Cl, and Al. Particularly nanoscale analysis from a grain boundary between two recrystallised neoblasts from Araguainha sample suggests the formation of the neoblasts is achieved by grain boundary migration process, which leads to resetting the grain yielding impact age.

As stated in the introduction, dating of impact events is strenuous and this study introduces a new impact geochronometer to the scientific community. The study also offers a workflow which helps in future impact deformed xenotime research on identification and detailed study of the microstructures formed, followed by targeted high precision dating of the microstructures using either SHRIMP or similar techniques such as LA-ICPMS. Nanoscale study of the samples give in-depth breakdown of the processes behind the U-Pb response of the sample.

5.7 Acknowledgements

Araguainha sample SF20 was provided by Natalia Hauser. Sample mount 05-12 used for xenotime standard in this project is part of the McNaughton Legacy Collection, in the John de Laeter Centre (JdLC). This study benefited from the Australian Science and Industry Endowment Fund (grant SIEF RI13-01) and the Discovery Early Career Research Award from the Australian Research Council to Denis Fougere (DE190101307). The authors acknowledge the support of Microscopy and Microscopy Facility and JdLC, Curtin University, whose instrumentation has been supported by University, State and Commonwealth Government funding. Jeffrey G. Catalano is thanked for editorial handling, and two anonymous reviewers are thanked for providing constructive comments.

5.8 References

- Aleinikoff J. N., Hayes T. S., Evans K. V., Mazdab F. K., Pillers R. M. and Fanning C. M. (2012) SHRIMP U-Pb ages of Xenotime and monazite from the Spar Lake red bed-associated Cu-Ag deposit, western Montana: Implications for ore genesis. *Econ. Geol.* **107**, 1251–1274.
- Altermann W. and Lenhardt N. (2012) The volcano-sedimentary succession of the Archean Sodium Group, Ventersdorp Supergroup, South Africa: Volcanology, sedimentology and geochemistry. *Precambrian Res.* **214–215**, 60–81.
- Armstrong R. A., Lana C., Uwe Reimold W. and Gibson R. L. (2006) SHRIMP zircon age constraints on Mesoarchean crustal development in the Vredefort dome, central Kaapvaal Craton, South Africa. In *Processes on the Early Earth* (eds. W. U. Reimold and R. L. Gibson). *Geological Society of America*.
- Bauer, P., Ralser, S., Daniel, C., Ilg, B., and Harrison, B., 1996, Geologic map of the McClure Reservoir quadrangle, Santa Fe County, New Mexico: New Mexico Bureau of Geology and Mineral Resources, Open-File Geologic Map 07, scale 1:24,000, 1 sheet.
- Bauer, P.W., and Ralser, S., 1995, The Picuris-Pecos fault: Repeatedly reactivated, from Proterozoic to Neogene, in Bauer, P.W., Kues, B.S., Dunbar, N.W., Karlstrom, K.E., and Harrison, B., eds., *Geology of the Santa Fe Region: Socorro, New Mexico, USA*, New Mexico Geological Society 46th Annual Fall Field Conference Guidebook, 111–115.
- Bodorkos S., Bowring J. F. and Rayner N. M. (2020) *Squid3: next-generation data processing software for sensitive high-resolution ion microprobe (SHRIMP).*,

- Brown S. M., Fletcher I. R., Stein H. J., Snee L. W. and Groves D. I. (2002) Geochronological Constraints on Pre-, Syn-, and Postmineralization Events at the World-Class Cleo Gold Deposit, Eastern Goldfields Province, Western Australia. *Econ. Geol.* **97**, 541–559.
- Cavosie A. J. and Folco L. (2021a) Shock-twinning zircon in ejecta from the 45-m-diameter Kamil crater in southern Egypt eds. W. U. Reimold and C. Koeberl. *Large Meteor. Impacts Planet. Evol.* **VI 550**, 0.
- Cavosie A. J., Erickson T. M., Timms N. E., Reddy S. M., Talavera C., Montalvo S. D., Pincus M. R., Gibbon R. J. and Moser D. (2015) A terrestrial perspective on using ex situ shocked zircons to date lunar impacts. *Geology* **43**, 999–1002.
- Cavosie A. J., Kirkland C. L., Reddy S. M., Timms N. E., Talavera C. and Pincus M. R. (2021b) Extreme plastic deformation and subsequent Pb loss in shocked xenotime from the Vredefort Dome, South Africa. *In Large Meteorite Impacts and Planetary Evolution VI Geological Society of America.* **VI 550**, 465–478.
- Cavosie A. J., Montalvo P. E., Timms N. E. and Reddy S. M. (2016a) Nanoscale deformation twinning in xenotime, a new shocked mineral, from the Santa Fe impact structure (New Mexico, USA). *Geology* **44**, 803–806.
- Cavosie A. J., Spencer C. J., Evans N., Rankenburg K., Thomas R. J. and Macey P. H. (2022) Granular titanite from the Roter Kamm crater in Namibia: Product of regional metamorphism, not meteorite impact. *Geosci. Front.* **13**, 101350.
- Cavosie A. J., Timms N. E., Erickson T. M., Hagerty J. J. and Hörz F. (2016b) Transformations to granular zircon revealed: Twinning, reidite, and ZrO₂ in shocked zircon from Meteor Crater (Arizona, USA). *Geology* **44**, 703–706.
- Cavosie A. J., Timms N. E., Ferrière L. and Rochette P. (2018c) FRIGN zircon-The only terrestrial mineral diagnostic of high-pressure and high-temperature shock deformation. *Geology* **46**, 891–894.
- Cavosie A. J., Timms N. E., Erickson T. M. and Koeberl C. (2018b) New clues from Earth's most elusive impact crater: Evidence of reidite in Australasian tektites from Thailand. *Geology* **46**, 203–206.
- Cavosie A. J., Erickson T. M., Montalvo P. E., Prado D. C., Cintron N. O. and Gibbon R. J. (2018a) The Rietputs Formation in South Africa. *In Microstructural Geochronology: Planetary Records Down to Atom Scale*, 203–224.

- Cherniak D. J. (2006) Pb and rare earth element diffusion in xenotime. *Lithos* **88**, 1–14.
- Cherniak D. J. (2010) Diffusion in accessory minerals: Zircon, titanite, apatite, monazite and xenotime. *Rev. Mineral. Geochemistry* **72**, 827–869.
- Chew D. M., Petrus J. A. and Kamber B. S. (2014) U–Pb LA–ICPMS dating using accessory mineral standards with variable common Pb. *Chem. Geol.* **363**, 185–199.
- Cox M. A., Cavosie A. J., Poelchau M., Kenkmann T., Bland P. A. and Miljković K. (2021) Shock deformation microstructures in xenotime from the Spider impact structure, Western Australia. In *Large Meteorite Impacts and Planetary Evolution VI* (eds. W. U. Reimold and C. Koeberl). *Geological Society of America*, 449–464.
- Cox M. A., Erickson T. M., Schmieder M., Christoffersen R., Ross D. K., Cavosie A. J., Bland P. A., Kring David A., Gulick S., Morgan J. V., Carter G., Chenot E., Christeson G., Claeys P., Cockell C., Coolen M. J. L., Ferrière L., Gebhardt C., Goto K., Jones H., Kring D. A., Lofi J., Lowery C., Ocampo-Torres R., Perez-Cruz L., Pickersgill A., Poelchau M., Rae A., Rasmussen C., Rebolledo-Vieyra M., Riller U., Sato H., Smit J., Tikoo S., Tomioka N., Whalen M., Wittmann A., Urrutia-Fucugauchi J., Xiao L. and Yamaguchi K. E. (2020) High-resolution microstructural and compositional analyses of shock deformed apatite from the peak ring of the Chicxulub impact crater. *Meteorit. Planet. Sci.* **55**, 1715–1733.
- Darling J. R., Moser D. E., Barker I. R., Tait K. T., Chamberlain K. R., Schmitt A. K. and Hyde B. C. (2016) Variable microstructural response of baddeleyite to shock metamorphism in young basaltic shergottite NWA 5298 and improved U–Pb dating of Solar System events. *Earth Planet. Sci. Lett.* **444**, 1–12.
- Doherty R. D., Hughes D. A., Humphreys F. J., Jonas J. J., Jensen D. J., Kassner M. E., King W. E., McNelley T. R., McQueen H. J. and Rollett A. D. (1997) Current issues in recrystallization: a review. *Mater. Sci. Eng. A* **238**, 219–274.
- Drury M. R. and Pennock G. M. (2007) Subgrain Rotation Recrystallization in Minerals. *Mater. Sci. Forum* **550**, 95–104.
- Dubosq R., Lawley C. J. M., Rogowitz A., Schneider D. A. and Jackson S. (2018) Pyrite deformation and connections to gold mobility: Insight from micro-structural analysis and trace element mapping. *Lithos* **310–311**, 86–104.

http://www.passc.net/EarthImpactDatabase/New%20website_05-2018/Index.html

Engelhardt W. V, Matthäi S. K. and Walzebuck J. (1992) Araguainha impact crater, Brazil. I. The interior part of the uplift. *Meteoritics* **27**, 442–457.

Erickson T. M, Cavosie A. J., Moser D. E., Barker I. R., Radovan H. A. and Wooden J. (2013b) Identification and provenance determination of distally transported, Vredefort-derived shocked minerals in the Vaal River, South Africa using SEM and SHRIMP-RG techniques. *Geochim. Cosmochim. Acta* **107**, 170–188.

Erickson T. M, Kirkland C. L., Timms N. E., Cavosie A. J. and Davison T. M. (2020) Precise radiometric age establishes Yarrabubba, Western Australia, as Earth's oldest recognised meteorite impact structure. *Nat. Commun.* **11**, 300.

Erickson T. M., Cavosie A. J., Moser D. E., Barker I. R. and Radovan H. A. (2013a) Correlating planar microstructures in shocked zircon from the Vredefort Dome at multiple scales: Crystallographic modeling, external and internal imaging, and EBSD structural analysis. *Am. Mineral.* **98**, 53–65.

Erickson T. M., Cavosie A. J., Pearce M. A., Timms N. E. and Reddy S. M. (2016) Empirical constraints on shock features in monazite using shocked zircon inclusions. *Geology* **44**, 635–638.

Erickson T. M., Pearce M. A., Taylor R. J. M., Timms N. E., Clark C., Reddy S. M. and Buick I. S. (2015) Deformed monazite yields high-temperature tectonic ages. *Geology* **43**, 383–386.

Erickson T. M., Timms N. E., Kirkland C. L., Tohver E., Cavosie A. J., Pearce M. A. and Reddy S. M. (2017) Shocked monazite chronometry: integrating microstructural and in situ isotopic age data for determining precise impact ages. *Contrib. to Mineral. Petrol.* **172**, 11.

Fackelman S. P., Morrow J. R., Koeberl C. and McElvain T. H. (2008) Shatter cone and microscopic shock-alteration evidence for a post-Paleoproterozoic terrestrial impact structure near Santa Fe, New Mexico, USA. *Earth Planet. Sci. Lett.* **270**, 290–299.

Fletcher I. R., McNaughton N. J., Aleinikoff J. A., Rasmussen B. and Kamo S. L. (2004) Improved calibration procedures and new standards for U - Pb and Th - Pb dating of Phanerozoic xenotime by ion microprobe. *Chem. Geol.* **209**, 295–314.

- Fletcher I. R., Rasmussen B. and McNaughton N. J. (2000) SHRIMP U-Pb geochronology of authigenic xenotime and its potential for dating sedimentary basins. *Aust. J. Earth Sci.* **47**, 845–859.
- Flowers R. M., Moser D. E. and Hart R. J. (2003) Evolution of the Amphibolite-Granulite Facies Transition Exposed by the Vredefort Impact Structure, Kaapvaal Craton, South Africa. *J. Geol.* **111**.
- Fougerouse D., Cavosie A. J., Erickson T., Reddy S. M., Cox M. A., Saxey D. W., Rickard W. D. A. and Wingate M. T. D. (2021a) A new method for dating impact events – Thermal dependency on nanoscale Pb mobility in monazite shock twins. *Geochim. Cosmochim. Acta* **314**, 381–396.
- Fougerouse D., Reddy S. M., Kirkland C. L., Saxey D. W., Rickard W. D. and Hough R. M. (2019) Time-resolved, defect-hosted, trace element mobility in deformed Witwatersrand pyrite. *Geosci. Front.* **10**, 55–63.
- Fougerouse D., Reddy S. M., Saxey D. W., Erickson T. M., Kirkland C. L., Rickard W. D. A., Seydoux-Guillaume A.-M., Clark C. and Buick I. S. (2018) Nanoscale distribution of Pb in monazite revealed by atom probe microscopy. *Chem. Geol.* **479**, 251–258.
- Fougerouse D., Reddy S. M., Saxey D. W., Rickard W. D. A., van Riessen A. and Micklethwaite S. (2016) Nanoscale gold clusters in arsenopyrite controlled by growth rate not concentration: Evidence from atom probe microscopy. *Am. Mineral.* **101**, 1916–1919.
- Fougerouse D., Reddy S. M., Seydoux-Guillaume A.-M., Kirkland C. L., Erickson T. M., Saxey D. W., Rickard W. D. A., Jacob D., Leroux H. and Clark C. (2021b) Mechanical twinning of monazite expels radiogenic lead. *Geology* **49**, 417–421.
- Fougerouse D., Saxey D. W., Rickard W. D. A., Reddy S. M. and Verberne R. (2021c) Standardizing Spatial Reconstruction Parameters for the Atom Probe Analysis of Common Minerals. *Microsc. Microanal.*, 1–10.
- Gibson R. L. and Reimold W. U. (2005) Shock pressure distribution in the Vredefort impact structure, South Africa. In *Large Meteorite Impacts III* (eds. T. Kenkmann, F. Hörz, and A. Deutsch). Geological Society of America. p. 0.

- Gibson R. L., Armstrong R. A. and Reimold W. U. (1997) The age and thermal evolution of the Vredefort impact structure: A single-grain U-Pb zircon study. *Geochim. Cosmochim. Acta* **61**, 1531–1540.
- Gibson R. L., Reimold W. U. and Stevens G. (1998) Thermal-metamorphic signature of an impact event in the Vredefort dome, South Africa. *Geology* **26**, 787–790.
- Grieve R. and Therriault A. (2000) Vredefort, Sudbury, Chicxulub: Three of a Kind? *Annu. Rev. Earth Planet. Sci.* **28**, 305–338.
- Gumsley A., Stamsnijder J., Larsson E., Söderlund U., Naeraa T., de Kock M., Sałacińska A., Gawęda A., Humbert F. and Ernst R. (2020) Neoproterozoic large igneous provinces on the Kaapvaal Craton in southern Africa re-define the formation of the Ventersdorp Supergroup and its temporal equivalents. *GSA Bull.* **132**, 1829–1844.
- Harrison T. M., Catlos E. J. and Montel J.-M. (2002) U-Th-Pb Dating of Phosphate Minerals. *Rev. Mineral. Geochemistry* **48**, 524–558.
- Hart R. J., Nicolaysen L. O. and Gale N. H. (1981) Radioelement concentrations in the deep profile through Precambrian basement of the Vredefort structure. *J. Geophys. Res. Solid Earth* **86**, 10639–10652.
- Hauser N., Reimold W. U., Cavosie A. J., Crósta A. P., Schwarz W. H., Trieloff M., Da Silva Maia de Souza C., Pereira L. A., Rodrigues E. N. and Brown M. (2019) Linking shock textures revealed by BSE, CL, and EBSD with U-Pb data (LA-ICP-MS and SIMS) from zircon from the Araguinha impact structure, Brazil. *Meteorit. Planet. Sci.* **54**, 2286–2311.
- Hetherington C. J., Jercinovic M. J., Williams M. L. and Mahan K. (2008) Understanding geologic processes with xenotime: Composition, chronology, and a protocol for electron probe microanalysis. *Chem. Geol.* **254**, 133–147.
- Hiraga T., Anderson I. M. and Kohlstedt D. L. (2003) Chemistry of grain boundaries in mantle rocks. *Am. Mineral.* **88**, 1015–1019.
- Hodych J. P. and Dunning G. R. (1992) Did the Manicouagan impact trigger end-of-Triassic mass extinction? *Geology* **20**, 51–54.
- Hoskin P. W. O. and Black L. P. (2000) Metamorphic zircon formation by solid-state recrystallization of protolith igneous zircon. *J. Metamorph. Geol.* **18**, 423–439.

- Jessell M. W. (1987) Grain-boundary migration microstructures in a naturally deformed quartzite. *J. Struct. Geol.* **9**, 1007–1014.
- Joseph C., Fougereuse D., Reddy S. M., Olierook H. K. H., Tacchetto T., Kennedy A., Saxey D. W., Rickard W. D. A., Denyszyn S. and Dodd A. (2023) Radiogenic Pb in xenotime trapped in nanoscale inclusions of apatite during fluid alteration. *Chem. Geol.*, 121444.
- Joseph C., Fougereuse D., Saxey D. W., Verberne R., Reddy S. M. and Rickard W. D. A. (2021) Xenotime at the Nanoscale: U-Pb Geochronology and Optimisation of Analyses by Atom Probe Tomography. *Geostand. Geoanalytical Res.* **45**, 443–456.
- Jourdan F., Reimold W. U. and Deutsch A. (2012) Dating terrestrial impact structures. *Elements* **8**, 49–53.
- Jourdan F., Renne P. R. and Reimold W. U. (2009) An appraisal of the ages of terrestrial impact structures. *Earth Planet. Sci. Lett.* **286**, 1–13.
- Kamo S. L., Lana C. and Morgan J. V (2011) U–Pb ages of shocked zircon grains link distal K–Pg boundary sites in Spain and Italy with the Chicxulub impact. *Earth Planet. Sci. Lett.* **310**, 401–408.
- Kamo S. L., Reimold W. U., Krogh T. E. and Colliston W. P. (1996) A 2.023 Ga age for the Vredefort impact event and a first report of shock metamorphosed zircons in pseudotachylitic breccias and Granophyre. *Earth Planet. Sci. Lett.* **144**, 369–387.
- Kenkmann T. (2021) The terrestrial impact crater record: A statistical analysis of morphologies, structures, ages, lithologies, and more. *Meteorit. Planet. Sci.* **56**, 1024–1070.
- Kenny G. G., Harrigan C. O., Schmitz M. D., Crowley J. L., Wall C. J., Andreoli M. A. G., Gibson R. L. and Maier W. D. (2021) Timescales of impact melt sheet crystallization and the precise age of the Morokweng impact structure, South Africa. *Earth Planet. Sci. Lett.* **567**, 117013.
- Kenny G. G., Morales L. F., Whitehouse M. J., Petrus J. A. and Kamber B. S. (2017) The formation of large neoblasts in shocked zircon and their utility in dating impacts. *Geology* **45**, 1003–1006.

- Kirkland C. L., Yakymchuk C., Szilas K., Evans N., Hollis J., McDonald B. and Gardiner N. J. (2018) Apatite: a U-Pb thermochronometer or geochronometer? *Lithos* **318–319**, 143–157.
- Lana C., Filho C. R. S., Marangoni Y. R., Yokoyama E., Trindade R. I. F., Tohver E. and Reimold W. U. (2007) Insights into the morphology, geometry, and post-impact erosion of the Araguainha peak-ring structure, central Brazil. *Geol. Soc. Am. Bull.* **119**, 1135–1150.
- Lana C., Filho C. R. S., Marangoni Y. R., Yokoyama E., Trindade R. I. F., Tohver E. and Reimold W. U. (2008) Structural evolution of the 40 km wide Araguainha impact structure, central Brazil. *Meteorit. Planet. Sci.* **43**, 701–716.
- Langenhorst F. and Deutsch A. (2012) Shock Metamorphism of Minerals. *Elements* **8**, 31–36.
- Li Q. L., Li X. H., Lan Z. W., Guo C. L., Yang Y. N., Liu Y. and Tang G. Q. (2013) Monazite and xenotime U-Th-Pb geochronology by ion microprobe: Dating highly fractionated granites at Xihuashan tungsten mine, SE China. *Contrib. to Mineral. Petrol.* **166**, 65–80.
- Ludwig K. (2012) User's manual for Isoplot/Ex: a geochronological toolkit for Microsoft Excel. Berkeley Geochronol. *Cent. Spec. Publ. 1a*, **53**.
- McGregor M., Dence M. R., McFarlane C. R. M. and Spray J. G. (2020) U–Pb geochronology of apatite and zircon from the Brent impact structure, Canada: a Late Ordovician Sandbian–Katian boundary event associated with L-Chondrite parent body disruption. *Contrib. to Mineral. Petrol.* **175**, 63.
- McGregor M., Erickson T. M., Spray J. G. and Whitehouse M. J. (2021b) High-resolution EBSD and SIMS U–Pb geochronology of zircon, titanite, and apatite: insights from the Lac La Moinerie impact structure, Canada. *Contrib. to Mineral. Petrol.* **176**, 76.
- McGregor M., McFarlane C. R. M. and Spray J. G. (2018) In situ LA-ICP-MS apatite and zircon U–Pb geochronology of the Nicholson Lake impact structure, Canada: Shock and related thermal effects. *Earth Planet. Sci. Lett.* **504**, 185–197.
- McGregor M., McFarlane C. R. M. and Spray J. G. (2019) In situ multiphase U–Pb geochronology and shock analysis of apatite, titanite and zircon from the Lac La Moinerie impact structure, Canada. *Contrib. to Mineral. Petrol.* **174**, 62.

- McGregor M., McFarlane C. R. M. and Spray J. G. (2021a) U-Pb geochronology of apatite crystallized within a terrestrial impact melt sheet: Manicouagan as a geochronometer test site eds. W. U. Reimold and C. Koeberl. *Large Meteor. Impacts Planet. Evol.* **VI** 550, 0.
- McNaughton N. J. and Rasmussen B. (2018) Geochemical characterisation of xenotime formation environments using U-Th. *Chem. Geol.* **484**, 109–119.
- McNaughton N. J., Rasmussen B. and Fletcher I. R. (1999) SHRIMP uranium-lead dating of diagenetic xenotime in siliciclastic sedimentary rocks. *Science* **285**, 78–80.
- Montalvo P. E., Cavosie A. J., Kirkland C. L., Evans N. J., McDonald B. J., Talavera C., Erickson T. M. and Lugo-Centeno C. (2019) Detrital shocked zircon provides first radiometric age constraint (<1472 Ma) for the Santa Fe impact structure, New Mexico, USA. *GSA Bull.* **131**, 845–863.
- Montalvo S. D. (2020) Development and application of atom probe tomography to complex zircon grains.
- Montalvo S. D., Reddy S. M., Saxey D. W., Rickard W. D. A., Fougereuse D., Quadir Z. and Johnson T. E. (2019) Nanoscale constraints on the shock-induced transformation of zircon to reidite. *Chem. Geol.* **507**, 85–95.
- Moser D. E. (1997) Dating the shock wave and thermal imprint of the giant Vredefort impact, South Africa. *Geology* **25**, 7–10.
- Moser D. E., Cupelli C. L., Barker I. R., Flowers R. M., Bowman J. R., Wooden J. and Hart J. R. (2011) New zircon shock phenomena and their use for dating and reconstruction of large impact structures revealed by electron nanobeam (EBSD, CL, EDS) and isotopic U-Pb and (U-Th)/he analysis of the Vredefort dome. *Can. J. Earth Sci.* **48**, 117–139.
- Ni Y., Hughes J. M. and Mariano A. N. (1995) Crystal chemistry of the monazite and xenotime structures. *Am. Mineral.* **80**, 21–26.
- O'Neill C., Marchi S., Zhang S. and Bottke W. (2017) Impact-driven subduction on the Hadean Earth. *Nat. Geosci.* **10**, 793–797.
- Osinski G. R., Cockell C. S., Pontefract A. and Sapers H. M. (2020) The Role of Meteorite Impacts in the Origin of Life. *Astrobiology* **20**, 1121–1149.

- Osinski G. R., Grieve R. A. F., Ferrière L., Losiak A., Pickersgill A. E., Cavosie A. J., Hibbard S. M., Hill P. J. A., Bermudez J. J., Marion C. L., Newman J. D. and Simpson S. L. (2022) Impact Earth: A review of the terrestrial impact record. *Earth-Science Rev.* **232**, 104112.
- Pan Y. and Fleet M. E. (2002) Compositions of the Apatite-Group Minerals: Substitution Mechanisms and Controlling Factors. *Rev. Mineral. Geochemistry* **48**, 13–49.
- Papapavlou K., Darling J. R., Moser D. E., Barker I. R., White L. F., Lightfoot P. C., Storey C. D., Dunlop J. and EIMF (2018) U–Pb isotopic dating of titanite microstructures: potential implications for the chronology and identification of large impact structures. *Contrib. to Mineral. Petrol.* **173**, 82.
- Passchier C. W. and Trouw R. A. J. (2005) *Micro-tectonics.*,
- Peterman E. M., Reddy S. M., Saxey D. W., Fougereuse D., Snoeyenbos D. R. and Rickard W. D. A. (2019) Nanoscale processes of trace element mobility in metamorphosed zircon. *Contrib. to Mineral. Petrol.* **174**, 92.
- Peterman E. M., Reddy S. M., Saxey D. W., Snoeyenbos D. R., Rickard W. D. A., Fougereuse D. and Kylander-Clark A. R. C. (2016) Nanogeochronology of discordant zircon measured by atom probe microscopy of Pb-enriched dislocation loops. *Sci. Adv.* **2**.
- Piazolo S., Austrheim H. and Whitehouse M. (2012) Brittle-ductile microfabrics in naturally deformed zircon: Deformation mechanisms and consequences for U-Pb dating. *Am. Mineral.* **97**, 1544–1563.
- Piazolo S., La Fontaine A., Trimby P., Harley S., Yang L., Armstrong R. and Cairney J. M. (2016) Deformation-induced trace element redistribution in zircon revealed using atom probe tomography. *Nat. Commun.* **7**, 1–7.
- Poirier J.-P. (1985) *Creep of Crystals: High-Temperature Deformation Processes in Metals, Ceramics and Minerals.*, Cambridge University Press, Cambridge.
- Rasmussen B. (2005) Radiometric dating of sedimentary rocks: The application of diagenetic xenotime geochronology. *Earth-Science Rev.* **68**, 197–243.
- Read A. S., Koning D. J., Smith G. A., Ralser S., Rodgers J. B. and Bauer P. A. (2000) geologic map of Santa Fe quadrangle, Santa Fe County, New Mexico New Mexico Bureau of Geology and Mineral Resources. Open-File GM 32, scale 124,000, 1 sheet.

- Reddy S. M., van Riessen A., Saxey D. W., Johnson T. E., Rickard W. D. A., Fougereuse D., Fischer S., Prosa T. J., Rice K. P., Reinhard D. A., Chen Y. and Olson D. (2016) Mechanisms of deformation-induced trace element migration in zircon resolved by atom probe and correlative microscopy. *Geochim. Cosmochim. Acta* **195**, 158–170.
- Rickard W. D. A., Reddy S. M., Saxey D. W., Fougereuse D., Timms N. E., Daly L., Peterman E., Cavosie A. J. and Jourdan F. (2020) Novel Applications of FIB-SEM-Based ToF-SIMS in Atom Probe Tomography Workflows. *Microsc. Microanal.* **26**, 750–757.
- Schmieder M. and Kring D. A. (2020) Earth's Impact Events Through Geologic Time: A List of Recommended Ages for Terrestrial Impact Structures and Deposits. *Astrobiology* **20**, 91–141.
- Schmieder M., Shaulis B. J., Lapen T. J., Buchner E. and Kring D. A. (2019) In situ U–Pb analysis of shocked zircon from the Charlevoix impact structure, Québec, Canada. *Meteorit. Planet. Sci.* **54**, 1808–1827.
- Schmieder M., Tohver E., Jourdan F., Denyszyn S. W. and Haines P. W. (2015) Zircons from the Acraman impact melt rock (South Australia): Shock metamorphism, U–Pb and $^{40}\text{Ar}/^{39}\text{Ar}$ systematics, and implications for the isotopic dating of impact events. *Geochim. Cosmochim. Acta* **161**, 71–100.
- Schneiderhan E., Zimmermann U., Gutzmer J., Mezger K. and Armstrong R. (2011) Sedimentary Provenance of the Neoproterozoic Ventersdorp Supergroup, Southern Africa: Shedding Light on the Evolution of the Kaapvaal Craton during the Neoproterozoic. *J. Geol.* **119**, 575–596.
- Schulte P., Alegret L., Arenillas I., Arz J. A., Barton P. J., Bown P. R., Bralower T. J., Christeson G. L., Claeys P., Cockell C. S., Collins G. S., Deutsch A., Goldin T. J., Goto K., Grajales-Nishimura J. M., Grieve R. A. F., Gulick S. P. S., Johnson K. R., Kiessling W., Koeberl C., Kring D. A., MacLeod K. G., Matsui T., Melosh J., Montanari A., Morgan J. V., Neal C. R., Nichols D. J., Norris R. D., Pierazzo E., Ravizza G., Rebolledo-Vieyra M., Reimold W. U., Robin E., Salge T., Speijer R. P., Sweet A. R., Urrutia-Fucugauchi J., Vajda V., Whalen M. T. and Willumsen P. S. (2010) The Chicxulub Asteroid Impact and Mass Extinction at the Cretaceous-Paleogene Boundary. *Science* **327**, 1214–1218.
- Seydoux-Guillaume A.-M., Fougereuse D., Laurent A. T., Gardés E., Reddy S. M. and Saxey D. W. (2019) Nanoscale resetting of the Th/Pb system in an isotopically-closed

- monazite grain: A combined atom probe and transmission electron microscopy study. *Geosci. Front.* **10**, 65–76.
- Shannon R. D. (1976) Revised effective ionic radii and systematic studies of interatomic distances in halides and chalcogenides. *Acta Crystallogr. Sect. A* **32**, 751–767.
- Spear F. S. and Pyle J. M. (2002) Apatite, monazite, and xenotime in metamorphic rocks (in Phosphates; geochemical, geobiological, and materials importance) Reviews in Mineralogy and Geochemistry. *Rev. Mineral. Geochemistry* **48**, 293–335.
- Stacey J. S. and Kramers J. D. (1975) Approximation of terrestrial lead isotope evolution by a two-stage model. *Earth Planet. Sci. Lett.* **26**, 207–221.
- Stöffler D., Hamann C. and Metzler K. (2018) Shock metamorphism of planetary silicate rocks and sediments: Proposal for an updated classification system. *Meteorit. Planet. Sci.* **53**, 5–49.
- Suzuki K. (1987) Grain-boundary enrichment of incompatible elements in some mantle peridotites. *Chem. Geol.* **63**, 319–334.
- Tacchetto T., Reddy S. M., Fougereuse D., Clark C., Saxey D. W. and Rickard W. D. A. (2022) Crystal plasticity enhances trace element mobility in garnet. *Geology* **50**, 1387–1392.
- Tacchetto T., Reddy S. M., Saxey D. W., Fougereuse D., Rickard W. D. A. and Clark C. (2021) Disorientation control on trace element segregation in fluid-affected low-angle boundaries in olivine. *Contrib. to Mineral. Petrol.* **176**, 1–16.
- Timms N. E., Erickson T. M., Pearce M. A., Cavosie A. J., Schmieder M., Tohver E., Reddy S. M., Zanetti M. R., Nemchin A. A. and Wittmann A. (2017) A pressure-temperature phase diagram for zircon at extreme conditions. *Earth-Science Rev.* **165**, 185–202.
- Timms N. E., Kirkland C. L., Cavosie A. J., Rae A. S. P., Rickard W. D. A., Evans N. J., Erickson T. M., Wittmann A., Ferrière L., Collins G. S. and Gulick S. P. S. (2020) Shocked titanite records Chicxulub hydrothermal alteration and impact age. *Geochim. Cosmochim. Acta* **281**, 12–30.
- Tohver E., Lana C., Cawood P. A., Fletcher I. R., Jourdan F., Sherlock S., Rasmussen B., Trindade R. I. F., Yokoyama E., Souza Filho C. R. and Marangoni Y. (2012) Geochronological constraints on the age of a Permo–Triassic impact event: U–Pb and

- 40Ar/39Ar results for the 40km Araguainha structure of central Brazil. *Geochim. Cosmochim. Acta* **86**, 214–227.
- Valley J. W., Cavosie A. J., Ushikubo T., Reinhard D. A., Lawrence D. F., Larson D. J., Clifton P. H., Kelly T. F., Wilde S. A., Moser D. E. and Spicuzza M. J. (2014) Hadean age for a post-magma-ocean zircon confirmed by atom-probe tomography. *Nat. Geosci.* **7**, 219–223.
- Vallini D. A., Rasmussen B., Krapež B., Fletcher I. R. and McNaughton N. J. (2005) Microtextures, geochemistry and geochronology of authigenic xenotime: Constraining the cementation history of a Palaeoproterozoic metasedimentary sequence. *Sedimentology* **52**, 101–122.
- Van Emden B., Thornber M. R., Graham J. and Lincoln F. J. (1997) The incorporation of actinides in monazite and xenotime from placer deposits in Western Australia. *Can. Mineral.* **35**, 95–104.
- Verberne R., Reddy S. M., Saxey D. W., Fougereuse D., Rickard W. D. A., Plavsá D., Agangi A. and Kylander-Clark A. R. C. (2020) The geochemical and geochronological implications of nanoscale trace-element clusters in rutile. *Geology* **XX**, 1–5.
- Verberne R., Reddy S. M., Saxey D. W., Fougereuse D., Rickard W. D. A., Quadir Z., Evans N. J. and Clark C. (2022) Dislocations in minerals: Fast-diffusion pathways or trace-element traps? *Earth Planet. Sci. Lett.* **584**, 117517.
- Vermeesch P. (2018) IsoplotR: A free and open toolbox for geochronology. *Geosci. Front.* **9**, 1479–1493.
- Watanabe T. (1985) Structural effects on grain boundary segregation, hardening and fracture. *Le J. Phys. Colloq.* **46**, C4-555-C4-566.
- White L. F., Darling J. R., Moser D. E., Reinhard D. A., Prosa T. J., Bullen D., Olson D., Larson D. J., Lawrence D. and Martin I. (2017) Atomic-scale age resolution of planetary events. *Nat. Commun.* **8**, 1–6.
- Williams C. A., Haley D., Marquis E. A., Smith G. D. W. and Moody M. P. (2013) Defining clusters in APT reconstructions of ODS steels. *Ultramicroscopy* **132**, 271–278.
- Williams M. L., Jercinovic M. J., Harlov D. E., Budzyń B. and Hetherington C. J. (2011) Resetting monazite ages during fluid-related alteration. *Chem. Geol.* **283**, 218–225.

Synthesis and future work

This PhD project aimed to identify and understand mineralogical processes that impact geochronometers at the nanoscale. The project focused on the nanoscale geochemical behavior of the mineral xenotime and their implications in geochronology. This was achieved using a multi-scale approach and employing microanalytical techniques for characterising the sample before nanoscale analysis, including SEM imaging, SEM-EBSD, SHRIMP, EPMA, followed by nanoscale analysis using APT and TEM.

A methods chapter has been included, putting forward a new nanogeochronology method for dating and optimising APT analysis of xenotime. Following these newly developed methods, three case studies were selected from different geological contexts to comprehensively study the mineral xenotime and its implications in geochronology and other geochronometers. The significant outcomes of the project are summarised in this final chapter.

6.1 Optimisation of xenotime analysis using APT and nanogeochronology method.

Optimisation of xenotime analysis in APT was vital given that xenotime has never been analysed in APT before. Four standards, BS-1, MG-1, xtc and Y1 were selected for xenotime analysis (Fletcher et al., 2000, 2004; Stern and Rayner, 2003). The electric field, background, single hits percentage are lower at higher laser pulse energies, which directly equates to specimen yield (Joseph et al., 2021). Based on the findings from the study, it is advisable to use laser pulse energies in the range of 100 – 200 pJ in order to ensure good geochronology data, even though parameters such as general background, single hits percentage and electric field are ideal at higher laser pulse energies. A laser pulse frequency of 125 kHz is suggested to acquire all the peaks in xenotime up to 300 Da.

The geochronology component of this chapter included developing U-Pb and Pb-Pb methods of dating. This had not been done using APT in any other phases (e.g. zircon, monazite) due to isobaric interferences (Saxey et al., 2017; Fougereuse et al., 2020). In the case of U-Pb geochronology, the ^{238}U peaks were distributed in five peaks $^{238}\text{UO}_2^{2+}$ (135.02 Da), $^{238}\text{UO}^{2+}$ (127.02 Da), $^{238}\text{UO}^{3+}$ (84.68 Da), $^{238}\text{UO}^{2+}$ (270.04 Da) and $^{238}\text{UO}^{3+}$ (286.04 Da). Due to this spread of peaks and location of $^{238}\text{UO}^{3+}$ (84.68 Da) in the peak tail of YPO_3^{2+} , direct dating of U-Pb was challenging. Therefore, a fractionation correction method was employed. A linear correlation was determined between $\text{UO}_2^{2+}/\text{UO}^{2+}$ ratio and $^{206}\text{Pb}^{2+}/^{238}\text{UO}_2^{2+}$

fractionation coefficient, forming an equation $y = 12.06(\pm 0.621)x + 27.442(\pm 0.826)$. This method allows us to date samples of different compositions, age, and also correct for extrinsic instrumental parameters such as laser energy but also intrinsic parameters such as specimen geometry and voltage range. By taking weighted mean ages from multiple analyses the uncertainties associated can be reduced from ~10% to ~3-5%.

In the case of Pb-Pb ages, the main Pb peaks were found at 2+ charge state in the mass spectra, ($^{206}\text{Pb}^{2+}$ at 102.9 Da and $^{207}\text{Pb}^{2+}$ at 103.49 Da). The accuracy and precision of Pb-Pb dating is dependent on accurate characterisation of peaks. There are two main challenges on Pb-Pb dating of xenotime using APT. First, if the sample is older or has higher ^{206}Pb , the thermal tail of $^{206}\text{Pb}^{2+}$ overlaps the $^{207}\text{Pb}^{2+}$ peak, yielding erroneous old ages. The thermal peak tail of ^{206}Pb peak on ^{207}Pb peak is found to be higher at high laser pulse energies. The second challenge is the influence of ThPO_3^{3+} peak on $^{207}\text{Pb}^{2+}$ peak, if the sample contains high Th and therefore bigger ThPO_3^{3+} peak, it tends to increase the $^{207}\text{Pb}^{2+}$ counts by possible interference. Furthermore, ThPO_3^{3+} counts are greater at higher laser pulse energies. If the $^{207}\text{Pb}^{2+}$ counts are clearly above the background, and no thermal tail influence of ^{206}Pb is encountered, a constant background estimation can be applied to find the $^{207}\text{Pb}/^{206}\text{Pb}$ ages from xenotime. However, if the thermal tail of the ^{206}Pb peak is pronounced, a variable background correction method was developed to alleviate this challenge (Joseph et al., 2021). The effect of ThPO_3^{3+} still needs to be constrained, and for igneous samples with high Th concentration, the ThPO_3^{3+} peak impacted Pb-Pb ages.

Xenotime nanogeochronology method using APT can be used successfully on rocks containing high actinide content, commonly igneous rocks and xenotime from U-rich hydrothermal environments and metamorphic rocks. Diagenetic xenotime with lowest actinide content will not be ideal candidate for APT dating.

6.2 Pb mobility mechanisms in xenotime: insights from nanoscale analysis

Understanding the reasons behind the decoupling of parent-daughter isotopes is the primary challenge of a geochronologist, as in nature, it is more common for the mineral system to be unstable than stable. Previous nanoscale analyses of geochronometers have shown that these phases are even more complex in nanoscale, and different mineralogical mechanisms are causing these heterogeneities in minerals, including parent-daughter redistribution (Reddy et al., 2020). As previously mentioned, it is important to identify the mineralogical processes causing the heterogeneity in geochronometers for better data interpretation. From the case

studies presented in the thesis on xenotime, three main Pb* mobility mechanisms have been recognised, such as fluid activity, phase immiscibility and recrystallisation.

6.2.1 Fluid activity

Xenotime is regarded to be resilient to fluid alteration, especially when compared to monazite with comparable chemistry and structure (Harrison et al., 2002; Budzyń and Kozub-Budzyń, 2015). However, case studies on xenotime samples affected by fluid alteration show redistribution of Pb* in the form of Ca-Pb* apatite inclusions in the nanoscale. Samples studied in the project from chapter three and four are from igneous pegmatite and show fluid-assisted dissolution-precipitation textures in BSE imaging. SHRIMP U-Pb geochronology does not correlate with the textures observed, indicating the grain remained closed on the micron scale. Atom probe analysis was conducted on mineral zones with no evident fluid-related textures. In the case of sample z6413 (chapter three), dislocation enriched in elements such as Cl, Na, and Li are present inside the crystal lattice, indicative of fluid activity (Tacchetto et al., 2021). Furthermore, the Pb* concentration in apatite inclusions is up to ~7 at. %, indicating the process occurred later in the geological history of the grain. The second generation of apatite inclusions from sample Y1 (chapter four) also shows similar Pb* concentration in the apatite inclusions, even though the number of inclusions is fewer than sample z6413. This is attributed to pervasive fluid activity in the crystal, which is responsible for forming apatite inclusions in xenotime, thereby redistributing Pb*. Presence of fluid in the system can dramatically change the nature and extent of mass transfer processes in rocks as well as in minerals, reducing the kinetic barriers for the movement of atoms (Putnis, 2002). Based on the observations, the Pb* is getting trapped in apatite inclusions, which prevents Pb* from being lost from the crystal lattice. The entrapment of Pb* in inclusions suggests a closed system in microscale, and a pervasive fluid alteration event which does not get recognised by the conventional microanalytical techniques. This in turn explains the characterization of xenotime as a fluid resistant mineral (Joseph et al., 2023).

From the analysis of shocked xenotime sample from Vredefort, SHRIMP U-Pb lower intercept discordia age (1803 ± 270 Ma) corresponds to a basin-wide fluid alteration event in the Witwatersrand basin. The nanoscale study of the sample shows the presence of fluid-related ions (OH, Cl, Al, and Na) in dislocations and low-angle boundaries. Furthermore, Pb* enriched apatite inclusions were also present. The whole needle U-Pb nanogeochronology of the specimens studied from the grain gave an age (1596 ± 93 Ma) consistent with SHRIMP fluid alteration event ages. In this case, evidence of pervasive fluid activity can be found in the

nanoscale, which facilitated the Pb* mobility and the whole phase reset both in micro and nanoscale. High P-T shock metamorphism must have created abundant defects and fractures in the crystal, facilitating the fluid flow leading to the complete resetting of the grain, removing any impact isotope signature.

6.2.2 Phase immiscibility

A case study on a high impurity (Ca) sample in chapter four recognised another Pb* mobility mechanism in xenotime, phase immiscibility. Xenotime has a tight, well-ordered tetragonal crystal structure, in which the cation site is occupied by small 3+ ions of Y or HREE. The larger Ca²⁺, which is not a constituent ion in xenotime, gets incorporated by the cheralite coupled substitution process $(\text{Th/U})^{4+} + \text{Ca}^{2+} = 2\text{REE}^{3+}$ into the xenotime structure during its formation. Due to the similarity in ionic sizes, Ca is seen coupled with Pb in xenotime in almost all cases. Therefore, Ca concentration can influence the behaviour of Pb* in xenotime. In the case study (chapter four, Y1 and Fanad metamorphic xenotime), two samples are compared; one pegmatite xenotime sample with a high Ca concentration with no post-metamorphic history, and another sample with a low Ca concentration affected by later high-temperature metamorphism. Despite undergoing high-temperature metamorphism, the sample did not experience any redistribution of calcium (Ca) or lead (Pb*). However, the sample with high Ca concentration (Y1) showed two generations of apatite inclusions, differentiated by low and high Pb* content. The high concentration of Ca creates lattice strain in the crystal lattice due to its large size and tends to exsolve during cooling along with Pb, which is forming inside the crystal. The faster cooling rate of the pegmatite xenotime also must have assisted the exsolution of the apatite inclusions. The apatite inclusions formed during the cooling of the crystal can later act as traps to Pb* in later geological events, such as fluid activity forming the Pb* enriched apatite inclusions.

6.2.3 Recrystallisation

Chapter five provides an in-depth study of xenotime in shock deformation settings by studying samples from three impact structures. Combining the techniques SEM-EBSD and SHRIMP. Recrystallised neoblastic texture, an impact-related microstructure, has been identified in xenotime for the first time in this study. The degree of recrystallisation is correlated with the degree of resetting of the U-Pb system, yielding the impact age from fully recrystallised xenotime grain from the Araguinha impact structure. EBSD GROD angle map of the impact age generated grain generally show no misorientation in the neoblasts (strain-free

neoblasts). However, a few per cent of the neoblasts show internal misorientation, and grains with no misorientation have grown into neoblasts with high misorientation, forming a lobate texture (Passchier and Trouw, 2005). Atom probe analysis on a grain boundary between the neoblasts showing lobate textures shows a difference in chemistry (Si-Mg cluster variation) between two neoblasts. The grain with no misorientation has fewer Si-Mg clusters compared to a grain with high misorientation. The grain boundary is enriched in various elements such as Si, Ca, Mg, Al, Na, and Cl. The presence of elements Si, Ca, and Mg, which are not inherently part of the xenotime structure, must have migrated to the grain boundary during recrystallization to reduce the lattice strain caused by bigger ions (Reddy et al., 2016). The observations from EBSD data and APT data lead to the process of grain boundary migration for the formation of the neoblasts, in which grain with no misorientation grows into the grain with high misorientation and reflects in the chemistry of the specimens. During this process, it is implied that Pb is also moved to the grain boundary and diffused to the grain edges, facilitating the complete resetting of the grain. From the studied grains, where recrystallisation is not fully achieved, for example, grain X2 from Araguainha, mixed U-Pb ages are derived, indicating partial Pb loss.

6.3 Geochronometers in nanoscale: a revisit

This thesis explored the geochemical behaviour of xenotime from different geological contexts and identified different mechanisms causing the redistribution of radiogenic isotopes and other trace elements. However, combining the research outputs from this thesis and previous nanoscale studies on the geochronometers, some general observations can be made on Pb* mobility mechanisms.

Nanoscale studies on phosphates, particularly extensive studies have made on the mineral monazite (Laurent et al., 2016; Seydoux- Guillaume et al., 2018; Fougrouse et al., 2018, 2021a, 2021b; Seydoux-Guillaume et al., 2019; Turuani et al., 2022; Grand'Homme et al., 2018). Other phosphates, such as apatite nanoscale studies have only made in extra-terrestrial samples, lunar and martian meteorites and not discussed here (Černok et al., 2019, 2021; Darling et al., 2021). Fluid assisted dissolution reprecipitation reactions have shown to facilitate Pb* redistribution in monazite, similar to the findings from this thesis (Grand'Homme et al., 2018; Fougrouse et al., 2021a; Turuani et al., 2022). Partial retention of Pb* in Pb* nanocrystals (galena) formed during fluid assisted coupled dissolution reprecipitation process are proposed to be responsible for discordant data in monazite (Turuani et al., 2022). In case of xenotime sample z6413 (chapter three) the Pb* is fully retained in apatite inclusions making

the grain closed system in grain scale. Recent study on shocked monazite from Vredefort impact structure showed formation of britholite inclusions, containing Pb* upto ~8 at. % [(REE,Ca,Pb)₅((Si, P)O₄)₃OH] as a result of fluid alteration (Fougerouse et al., 2021a). Both these cases is similar to the apatite inclusions formed in xenotime due to fluid alteration. Particularly xenotime from the Vredefort impact structure (Chapter five) showed formation of apatite inclusions, and the U-Pb ages are consistent with britholite formation in monazite and SHRIMP U-Pb ages for the fluid alteration event (1803±270 Ma). It is to be noted that the fluid alteration event is only recorded in the phosphates from the Vredefort impact structure and not recorded in any other phases (Cavosie et al., 2021; Fougerouse et al., 2021).

Phase immiscibility, the process of exsolution of phases during temperature change, has been reported to redistribute Pb* in monazite, similar to the findings on sample Y1 (chapter four). In this particular model, the impurity content in the mineral phase is the driving factor for exsolution that can occur during cooling (Putnis, 1992; Ferraris et al., 2005) or subsequent heating after fast cooling (Putnis, 1978). In monazite, apatite inclusions are formed due to exsolution from a metamorphic monazite sample during cooling (Fougerouse et al., 2018). Similar to this, metamorphic monazite from UHT zone osumilite gneiss from Rogaland (S-Norway) has reported Ca-S-Pb* clusters to form as a result of exsolution during cooling (Seydoux-Guillaume et al., 2019). It is observed that the Ca content in the clusters or phases exsolved that also contain the radiogenic Pb* is a common factor. Ca is incorporated into both xenotime and monazite via cheralite substitution $\text{Ca}^{2+}+(\text{Th/U})^{4+}=2\text{REE}^{3+}$ (Spear and Pyle, 2002). Due to the similarity of Ca (1.12 Å) and Pb (1.29 Å) in ionic sizes of 2+ ions, their behaviour in geological settings is also similar (Shannon, 1976). Therefore as stated in chapter four, the Ca and Pb mobility is interlinked. Provided the Ca content in the sample is high, the chances of exsolution and consequent Pb* mobility are highly likely. Based on the crystal structure, monazite has a less ordered monoclinic structure and therefore cheralite substitution is more favoured (Ni et al., 1995; Spear and Pyle, 2002). In the case of xenotime, huttonite substitution $[(\text{Th/U})^{4+}+\text{Si}^{4+}=\text{REE}^{3+}+\text{P}^{5+}]$ is more favourable, owing to the tight tetragonal crystal structure (Ni et al., 1995; Spear and Pyle, 2002). Therefore, high levels of Ca likely get incorporated more into monazite and drive Pb* mobility. However, the Ca or any other trace element incorporation into a phase is determined by its crystallising environment (Förster, 1998, 2006).

Recrystallisation as a means of Pb* mobility has been shown in many geochronometers. Especially in shock-deformed settings, recrystallised granular neoblastic zircon and monazite are the prime candidates for impact geochronology (Moser et al., 2011; Erickson et al., 2017;

Kenny et al., 2017; Cavosie et al., 2018; Erickson et al., 2020). The formation of neoblasts is particularly related to a high T environment post-impact (Moser et al., 2011). The unequivocal high pressure from the initial impact will form lattice deformation in minerals, and high temperature, followed by the impact by the formation of melt sheets, provides ambient temperature for the crystal to be healed and recrystallised, facilitating processes such as grain boundary migration (chapter 5). This high temperature will facilitate faster Pb mobility and eventually partial to total Pb loss through grain boundaries.

Previous nanoscale analysis of minerals, especially studies on zircon and rutile, has shown the effect of radiation damage and high-temperature metamorphism on Pb* mobility (Valley et al., 2014, 2015; Peterman et al., 2016, 2019, 2021; Verberne et al., 2020). The radiation damage in zircon traps Pb*, which diffuses to the damaged site during high-temperature metamorphism (Valley et al., 2014, 2015; Peterman et al., 2016, 2019). In the case of xenotime, the effect of high-temperature metamorphism on contact metamorphic xenotime from Fanad contact aureole was tested in this project (chapter four), and no heterogeneity in either Ca or Pb* was observed. This observation is consistent with the fact that xenotime is resistant to radiation damage, owing to its lower activation energy for annealing compared to zircon and slow Pb diffusion (Lenz et al., 2019, Cherniak 2006). In zircon, the Pb* mobility is enhanced by diffusion through interconnected radiation damage sites (Utsunomiya et al., 2004). However, quick annealing of the damaged sites and slower diffusion of Pb in xenotime hinders Pb* mobility in high temperature (chapter four). Therefore, the response of xenotime to high-temperature metamorphism differs from previous studies on geochronometers.

6.4 Scope of future work

This thesis investigated nanoscale geochemistry of xenotime, with the purpose of understanding the mineral as a geochronometer. Moreover, extrapolating the information to better understand the behavior of other geochronometers (e.g., zircon and monazite). However, the following points have been identified from the current state of knowledge which can be considered for future study.

- In chapter 2, methods were developed for U-Pb and Pb-Pb geochronology using APT. One of the major challenges remaining is the characterisation and quantification of ThPO₃ peak on to ²⁰⁷Pb peak. Since the Th content was high in pegmatite xenotime (chapter 3), Pb-Pb dating couldn't be employed in that sample. Investigating this issue will be crucial in Pb-Pb dating of xenotime using APT, especially in dating high Th

samples (commonly of igneous origin). Of particular interest, the development of energy sensitive detectors could offer the opportunity to discriminate and deconvolve doubly and triply charged ionic species. This could potentially remove entirely the ThPO_3^{3+} peak from the $^{207}\text{Pb}^{2+}$ peak.

- Xenotime dating to find diagenetic ages is a major application of xenotime geochronology. However, with the current chemical sensitivity of APT, obtaining peaks for nanogeochronology of diagenetic xenotime with lower U content is difficult to achieve. If the chemical sensitivity of the instrument can enhance and better background reduction in the mass spectrum, diagenetic xenotime ages can be constrained using APT. This would be particularly useful given the innate nature of diagenetic xenotime to form small grain outgrowths ($\sim 5 \mu\text{m}$) around zircon, is an obstacle to conventional techniques. As a general point, reducing the background in the mass spectrum will enhance the quality of data and broaden application of the method.
- The mass spectrum of xenotime is really complex, because of the presence of REEs. They combine with O, P and form complex molecules and present in different charge states. Deconvolving all the peaks, with background correction is almost impossible with our current state of knowledge. If we could confidently quantify these peaks, it can be used to ascertain the origin of an unknown xenotime grain from REE pattern. Therefore, both analytical and software improvements on deconvolving complex mass spectrum from APT analysis is a future task.
- In chapter three, nanoscale analysis of xenotime sample showed evidence of fluid activity beyond the textural domain of fluid alteration identified by conventional microscale imaging techniques. This questions the belief that “homogenous” appearing domains imaged by microscale imaging techniques, whether it is really homogeneous? What is the extent of fluid activity in minerals? More nanoscale analysis on fluid altered mineral phases is required to answer these questions. This could have major implications in geochronology as fluid activity is a common geological phenomenon affecting minerals.

Furthermore, due to time and analytical constraints, nanoscale analysis could only be done on domain beyond fluid alteration (Chapter 3). It would be beneficial to also have data from the altered domains in the sample to compare the results.

- In chapter five, nanoscale analyses of twins from the shocked xenotime grains showed an indication of impact related Pb^* mobility, in which Pb^* enriched clusters were only

present in twins and not in the host. Furthermore, twins in Vredefort xenotime yielded impact ages, however high uncertainty associated precluded any definitive conclusion. Shock deformed twins from monazite has shown to yield impact age using APT (Denis Fougrouse et al., 2021a). Therefore, analysis of more shocked xenotime twins using atom probe tomography will help us to define if there is any connection between nanoscale resetting and twin formation. This would be a major finding and would aid future work in constraining impact ages from micro twins from xenotime, which would not be reflected in conventional analytical techniques.

- EBSD microstructural analysis of shocked xenotime grains from Araguainha showed neoblastic texture, in which grain AR 02 showed lineation of neoblasts and fabric development in analysis. The speculation is that this fabric development could be associated with a high-pressure phase of xenotime, like in zircon (zircon-reidite). Hence more studies on this aspect (e.g., whether there is a high-pressure phase of xenotime) would help better constrain the physical conditions of impact events.
- More analysis on xenotime from different impact locations are necessary to better constrain the shock deformation of xenotime and its geochronological implications.

6.5 References

- Budzyń B. and Kozub-Budzyń G. (2015) The stability of xenotime in high Ca and Ca-Na systems, under experimental conditions of 250-350°C and 200-400 MPa: the implications for fluid-mediated low-temperature processes in granitic rocks. *Geol. Q.* **59**, 316–324.
- Cavosie A. J., Kirkland C. L., Reddy S. M., Timms N. E., Talavera C. and Pincus M. R. (2021) Extreme plastic deformation and subsequent Pb loss in shocked xenotime from the Vredefort Dome, South Africa eds. W. U. Reimold and C. Koeberl. *Large Meteor. Impacts Planet. Evol. VI* **550**, 0.
- Cavosie A. J., Timms N. E., Ferrière L. and Rochette P. (2018) FRIGN zircon-The only terrestrial mineral diagnostic of high-pressure and high-temperature shock deformation. *Geology* **46**, 891–894.
- Černok A., White L. F., Anand M., Tait K. T., Darling J. R., Whitehouse M., Miljković K., Lemelin M., Reddy S. M., Fougereuse D., Rickard W. D. A., Saxey D. W. and Ghent R. (2021) Lunar samples record an impact 4.2 billion years ago that may have formed the Serenitatis Basin. *Commun. Earth Environ.* **2**, 120.
- Černok A., White L. F., Darling J., Dunlop J. and Anand M. (2019) Shock-induced microtextures in lunar apatite and merrillite. *Meteorit. Planet. Sci.* **54**, 1262–1282.
- Cherniak D. J. (2006) Pb and rare earth element diffusion in xenotime. *Lithos* **88**, 1–14.
- Darling J. R., White L. F., Kizovski T., Černok A., Moser D. E., Tait K. T., Dunlop J., Langelier B., Douglas J. O., Zhao X., Franchi I. A. and Anand M. (2021) The shocking state of apatite and merrillite in shergottite Northwest Africa 5298 and extreme nanoscale chlorine isotope variability revealed by atom probe tomography. *Geochim. Cosmochim. Acta* **293**, 422–437.
- Erickson T. M., Kirkland C. L., Timms N. E., Cavosie A. J. and Davison T. M. (2020) Precise radiometric age establishes Yarrabubba, Western Australia, as Earth's oldest recognised meteorite impact structure. *Nat. Commun.* **11**, 300.
- Erickson T. M., Timms N. E., Kirkland C. L., Tohver E., Cavosie A. J., Pearce M. A. and Reddy S. M. (2017) Shocked monazite chronometry: integrating microstructural and in situ isotopic age data for determining precise impact ages. *Contrib. to Mineral. Petrol.*

- Ferraris C., White T. J., Plévert J. and Wegner R. (2005) Nanometric modulation in apatite. *Phys. Chem. Miner.* **32**, 485–492.
- Fletcher I. R., McNaughton N. J., Aleinikoff J. A., Rasmussen B. and Kamo S. L. (2004) Improved calibration procedures and new standards for U - Pb and Th - Pb dating of Phanerozoic xenotime by ion microprobe. *Chem. Geol.* **209**, 295–314.
- Fletcher I. R., Rasmussen B. and McNaughton N. J. (2000) SHRIMP U-Pb geochronology of authigenic xenotime and its potential for dating sedimentary basins. *Aust. J. Earth Sci.* **47**, 845–859.
- Förster H. J. (2006) Composition and origin of intermediate solid solutions in the system thorite-xenotime-zircon-coffinite. *Lithos* **88**, 35–55.
- Förster H. J. (1998) The chemical composition of REE-Y-Th-U-rich accessory minerals in peraluminous granites of the Erzgebirge-Fichtelgebirge region, Germany. Part II: Xenotime. *Am. Mineral.* **83**, 1302–1315.
- Fougerouse D., Cavosie A. J., Erickson T., Reddy S. M., Cox M. A., Saxey D. W., Rickard W. D. A. and Wingate M. T. D. (2021a) A new method for dating impact events – Thermal dependency on nanoscale Pb mobility in monazite shock twins. *Geochim. Cosmochim. Acta* **314**, 381–396.
- Fougerouse D., Kirkland C. L., Saxey D. W., Seydoux-Guillaume A., Rowles M. R., Rickard W. D. A. and Reddy S. M. (2020) Nanoscale Isotopic Dating of Monazite. *Geostand. Geoanalytical Res.* **44**, 637–652.
- Fougerouse D., Reddy S. M., Saxey D. W., Erickson T. M., Kirkland C. L., Rickard W. D. A., Seydoux-Guillaume A.-M., Clark C. and Buick I. S. (2018) Nanoscale distribution of Pb in monazite revealed by atom probe microscopy. *Chem. Geol.* **479**, 251–258.
- Fougerouse D., Reddy S. M., Seydoux-Guillaume A.-M., Kirkland C. L., Erickson T. M., Saxey D. W., Rickard W. D. A., Jacob D., Leroux H. and Clark C. (2021b) Mechanical twinning of monazite expels radiogenic lead. *Geology* **49**, 417–421.
- Grand’Homme A., Janots E., Seydoux-Guillaume A. M., Guillaume D., Magnin V., Hövelmann J., Höschen C. and Boiron M. C. (2018) Mass transport and fractionation during monazite alteration by anisotropic replacement. *Chem. Geol.* **484**, 51–68.

- Harrison T. M., Catlos E. J. and Montel J.-M. (2002) U-Th-Pb Dating of Phosphate Minerals. *Rev. Mineral. Geochemistry* **48**, 524–558.
- Joseph C., Fougereuse D., Saxey D. W., Verberne R., Reddy S. M. and Rickard W. D. A. (2021) Xenotime at the Nanoscale: U-Pb Geochronology and Optimisation of Analyses by Atom Probe Tomography. *Geostand. Geoanalytical Res.* **45**, 443–456.
- Joseph C., Fougereuse D., Reddy S. M., Olierook H. K. H., Tacchetto T., Kennedy A., Saxey D. W., Rickard W. D. A., Denyszyn S. and Dodd A. (2023) Radiogenic Pb in xenotime trapped in nanoscale inclusions of apatite during fluid alteration. *Chem. Geol.*, 121444.
- Kenny G. G., Morales L. F., Whitehouse M. J., Petrus J. A. and Kamber B. S. (2017) The formation of large neoblasts in shocked zircon and their utility in dating impacts. *Geology* **45**, 1003–1006.
- Laurent A. T., Seydoux-Guillaume A.-M., Duchene S., Bingen B., Bosse V. and Datas L. (2016) Sulphate incorporation in monazite lattice and dating the cycle of sulphur in metamorphic belts. *Contrib. to Mineral. Petrol.* **171**, 94.
- Lenz C., Thorogood G., Aughterson R., Ionescu M., Gregg D. J., Davis J. and Lumpkin G. R. (2019) The Quantification of Radiation Damage in Orthophosphates Using Confocal μ -Luminescence Spectroscopy of Nd³⁺. *Front. Chem.* **7**.
- Moser D. E., Cupelli C. L., Barker I. R., Flowers R. M., Bowman J. R., Wooden J. and Hart J. R. (2011) New zircon shock phenomena and their use for dating and reconstruction of large impact structures revealed by electron nanobeam (EBSD, CL, EDS) and isotopic U-Pb and (U-Th)/he analysis of the vredefort dome. *Can. J. Earth Sci.* **48**, 117–139.
- Ni, Y., Hughes, J.M., Mariano, A.N., 1995. Crystal chemistry of the monazite and xenotime structures. *Am. Mineral.* **80**, 21–26. <https://doi.org/10.2138/am-1995-1-203>
- Passchier C. W. and Trouw R. A. J. (2005) *Micro-tectonics.*,
- Peterman E. M., Reddy S. M., Saxey D. W., Fougereuse D., Quadir M. Z. and Jercinovic M. J. (2021) Trace-element segregation to dislocation loops in experimentally heated zircon. *Am. Mineral.* **106**, 1971–1979.
- Peterman E. M., Reddy S. M., Saxey D. W., Fougereuse D., Snoeyenbos D. R. and Rickard W. D. A. (2019) Nanoscale processes of trace element mobility in metamorphosed zircon. *Contrib. to Mineral. Petrol.* **174**, 92.

- Peterman E. M., Reddy S. M., Saxey D. W., Snoeyenbos D. R., Rickard W. D. A., Fougrouse D. and Kylander-Clark A. R. C. (2016) Nanogeochronology of discordant zircon measured by atom probe microscopy of Pb-enriched dislocation loops. *Sci. Adv.* **2**.
- Putnis A. (1992) *An Introduction to Mineral Sciences.*, Cambridge University Press.
- Putnis A. (2002) Mineral replacement reactions: from macroscopic observations to microscopic mechanisms. *Mineral. Mag.* **66**, 689–708.
- Putnis A. (1978) The mechanism of exsolution of hematite from iron-bearing rutile. *Phys. Chem. Miner.* **3**, 183–197.
- Reddy S. M., van Riessen A., Saxey D. W., Johnson T. E., Rickard W. D. A., Fougrouse D., Fischer S., Prosa T. J., Rice K. P., Reinhard D. A., Chen Y. and Olson D. (2016) Mechanisms of deformation-induced trace element migration in zircon resolved by atom probe and correlative microscopy. *Geochim. Cosmochim. Acta* **195**, 158–170.
- Reddy S. M., Saxey D. W., Rickard W. D. A., Fougrouse D., Montalvo S. D., Verberne R. and van Riessen A. (2020) Atom Probe Tomography: Development and Application to the Geosciences. *Geostand. Geoanalytical Res.* **44**, 5–50.
- Saxey D. W., Reddy S. M., Fougrouse D. and Rickard W. D. A. (2017) The Optimization of Zircon Analyses by Laser-Assisted Atom Probe Microscopy. In *Microstructural Geochronology: Planetary Records Down to Atom Scale* pp. 293–313.
- Seydoux-Guillaume A. M., Deschanelsls X., Baumier C., Neumeier S., Weber W. J. and Peugot S. (2018) Why natural monazite never becomes amorphous: Experimental evidence for alpha self-healing. *Am. Mineral.* **103**, 824–827.
- Seydoux-Guillaume A.-M., Fougrouse D., Laurent A. T., Gardés E., Reddy S. M. and Saxey D. W. (2019) Nanoscale resetting of the Th/Pb system in an isotopically-closed monazite grain: A combined atom probe and transmission electron microscopy study. *Geosci. Front.* **10**, 65–76.
- Shannon R. D. (1976) Revised effective ionic radii and systematic studies of interatomic distances in halides and chalcogenides. *Acta Crystallogr. Sect. A* **32**, 751–767.
- Spear F. S. and Pyle J. M. (2002) Apatite, monazite, and xenotime in metamorphic rocks (in Phosphates; geochemical, geobiological, and materials importance) Reviews in Mineralogy and Geochemistry. *Rev. Mineral. Geochemistry* **48**, 293–335.

- Stern R. A. and Rayner N. (2003) *Ages of several xenotime megacrysts by ID-TIMS: potential reference materials for ion microprobe U-Pb geochronology.*
- Tacchetto T., Reddy S. M., Saxey D. W., Fougereuse D., Rickard W. D. A. and Clark C. (2021) Disorientation control on trace element segregation in fluid-affected low-angle boundaries in olivine. *Contrib. to Mineral. Petrol.* **176**, 59.
- Turuani M. J., Laurent A. T., Seydoux-Guillaume A.-M., Fougereuse D., Saxey D., Reddy S. M., Harley S. L., Reynaud S. and Rickard W. D. A. (2022) Partial retention of radiogenic Pb in galena nanocrystals explains discordance in monazite from Napier Complex (Antarctica). *Earth Planet. Sci. Lett.* **588**, 117567.
- Utsunomiya S., Palenik C. S., Valley J. W., Cavosie A. J., Wilde S. A. and Ewing R. C. (2004) Nanoscale occurrence of Pb in an Archean zircon. *Geochim. Cosmochim. Acta* **68**, 4679–4686.
- Valley J. W., Cavosie A. J., Ushikubo T., Reinhard D. A., Lawrence D. F., Larson D. J., Clifton P. H., Kelly T. F., Wilde S. A., Moser D. E. and Spicuzza M. J. (2014) Hadean age for a post-magma-ocean zircon confirmed by atom-probe tomography. *Nat. Geosci.* **7**, 219–223.
- Valley J. W., Reinhard D. A., Cavosie A. J., Ushikubo T., Lawrence D. F., Larson D. J., Kelly T. F., Snoeyenbos D. R. and Strickland A. (2015) Presidential Address. Nano- and micro-geochronology in Hadean and Archean zircons by atom-probe tomography and SIMS: New tools for old minerals. *Am. Mineral.* **100**, 1355–1377.
- Verberne R., Reddy S. M., Saxey D. W., Fougereuse D., Rickard W. D. A., Plavsa D., Agangi A. and Kylander-Clark A. R. C. (2020) The geochemical and geochronological implications of nanoscale trace-element clusters in rutile. *Geology* **XX**, 1–5.

Bibliography

- Aleinikoff J. N., Hayes T. S., Evans K. V., Mazdab F. K., Pillers R. M. and Fanning C. M. (2012a) SHRIMP U-Pb ages of Xenotime and monazite from the Spar Lake red bed-associated Cu-Ag deposit, western Montana: Implications for ore genesis. *Econ. Geol.* **107**, 1251–1274.
- Aleinikoff J. N., Lack J. F. S., Lund K., Evans K. V., Fanning C. M., Mazdab F. K., Wooden J. L. and Pillers R. M. (2012b) Constraints on the timing of Co-Cu ± Au mineralization in the Blackbird district, Idaho, using SHRIMP U-Pb ages of monazite and xenotime plus zircon ages of related Mesoproterozoic orthogneisses and metasedimentary rocks. *Econ. Geol.* **107**, 1143–1175.
- Aleinikoff J. N., Lund K. and Fanning C. M. (2015) SHRIMP U-Pb and REE data pertaining to the origins of xenotime in belt supergroup rocks: Evidence for ages of deposition, hydrothermal alteration, and metamorphism. *Can. J. Earth Sci.* **52**, 722–745.
- Altermann W. and Lenhardt N. (2012) The volcano-sedimentary succession of the Archean Sodium Group, Ventersdorp Supergroup, South Africa: Volcanology, sedimentology and geochemistry. *Precambrian Res.* **214–215**, 60–81.
- Amlı R. (1975) Mineralogy and Rare Earth Geochemistry of Apatite and Xenotime from the Gloserheia Granite Pegmatite, Froland, Southern Norway. *Am. Mineral.* **60**, 607–620.
- Andrehs G. and Heinrich W. (1998) Experimental determination of REE distributions between monazite and xenotime: potential for temperature-calibrated geochronology. *Chem. Geol.* **149**, 83–96.
- Arcuri G. A., Moser D. E., Reinhard D. A., Langelier B. and Larson D. J. (2020) Impact-triggered nanoscale Pb clustering and Pb loss domains in Archean zircon. *Contrib. to Mineral. Petrol.* **175**, 59.
- Armstrong J. T. (1988) Quantitative analysis of silicates and oxide minerals comparison of Monte-Carlo, ZAF and procedures. *Microbeam Anal.*, 239–246.
- Armstrong R. A., Lana C., Uwe Reimold W. and Gibson R. L. (2006) SHRIMP zircon age constraints on Mesoarchean crustal development in the Vredefort dome, central Kaapvaal Craton, South Africa. In Processes on the Early Earth (eds. W. U. Reimold and R. L. Gibson). *Geological Society of America*.
- Asadabad M. A. and Eskandari M. J. (2016) Electron Diffraction. In *Modern Electron*

- Microscopy in Physical and Life Sciences* (ed. M. J. E. E.-M. J. E.-R. Kral). InTech, Rijeka. p. Ch. 1.
- Asadi Asadabad M. and Jafari Eskandari M. (2015) Transmission Electron Microscopy as Best Technique for Characterization in Nanotechnology. *Synth. React. Inorganic, Met. Nano-Metal Chem.* **45**, 323–326.
- Asami M., Suzuki K. and Grew E. S. (2002) Chemical Th-U-total Pb dating by electron microprobe analysis of monazite, xenotime and zircon from the Archean Napier complex, East Antarctica: Evidence for ultra-high-temperature metamorphism at 2400 Ma. *Precambrian Res.* **114**, 249–275.
- Bachhav M., Danoix R., Danoix F., Hannover B., Ogale S. and Vurpillot F. (2011) Investigation of wustite (Fe_{1-x}O) by femtosecond laser assisted atom probe tomography. *Ultramicroscopy* **111**, 584–588.
- Barber D. J., Wenk H.-R., Hirth G. and Kohlstedt D. L. (2010) Chapter 95 Dislocations in Minerals. In (eds. J. P. Hirth and L. B. T.-D. in S. Kubin). Elsevier. 171–232.
- Bauer, P., Ralser, S., Daniel, C., Ilg, B., and Harrison, B., 1996, Geologic map of the McClure Reservoir quadrangle, Santa Fe County, New Mexico: New Mexico Bureau of Geology and Mineral Resources, Open-File Geologic Map 07, scale 1:24,000, 1 sheet.
- Bauer, P.W., and Ralser, S., 1995, The Picuris-Pecos fault: Repeatedly reactivated, from Proterozoic to Neogene, in Bauer, P.W., Kues, B.S., Dunbar, N.W., Karlstrom, K.E., and Harrison, B., eds., *Geology of the Santa Fe Region: Socorro, New Mexico, USA*, New Mexico Geological Society 46th Annual Fall Field Conference Guidebook, 111–115.
- Bea F. and Montero P. (1999) Behavior of accessory phases and redistribution of Zr, REE, Y, Th, and U during metamorphism and partial melting of metapelites in the lower crust: An example from the Kinzigite Formation of Ivrea-Verbano, NW Italy. *Geochim. Cosmochim. Acta* **63**, 1133–1153.
- Beccaletto L., Bonev N., Bosch D. and Bruguier O. (2007) Record of a Palaeogene syn-collisional extension in the north Aegean region: Evidence from the Kemer micaschists (NW Turkey). *Geol. Mag.* **144**, 393–400.
- Blum T. B., Reinhard D. A., Chen Y., Prosa T. J., Larson D. J. and Valley J. W. (2017) Uncertainty and sensitivity analysis for spatial and spectral processing of Pb isotopes in zircon by atom probe tomography. *Geophys. Monogr. Ser.* **232**, 327–350.
- Bodorkos S., Bowring J. F. and Rayner N. M. (2020) *Squid3: next-generation data processing*

- software for sensitive high-resolution ion microprobe (SHRIMP).*
- Breiter K. and Förster H. (2021) Compositional Variability of Monazite–Cheralite–Huttonite Solid Solutions, Xenotime, and Uraninite in Geochemically Distinct Granites with Special Emphasis to the Strongly Fractionated Peraluminous Li–F–P-Rich Podlesí Granite System (Erzgebirge/Krušné Hor. *Minerals* **11**, 127.
- Broska I., Williams C. T., Janák M. and Nagy G. (2005) Alteration and breakdown of xenotime-(Y) and monazite-(Ce) in granitic rocks of the Western Carpathians, Slovakia. *Lithos* **82**, 71–83.
- Brown S. M., Fletcher I. R., Stein H. J., Snee L. W. and Groves D. I. (2002) Geochronological Constraints on Pre-, Syn-, and Postmineralization Events at the World-Class Cleo Gold Deposit, Eastern Goldfields Province, Western Australia. *Econ. Geol.* **97**, 541–559.
- Budzyń B. and Kozub-Budzyń G. (2015) The stability of xenotime in high Ca and Ca-Na systems, under experimental conditions of 250-350°C and 200-400 MPa: the implications for fluid-mediated low-temperature processes in granitic rocks. *Geol. Q.* **59**, 316–324.
- Budzyń B. and Sláma J. (2019) Partial resetting of U–Pb ages during experimental fluid-induced re-equilibration of xenotime. *Lithos* **346–347**, 105163.
- Budzyń B., Sláma J., Kozub-Budzyń G. A., Konečný P., Holický I., Rzepa G. and Jastrzębski M. (2018) Constraints on the timing of multiple thermal events and re-equilibration recorded by high-U zircon and xenotime: Case study of pegmatite from Piława Górna (Góry Sowie Block, SW Poland). *Lithos* **310–311**, 65–85.
- Budzyń B., Wirth R., Sláma J., Kozub-Budzyń G. A. and Schreiber A. (2023) Atomic-scale Th and U segregation into dislocation cores and U-Pb age discordance in xenotime. *Lithos*, 107105.
- Cairney J. M., Rajan K., Haley D., Gault B., Bagot P. A. J., Choi P.-P., Felfer P. J., Ringer S. P., Marceau R. K. W. and Moody M. P. (2015) Mining information from atom probe data. *Ultramicroscopy* **159**, 324–337.
- Cappelli C., Smart S., Stowell H. and Pérez-Huerta A. (2021) Exploring Biases in Atom Probe Tomography Compositional Analysis of Minerals. *Geostand. Geoanalytical Res.* **45**, 457–476.
- Carr S. D., Easton R. M., Jamieson R. A. and Culshaw N. G. (2000) Geologic transect across the Grenville orogen of Ontario and New York. *Can. J. Earth Sci.* **37**, 193–216.

- Cavosie A. J., Timms N. E., Erickson T. M. and Koeberl C. (2018b) New clues from Earth's most elusive impact crater: Evidence of reidite in Australasian tektites from Thailand. *Geology* **46**, 203–206.
- Cavosie A. J. and Folco L. (2021a) Shock-twinned zircon in ejecta from the 45-m-diameter Kamil crater in southern Egypt eds. W. U. Reimold and C. Koeberl. *Large Meteor. Impacts Planet. Evol.* **VI 550**, 0.
- Cavosie A. J., Erickson T. M., Montalvo P. E., Prado D. C., Cintron N. O. and Gibbon R. J. (2018a) The Rietputs Formation in South Africa. In *Microstructural Geochronology: Planetary Records Down to Atom Scale*, 203–224.
- Cavosie A. J., Erickson T. M., Timms N. E., Reddy S. M., Talavera C., Montalvo S. D., Pincus M. R., Gibbon R. J. and Moser D. (2015) A terrestrial perspective on using ex situ shocked zircons to date lunar impacts. *Geology* **43**, 999–1002.
- Cavosie A. J., Kirkland C. L., Reddy S. M., Timms N. E., Talavera C. and Pincus M. R. (2021b) Extreme plastic deformation and subsequent Pb loss in shocked xenotime from the Vredefort Dome, South Africa. In *Large Meteorite Impacts and Planetary Evolution VI Geological Society of America.* **VI 550**, 465–478.
- Cavosie A. J., Montalvo P. E., Timms N. E. and Reddy S. M. (2016a) Nanoscale deformation twinning in xenotime, a new shocked mineral, from the Santa Fe impact structure (New Mexico, USA). *Geology* **44**, 803–806.
- Cavosie A. J., Spencer C. J., Evans N., Rankenburg K., Thomas R. J. and Macey P. H. (2022) Granular titanite from the Roter Kamm crater in Namibia: Product of regional metamorphism, not meteorite impact. *Geosci. Front.* **13**, 101350.
- Cavosie A. J., Timms N. E., Erickson T. M., Hagerty J. J. and Hörz F. (2016b) Transformations to granular zircon revealed: Twinning, reidite, and ZrO₂ in shocked zircon from Meteor Crater (Arizona, USA). *Geology* **44**, 703–706.
- Cavosie A. J., Timms N. E., Ferrière L. and Rochette P. (2018c) FRIGN zircon-The only terrestrial mineral diagnostic of high-pressure and high-temperature shock deformation. *Geology* **46**, 891–894.
- Černok A., White L. F., Anand M., Tait K. T., Darling J. R., Whitehouse M., Miljković K., Lemelin M., Reddy S. M., Fougereuse D., Rickard W. D. A., Saxey D. W. and Ghent R. (2021) Lunar samples record an impact 4.2 billion years ago that may have formed the

- Serenitatis Basin. *Commun. Earth Environ.* **2**, 120.
- Černok A., White L. F., Darling J., Dunlop J. and Anand M. (2019) Shock-induced microtextures in lunar apatite and merrillite. *Meteorit. Planet. Sci.* **54**, 1262–1282.
- Cherniak D. J. (2006) Pb and rare earth element diffusion in xenotime. *Lithos* **88**, 1–14.
- Cherniak D. J. (2010) Diffusion in accessory minerals: Zircon, titanite, apatite, monazite and xenotime. *Rev. Mineral. Geochemistry* **72**, 827–869.
- Chew D. M., Petrus J. A. and Kamber B. S. (2014) U–Pb LA–ICPMS dating using accessory mineral standards with variable common Pb. *Chem. Geol.* **363**, 185–199.
- Cocherie A. and Legendre O. (2007) Potential minerals for determining U–Th–Pb chemical age using electron microprobe. *Lithos* **93**, 288–309.
- Cox M. A., Cavosie A. J., Poelchau M., Kenkmann T., Bland P. A. and Miljković K. (2021) Shock deformation microstructures in xenotime from the Spider impact structure, Western Australia. In *Large Meteorite Impacts and Planetary Evolution VI* (eds. W. U. Reimold and C. Koeberl). *Geological Society of America*, 449–464.
- Cox M. A., Erickson T. M., Schmieder M., Christoffersen R., Ross D. K., Cavosie A. J., Bland P. A., Kring David A., Gulick S., Morgan J. V., Carter G., Chenot E., Christeson G., Claeys P., Cockell C., Coolen M. J. L., Ferrière L., Gebhardt C., Goto K., Jones H., Kring D. A., Lofi J., Lowery C., Ocampo-Torres R., Perez-Cruz L., Pickersgill A., Poelchau M., Rae A., Rasmussen C., Rebolledo-Vieyra M., Riller U., Sato H., Smit J., Tikoo S., Tomioka N., Whalen M., Wittmann A., Urrutia-Fucugauchi J., Xiao L. and Yamaguchi K. E. (2020) High-resolution microstructural and compositional analyses of shock deformed apatite from the peak ring of the Chicxulub impact crater. *Meteorit. Planet. Sci.* **55**, 1715–1733.
- Cross A. J. and Williams I. S. (2018) SHRIMP U–Pb–Th xenotime (YPO₄) geochronology: A novel approach for the correction of SIMS matrix effects. *Chem. Geol.* **484**, 81–108.
- Culshaw N., Foster J., Marsh J., Slagstad T. and Gerbi C. (2016) Kiosk domain, Central Gneiss Belt, Grenville Province, Ontario: A Labradorian palimpsest preserved in the ductile deep crust. *Precambrian Res.* **280**, 249–278.
- Daly L., Bland P. A., Tessalina S., Saxey D. W., Reddy S. M., Fougereuse D., Rickard W. D. A., Forman L. V., La Fontaine A., Cairney J. M., Ringer S. P., Schaefer B. F. and Schwander D. (2018) Defining the Potential of Nanoscale Re–Os Isotope Systematics

Using Atom Probe Microscopy. *Geostand. Geoanalytical Res.* **42**, 279–299.

- Darling J. R., Moser D. E., Barker I. R., Tait K. T., Chamberlain K. R., Schmitt A. K. and Hyde B. C. (2016) Variable microstructural response of baddeleyite to shock metamorphism in young basaltic shergottite NWA 5298 and improved U–Pb dating of Solar System events. *Earth Planet. Sci. Lett.* **444**, 1–12.
- Darling J. R., White L. F., Kizovski T., Černok A., Moser D. E., Tait K. T., Dunlop J., Langelier B., Douglas J. O., Zhao X., Franchi I. A. and Anand M. (2021) The shocking state of apatite and merrillite in shergottite Northwest Africa 5298 and extreme nanoscale chlorine isotope variability revealed by atom probe tomography. *Geochim. Cosmochim. Acta* **293**, 422–437.
- Devaraj A., Colby R., Hess W. P., Perea D. E. and Thevuthasan S. (2013) Role of Photoexcitation and Field Ionization in the Measurement of Accurate Oxide Stoichiometry by Laser-Assisted Atom Probe Tomography. *J. Phys. Chem. Lett.* **4**, 993–998.
- Devaraj A., Colby R., Vurpillot F. and Thevuthasan S. (2014) Understanding Atom Probe Tomography of Oxide-Supported Metal Nanoparticles by Correlation with Atomic-Resolution Electron Microscopy and Field Evaporation Simulation. *J. Phys. Chem. Lett.* **5**, 1361–1367.
- Didier A., Bosse V., Boulvais P., Bouloton J., Paquette J.-L., Montel J.-M. and Devidal J.-L. (2013) Disturbance versus preservation of U–Th–Pb ages in monazite during fluid–rock interaction: textural, chemical and isotopic in situ study in microgranites (Velay Dome, France). *Contrib. to Mineral. Petrol.* **165**, 1051–1072.
- Diercks D. R. and Gorman B. P. (2015) Nanoscale Measurement of Laser-Induced Temperature Rise and Field Evaporation Effects in CdTe and GaN. *J. Phys. Chem. C* **119**, 20623–20631.
- Diercks D. R., Gorman B. P., Kirchhofer R., Sanford N., Bertness K. and Brubaker M. (2013) Atom probe tomography evaporation behavior of C-axis GaN nanowires: Crystallographic, stoichiometric, and detection efficiency aspects. *J. Appl. Phys.* **114**, 184903.
- Diercks D. R., Gorman B. P., Manerbino A. and Coors G. (2014) Atom Probe Tomography of Yttrium-Doped Barium–Cerium–Zirconium Oxide with NiO Addition ed. P. Salvador. *J. Am. Ceram. Soc.* **97**, 3301–3306.

- Doherty R. D., Hughes D. A., Humphreys F. J., Jonas J. J., Jensen D. J., Kassner M. E., King W. E., McNelley T. R., McQueen H. J. and Rollett A. D. (1997) Current issues in recrystallization: a review. *Mater. Sci. Eng. A* **238**, 219–274.
- Donelick R. A., O’Sullivan P. B. and Ketcham R. A. (2005) Apatite Fission-Track Analysis. *Rev. Mineral. Geochemistry* **58**, 49–94.
- Donovan J. J., Hanchar J. M., Picolli P. M., Schrier M. D., Boatner L. A. and Jarosewich E. (2003) A re-examination of the rare-earth-element orthophosphate standards in use for electron-microprobe analysis. *Can. Mineral.* **41**, 221–232.
- Donovan J. J., Snyder D. A. and Rivers M. L. (1993) An improved interference correction for trace element analysis.
- Drake M. J. and Weill D. F. (1972) New rare earth element standards for electron microprobe analysis. *Chem. Geol.* **10**, 179–181.
- Drost K., Wirth R., Košler J., Fonneland Jørgensen H. and Ntaflos T. (2013) Chemical and structural relations of epitaxial xenotime and zircon substratum in sedimentary and hydrothermal environments: a TEM study. *Contrib. to Mineral. Petrol.* **165**, 737–756.
- Drury M. R. and Pennock G. M. (2007) Subgrain Rotation Recrystallization in Minerals. *Mater. Sci. Forum* **550**, 95–104.
- Dubosq R., Lawley C. J. M., Rogowitz A., Schneider D. A. and Jackson S. (2018) Pyrite deformation and connections to gold mobility: Insight from micro-structural analysis and trace element mapping. *Lithos* **310–311**, 86–104.
- Dubosq R., Rogowitz A., Schweinar K., Gault B. and Schneider D. A. (2019) A 2D and 3D nanostructural study of naturally deformed pyrite: assessing the links between trace element mobility and defect structures. *Contrib. to Mineral. Petrol.* **174**, 72.
- Earth impact database
http://www.passc.net/EarthImpactDatabase/New%20website_05-2018/Index.html
- Edmunds W. M. and Atherton M. P. (1971) Polymetamorphic evolution of garnet in the Fanad aureole, Donegal, eire. *Lithos* **4**, 147–161.
- Engelhardt W. V, Matthäi S. K. and Walzebuck J. (1992) Araguinha impact crater, Brazil. I. The interior part of the uplift. *Meteoritics* **27**, 442–457.
- Engi M. (2017) Petrochronology Based on REE-Minerals: Monazite, Allanite, Xenotime, Apatite. *Rev. Mineral. Geochemistry* **83**, 365–418.

- Erickson T. M., Cavosie A. J., Moser D. E., Barker I. R., Radovan H. A. and Wooden J. (2013b) Identification and provenance determination of distally transported, Vredefort-derived shocked minerals in the Vaal River, South Africa using SEM and SHRIMP-RG techniques. *Geochim. Cosmochim. Acta* **107**, 170–188.
- Erickson T. M., Cavosie A. J., Moser D. E., Barker I. R. and Radovan H. A. (2013a) Correlating planar microstructures in shocked zircon from the Vredefort Dome at multiple scales: Crystallographic modeling, external and internal imaging, and EBSD structural analysis. *Am. Mineral.* **98**, 53–65.
- Erickson T. M., Cavosie A. J., Pearce M. A., Timms N. E. and Reddy S. M. (2016) Empirical constraints on shock features in monazite using shocked zircon inclusions. *Geology* **44**, 635–638.
- Erickson T. M., Kirkland C. L., Timms N. E., Cavosie A. J. and Davison T. M. (2020) Precise radiometric age establishes Yarrabubba, Western Australia, as Earth's oldest recognised meteorite impact structure. *Nat. Commun.* **11**, 300.
- Erickson T. M., Pearce M. A., Taylor R. J. M., Timms N. E., Clark C., Reddy S. M. and Buick I. S. (2015) Deformed monazite yields high-temperature tectonic ages. *Geology* **43**, 383–386.
- Erickson T. M., Timms N. E., Kirkland C. L., Tohver E., Cavosie A. J., Pearce M. A. and Reddy S. M. (2017) Shocked monazite chronometry: integrating microstructural and in situ isotopic age data for determining precise impact ages. *Contrib. to Mineral. Petrol.* **172**, 11.
- Exertier F., La Fontaine A., Corcoran C., Piazzolo S., Belousova E., Peng Z., Gault B., Saxey D. W., Fougereuse D., Reddy S. M., Pedrazzini S., Bagot P. A. J., Moody M. P., Langelier B., Moser D. E., Botton G. A., Vogel F., Thompson G. B., Blanchard P. T., Chiaramonti A. N., Reinhard D. A., Rice K. P., Schreiber D. K., Kruska K., Wang J. and Cairney J. M. (2018) Atom probe tomography analysis of the reference zircon gj-1: An interlaboratory study. *Chem. Geol.* **495**, 27–35.
- Fackelman S. P., Morrow J. R., Koeberl C. and McElvain T. H. (2008) Shatter cone and microscopic shock-alteration evidence for a post-Paleoproterozoic terrestrial impact structure near Santa Fe, New Mexico, USA. *Earth Planet. Sci. Lett.* **270**, 290–299.
- Ferraris C., White T. J., Plévert J. and Wegner R. (2005) Nanometric modulation in apatite. *Phys.*

- Chem. Miner.* **32**, 485–492.
- Fletcher I. R., McNaughton N. J., Aleinikoff J. A., Rasmussen B. and Kamo S. L. (2004) Improved calibration procedures and new standards for U - Pb and Th - Pb dating of Phanerozoic xenotime by ion microprobe. *Chem. Geol.* **209**, 295–314.
- Fletcher I. R., Rasmussen B. and McNaughton N. J. (2000) SHRIMP U-Pb geochronology of authigenic xenotime and its potential for dating sedimentary basins. *Aust. J. Earth Sci.* **47**, 845–859.
- Flowers R. M., Moser D. E. and Hart R. J. (2003) Evolution of the Amphibolite-Granulite Facies Transition Exposed by the Vredefort Impact Structure, Kaapvaal Craton, South Africa. *J. Geol.* **111**.
- Förster H. J. (1998) The chemical composition of REE-Y-Th-U-rich accessory minerals in peraluminous granites of the Erzgebirge-Fichtelgebirge region, Germany. Part II: Xenotime. *Am. Mineral.* **83**, 1302–1315.
- Förster H. J. (2006) Composition and origin of intermediate solid solutions in the system thorite-xenotime-zircon-coffinite. *Lithos* **88**, 35–55.
- Fougerouse D, Cavosie A. J., Erickson T., Reddy S. M., Cox M. A., Saxey D. W., Rickard W. D. A. and Wingate M. T. D. (2021a) A new method for dating impact events – Thermal dependency on nanoscale Pb mobility in monazite shock twins. *Geochim. Cosmochim. Acta* **314**, 381–396.
- Fougerouse D, Reddy S. M., Seydoux-Guillaume A.-M., Kirkland C. L., Erickson T. M., Saxey D. W., Rickard W. D. A., Jacob D., Leroux H. and Clark C. (2021b) Mechanical twinning of monazite expels radiogenic lead. *Geology* **49**, 417–421.
- Fougerouse D, Saxey D. W., Rickard W. D. A., Reddy S. M. and Verberne R. (2021c) Standardizing Spatial Reconstruction Parameters for the Atom Probe Analysis of Common Minerals. *Microsc. Microanal.*, 1–10.
- Fougerouse D., Kirkland C. L., Saxey D. W., Seydoux-Guillaume A. M., Rowles M. R., Rickard W. D. A. and Reddy S. M. (2020) Nanoscale Isotopic Dating of Monazite. *Geostand. Geoanalytical Res.* **44**, 637–652.
- Fougerouse D., Reddy S. M., Kirkland C. L., Saxey D. W., Rickard W. D. and Hough R. M. (2019) Time-resolved, defect-hosted, trace element mobility in deformed Witwatersrand pyrite. *Geosci. Front.* **10**, 55–63.
- Fougerouse D., Reddy S. M., Saxey D. W., Erickson T. M., Kirkland C. L., Rickard W. D. A.,

- Seydoux-Guillaume A.-M., Clark C. and Buick I. S. (2018) Nanoscale distribution of Pb in monazite revealed by atom probe microscopy. *Chem. Geol.* **479**, 251–258.
- Fougerouse D., Reddy S. M., Saxey D. W., Rickard W. D. A., van Riessen A. and Micklethwaite S. (2016) Nanoscale gold clusters in arsenopyrite controlled by growth rate not concentration: Evidence from atom probe microscopy. *Am. Mineral.* **101**, 1916–1919.
- Franz G., Andrehs G. and Rhede D. (1996) Crystal chemistry of monazite and xenotime from Saxothuringian-Moldanubian metapelites, NE Bavaria, Germany. *Eur. J. Mineral.* **8**, 1097–1118.
- Gault B., Danoix F., Hoummada K., Mangelinck D. and Leitner H. (2012) Impact of directional walk on atom probe microanalysis. *Ultramicroscopy* **113**, 182–191.
- Gault B., Moody M. P., Cairney J. M. and Ringer S. P. (2012) *Atom Probe Microscopy*, Springer New York, New York, NY.
- Geisler T., Dohmen L., Lenting C. and Fritzsche M. B. K. (2019) Real-time in situ observations of reaction and transport phenomena during silicate glass corrosion by fluid-cell Raman spectroscopy. *Nat. Mater.* **18**, 342–348.
- Geisler T., Schaltegger U. and Tomaschek F. (2007) Re-equilibration of zircon in aqueous fluids and melts. *Elements* **3**, 43–50.
- Geisser S. (1993) *Predictive inference: an introduction*, Chapman and Hall, New York, NY, 240.
- Gibson R. L. and Reimold W. U. (2005) Shock pressure distribution in the Vredefort impact structure, South Africa. In *Large Meteorite Impacts III* (eds. T. Kenkmann, F. Hörz, and A. Deutsch). Geological Society of America. p. 0.
- Gibson R. L., Armstrong R. A. and Reimold W. U. (1997) The age and thermal evolution of the Vredefort impact structure: A single-grain U-Pb zircon study. *Geochim. Cosmochim. Acta* **61**, 1531–1540.
- Gibson R. L., Reimold W. U. and Stevens G. (1998) Thermal-metamorphic signature of an impact event in the Vredefort dome, South Africa. *Geology* **26**, 787–790.
- Grand'Homme A., Janots E., Seydoux-Guillaume A. M., Guillaume D., Magnin V., Hövelmann J., Höschen C. and Boiron M. C. (2018) Mass transport and fractionation during monazite alteration by anisotropic replacement. *Chem. Geol.* **484**, 51–68.
- Grand'Homme A., Janots E., Seydoux-Guillaume A.-M., Guillaume D., Bosse V. and Magnin

- V. (2016) Partial resetting of the U-Th-Pb systems in experimentally altered monazite: Nanoscale evidence of incomplete replacement. *Geology* **44**, 431–434.
- Gratz R. and Heinrich W. (1998) Monazite-xenotime thermometry. III. Experimental calibration of the partitioning of gadolinium between monazite and xenotime. *Eur. J. Mineral.* **10**, 579–588.
- Grieve R. and Therriault A. (2000) Vredefort, Sudbury, Chicxulub: Three of a Kind? *Annu. Rev. Earth Planet. Sci.* **28**, 305–338.
- Gumsley A., Stamsnijder J., Larsson E., Söderlund U., Naeraa T., de Kock M., Sałacińska A., Gawęda A., Humbert F. and Ernst R. (2020) Neoproterozoic large igneous provinces on the Kaapvaal Craton in southern Africa re-define the formation of the Ventersdorp Supergroup and its temporal equivalents. *GSA Bull.* **132**, 1829–1844.
- Harlov D. E. (2015) Apatite: A fingerprint for metasomatic processes. *Elements* **11**, 171–176.
- Harlov D. E., Wirth R. and Förster H.-J. (2005) An experimental study of dissolution–reprecipitation in fluorapatite: fluid infiltration and the formation of monazite. *Contrib. to Mineral. Petrol.* **150**, 268–286.
- Harlov D. E., Wirth R. and Hetherington C. J. (2011) Fluid-mediated partial alteration in monazite: the role of coupled dissolution–reprecipitation in element redistribution and mass transfer. *Contrib. to Mineral. Petrol.* **162**, 329–348.
- Harrison T. M., Catlos E. J. and Montel J.-M. (2002) U-Th-Pb Dating of Phosphate Minerals. *Rev. Mineral. Geochemistry* **48**, 524–558.
- Hart R. J., Nicolaysen L. O. and Gale N. H. (1981) Radioelement concentrations in the deep profile through Precambrian basement of the Vredefort structure. *J. Geophys. Res. Solid Earth* **86**, 10639–10652.
- Hauser N., Reimold W. U., Cavosie A. J., Crósta A. P., Schwarz W. H., Tieloff M., Da Silva Maia de Souza C., Pereira L. A., Rodrigues E. N. and Brown M. (2019) Linking shock textures revealed by BSE, CL, and EBSD with U-Pb data (LA-ICP-MS and SIMS) from zircon from the Araguinha impact structure, Brazil. *Meteorit. Planet. Sci.* **54**, 2286–2311.
- Hawkins D. P. and Bowring S. A. (1999) U-Pb monazite, xenotime and titanite geochronological constraints on the prograde to post-peak metamorphic thermal history of Paleoproterozoic migmatites from the Grand Canyon, Arizona. *Contrib. to Mineral. Petrol.* **134**, 150–169.

- Heinrich W., Andrehs G. and Franz G. (1997) Monazite-xenotime miscibility gap thermometry. I. An empirical calibration. *J. Metamorph. Geol.* **15**, 3–16.
- Hellman O. C., Vandenbroucke J. A., Rüsing J., Isheim D. and Seidman D. N. (2000) Analysis of Three-dimensional Atom-probe Data by the Proximity Histogram. *Microsc. Microanal.* **6**, 437–444.
- Hetherington C. J., Harlov D. E. and Budzyń B. (2010) Experimental metasomatism of monazite and xenotime: Mineral stability, REE mobility and fluid composition. *Mineral. Petrol.* **99**, 165–184.
- Hetherington C. J., Jercinovic M. J., Williams M. L. and Mahan K. (2008) Understanding geologic processes with xenotime: Composition, chronology, and a protocol for electron probe microanalysis. *Chem. Geol.* **254**, 133–147.
- Hiraga T., Anderson I. M. and Kohlstedt D. L. (2003) Chemistry of grain boundaries in mantle rocks. *Am. Mineral.* **88**, 1015–1019.
- Hirth J. P. and Pond R. C. (1996) Steps, dislocations and disconnections as interface defects relating to structure and phase transformations. *Acta Mater.* **44**, 4749–4763.
- Hodych J. P. and Dunning G. R. (1992) Did the Manicouagan impact trigger end-of-Triassic mass extinction? *Geology* **20**, 51–54.
- Holmes A. (1913) *The Age of the Earth.*, Harper & Brothers.
- Hoskin P. W. O. and Black L. P. (2000) Metamorphic zircon formation by solid-state recrystallization of protolith igneous zircon. *J. Metamorph. Geol.* **18**, 423–439.
- Howie R. A. (1974) W. S. Pitcher and A. R. Berger. The geology of Donegal: a study of granite emplacement and unroofing (with a coloured r : 63 360 geol. map compiled by Margaret O. Spencer). New York and London (Wiley-Interscience), 1972. xii+435 pp., 150 figs., 2 maps. *Mineral. Mag.* **39**, 614–616.
- Hull D. and Bacon D. J. (2001) Origin and Multiplication of Dislocations. In *Introduction to Dislocations* (eds. D. Hull and D. J. B. T.-I. to D. (Fourth E. Bacon). Elsevier, Oxford. pp. 145–156.
- Ireland T. R., Clement S., Compston W., Foster J. J., Holden P., Jenkins B., Lanc P., Schram N. and Williams I. S. (2008) Development of SHRIMP. *Aust. J. Earth Sci.* **55**, 937–954.
- Janots E., Engi M., Berger A., Allaz J., Schwarz J. O. and Spandler C. (2008) Prograde metamorphic sequence of REE minerals in pelitic rocks of the Central Alps: Implications

- for allanite-monazite-xenotime phase relations from 250 to 610°C. *J. Metamorph. Geol.* **26**, 509–526.
- Jarosewich e., Nelen J. A. and Norberg J. A. (1980) Reference Samples for Electron Microprobe Analysis*. *Geostand. Geoanalytical Res.* **4**, 43–47.
- Jessell M. W. (1987) Grain-boundary migration microstructures in a naturally deformed quartzite. *J. Struct. Geol.* **9**, 1007–1014.
- Johnson L. J. S., Thuvander M., Stiller K., Odén M. and Hultman L. (2013) Blind deconvolution of time-of-flight mass spectra from atom probe tomography. *Ultramicroscopy* **132**, 60–64.
- Johnson S.P., Sheppard S. (2015) Davey Well Granite (P _ -DUda-mgmu). *WA Geol. Online, Explan. Notes Extr.*, 4–8.
- Johnson S.P., Sheppard S., and Korhonen F.J., (2013) Mulka Tectonic Event (MK): Geological Survey of Western Australia, WA Geology Online, *Explanatory Notes extract* <www.dmp.wa.gov.au/ens>
- Joseph C., Fougrouse D., Reddy S. M., Olierook H. K. H., Tacchetto T., Kennedy A., Saxey D. W., Rickard W. D. A., Denyszyn S. and Dodd A. (2023) Radiogenic Pb in xenotime trapped in nanoscale inclusions of apatite during fluid alteration. *Chem. Geol.*, 121444.
- Joseph C., Fougrouse D., Saxey D. W., Verberne R., Reddy S. M. and Rickard W. D. A. (2021) Xenotime at the Nanoscale: U-Pb Geochronology and Optimisation of Analyses by Atom Probe Tomography. *Geostand. Geoanalytical Res.* **45**, 443–456.
- Jourdan F., Reimold W. U. and Deutsch A. (2012) Dating terrestrial impact structures. *Elements* **8**, 49–53.
- Jourdan F., Renne P. R. and Reimold W. U. (2009) An appraisal of the ages of terrestrial impact structures. *Earth Planet. Sci. Lett.* **286**, 1–13.
- Kamo S. L., Krogh T. E. and Kumarapeli P. S. (1995) Age of the Grenville dyke swarm, Ontario - Quebec: implications for the timing of Iapetan rifting. *Can. J. Earth Sci.* **32**, 273–280.
- Kamo S. L., Lana C. and Morgan J. V (2011) U–Pb ages of shocked zircon grains link distal K–Pg boundary sites in Spain and Italy with the Chicxulub impact. *Earth Planet. Sci. Lett.* **310**, 401–408.

- Kamo S. L., Reimold W. U., Krogh T. E. and Colliston W. P. (1996) A 2.023 Ga age for the Vredefort impact event and a first report of shock metamorphosed zircons in pseudotachylitic breccias and Granophyre. *Earth Planet. Sci. Lett.* **144**, 369–387.
- Kenkmann T. (2021) The terrestrial impact crater record: A statistical analysis of morphologies, structures, ages, lithologies, and more. *Meteorit. Planet. Sci.* **56**, 1024–1070.
- Kenny G. G., Harrigan C. O., Schmitz M. D., Crowley J. L., Wall C. J., Andreoli M. A. G., Gibson R. L. and Maier W. D. (2021) Timescales of impact melt sheet crystallization and the precise age of the Morokweng impact structure, South Africa. *Earth Planet. Sci. Lett.* **567**, 117013.
- Kenny G. G., Morales L. F., Whitehouse M. J., Petrus J. A. and Kamber B. S. (2017) The formation of large neoblasts in shocked zircon and their utility in dating impacts. *Geology* **45**, 1003–1006.
- Kerckhove S. R. Van De (2016) Tectonic history of the Nepewassi domain, Central Gneiss Belt, Grenville Province, Ontario: A lithological, structural, metamorphic and geochronological study.
- Kerrick D. M. (1987) Fibrolite in contact aureoles of Donegal, Ireland. *Am. Mineral.* **72**, 240–254.
- Ketchum J. W. F. and Davidson A. (2000) Crustal architecture and tectonic assembly of the Central Gneiss Belt, southwestern Grenville Province, Canada: A new interpretation. *Can. J. Earth Sci.* **37**, 217–234.
- Kingham D. R. (1982) The post-ionization of field evaporated ions: A theoretical explanation of multiple charge states. *Surf. Sci.* **116**, 273–301.
- Kirchhofer R., Diercks D. R., Gorman B. P., Ihlefeld J. F., Kotula P. G., Shelton C. T. and Brennecka G. L. (2014) Quantifying Compositional Homogeneity in Pb(Zr,Ti)O₃ Using Atom Probe Tomography. *J. Am. Ceram. Soc.* **97**, 2677–2697.
- Kirchhofer R., Teague M. C. and Gorman B. P. (2013) Thermal effects on mass and spatial resolution during laser pulse atom probe tomography of cerium oxide. *J. Nucl. Mater.* **436**, 23–28.
- Kirkland C. L., Yakymchuk C., Szilas K., Evans N., Hollis J., McDonald B. and Gardiner N. J. (2018) Apatite: a U-Pb thermochronometer or geochronometer? *Lithos* **318–319**, 143–157.

- Kirkland C.L., Fougere D., Reddy S. M., Hollis J. and Saxey D. W. (2018) Assessing the mechanisms of common Pb incorporation into titanite. *Chem. Geol.* **483**, 558–566.
- Klapper H. (2010) Generation and Propagation of Defects During Crystal Growth. In *Springer Handbook of Crystal Growth* (eds. G. Dhanaraj, K. Byrappa, V. Prasad, and M. Dudley). Springer Berlin Heidelberg, Berlin, Heidelberg. pp. 93–132.
- Klapper H. and Rudolph P. (2015) Defect Generation and Interaction during Crystal Growth. In *Handbook of Crystal Growth* Elsevier. pp. 1093–1141.
- Kositcin N., McNaughton N. J., Griffin B. J., Fletcher I. R., Groves D. I. and Rasmussen B. (2003) Textural and geochemical discrimination between xenotime of different origin in the Archaean Witwatersrand Basin, South Africa. *Geochim. Cosmochim. Acta* **67**, 709–731.
- Kozłowski A. (1978) Pneumatolytic and hydrothermal activity in the Karkonosze-Izera block. *Acta Geol. Pol.* **28**, 171–222.
- Kozłowski A. and Marcinowska A. (2007) Hydrothermal activity in the Karkonosze, Strzegom and Strzelin massifs—a fluid inclusion study. *Granitoids Poland. AM Monogr.* **1**, 243–252.
- Kusiak M. A., Dunkley D. J., Wirth R., Whitehouse M. J., Wilde S. A. and Marquardt K. (2015) Metallic lead nanospheres discovered in ancient zircons. *Proc. Natl. Acad. Sci.* **112**, 4958–4963.
- La Fontaine A., Gault B., Breen A., Stephenson L., Ceguerra A. V., Yang L., Dinh Nguyen T., Zhang J., Young D. J. and Cairney J. M. (2015) Interpreting atom probe data from chromium oxide scales. *Ultramicroscopy* **159**, 354–359.
- La Fontaine A., Piazzolo S., Trimby P., Yang L. and Cairney J. M. (2017) Laser-Assisted Atom Probe Tomography of Deformed Minerals: A Zircon Case Study. *Microsc. Microanal.* **23**, 404–413.
- Lambert R. S. J. and McKerrow W. S. (1976) The Grampian Orogeny. *Scottish J. Geol.* **12**, 271–292.
- Lana C., Filho C. R. S., Marangoni Y. R., Yokoyama E., Trindade R. I. F., Tohver E. and Reimold W. U. (2007) Insights into the morphology, geometry, and post-impact erosion of the Araguainha peak-ring structure, central Brazil. *Geol. Soc. Am. Bull.* **119**, 1135–1150.

- Lana C., Filho C. R. S., Marangoni Y. R., Yokoyama E., Trindade R. I. F., Tohver E. and Reimold W. U. (2008) Structural evolution of the 40 km wide Araguainha impact structure, central Brazil. *Meteorit. Planet. Sci.* **43**, 701–716.
- Langenhorst F. and Deutsch A. (2012) Shock Metamorphism of Minerals. *Elements* **8**, 31–36.
- Larson D. J., Prosa T. J., Ulfig R. M., Geiser B. P. and Kelly T. F. (2013) Local Electrode Atom Probe Tomography.,318
- Laurent A. T., Seydoux-Guillaume A.-M., Duchene S., Bingen B., Bosse V. and Datas L. (2016) Sulphate incorporation in monazite lattice and dating the cycle of sulphur in metamorphic belts. *Contrib. to Mineral. Petrol.* **171**, 94.
- Lenting C., Plümper O., Kilburn M., Guagliardo P., Klinkenberg M. and Geisler T. (2018) Towards a unifying mechanistic model for silicate glass corrosion. *npj Mater. Degrad.* **2**, 28.
- Lenz C., Thorogood G., Aughterson R., Ionescu M., Gregg D. J., Davis J. and Lumpkin G. R. (2019) The Quantification of Radiation Damage in Orthophosphates Using Confocal μ -Luminescence Spectroscopy of Nd³⁺. *Front. Chem.* **7**, 1–13.
- Li L. X., Zi J. W., Meng J., Li H. M., Rasmussen B., Sheppard S., Wilde S. A. and Li Y. H. (2020) Using in situ monazite and xenotime U-Pb geochronology to resolve the fate of the “missing” banded iron formation-hosted high-grade hematite ores of the North China craton. *Econ. Geol.* **115**, 189–204.
- Li Q. L., Li X. H., Lan Z. W., Guo C. L., Yang Y. N., Liu Y. and Tang G. Q. (2013) Monazite and xenotime U-Th-Pb geochronology by ion microprobe: Dating highly fractionated granites at Xihuashan tungsten mine, SE China. *Contrib. to Mineral. Petrol.* **166**, 65–80.
- Lind C. J. (1983) *Characterization of mineral precipitates by electron microscope photographs and electron diffraction patterns.*,
- Liu Z. C., Wu F. Y., Guo C. L., Zhao Z. F., Yang J. H. and Sun J. F. (2011) In situ U-Pb dating of xenotime by laser ablation (LA)-ICP-MS. *Chinese Sci. Bull.* **56**, 2948–2956.
- London A. J., Haley D. and Moody M. P. (2017) Single-Ion Deconvolution of Mass Peak Overlaps for Atom Probe Microscopy. *Microsc. Microanal.* **23**, 300–306.
- London D. and Kontak D. J. (2012) Granitic Pegmatites: Scientific Wonders and Economic Bonanzas. *Elements* **8**, 257–261.

- Ludwig K. (2012) User's manual for Isoplot/Ex: a geochronological toolkit for Microsoft Excel. *Berkeley Geochronol. Cent. Spec. Publ. 1a*, **53**.
- McGregor M., Dence M. R., McFarlane C. R. M. and Spray J. G. (2020) U–Pb geochronology of apatite and zircon from the Brent impact structure, Canada: a Late Ordovician Sandbian–Katian boundary event associated with L-Chondrite parent body disruption. *Contrib. to Mineral. Petrol.* **175**, 63.
- McGregor M., Erickson T. M., Spray J. G. and Whitehouse M. J. (2021b) High-resolution EBSD and SIMS U–Pb geochronology of zircon, titanite, and apatite: insights from the Lac La Moinerie impact structure, Canada. *Contrib. to Mineral. Petrol.* **176**, 76.
- McGregor M., McFarlane C. R. M. and Spray J. G. (2018) In situ LA-ICP-MS apatite and zircon U–Pb geochronology of the Nicholson Lake impact structure, Canada: Shock and related thermal effects. *Earth Planet. Sci. Lett.* **504**, 185–197.
- McGregor M., McFarlane C. R. M. and Spray J. G. (2019) In situ multiphase U–Pb geochronology and shock analysis of apatite, titanite and zircon from the Lac La Moinerie impact structure, Canada. *Contrib. to Mineral. Petrol.* **174**, 62.
- McGregor M., McFarlane C. R. M. and Spray J. G. (2021a) U-Pb geochronology of apatite crystallized within a terrestrial impact melt sheet: Manicouagan as a geochronometer test site eds. W. U. Reimold and C. Koeberl. *Large Meteor. Impacts Planet. Evol.* **VI 550**, 0.
- McNaughton N. J. and Rasmussen B. (2018) Geochemical characterisation of xenotime formation environments using U-Th. *Chem. Geol.* **484**, 109–119.
- McNaughton N. J., Rasmussen B. and Fletcher I. R. (1999) SHRIMP uranium-lead dating of diagenetic xenotime in siliciclastic sedimentary rocks. *Science* (80-.). **285**, 78–80.
- Meisenkothen F., Samarov D. V., Kalish I. and Steel E. B. (2020) Exploring the accuracy of isotopic analyses in atom probe mass spectrometry. *Ultramicroscopy* **216**, 113018.
- Meldrum A, Boatner L. A. and Ewing R. C. (1997) Displacive radiation effects in the monazite- and zircon-structure orthophosphates. *Phys. Rev. B* **56**, 13805–13814.
- Montalvo P. E, Cavosie A. J., Kirkland C. L., Evans N. J., McDonald B. J., Talavera C., Erickson T. M. and Lugo-Centeno C. (2019) Detrital shocked zircon provides first radiometric age constraint (<1472 Ma) for the Santa Fe impact structure, New Mexico, USA. *GSA Bull.* **131**, 845–863.

- Montalvo S. D. (2020) Development and application of atom probe tomography to complex zircon grains.
- Montalvo S. D., Reddy S. M., Saxey D. W., Rickard W. D. A., Fougere D., Quadir Z. and Johnson T. E. (2019) Nanoscale constraints on the shock-induced transformation of zircon to reidite. *Chem. Geol.* **507**, 85–95.
- Moser A. C., Hacker B. R., Gehrels G. E., Seward G. G. E., Kylander-Clark A. R. C. and Garber J. M. (2022) Linking titanite U–Pb dates to coupled deformation and dissolution–reprecipitation. *Contrib. to Mineral. Petrol.* **177**, 42.
- Moser D. E. (1997) Dating the shock wave and thermal imprint of the giant Vredefort impact, South Africa. *Geology* **25**, 7–10.
- Moser D. E., Arcuri G. A., Reinhard D. A., White L. F., Darling J. R., Barker I. R., Larson D. J., Irving A. J., McCubbin F. M., Tait K. T., Roszjar J., Wittmann A. and Davis C. (2019) Decline of giant impacts on Mars by 4.48 billion years ago and an early opportunity for habitability. *Nat. Geosci.* **12**, 522–527.
- Moser D. E., Cupelli C. L., Barker I. R., Flowers R. M., Bowman J. R., Wooden J. and Hart J. R. (2011) New zircon shock phenomena and their use for dating and reconstruction of large impact structures revealed by electron nanobeam (EBSD, CL, EDS) and isotopic U-Pb and (U-Th)/he analysis of the Vredefort dome. *Can. J. Earth Sci.* **48**, 117–139.
- Muhling J. R., Fletcher I. R. and Rasmussen B. (2012) Dating fluid flow and Mississippi Valley type base-metal mineralization in the Paleoproterozoic Earraheedy Basin, Western Australia. *Precambrian Res.* **212–213**, 75–90.
- Naggar M. H. and Atherton M. P. (1970) The composition and metamorphic history of some aluminium silicate-bearing rocks from the aureoles of the Donegal granites. *J. Petrol.* **11**, 549–589.
- Nasdala L., Akhmadaliev S., Burakov B. E., Chanmuang N C. and Škoda R. (2020) The absence of metamictisation in natural monazite. *Sci. Rep.* **10**, 14676.
- Ni, Y., Hughes, J.M., Mariano, A.N., 1995. Crystal chemistry of the monazite and xenotime structures. *Am. Mineral.* **80**, 21–26. <https://doi.org/10.2138/am-1995-1-203>
- O'Connor P. J., Long C. B. and Evans J. A. (1987) Rb-Sr whole-rock isochron studies of the Barnesmore and Fanad plutons, Donegal, Ireland. *Geol. J.* **22**, 11–23.

- O'Neill C., Marchi S., Zhang S. and Bottke W. (2017) Impact-driven subduction on the Hadean Earth. *Nat. Geosci.* **10**, 793–797.
- Olierook H. K. H., Agangi A., Plavsa D., Reddy S. M., Yao W., Clark C., Occhipinti S. A. and Kylander-Clark A. R. C. (2019) Neoproterozoic hydrothermal activity in the West Australian Craton related to Rodinia assembly or breakup? *Gondwana Res.* **68**, 1–12.
- Ondrejka M., Putiš M., Uher P., Schmiedt I., Pukančík L. and Konečný P. (2016) Fluid-driven destabilization of REE-bearing accessory minerals in the granitic orthogneisses of North Veporic basement (Western Carpathians, Slovakia). *Mineral. Petrol.* **110**, 561–580.
- Osinski G. R., Cockell C. S., Pontefract A. and Sapers H. M. (2020) The Role of Meteorite Impacts in the Origin of Life. *Astrobiology* **20**, 1121–1149.
- Osinski G. R., Grieve R. A. F., Ferrière L., Losiak A., Pickersgill A. E., Cavosie A. J., Hibbard S. M., Hill P. J. A., Bermudez J. J., Marion C. L., Newman J. D. and Simpson S. L. (2022) Impact Earth: A review of the terrestrial impact record. *Earth-Science Rev.* **232**, 104112.
- Pan Y. and Fleet M. E. (2002) Compositions of the Apatite-Group Minerals: Substitution Mechanisms and Controlling Factors. *Rev. Mineral. Geochemistry* **48**, 13–49.
- Papapavlou K., Darling J. R., Moser D. E., Barker I. R., White L. F., Lightfoot P. C., Storey C. D., Dunlop J. and EIMF (2018) U–Pb isotopic dating of titanite microstructures: potential implications for the chronology and identification of large impact structures. *Contrib. to Mineral. Petrol.* **173**, 82.
- Passchier C. W. and Trouw R. A. J. (2005) Micro-tectonics.,
- Peterman E. M., Reddy S. M., Saxey D. W., Fougerouse D., Quadir M. Z. and Jercinovic M. J. (2021) Trace-element segregation to dislocation loops in experimentally heated zircon. *Am. Mineral.* **106**, 1971–1979.
- Peterman E. M., Reddy S. M., Saxey D. W., Fougerouse D., Snoeyenbos D. R. and Rickard W. D. A. (2019) Nanoscale processes of trace element mobility in metamorphosed zircon. *Contrib. to Mineral. Petrol.* **174**.
- Peterman E. M., Reddy S. M., Saxey D. W., Snoeyenbos D. R., Rickard W. D. A., Fougerouse D. and Kylander-Clark A. R. C. (2016) Nanogeochronology of discordant zircon measured by atom probe microscopy of Pb-enriched dislocation loops. *Sci. Adv.* **2**.
- Phelps P. R., Lee C.-T. A. and Morton D. M. (2020) Episodes of fast crystal growth in

- pegmatites. *Nat. Commun.* **11**, 4986.
- Philippe T., Gruber M., Vurpillot F. and Blavette D. (2010) Clustering and Local Magnification Effects in Atom Probe Tomography: A Statistical Approach. *Microsc. Microanal.* **16**, 643–648.
- Piazolo S., Austrheim H. and Whitehouse M. (2012) Brittle-ductile microfabrics in naturally deformed zircon: Deformation mechanisms and consequences for U-Pb dating. *Am. Mineral.* **97**, 1544–1563.
- Piazolo S., Belousova E., La Fontaine A., Corcoran C. and Cairney J. M. (2017) Trace element homogeneity from micron- to atomic scale: Implication for the suitability of the zircon GJ-1 as a trace element reference material. *Chem. Geol.* **456**, 10–18.
- Piazolo S., La Fontaine A., Trimby P., Harley S., Yang L., Armstrong R. and Cairney J. M. (2016) Deformation-induced trace element redistribution in zircon revealed using atom probe tomography. *Nat. Commun.* **7**, 10490.
- Pidgeon R. T. (2014) Zircon radiation damage ages. *Chem. Geol.* **367**, 13–22.
- Piechocka A. M., Gregory C. J., Zi J. W., Sheppard S., Wingate M. T. D. and Rasmussen B. (2017) Monazite trumps zircon: applying SHRIMP U-Pb geochronology to systematically evaluate emplacement ages of leucocratic, low-temperature granites in a complex Precambrian orogen. *Contrib. to Mineral. Petrol.* **172**, 1–17.
- Pitcher W. S. and Read H. H. (1963) Contact Metamorphism in Relation to Manner of Emplacement of the Granites of Donegal, Ireland. *J. Geol.* **71**, 261–296.
- Poirier J.-P. (1985) *Creep of Crystals: High-Temperature Deformation Processes in Metals, Ceramics and Minerals.*, Cambridge University Press, Cambridge.
- Putnis A. (1978) The mechanism of exsolution of hematite from iron-bearing rutile. *Phys. Chem. Miner.* **3**, 183–197.
- Putnis A. (1992) *An Introduction to Mineral Sciences.*, Cambridge University Press.
- Putnis A. (2002) Mineral replacement reactions: from macroscopic observations to microscopic mechanisms. *Mineral. Mag.* **66**, 689–708.
- Putnis A. (2009) Mineral replacement reactions. *Rev. Mineral. Geochemistry* **70**, 87–124.
- Putnis A. and Austrheim H. (2010) Fluid-induced processes: metasomatism and metamorphism. *Geofluids* **10**, 254–269.
- Pyle J. M. and Spear F. S. (2000) An empirical garnet (YAG) - xenotime thermometer. *Contrib. to Mineral. Petrol.* **138**, 51–58.

- Pyle J. M. and Spear F. S. (2003) Yttrium zoning in garnet: Coupling of major and accessory phases during metamorphic reactions. *Am. Mineral.* **88**, 708.
- Pyle J. M., Spear F. S., Rudnick R. L. and McDonough W. F. (2001) Monazite-xenotime-garnet equilibrium in metapelites and a new monazite-garnet thermometer. *J. Petrol.* **42**, 2083–2107.
- Rafiuddin M. R., Seydoux-Guillaume A.-M., Deschanel X., Mesbah A., Baumier C., Szenknect S. and Dacheux N. (2020) An in-situ electron microscopy study of dual ion-beam irradiated xenotime-type ErPO₄. *J. Nucl. Mater.* **539**, 152265.
- Rasmussen B. (2005) Radiometric dating of sedimentary rocks: The application of diagenetic xenotime geochronology. *Earth-Science Rev.* **68**, 197–243.
- Rasmussen B., Fletcher I. R. and Muhling J. R. (2011) Response of xenotime to prograde metamorphism. *Contrib. to Mineral. Petrol.* **162**, 1259–1277.
- Rasmussen B., Fletcher I. R., Bengtson S. and McNaughton N. J. (2004) SHRIMP U-Pb dating of diagenetic xenotime in the Stirling Range Formation, Western Australia: 1.8 Billion year minimum age for the Stirling biota. *Precambrian Res.* **133**, 329–337.
- Rasmussen B., Fletcher I. R., Muhling J. R. and Wilde S. A. (2010) In situ U-Th-Pb geochronology of monazite and xenotime from the Jack Hills belt: Implications for the age of deposition and metamorphism of Hadean zircons. *Precambrian Res.* **180**, 26–46.
- Rasmussen B., Fletcher I. R., Muhling J. R., Thorne W. S. and Broadbent G. C. (2007) Prolonged history of episodic fluid flow in giant hematite ore bodies: Evidence from in situ U-Pb geochronology of hydrothermal xenotime. *Earth Planet. Sci. Lett.* **258**, 249–259.
- Rasmussen B., Mueller A. G. and Fletcher I. R. (2009) Zirconolite and xenotime U-Pb age constraints on the emplacement of the golden mile dolerite sill and gold mineralization at the Mt charlotte mine, Eastern Goldfields Province, Yilgarn Craton, Western Australia. *Contrib. to Mineral. Petrol.* **157**, 559–572.
- Rasmussen B., Zi J. W., Sheppard S., Krapež B. and Muhling J. R. (2016) Multiple episodes of hematite mineralization indicated by U-Pb dating of iron-ore deposits, Marquette Range, Michigan, USA. *Geology* **44**, 547–550.
- Read A. S., Koning D. J., Smith G. A., Ralser S., Rodgers J. B. and Bauer P. A. (2000) geologic map of Santa Fe quadrangle, Santa Fe County, New Mexico New Mexico Bureau of Geology and Mineral Resources. Open-File GM 32, scale 124,000, 1 sheet.

- Reddy S. M., Saxey D. W., Rickard W. D. A., Fougereuse D., Montalvo S. D., Verberne R. and van Riessen A. (2020) Atom Probe Tomography: Development and Application to the Geosciences. *Geostand. Geoanalytical Res.* **44**, 5–50.
- Reddy S. M., van Riessen A., Saxey D. W., Johnson T. E., Rickard W. D. A., Fougereuse D., Fischer S., Prosa T. J., Rice K. P., Reinhard D. A., Chen Y. and Olson D. (2016) Mechanisms of deformation-induced trace element migration in zircon resolved by atom probe and correlative microscopy. *Geochim. Cosmochim. Acta* **195**, 158–170.
- Reinhard D. A., Moser D. E., Martin I., Rice K. P., Chen Y., Olson D., Lawrence D., Prosa T. J. and Larson D. J. (2017) Atom probe tomography of phalaborwa baddeleyite and reference zircon BR266. *Microstruct. Geochronol. Planet. Rec. Down to Atom Scale*, 315–326.
- Rickard W. D. A., Reddy S. M., Saxey D. W., Fougereuse D., Timms N. E., Daly L., Peterman E., Cavosie A. J. and Jourdan F. (2020) Novel Applications of FIB-SEM-Based ToF-SIMS in Atom Probe Tomography Workflows. *Microsc. Microanal.* **26**, 750–757.
- Ríos S., Salje E. K. H., Zhang M. and Ewing R. C. (2000) Amorphization in zircon: evidence for direct impact damage. *J. Phys. Condens. Matter* **12**, 2401.
- Rivers T., Culshaw N., Hynes A., Indares A., Jamieson R. and Martignole J. (2012) The Grenville Orogen - A post-Lithoprobe perspective. *Tecton. Styles Canada Lithoprobe Perspect.* **49**, 97–236.
- Rubatto D., Williams I. S. and Buick I. S. (2001) Zircon and monazite response to prograde metamorphism in the Reynolds Range, central Australia. *Contrib. to Mineral. Petrol.* **140**, 458–468.
- Ruiz-Agudo E., Putnis C. V and Putnis A. (2014) Coupled dissolution and precipitation at mineral–fluid interfaces. *Chem. Geol.* **383**, 132–146.
- Salier B. P., Groves D. I., McNaughton N. J. and Fletcher I. R. (2005) Geochronological and stable isotope evidence for widespread orogenic gold mineralization from a deep-seated fluid source at ca 2.65 Ga in the Laverton Gold Province, Western Australia. *Econ. Geol.* **100**, 1363–1388.
- Salje E. K. H., Chrosch J. and Ewing R. C. (1999) Is “metamictization” of zircon a phase transition? *Am. Mineral.* **84**, 1107–1116.
- Santhanagopalan D., Schreiber D. K., Perea D. E., Martens R. L., Janssen Y., Khalifah P. and

- Meng Y. S. (2015) Effects of laser energy and wavelength on the analysis of LiFePO₄ using laser assisted atom probe tomography. *Ultramicroscopy* **148**, 57–66.
- Schaltegger U., Pettke T., Audétat A., Reusser E. and Heinrich C. A. (2005) Magmatic-to-hydrothermal crystallization in the W–Sn mineralized Mole Granite (NSW, Australia). *Chem. Geol.* **220**, 215–235.
- Schaltegger U., Schmitt A. K. and Horstwood M. S. A. (2015) U–Th–Pb zircon geochronology by ID-TIMS, SIMS, and laser ablation ICP-MS: Recipes, interpretations, and opportunities. *Chem. Geol.* **402**, 89–110.
- Schipper C. I., Rickard W. D. A., Reddy S. M., Saxey D. W., Castro J. M., Fougereuse D., Quadir Z., Conway C., Prior D. J. and Lilly K. (2020) Volcanic SiO₂-cristobalite: A natural product of chemical vapor deposition. *Am. Mineral.* **105**, 510–524.
- Schmieder M. and Kring D. A. (2020) Earth's Impact Events Through Geologic Time: A List of Recommended Ages for Terrestrial Impact Structures and Deposits. *Astrobiology* **20**, 91–141.
- Schmieder M., Shaulis B. J., Lapen T. J., Buchner E. and Kring D. A. (2019) In situ U–Pb analysis of shocked zircon from the Charlevoix impact structure, Québec, Canada. *Meteorit. Planet. Sci.* **54**, 1808–1827.
- Schmieder M., Tohver E., Jourdan F., Denyszyn S. W. and Haines P. W. (2015) Zircons from the Acraman impact melt rock (South Australia): Shock metamorphism, U–Pb and ⁴⁰Ar/ ³⁹Ar systematics, and implications for the isotopic dating of impact events. *Geochim. Cosmochim. Acta* **161**, 71–100.
- Schneiderhan E., Zimmermann U., Gutzmer J., Mezger K. and Armstrong R. (2011) Sedimentary Provenance of the Neoproterozoic Ventersdorp Supergroup, Southern Africa: Shedding Light on the Evolution of the Kaapvaal Craton during the Neoproterozoic. *J. Geol.* **119**, 575–596.
- Schoene B., Crowley J. L., Condon D. J., Schmitz M. D. and Bowring S. A. (2006) Reassessing the uranium decay constants for geochronology using ID-TIMS U–Pb data. *Geochim. Cosmochim. Acta* **70**, 426–445.
- Schreiber D. K., Chiaramonti A. N., Gordon L. M. and Kruska K. (2014) Applicability of post-ionization theory to laser-assisted field evaporation of magnetite. *Appl. Phys. Lett.* **105**, 18–23.

- Schulte P., Alegret L., Arenillas I., Arz J. A., Barton P. J., Bown P. R., Bralower T. J., Christeson G. L., Claeys P., Cockell C. S., Collins G. S., Deutsch A., Goldin T. J., Goto K., Grajales-Nishimura J. M., Grieve R. A. F., Gulick S. P. S., Johnson K. R., Kiessling W., Koeberl C., Kring D. A., MacLeod K. G., Matsui T., Melosh J., Montanari A., Morgan J. V., Neal C. R., Nichols D. J., Norris R. D., Pierazzo E., Ravizza G., Rebolledo-Vieyra M., Reimold W. U., Robin E., Salge T., Speijer R. P., Sweet A. R., Urrutia-Fucugauchi J., Vajda V., Whalen M. T. and Willumsen P. S. (2010) The Chicxulub Asteroid Impact and Mass Extinction at the Cretaceous-Paleogene Boundary. *Science* **327**, 1214–1218.
- Seydoux-Guillaume A. M., Deschanelsls X., Baumier C., Neumeier S., Weber W. J. and Peugot S. (2018) Why natural monazite never becomes amorphous: Experimental evidence for alpha self-healing. *Am. Mineral.* **103**, 824–827.
- Seydoux-Guillaume A. M., Fougereuse D., Laurent A. T., Gardés E., Reddy S. M. and Saxey D. W. (2019) Nanoscale resetting of the Th/Pb system in an isotopically-closed monazite grain: A combined atom probe and transmission electron microscopy study. *Geosci. Front.* **10**, 65–76.
- Seydoux-Guillaume A.-M., Paquette J.-L., Wiedenbeck M., Montel J.-M. and Heinrich W. (2002a) Experimental resetting of the U–Th–Pb systems in monazite. *Chem. Geol.* **191**, 165–181.
- Seydoux-Guillaume A.-M., Wirth R., Heinrich W. and Montel J.-M. (2002b) Experimental determination of Thorium partitioning between monazite and xenotime using analytical electron microscopy and X-ray diffraction Rietveld analysis. *Eur. J. Mineral.* **14**, 869–878.
- Shannon R. D. (1976) Revised effective ionic radii and systematic studies of interatomic distances in halides and chalcogenides. *Acta Crystallogr. Sect. A* **32**, 751–767.
- Sheppard S., Rasmussen B., Muhling J. R., Farrell T. R. and Fletcher I. R. (2007) Grenvillian-aged orogenesis in the Palaeoproterozoic Gascoyne complex, Western Australia: 1030–950Ma reworking of the Proterozoic Capricorn Orogen. *J. Metamorph. Geol.* **25**, 477–494.
- Slagstad T., Hamilton M. A., Jamieson R. A. and Culshaw N. G. (2004) Timing and duration of melting in the mid orogenic crust: Constraints from U-Pb (SHRIMP) data, Muskoka and Shawanaga domains, Grenville Province, Ontario. *Can. J. Earth Sci.* **41**, 1339–1365.
- Soddy F. (1913) Intra-atomic Charge. *Nature* **92**, 399–400.

- Spear F. S. and Pyle J. M. (2002) Apatite, monazite, and xenotime in metamorphic rocks (in Phosphates; geochemical, geobiological, and materials importance) *Reviews in Mineralogy and Geochemistry. Rev. Mineral. Geochemistry* **48**, 293–335.
- Spencer C. J., Cawood P. A., Hawkesworth C. J., Prave A. R., Roberts N. M. W., Horstwood M. S. A. and Whitehouse M. J. (2015) Generation and preservation of continental crust in the Grenville Orogeny. *Geosci. Front.* **6**, 357–372.
- Stacey J. S. and Kramers J. D. (1975) Approximation of terrestrial lead isotope evolution by a two-stage model. *Earth Planet. Sci. Lett.* **26**, 207–221.
- Stern R. A. and Rayner N. (2003) Ages of several xenotime megacrysts by ID-TIMS: potential reference materials for ion microprobe U-Pb geochronology.,
- Stöffler D., Hamann C. and Metzler K. (2018) Shock metamorphism of planetary silicate rocks and sediments: Proposal for an updated classification system. *Meteorit. Planet. Sci.* **53**, 5–49.
- Stott, G.M., Sutcliffe, R.H., Thurston, P.C., Williams H. R. (1991) *The Grenville Province and the Proterozoic history of central and southern Ontario.*,
- Suzuki K. (1987) Grain-boundary enrichment of incompatible elements in some mantle peridotites. *Chem. Geol.* **63**, 319–334.
- Suzuki K. and Adachi I. M. (1991) Precambrian provenance and Silurian metamorphism of the Tsubonosawa paragneiss in the South Kitakami terrane, Northeast Japan, revealed by the chemical Th-U-total Pb isochron ages of monazite, zircon and xenotime. *Geochem. J.* **25**, 357–376.
- Suzuki K. and Kato T. (2008) CHIME dating of monazite, xenotime, zircon and polycrase: Protocol, pitfalls and chemical criterion of possibly discordant age data. *Gondwana Res.* **14**, 569–586.
- Tacchetto T., Clark C., Erickson T., Reddy S. M., Bhowany K. and Hand M. (2022a) Weakening the lower crust: conditions, reactions and deformation. *Lithos* **422–423**, 106738.
- Tacchetto T., Reddy S. M., Fougereuse D., Clark C., Saxey D. W. and Rickard W. D. A. (2022b) Crystal plasticity enhances trace element mobility in garnet. *Geology* **50**, 1387–1392.
- Tacchetto T., Reddy S. M., Saxey D. W., Fougereuse D., Rickard W. D. A. and Clark C. (2021) Disorientation control on trace element segregation in fluid-affected low-angle boundaries in olivine. *Contrib. to Mineral. Petrol.* **176**, 59.
- Thuvander M., Kvist A., Johnson L. J. S., Weidow J. and Andrén H.-O. (2013) Reduction of

- multiple hits in atom probe tomography. *Ultramicroscopy* **132**, 81–85.
- Timmermann H., Jamieson R. A., Culshaw N. G. and Parrish R. R. (1997) Time of metamorphism beneath the Central Metasedimentary Belt boundary thrust zone, Grenville Orogen, Ontario: accretion at 1080 Ma? *Can. J. Earth Sci.* **34**, 1023–1029.
- Timms N. E., Erickson T. M., Pearce M. A., Cavosie A. J., Schmieder M., Tohver E., Reddy S. M., Zanetti M. R., Nemchin A. A. and Wittmann A. (2017) A pressure-temperature phase diagram for zircon at extreme conditions. *Earth-Science Rev.* **165**, 185–202.
- Timms N. E., Kirkland C. L., Cavosie A. J., Rae A. S. P., Rickard W. D. A., Evans N. J., Erickson T. M., Wittmann A., Ferrière L., Collins G. S. and Gulick S. P. S. (2020) Shocked titanite records Chicxulub hydrothermal alteration and impact age. *Geochim. Cosmochim. Acta* **281**, 12–30.
- Tohver E., Lana C., Cawood P. A., Fletcher I. R., Jourdan F., Sherlock S., Rasmussen B., Trindade R. I. F., Yokoyama E., Souza Filho C. R. and Marangoni Y. (2012) Geochronological constraints on the age of a Permo–Triassic impact event: U–Pb and $40\text{Ar}/39\text{Ar}$ results for the 40km Araguinha structure of central Brazil. *Geochim. Cosmochim. Acta* **86**, 214–227.
- Trachenko K., Dove M. T. and Salje E. K. H. (2003) Large swelling and percolation in irradiated zircon. *J. Phys. Condens. Matter* **15**, L1–L7.
- Turuani M. J., Laurent A. T., Seydoux-Guillaume A.-M., Fougereuse D., Saxey D., Reddy S. M., Harley S. L., Reynaud S. and Rickard W. D. A. (2022) Partial retention of radiogenic Pb in galena nanocrystals explains discordance in monazite from Napier Complex (Antarctica). *Earth Planet. Sci. Lett.* **588**, 117567.
- Tuttle O. F. and Bowen N. L. (1958) Origin of granite in the light of experimental studies in the system $\text{NaAlSi}_3\text{O}_8\text{--KAlSi}_3\text{O}_8\text{--SiO}_2\text{--H}_2\text{O}$.
- Utsunomiya S., Palenik C. S., Valley J. W., Cavosie A. J., Wilde S. A. and Ewing R. C. (2004) Nanoscale occurrence of Pb in an Archean zircon. *Geochim. Cosmochim. Acta* **68**, 4679–4686.
- Valley J. W., Cavosie A. J., Ushikubo T., Reinhard D. A., Lawrence D. F., Larson D. J., Clifton P. H., Kelly T. F., Wilde S. A., Moser D. E. and Spicuzza M. J. (2014) Hadean age for a post-magma-ocean zircon confirmed by atom-probe tomography. *Nat. Geosci.* **7**, 219–223.

- Valley J. W., Reinhard D. A., Cavosie A. J., Ushikubo T., Lawrence D. F., Larson D. J., Kelly T. F., Snoeyenbos D. R. and Strickland A. (2015) Presidential Address. Nano-and micro-geochronology in Hadean and Archean zircons by atom-probe tomography and SIMS: New tools for old minerals. *Am. Mineral.* **100**, 1355–1377.
- Vallini D. A., Groves D. I., McNaughton N. J. and Fletcher I. R. (2007) Uraniferous diagenetic xenotime in northern Australia and its relationship to unconformity-associated uranium mineralisation. *Miner. Depos.* **42**, 51–64.
- Vallini D. A., Rasmussen B., Krapež B., Fletcher I. R. and McNaughton N. J. (2005) Microtextures, geochemistry and geochronology of authigenic xenotime: Constraining the cementation history of a Palaeoproterozoic metasedimentary sequence. *Sedimentology* **52**, 101–122.
- Vallini D., Rasmussen B., Krapež B., Fletcher I. R. and McNaughton N. J. (2002) Obtaining diagenetic ages from metamorphosed sedimentary rocks: U-Pb dating of unusually coarse xenotime cement in phosphatic sandstone. *Geology* **30**, 1083–1086.
- Van Emden B., Thornber M. R., Graham J. and Lincoln F. J. (1997) The incorporation of actinides in monazite and xenotime from placer deposits in Western Australia. *Can. Mineral.* **35**, 95–104.
- Vella A., Mazumder B., Da Costa G. and Deconihout B. (2011) Field evaporation mechanism of bulk oxides under ultra-fast laser illumination. *J. Appl. Phys.* **110**, 044321.
- Verberne R., Reddy S. M., Saxey D. W., Fougereuse D., Rickard W. D. A., Plavska D., Agangi A. and Kylander-Clark A. R. C. (2020) The geochemical and geochronological implications of nanoscale trace-element clusters in rutile. *Geology* **XX**, 1–5.
- Verberne R., Reddy S. M., Saxey D. W., Fougereuse D., Rickard W. D. A., Quadir Z., Evans N. J. and Clark C. (2022) Dislocations in minerals: Fast-diffusion pathways or trace-element traps? *Earth Planet. Sci. Lett.* **584**, 117517.
- Verberne R., Saxey D. W., Reddy S. M., Rickard W. D. A., Fougereuse D. and Clark C. (2019) Analysis of Natural Rutile (TiO₂) by Laser-assisted Atom Probe Tomography. *Microsc. Microanal.* **25**, 539–546.
- Verberne R., van Schroyen Lantman H. W., Reddy S. M., Alvaro M., Wallis D., Fougereuse D., Langone A., Saxey D. W. and Rickard W. D. A. (2023) Trace-element heterogeneity in rutile linked to dislocation structures: Implications for Zr-in-rutile geothermometry. *J.*

- Metamorph. Geol.* **41**, 3–24.
- Vermeesch P. (2018) IsoplotR: A free and open toolbox for geochronology. *Geosci. Front.* **9**, 1479–1493.
- Villa I. M. and Hanchar J. M. (2017) Age discordance and mineralogy. *Am. Mineral.* **102**, 2422–2439.
- Vurpillot F., Bostel A. and Blavette D. (2000) Trajectory overlaps and local magnification in three-dimensional atom probe. *Appl. Phys. Lett.* **76**, 3127–3129.
- Watanabe T. (1985) Structural effects on grain boundary segregation, hardening and fracture. *Le J. Phys. Colloq.* **46**, C4-555-C4-566.
- Watson E. B. (1996) Surface enrichment and trace-element uptake during crystal growth. *Geochim. Cosmochim. Acta* **60**, 5013–5020.
- White L. F., Darling J. R., Moser D. E., Cayron C., Barker I., Dunlop J. and Tait K. T. (2018) Baddeleyite as a widespread and sensitive indicator of meteorite bombardment in planetary crusts. *Geology* **46**, 719–722.
- White L. F., Darling J. R., Moser D. E., Reinhard D. A., Dunlop J., Larson D. J., Lawrence D. and Martin I. (2017) Complex Nanostructures in Shocked, Annealed, and Metamorphosed Baddeleyite Defined by Atom Probe Tomography. In *Microstructural Geochronology: Planetary Records Down to Atom Scale* pp. 351–367.
- White L. F., Darling J. R., Moser D. E., Reinhard D. A., Prosa T. J., Bullen D., Olson D., Larson D. J., Lawrence D. and Martin I. (2017) Atomic-scale age resolution of planetary events. *Nat. Commun.* **8**, 1–6.
- White L. F., Moser D. E., Tait K. T., Langelier B., Barker I. and Darling J. R. (2019) Crystallization and impact history of a meteoritic sample of early lunar crust (NWA 3163) refined by atom probe geochronology. *Geosci. Front.* **10**, 1841–1848.
- White L. F., Moser D. E., Tait K. T., Langelier B., Barker I. and Darling J. R. (2019) Crystallization and impact history of a meteoritic sample of early lunar crust (NWA 3163) refined by atom probe geochronology. *Geosci. Front.* **10**, 1841–1848.
- Williams C. A., Haley D., Marquis E. A., Smith G. D. W. and Moody M. P. (2013) Defining clusters in APT reconstructions of ODS steels. *Ultramicroscopy* **132**, 271–278.
- Williams C. A., Smith G. D. W. and Marquis E. A. (2013) Quantifying the composition of yttrium and oxygen rich nanoparticles in oxide dispersion strengthened steels.

Ultramicroscopy **125**, 10–17.

Williams M. L., Jercinovic M. J., Harlov D. E., Budzyń B. and Hetherington C. J. (2011) Resetting monazite ages during fluid-related alteration. *Chem. Geol.* **283**, 218–225.

Zi J. W., Rasmussen B., Muhling J. R., Fletcher I. R., Thorne A. M., Johnson S. P., Cutten H. N., Dunkley D. J. and Korhonen F. J. (2015) In situ U-Pb geochronology of xenotime and monazite from the Abra polymetallic deposit in the Capricorn Orogen, Australia: Dating hydrothermal mineralization and fluid flow in a long-lived crustal structure. *Precambrian Res.* **260**, 91–112.

Appendices

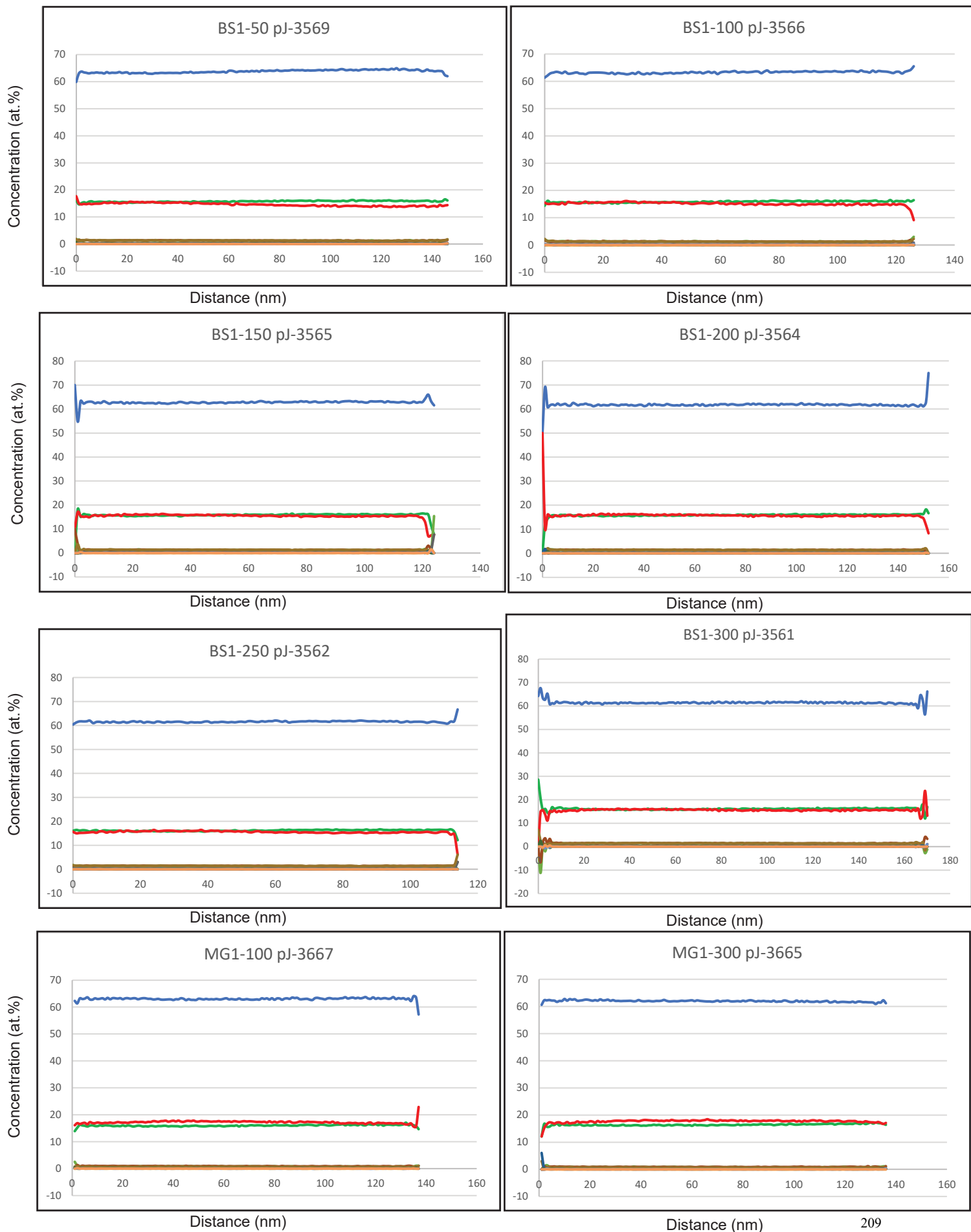
Appendix 2.1

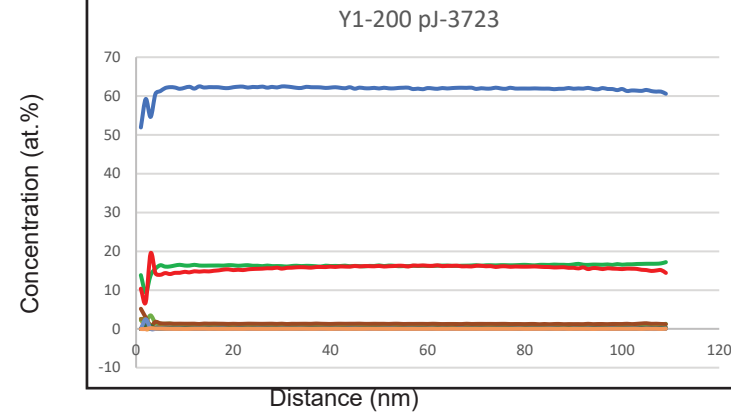
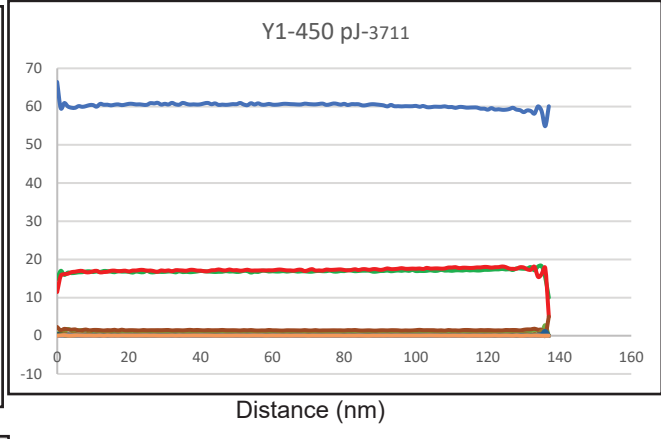
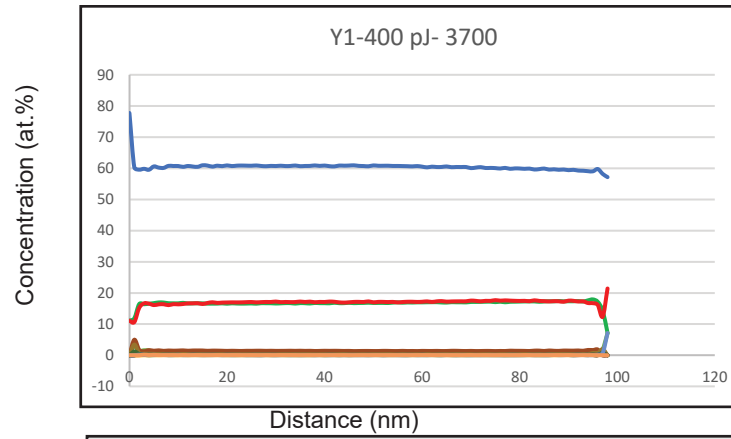
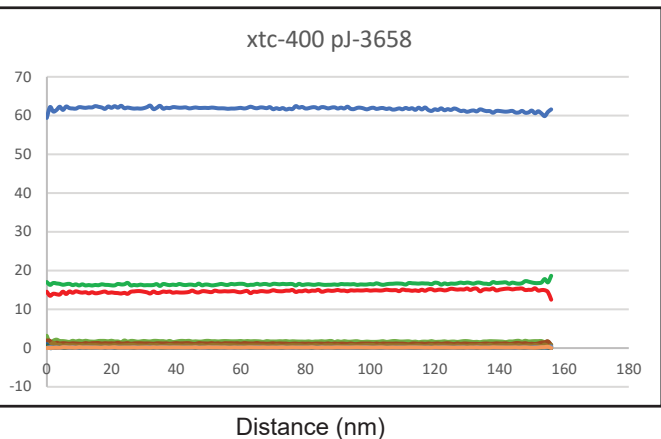
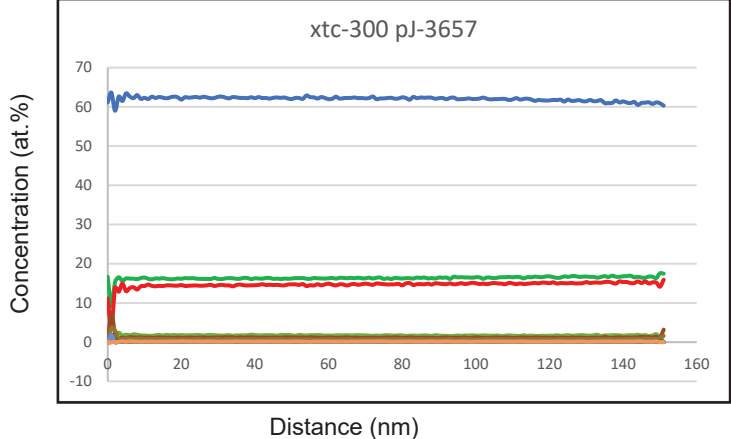
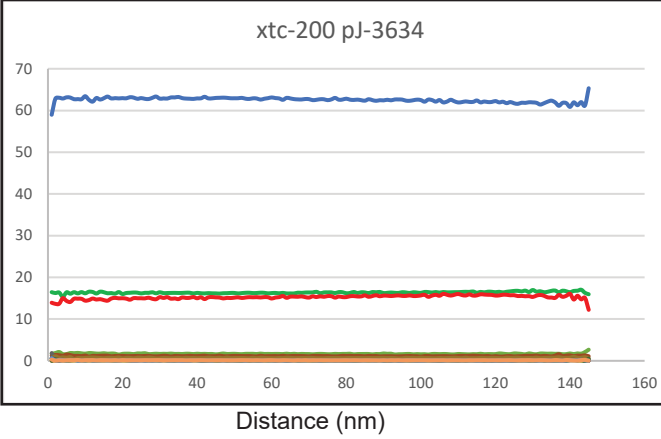
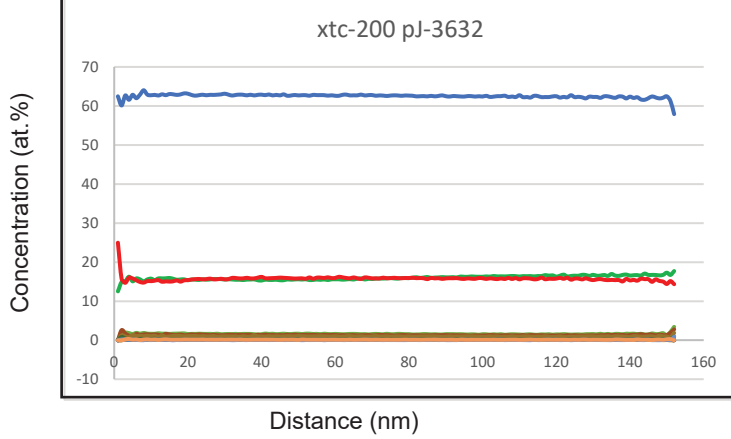
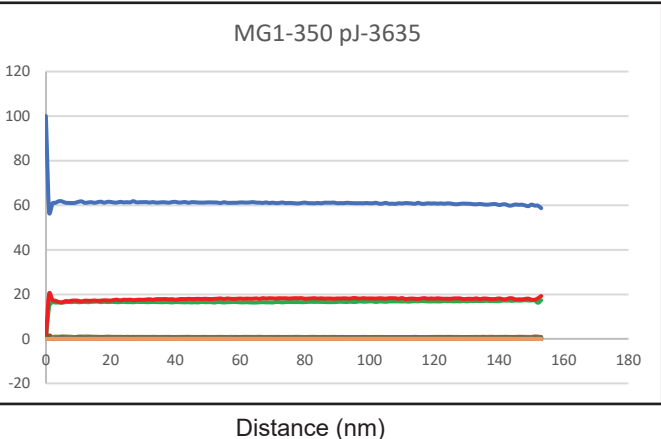
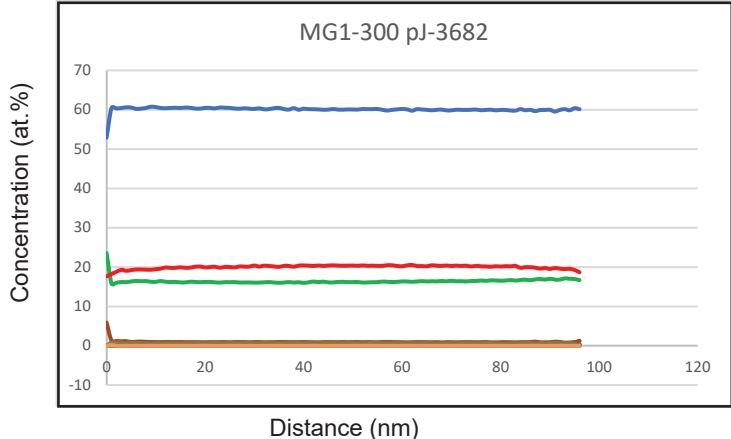
Laser pulse energy and surface diffusion in xenotime analysis

In laser assisted atom probe tomography, field evaporation of atoms from the surface of the specimen, which is held under a high electric field, is triggered by a laser pulse. The atom absorbs the heat energy from the laser pulse, gets ionized, and is accelerated by the high field to the position-sensitive detector. The detector records the x,y position of the ionic species and the z coordinate is acquired from the order in which the ions are evaporated, giving the 3d reconstruction of the sample analysed. The time of flight of the ionic specie, initiated by the laser pulse, from the apex of the specimen to the detector, helps to identify the ion species from mass-to-charge ratio and gives compositional detail of the sample. Previous studies on oxides and metals have identified a laser energy dependent surface diffusion of ionic species (Kirchhofer et al., 2013; Devaraj et al., 2013; Diercks et al., 2013, 2014; Diercks and Gorman, 2015). Surface diffusion of ionic species is attributed to the high temperature availed from high laser pulse energies, creating mobile ions on the surface of the tip apex which are then evaporated and detected at locations different from their original position in the sample. This phenomenon can lead to differences in local and stoichiometric compositions (Kirchhofer et al., 2013; Diercks et al., 2014). In many minerals, a compositional gradient is observed related to the laser direction, often with more complex molecular ionic species forming on the laser incident side of the specimen (Cappelli et al., 2021). The crystallography of a sample can also the migration of ionic species to particular crystallographic directions (Gault et al., 2012). Therefore, in order to assess if there are any compositional differences due to surface migration of ions with different laser pulse energies in xenotime, 1D concentration profiles of decomposed ionic species are plotted for every analysis from 50 pJ to 450 pJ. The data quality test is performed by creating a rectangular ROI that encompasses the whole dataset and rotating around the z-axis such that one of the ROI axes aligns with the laser direction. A compositional profile then shows the profiles across xy plane, parallel with the laser direction and perpendicular to the z axis. Composition of major atomic species (Y,P,O) and minor species of interest (HREEs-Gd, Tb, Dy, Ho, Er, Tm, Yb, and Lu, Pb, Ca) in xenotime is plotted. The results show no significant compositional variation in all the datasets analysed. There is variation at each end of the compositional graph which corresponds to places where there are very low counts in each (1 nm) bin of the 1D profile, as it reaches the edges of the dataset. Therefore, this data analysis reveals that negligible surface diffusion occurs during laser

assisted analysis of xenotime. This characteristic is probably due to high thermal diffusivity of xenotime as observed in the case of zircon (La Fontaine et al., 2017).

Compositional profiles of elements from xenotime standards



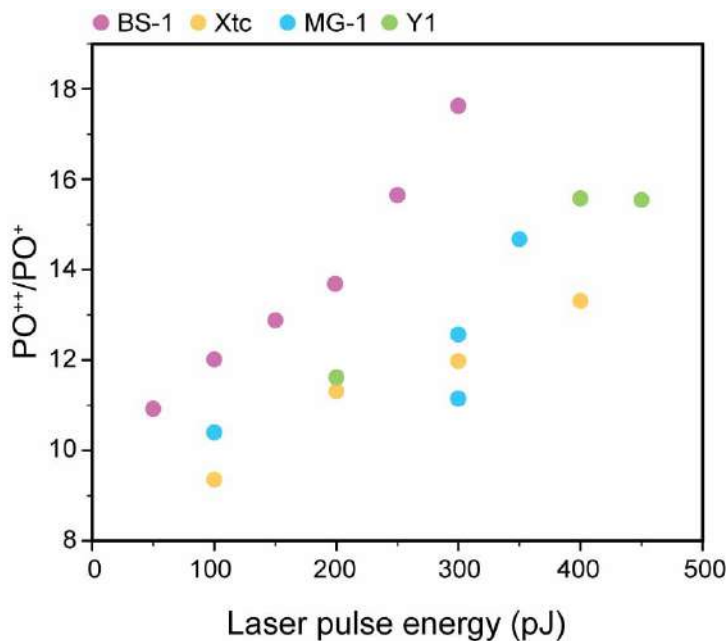


Composition profiles of Y, P, O, HREEs (Gd-Lu), Ca and Pb (decomposed) from different xenotime standards analysed at varied laser pulse energies (50-450 pJ) across x-y plane, parallel to the laser incident direction.

References

- Cappelli C., Smart S., Stowell H. and Pérez-Huerta A. (2021) Exploring Biases in Atom Probe Tomography Compositional Analysis of Minerals. *Geostand. Geoanalytical Res.* **45**, 457–476.
- Devaraj A., Colby R., Hess W. P., Perea D. E. and Thevuthasan S. (2013) Role of Photoexcitation and Field Ionization in the Measurement of Accurate Oxide Stoichiometry by Laser-Assisted Atom Probe Tomography. *J. Phys. Chem. Lett.* **4**, 993–998.
- Diercks D. R. and Gorman B. P. (2015) Nanoscale Measurement of Laser-Induced Temperature Rise and Field Evaporation Effects in CdTe and GaN. *J. Phys. Chem. C* **119**, 20623–20631.
- Diercks D. R., Gorman B. P., Kirchhofer R., Sanford N., Bertness K. and Brubaker M. (2013) Atom probe tomography evaporation behavior of C-axis GaN nanowires: Crystallographic, stoichiometric, and detection efficiency aspects. *J. Appl. Phys.* **114**, 184903.
- Diercks D. R., Gorman B. P., Manerbino A. and Coors G. (2014) Atom Probe Tomography of Yttrium-Doped Barium–Cerium–Zirconium Oxide with NiO Addition ed. P. Salvador. *J. Am. Ceram. Soc.* **97**, 3301–3306.
- La Fontaine A., Piazzolo S., Trimby P., Yang L. and Cairney J. M. (2017) Laser-Assisted Atom Probe Tomography of Deformed Minerals: A Zircon Case Study. *Microsc. Microanal.* **23**, 404–413.
- Gault B., Danoix F., Hoummada K., Mangelinck D. and Leitner H. (2012) Impact of directional walk on atom probe microanalysis. *Ultramicroscopy* **113**, 182–191.
- Kirchhofer R., Teague M. C. and Gorman B. P. (2013) Thermal effects on mass and spatial resolution during laser pulse atom probe tomography of cerium oxide. *J. Nucl. Mater.* **436**, 23–28.

Appendix 2.2



Mass spectra from xenotime are complex, containing many molecular combinations of Y,P,O and REEs. The charge state ratio (CSR) of a major ion in xenotime PO (PO^{++}/PO^+) is plotted as a function of laser pulse energy. It is observed that the PO CSR increases with increasing laser pulse energy for each sample analysed. This positive trend indicates the formation of higher charge state species at higher laser pulse energy. A similar trend has also observed in rutile (Verberne et al., 2019) and magnetite (Schreiber et al., 2014). Even though the background counts are low at higher laser pulse energies (Figure 2.4) the $ThPO_3^{+++}$ ion formation is found to be higher in higher laser pulse energies (Figure 2.4), as shown by PO CSR where higher charge state is favoured in higher laser pulse energies, which is critical in xenotime nanogeochronology. Therefore, considering all the results the optimum laser pulse energy for xenotime analysis can be suggested is 100 to 200 pJ, where the a balance can find between background counts and higher charge state formation of ionic species.

References

- Schreiber D. K., Chiaramonti A. N., Gordon L. M. and Kruska K. (2014) Applicability of post ionization theory to laser-assisted field evaporation of magnetite. *Appl. Phys. Lett.* **105**, 18–23.
- Verberne R., Saxey D. W., Reddy S. M., Rickard W. D. A., Fougereuse D. and Clark C. (2019) Analysis of Natural Rutile (TiO₂) by Laser-assisted Atom Probe Tomography. *Microsc. Microanal.* **25**, 539–546.

Appendix 3.1

SHRIMP standard data

Summary										
Standard	Session	$^{206}\text{Pb}^*/^{238}\text{U}$ Age (Ma)	± 2 s.d .	MSWD	p	$^{207}\text{Pb}^*/^{206}\text{Pb}^*$ Age (Ma)	± 2 s.d .	MSWD	p	n
MG-1 (Primary)	10- 12/01/20 22	489	44	1.02	0.4 3	517	275	1	0.4 5	19 of 21
MG-1 (Primary)	15- 17/03/20 22	490	38	0.96	0.5 0	621	221	0.97	0.4 8	18 of 18
Published age		489.96	0.5 4			491.8	1.1	<i>Fletcher et al., 2004</i>		
Y1	15- 17/03/20 22	974	57	0.31	0.9 6	949	21	1.5	0.1 6	9 of 10
Published age		~948				948	5	<i>Fletcher et al., 2000</i>		

Appendix 3.1

SHRIMP results - standard data

10-12 January

Sample	Spot	Th		Th/U
		U (ppm) ^c	(ppm) ^c	
MG-1	MG1.2.1	1019	874	0.89
MG-1	MG1.2.2	1107	1166	1.09
MG-1	MG1.2.3	966	863	0.92
MG-1	MG1.2.4	1010	845	0.87
MG-1	MG1.2.5	837	772	0.95
MG-1	MG1.2.6	1005	946	0.97
MG-1	MG1.2.7	1196	1246	1.08
MG-1	MG1.2.8	926	900	1.00
MG-1	MG1.2.9	989	826	0.86
MG-1	MG1.2.11	839	900	1.11
MG-1	MG1.2.12	914	811	0.92
MG-1	MG1.2.13	846	930	1.14
MG-1	MG1.2.14	993	962	1.00
MG-1	MG1.2.15	1156	1254	1.12
MG-1	MG1.2.16	989	870	0.91
MG-1	MG1.2.17	942	1072	1.18
MG-1	MG1.2.18	988	1051	1.10
MG-1	MG1.2.19	1211	1336	1.14
MG-1	MG1.2.20	1064	1049	1.02
MG-1	MG1.2.10	852	717	0.87
MG-1	MG1.3.1	1151	933	0.84

Session 2 - 15-17/03/2022 (U-Pb)**10-12 January**

Sample	Spot	Th		Th/U
		U (ppm) ^c	(ppm) ^c	
MG1	MG1.2.3	1038	961	0.93
MG1	MG1.2.5	1000	880	0.88
MG1	MG1.2.6	928	827	0.89
MG1	MG1.2.7	1023	933	0.91
MG1	MG1.2.8	1080	1028	0.95
MG1	MG1.2.9	823	808	0.98
MG1	MG1.2.10	942	935	0.99
MG1	MG1.2.11	879	805	0.92
MG1	MG1.2.12	1143	1060	0.93
MG1	MG1.2.13	844	978	1.16
MG1	MG1.2.14	1025	1125	1.10
MG1	MG1.2.15	1045	1061	1.02
MG1	MG1.2.16	847	903	1.07
MG1	MG1.2.17	953	1018	1.07
MG1	MG1.2.18	1134	1334	1.18
MG1	MG1.2.19	1030	1101	1.07
MG1	MG1.2.20	1171	1148	0.98
MG1	MG1.2.21	1094	1221	1.12

²⁰⁴Pb-corrected ratios (not matrix-corrected)

²⁰⁶ Pb*/ ²³⁸ U	± 2 s.e.	²³⁸ U/ ²⁰⁶ Pb	± 2 s.e.	²⁰⁷ Pb*/ ²⁰⁶ Pb	± 2 s.e.	²⁰⁸ Pb*/ ²³² Th	± 2 s.e.	²⁰⁸ Pb*/ ²⁰⁶ Pb	± 2 s.e.
0.07792	0.00588	12.83348	0.96902	0.05254	0.00752	0.02728	0.00298	0.30405	0.02482
0.08117	0.02155	12.32002	3.27097	0.05673	0.02836	0.02688	0.01169	0.35740	0.12406
0.07979	0.00584	12.53289	0.91728	0.06111	0.00424	0.02514	0.00288	0.29414	0.02471
0.08681	0.00662	11.51958	0.87783	0.06127	0.00795	0.03013	0.00353	0.30390	0.02552
0.07656	0.01107	13.06250	1.88898	0.05604	0.00869	0.02525	0.00428	0.30670	0.02753
0.07687	0.00582	13.00921	0.98439	0.05677	0.00760	0.02578	0.00292	0.32960	0.02629
0.07704	0.00567	12.98107	0.95534	0.05012	0.00713	0.02569	0.00271	0.36492	0.02597
0.07367	0.00669	13.57424	1.23329	0.06039	0.00447	0.02350	0.00305	0.32037	0.02776
0.08421	0.00672	11.87489	0.94802	0.05718	0.00758	0.02794	0.00346	0.28636	0.02534
0.07743	0.00653	12.91554	1.09009	0.05753	0.00796	0.02668	0.00314	0.38555	0.02935
0.08076	0.00627	12.38240	0.96183	0.06087	0.00747	0.02632	0.00242	0.30223	0.01239
0.07569	0.00624	13.21231	1.09016	0.05520	0.01375	0.02424	0.00285	0.35281	0.03031
0.07562	0.00614	13.22430	1.07463	0.05554	0.00890	0.02348	0.00296	0.30635	0.02902
0.07569	0.00541	13.21224	0.94500	0.04952	0.00761	0.02284	0.00252	0.33461	0.02729
0.08099	0.00656	12.34713	0.99933	0.05390	0.00749	0.02699	0.00335	0.30299	0.02661
0.07891	0.00591	12.67279	0.94977	0.06017	0.00739	0.02500	0.00270	0.37590	0.02734
0.07494	0.00563	13.34479	1.00303	0.05488	0.00693	0.02324	0.00258	0.34100	0.02599
0.08570	0.00599	11.66911	0.81552	0.05571	0.00748	0.02708	0.00286	0.35691	0.02705
0.07986	0.00609	12.52160	0.95510	0.05640	0.00763	0.02534	0.00290	0.31998	0.02643
0.07708	0.00624	12.97406	1.05004	0.04694	0.00724	0.02360	0.00304	0.26620	0.02508
0.08455	0.00590	11.82712	0.82534	0.04868	0.00691	0.02793	0.00302	0.27961	0.02193

²⁰⁴Pb-corrected ratios (not matrix-corrected)

²⁰⁶ Pb*/ ²³⁸ U	± 2 s.e.	²³⁸ U/ ²⁰⁶ Pb	± 2 s.e.	²⁰⁷ Pb*/ ²⁰⁶ Pb	± 2 s.e.	²⁰⁸ Pb*/ ²³² Th	± 2 s.e.	²⁰⁸ Pb*/ ²⁰⁶ Pb	± 2 s.e.
0.08398	0.00528	11.90806	0.74852	0.05712	0.00558	0.28880	0.01791	0.02477	0.00230
0.07946	0.00523	12.58459	0.82785	0.06201	0.00699	0.29417	0.02001	0.02397	0.00230
0.07447	0.00499	13.42818	0.90006	0.06103	0.00546	0.31922	0.01831	0.02541	0.00237
0.07691	0.00522	13.00167	0.88161	0.05963	0.00585	0.30539	0.01871	0.02410	0.00230
0.08211	0.00541	12.17896	0.80299	0.06518	0.00737	0.32041	0.02113	0.02463	0.00233
0.07825	0.00517	12.78017	0.84496	0.05890	0.00628	0.33587	0.03503	0.02487	0.00320
0.07668	0.00507	13.04082	0.86192	0.05423	0.00553	0.32618	0.01873	0.02487	0.00226
0.08203	0.00530	12.19054	0.78824	0.05107	0.00646	0.27256	0.01968	0.02472	0.00236
0.08066	0.00506	12.39805	0.77736	0.06087	0.00557	0.30693	0.01824	0.02541	0.00254
0.08084	0.00481	12.36997	0.73590	0.07101	0.00637	0.39262	0.02048	0.02521	0.00209
0.07924	0.00515	12.61987	0.81970	0.06132	0.00525	0.34523	0.01828	0.02382	0.00212
0.08487	0.00608	11.78322	0.84377	0.06130	0.00704	0.34028	0.02253	0.02661	0.00270
0.07811	0.00556	12.80235	0.91207	0.06621	0.00793	0.37799	0.04324	0.02484	0.00353
0.07576	0.00600	13.19889	1.04557	0.06566	0.00757	0.37021	0.02431	0.02429	0.00285
0.07671	0.00560	13.03638	0.95122	0.06153	0.00527	0.39193	0.02037	0.02463	0.00236
0.07597	0.00584	13.16330	1.01217	0.05859	0.00726	0.38361	0.01542	0.02569	0.00236
0.07474	0.00552	13.37980	0.98877	0.06028	0.00351	0.34187	0.02207	0.02523	0.00263
0.08084	0.00576	12.37074	0.88090	0.05674	0.00617	0.34387	0.02284	0.02393	0.00246

²⁰⁴Pb-corrected, matrix-corrected ratios^d

^{(238)U/²⁰⁶Pb*)_m}	± 2 s.e.	^{(207)Pb*/²⁰⁶Pb*)_m}	± 2 s.e.	^{(206)Pb*/²³⁸U)_m}	± 2 s.e.	^{(207)Pb*/²³⁵U)_m}	± 2 s.e.	^{(208)Pb*/²³²Th)_m}	± 2 s.e.
12.83126	1.10167	0.05254	0.00752	0.07793	0.00669	0.56437	0.09420	#N/A	#N/A
12.33703	3.40807	0.05673	0.02836	0.08106	0.02239	0.63373	0.36192	#N/A	#N/A
12.52567	1.04600	0.06111	0.00424	0.07984	0.00667	0.67235	0.07301	#N/A	#N/A
11.51578	0.99659	0.06127	0.00795	0.08684	0.00752	0.73331	0.11438	#N/A	#N/A
13.03952	2.01727	0.05604	0.00869	0.07669	0.01186	0.59231	0.12977	#N/A	#N/A
13.00876	1.11916	0.05677	0.00760	0.07687	0.00661	0.60145	0.09571	#N/A	#N/A
13.01046	1.09484	0.05012	0.00713	0.07686	0.00647	0.53090	0.08771	#N/A	#N/A
13.56437	1.37200	0.06039	0.00447	0.07372	0.00746	0.61362	0.07691	#N/A	#N/A
11.86858	1.06998	0.05718	0.00758	0.08426	0.00760	0.66397	0.10640	#N/A	#N/A
12.89834	1.22072	0.05753	0.00796	0.07753	0.00734	0.61473	0.10307	#N/A	#N/A
12.36875	1.08779	0.06087	0.00747	0.08085	0.00711	0.67827	0.10245	#N/A	#N/A
13.19658	1.22420	0.05520	0.01375	0.07578	0.00703	0.57645	0.15325	#N/A	#N/A
13.22342	1.21156	0.05554	0.00890	0.07562	0.00693	0.57885	0.10686	#N/A	#N/A
13.23880	1.08632	0.04952	0.00761	0.07554	0.00620	0.51550	0.08983	#N/A	#N/A
12.34223	1.12643	0.05390	0.00749	0.08102	0.00739	0.60187	0.10004	#N/A	#N/A
12.67193	1.08099	0.06017	0.00739	0.07891	0.00673	0.65438	0.09790	#N/A	#N/A
13.34722	1.14178	0.05488	0.00693	0.07492	0.00641	0.56664	0.08640	#N/A	#N/A
11.70010	0.94147	0.05571	0.00748	0.08547	0.00688	0.65624	0.10273	#N/A	#N/A
12.53041	1.08643	0.05640	0.00763	0.07981	0.00692	0.62027	0.09965	#N/A	#N/A
12.95030	1.18020	0.04694	0.00724	0.07722	0.00704	0.49957	0.08947	#N/A	#N/A
11.83820	0.94972	0.04868	0.00691	0.08447	0.00678	0.56672	0.09239	#N/A	#N/A

²⁰⁴Pb-corrected, matrix-corrected ratios^d

^{(238)U/²⁰⁶Pb*)_m}	± 2 s.e.	^{(207)Pb*/²⁰⁶Pb*)_m}	± 2 s.e.	^{(206)Pb*/²³⁸U)_m}	± 2 s.e.	^{(207)Pb*/²³⁵U)_m}	± 2 s.e.	^{(208)Pb*/²³²Th)_m}	± 2 s.e.
11.90941	0.87215	0.05712	0.00558	0.08397	0.00615	0.66103	0.08075	#N/A	#N/A
12.57942	0.95751	0.06201	0.00699	0.07949	0.00605	0.67941	0.09241	#N/A	#N/A
13.41363	1.03700	0.06103	0.00546	0.07455	0.00576	0.62706	0.07413	#N/A	#N/A
13.00061	1.01622	0.05963	0.00585	0.07692	0.00601	0.63214	0.07930	#N/A	#N/A
12.18658	0.93040	0.06518	0.00737	0.08206	0.00626	0.73707	0.10057	#N/A	#N/A
12.75635	0.97380	0.05890	0.00628	0.07839	0.00598	0.63637	0.08345	#N/A	#N/A
13.03259	0.99585	0.05423	0.00553	0.07673	0.00586	0.57344	0.07303	#N/A	#N/A
12.17237	0.91188	0.05107	0.00646	0.08215	0.00615	0.57827	0.08497	#N/A	#N/A
12.41252	0.90799	0.06087	0.00557	0.08056	0.00589	0.67588	0.07921	#N/A	#N/A
12.35547	0.86211	0.07101	0.00637	0.08094	0.00565	0.79204	0.09004	#N/A	#N/A
12.62687	0.95157	0.06132	0.00525	0.07920	0.00597	0.66930	0.07636	#N/A	#N/A
11.78899	0.96687	0.06130	0.00704	0.08482	0.00696	0.71662	0.10117	#N/A	#N/A
12.78451	1.04187	0.06621	0.00793	0.07822	0.00637	0.71375	0.10339	#N/A	#N/A
13.19504	1.18170	0.06566	0.00757	0.07579	0.00679	0.68582	0.10011	#N/A	#N/A
13.06229	1.09068	0.06153	0.00527	0.07656	0.00639	0.64924	0.07764	#N/A	#N/A
13.17004	1.14980	0.05859	0.00726	0.07593	0.00663	0.61314	0.09294	#N/A	#N/A
13.40183	1.13119	0.06028	0.00351	0.07462	0.00630	0.61992	0.06355	#N/A	#N/A
12.38737	1.01185	0.05674	0.00617	0.08073	0.00659	0.63130	0.08590	#N/A	#N/A

²⁰⁴Pb-corrected, matrix-corrected dates^d						
$(^{206}\text{Pb}^*/^{238}\text{U})_m$ Age		$(^{207}\text{Pb}^*/^{206}\text{Pb}^*)_m$		$(^{207}\text{Pb}^*/^{235}\text{U})_m$ Age		
(Ma)	± 2 s.e.	Age (Ma)	± 2 s.e.	(Ma)	± 2 s.e.	Disc. (%)
484	40	308	326	454	61	-57.2
502	134	480	1104	498	229	-4.8
495	40	642	149	522	44	22.8
537	45	648	279	558	67	17.0
476	71	453	344	472	83	-5.3
477	40	482	296	478	61	0.7
477	39	199	330	432	58	-139.7
459	45	617	160	486	48	25.6
521	45	497	292	517	65	-5.0
481	44	511	304	487	65	5.7
501	42	634	264	526	62	20.8
471	42	419	556	462	99	-12.5
470	42	433	357	464	69	-8.7
469	37	171	359	422	60	-174.2
502	44	366	313	478	63	-37.5
490	40	609	266	511	60	19.4
466	38	406	282	456	56	-14.8
529	41	440	299	512	63	-20.3
495	41	467	300	490	63	-6.1
479	42	45	368	411	61	-961.3
523	40	131	334	456	60	-298.5

²⁰⁴Pb-corrected, matrix-corrected dates^d						
$(^{206}\text{Pb}^*/^{238}\text{U})_m$ Age		$(^{207}\text{Pb}^*/^{206}\text{Pb}^*)_m$		$(^{207}\text{Pb}^*/^{235}\text{U})_m$ Age		
(Ma)	± 2 s.e.	Age (Ma)	± 2 s.e.	(Ma)	± 2 s.e.	Disc. (%)
520	37	495	215	515	49	-4.9
493	36	674	241	526	56	26.8
464	35	639	192	494	46	27.5
478	36	589	213	497	49	18.9
508	37	779	238	561	59	34.7
487	36	563	232	500	52	13.5
477	35	379	229	460	47	-25.6
509	37	243	291	463	55	-109.3
499	35	634	197	524	48	21.2
502	34	957	183	592	51	47.6
491	36	650	184	520	46	24.4
525	41	649	247	549	60	19.1
485	38	812	250	547	61	40.2
471	41	795	242	530	60	40.7
476	38	657	184	508	48	27.6
472	40	551	270	486	59	14.4
464	38	613	126	490	40	24.3
500	39	481	240	497	54	-4.1

Appendix 3.1

SHRIMP results - sample 6413 - color coded with SHRIMP spot

location

Sample	Spot	U (ppm) ^c	Th (ppm) ^c	Th/U	²⁰⁶ Pb/ ²⁰⁴ Pb
z6413/XE\XNO1.3		14844	2558	0.18	10000000000000000000000000000000
z6413/XE\XNO1.5		14009	2438	0.18	167575
z6413/XE\XNO1.6		13776	2384	0.18	166036
z6413/XE\XNO1.7		15043	2574	0.18	349902
z6413/XE\XNO1.9		11714	2044	0.18	271627
z6413/XE\XNO1.10		11898	2033	0.18	99213
z6413/XE\XNO1.12		12017	2090	0.18	-174127
z6413/XE\XNO1.13		13613	2378	0.18	158146
z6413/XE\XNO1.14		14227	2457	0.18	325780
z6413/XE\XNO1.15		15019	2615	0.18	106284
z6413/XE\XNO1.4		15033	2591	0.18	181895
z6413/XE\XNO1.11		13264	2279	0.18	-330511
z6413/XE\XNO1.16		13523	2369	0.18	334269
z6413/XE\XNO1.17		12687	2232	0.18	107759
z6413/XE\XNO1.18		16440	2827	0.18	-389105
z6413/XE\XNO1.19		14899	2602	0.18	10000000000000000000000000000000
z6413/XE\XNO1.1		14361	2539	0.18	343135
z6413/XE\XNO1.2		14625	2599	0.18	47524446060138
z6413/XE\XNO1.3		14297	2513	0.18	141685
z6413/XE\XNO1.4		15849	2819	0.18	248465
z6413/XE\XNO1.5		14381	2557	0.18	-79358
z6413/XE\XNO1.6		15812	2773	0.18	-71133
z6413/XE\XNO1.7		14639	2593	0.18	-120417
z6413/XE\XNO1.8		15178	2701	0.18	126045
z6413/XE\XNO1.9		14898	2688	0.19	-54965
z6413/XE\XNO1.10		14396	2516	0.18	-119850
z6413/XE\XNO1.11		14658	2555	0.18	-82448
z6413/XE\XNO1.13		13660	2418	0.18	-110051
z6413/XE\XNO1.14		12919	2256	0.18	-107945
z6413/XE\ZNO1.1		13689	2331	0.18	-45946
z6413/XE\ZNO1.2		13446	2382	0.18	-153627
z6413/XE\ZNO1.3		13327	2303	0.18	-231786
z6413/XE\ZNO1.4		13721	2450	0.18	60686
z6413/XE\ZNO1.7		12859	2186	0.18	10721361330510
z6413/XE\ZNO1.8		11644	2077	0.18	48346
z6413/XE\ZNO1.8.1		11627	2047	0.18	-292959
z6413/XE\ZNO1.9		12720	2260	0.18	237233
z6413/XE\ZNO1.14		12494	2195	0.18	220017
z6413/XE\ZNO1.14.1		12553	2099	0.17	389870
z6413/XE\XNO1.12		15220	2738	0.19	-79991
z6413/XE\XNO1.15		12543	2156	0.18	-92380
z6413/XE\ZNO1.5		12378	2331	0.19	131220
z6413/XE\ZNO1.6		11611	2173	0.19	56154
z6413/XE\ZNO1.10		9492	1723	0.19	4901751
z6413/XE\ZNO1.11		10688	1967	0.19	-181889
z6413/XE\ZNO1.12		11099	1999	0.19	-361288
z6413/XE\ZNO1.13		9113	1939	0.22	111801

Uncorrected ratios								
$^{207}\text{Pb}/^{206}\text{Pb}$	$\pm 2 \text{ s.e.}$	$^{208}\text{Pb}/^{232}\text{Th}$	$\pm 2 \text{ s.e.}$	$^{208}\text{Pb}/^{206}\text{Pb}$	$\pm 2 \text{ s.e.}$	$^{206}\text{Pb}^*/^{238}\text{U}$	$\pm 2 \text{ s.e.}$	$^{238}\text{U}/^{206}\text{Pb}^*$
0.07189	0.00141	0.05997	0.00235	0.05464	0.00177	0.19395	0.00366	5.15606
0.07231	0.00145	0.06199	0.00267	0.05615	0.00182	0.19729	0.00511	5.06861
0.07214	0.00146	0.06100	0.00269	0.05547	0.00184	0.19550	0.00521	5.11509
0.07266	0.00079	0.06262	0.00267	0.05573	0.00178	0.19745	0.00505	5.06447
0.07218	0.00160	0.05887	0.00282	0.05645	0.00203	0.18650	0.00535	5.36194
0.07448	0.00155	0.06094	0.00281	0.05608	0.00193	0.19025	0.00527	5.25628
0.07315	0.00143	0.06088	0.00262	0.05595	0.00178	0.19414	0.00510	5.15090
0.07362	0.00149	0.06204	0.00295	0.05483	0.00185	0.20302	0.00546	4.92555
0.07205	0.00147	0.05998	0.00338	0.05278	0.00182	0.20149	0.00867	4.96292
0.07186	0.00147	0.06146	0.00267	0.05581	0.00184	0.19697	0.00506	5.07684
0.07128	0.00138	0.06021	0.00259	0.05282	0.00173	0.20176	0.00511	4.95640
0.07015	0.00144	0.06175	0.00332	0.05553	0.00183	0.19602	0.00799	5.10141
0.07265	0.00144	0.05250	0.00227	0.05392	0.00181	0.17503	0.00437	5.71329
0.07361	0.00260	0.05285	0.00234	0.05515	0.00189	0.17416	0.00447	5.74189
0.07522	0.00137	0.06539	0.00239	0.05763	0.00172	0.20161	0.00370	4.96006
0.07577	0.00140	0.05380	0.00368	0.05784	0.00339	0.16783	0.00571	5.95858
0.07185	0.00113	0.06123	0.00336	0.05508	0.00137	0.20309	0.00890	4.92398
0.07233	0.00052	0.05913	0.00590	0.05464	0.00134	0.19873	0.01781	5.03206
0.07052	0.00259	0.06052	0.00382	0.05483	0.00224	0.20044	0.00862	4.98896
0.07229	0.00109	0.06396	0.00342	0.05511	0.00132	0.21332	0.00908	4.68780
0.07215	0.00111	0.06466	0.00196	0.05522	0.00065	0.21517	0.00550	4.64743
0.07129	0.00110	0.06174	0.00329	0.05632	0.00136	0.19872	0.00850	5.03232
0.07233	0.00109	0.05730	0.00312	0.05527	0.00133	0.18982	0.00839	5.26810
0.07205	0.00108	0.06205	0.00255	0.05493	0.00130	0.20769	0.00541	4.81490
0.07251	0.00106	0.06017	0.00308	0.05516	0.00128	0.20350	0.00833	4.91404
0.07188	0.00103	0.05930	0.00454	0.05455	0.00125	0.19640	0.01374	5.09173
0.07331	0.00118	0.05820	0.00359	0.05449	0.00141	0.19240	0.00962	5.19744
0.07103	0.00116	0.05958	0.00442	0.05479	0.00288	0.19897	0.00929	5.02601
0.07318	0.00119	0.06221	0.00364	0.05734	0.00145	0.19585	0.00922	5.10585
0.07203	0.00208	0.06069	0.00338	0.05536	0.00141	0.19300	0.00856	5.18140
0.07222	0.00117	0.05957	0.00317	0.05442	0.00142	0.20045	0.00833	4.98877
0.07212	0.00112	0.06100	0.00632	0.05579	0.00305	0.19525	0.01666	5.12162
0.07250	0.00052	0.05984	0.00316	0.05400	0.00132	0.20443	0.00856	4.89169
0.07209	0.00109	0.06149	0.00250	0.05494	0.00132	0.19662	0.00482	5.08591
0.07253	0.00115	0.05913	0.00324	0.05590	0.00140	0.19498	0.00853	5.12877
0.07262	0.00058	0.05845	0.00220	0.05460	0.00069	0.19478	0.00500	5.13400
0.07191	0.00112	0.05846	0.00378	0.05363	0.00134	0.20017	0.00906	4.99580
0.07343	0.00110	0.06074	0.00297	0.05553	0.00064	0.19855	0.00845	5.03662
0.07222	0.00111	0.05793	0.00314	0.05497	0.00134	0.18206	0.00795	5.49272
0.07350	0.00068	0.06333	0.00464	0.05634	0.00270	0.20904	0.01029	4.78381
0.07480	0.00209	0.05871	0.00372	0.05629	0.00144	0.18531	0.00957	5.39635
0.07397	0.00118	0.05923	0.00325	0.05883	0.00146	0.19592	0.00859	5.10423
0.07265	0.00260	0.05718	0.00324	0.05610	0.00151	0.19712	0.00881	5.07297
0.07208	0.00123	0.05849	0.00314	0.05619	0.00152	0.19532	0.00520	5.11978
0.07169	0.00112	0.05991	0.00206	0.05793	0.00139	0.19671	0.00449	5.08353
0.07222	0.00110	0.05694	0.00285	0.05578	0.00074	0.18996	0.00823	5.26416
0.07194	0.00129	0.05386	0.00480	0.06329	0.00170	0.18708	0.01538	5.34536

¹⁴ Pb-corrected ratios (not matrix-corrected)							
± 2 s.e.	²⁰⁷ Pb*/ ²⁰⁶ Pb*	± 2 s.e.	²⁰⁸ Pb*/ ²³² Th	± 2 s.e.	²⁰⁸ Pb*/ ²⁰⁶ Pb*	± 2 s.e.	(²³⁸ U/ ²⁰⁶ Pb*) _m
0.09719	0.07189	0.00141	0.05997	0.00235	0.05464	0.00177	5.86914
0.13118	0.07222	0.00145	0.06174	0.00268	0.05593	0.00184	5.71482
0.13624	0.07205	0.00146	0.06075	0.00271	0.05525	0.00186	5.79598
0.12954	0.07261	0.00079	0.06250	0.00267	0.05563	0.00180	5.77375
0.15369	0.07213	0.00161	0.05873	0.00283	0.05632	0.00205	5.94686
0.14565	0.07434	0.00156	0.06053	0.00283	0.05571	0.00198	5.84575
0.13525	0.07323	0.00143	0.06112	0.00265	0.05616	0.00181	5.74050
0.13256	0.07353	0.00150	0.06177	0.00296	0.05460	0.00188	5.56020
0.21353	0.07201	0.00147	0.05985	0.00339	0.05266	0.00183	5.63866
0.13052	0.07172	0.00148	0.06106	0.00270	0.05547	0.00189	5.79912
0.12557	0.07120	0.00138	0.05998	0.00260	0.05262	0.00175	5.64803
0.20795	0.07019	0.00145	0.06188	0.00334	0.05564	0.00184	5.72957
0.14270	0.07260	0.00144	0.05239	0.00228	0.05381	0.00182	6.43729
0.14751	0.07348	0.00260	0.05251	0.00236	0.05481	0.00193	6.42440
0.09103	0.07525	0.00137	0.06550	0.00241	0.05773	0.00173	5.72863
0.20257	0.07577	0.00140	0.05380	0.00368	0.05784	0.00339	6.79240
0.21580	0.07181	0.00113	0.06111	0.00336	0.05497	0.00138	5.58799
0.45103	0.07233	0.00052	0.05913	0.00590	0.05464	0.00134	5.72379
0.21459	0.07042	0.00259	0.06023	0.00381	0.05457	0.00226	5.65835
0.19961	0.07223	0.00110	0.06379	0.00341	0.05496	0.00133	5.38853
0.11869	0.07233	0.00111	0.06521	0.00201	0.05568	0.00072	5.27533
0.21520	0.07149	0.00110	0.06232	0.00335	0.05684	0.00139	5.78187
0.23279	0.07245	0.00110	0.05762	0.00315	0.05558	0.00135	5.99279
0.12542	0.07193	0.00108	0.06172	0.00255	0.05464	0.00133	5.50282
0.20118	0.07277	0.00107	0.06091	0.00314	0.05582	0.00133	5.60343
0.35624	0.07200	0.00104	0.05964	0.00458	0.05485	0.00127	5.77948
0.25980	0.07349	0.00118	0.05868	0.00363	0.05494	0.00145	5.91247
0.23471	0.07116	0.00116	0.05995	0.00446	0.05513	0.00289	5.67000
0.24024	0.07331	0.00120	0.06259	0.00368	0.05767	0.00148	5.72356
0.22979	0.07234	0.00209	0.06159	0.00346	0.05616	0.00147	5.84478
0.20735	0.07231	0.00117	0.05984	0.00320	0.05466	0.00144	5.61787
0.43706	0.07218	0.00112	0.06118	0.00634	0.05595	0.00306	5.76045
0.20476	0.07227	0.00053	0.05915	0.00314	0.05339	0.00136	5.52175
0.12460	0.07209	0.00109	0.06149	0.00250	0.05494	0.00132	5.69706
0.22435	0.07223	0.00116	0.05831	0.00323	0.05514	0.00146	5.68921
0.13191	0.07266	0.00059	0.05859	0.00221	0.05473	0.00071	5.69363
0.22618	0.07185	0.00112	0.05829	0.00378	0.05347	0.00136	5.59162
0.21446	0.07337	0.00110	0.06055	0.00297	0.05536	0.00067	5.62611
0.23993	0.07218	0.00111	0.05783	0.00314	0.05487	0.00135	6.13626
0.23550	0.07368	0.00069	0.06386	0.00469	0.05680	0.00272	5.46985
0.27863	0.07495	0.00210	0.05913	0.00376	0.05669	0.00147	6.02941
0.22373	0.07386	0.00118	0.05894	0.00324	0.05855	0.00148	5.69932
0.22672	0.07239	0.00261	0.05650	0.00323	0.05545	0.00156	5.62780
0.13628	0.07207	0.00123	0.05848	0.00314	0.05618	0.00152	5.57983
0.11595	0.07177	0.00112	0.06012	0.00208	0.05813	0.00141	5.59566
0.22815	0.07226	0.00110	0.05705	0.00286	0.05588	0.00075	5.81341
0.43942	0.07181	0.00129	0.05357	0.00478	0.06296	0.00173	5.81346

²⁰⁴Pb-corrected, matrix-corrected ratios^d

± 2 s.e.	$(^{207}\text{Pb}^*/^{206}\text{Pb}^*)_m$	± 2 s.e.	$(^{206}\text{Pb}^*/^{238}\text{U})_m$	± 2 s.e.	$(^{207}\text{Pb}^*/^{235}\text{U})_m$	± 2 s.e.	$(^{208}\text{Pb}^*/^{232}\text{Th})_m$
0.18211	0.07189	0.00141	0.17038	0.00529	1.68818	0.06200	#N/A
0.22095	0.07222	0.00145	0.17498	0.00677	1.74176	0.07589	#N/A
0.23015	0.07205	0.00146	0.17253	0.00685	1.71322	0.07641	#N/A
0.22372	0.07261	0.00079	0.17320	0.00671	1.73329	0.06979	#N/A
0.24451	0.07213	0.00161	0.16816	0.00691	1.67155	0.07815	#N/A
0.23482	0.07434	0.00156	0.17106	0.00687	1.75259	0.07942	#N/A
0.22178	0.07323	0.00143	0.17420	0.00673	1.75811	0.07614	#N/A
0.22169	0.07353	0.00150	0.17985	0.00717	1.82260	0.08160	#N/A
0.32951	0.07201	0.00147	0.17735	0.01036	1.75996	0.10895	#N/A
0.22600	0.07172	0.00148	0.17244	0.00672	1.70452	0.07518	#N/A
0.21718	0.07120	0.00138	0.17705	0.00681	1.73733	0.07486	#N/A
0.31643	0.07019	0.00145	0.17453	0.00964	1.68835	0.09953	#N/A
0.24215	0.07260	0.00144	0.15534	0.00584	1.55442	0.06613	#N/A
0.24511	0.07348	0.00260	0.15566	0.00594	1.57623	0.08208	#N/A
0.17706	0.07525	0.00137	0.17456	0.00540	1.81047	0.06493	#N/A
0.32834	0.07577	0.00140	0.14722	0.00712	1.53736	0.07955	#N/A
0.33125	0.07181	0.00113	0.17896	0.01061	1.77110	0.10866	#N/A
0.63830	0.07233	0.00052	0.17471	0.01948	1.74147	0.19461	#N/A
0.33000	0.07042	0.00259	0.17673	0.01031	1.71524	0.11831	#N/A
0.31583	0.07223	0.00110	0.18558	0.01088	1.84739	0.11185	#N/A
0.20328	0.07233	0.00111	0.18956	0.00730	1.88960	0.07840	#N/A
0.33995	0.07149	0.00110	0.17295	0.01017	1.70412	0.10359	#N/A
0.35856	0.07245	0.00110	0.16687	0.00998	1.66609	0.10282	#N/A
0.21670	0.07193	0.00108	0.18172	0.00716	1.80156	0.07596	#N/A
0.31532	0.07277	0.00107	0.17846	0.01004	1.78989	0.10410	#N/A
0.51414	0.07200	0.00104	0.17303	0.01539	1.71699	0.15473	#N/A
0.39276	0.07349	0.00118	0.16913	0.01124	1.71295	0.11709	#N/A
0.35250	0.07116	0.00116	0.17637	0.01096	1.72956	0.11117	#N/A
0.35584	0.07331	0.00120	0.17472	0.01086	1.76535	0.11348	#N/A
0.34784	0.07234	0.00209	0.17109	0.01018	1.70582	0.11282	#N/A
0.31614	0.07231	0.00117	0.17800	0.01002	1.77398	0.10387	#N/A
0.60737	0.07218	0.00112	0.17360	0.01830	1.72692	0.18405	#N/A
0.31331	0.07227	0.00053	0.18110	0.01028	1.80377	0.10321	#N/A
0.21000	0.07209	0.00109	0.17553	0.00647	1.74397	0.06947	#N/A
0.32912	0.07223	0.00116	0.17577	0.01017	1.74977	0.10507	#N/A
0.21533	0.07266	0.00059	0.17563	0.00664	1.75890	0.06803	#N/A
0.33597	0.07185	0.00112	0.17884	0.01075	1.77086	0.10995	#N/A
0.32045	0.07337	0.00110	0.17774	0.01012	1.79727	0.10588	#N/A
0.35709	0.07218	0.00111	0.16297	0.00948	1.62116	0.09757	#N/A
0.36048	0.07368	0.00069	0.18282	0.01205	1.85644	0.12359	#N/A
0.40449	0.07495	0.00210	0.16585	0.01113	1.71325	0.12452	#N/A
0.33245	0.07386	0.00118	0.17546	0.01023	1.78607	0.10802	#N/A
0.33152	0.07239	0.00261	0.17769	0.01047	1.77285	0.12241	#N/A
0.21300	0.07207	0.00123	0.17922	0.00684	1.78016	0.07445	#N/A
0.19228	0.07177	0.00112	0.17871	0.00614	1.76764	0.06671	#N/A
0.33223	0.07226	0.00110	0.17202	0.00983	1.71297	0.10131	#N/A
0.57292	0.07181	0.00129	0.17201	0.01695	1.70240	0.17056	#N/A

²⁰⁴Pb-corrected, matrix-corrected dates^d							
	(²⁰⁶Pb*/²³⁸U)_m Age		(²⁰⁷Pb*/²⁰⁶Pb*)_m		(²⁰⁷Pb*/²³⁵U)_m Age		
± 2 s.e.	(Ma)	± 2 s.e.	Age (Ma)	± 2 s.e.	(Ma)	± 2 s.e.	Disc. (%)
#N/A	1014	29	982	40	1004	23	-3.3
#N/A	1040	37	991	41	1024	28	-4.9
#N/A	1026	38	986	41	1013	29	-4.0
#N/A	1030	37	1002	22	1021	26	-2.7
#N/A	1002	38	989	45	998	30	-1.3
#N/A	1018	38	1050	42	1028	29	3.0
#N/A	1035	37	1019	40	1030	28	-1.5
#N/A	1066	39	1028	41	1054	29	-3.7
#N/A	1052	57	985	42	1031	40	-6.8
#N/A	1026	37	977	42	1010	28	-5.0
#N/A	1051	37	962	40	1022	28	-9.2
#N/A	1037	53	933	42	1004	38	-11.1
#N/A	931	33	1002	40	952	26	7.1
#N/A	933	33	1026	72	961	32	9.1
#N/A	1037	30	1074	37	1049	23	3.5
#N/A	885	40	1088	37	945	32	18.6
#N/A	1061	58	980	32	1035	40	-8.3
#N/A	1038	107	994	15	1024	72	-4.4
#N/A	1049	56	940	75	1014	44	-11.6
#N/A	1097	59	992	31	1062	40	-10.7
#N/A	1119	40	994	31	1077	28	-12.5
#N/A	1028	56	971	32	1010	39	-6.0
#N/A	995	55	998	31	996	39	0.3
#N/A	1076	39	983	31	1046	28	-9.5
#N/A	1059	55	1007	30	1042	38	-5.1
#N/A	1029	85	985	29	1015	58	-4.4
#N/A	1007	62	1026	33	1013	44	1.9
#N/A	1047	60	961	33	1020	41	-9.0
#N/A	1038	60	1022	33	1033	42	-1.6
#N/A	1018	56	995	59	1011	42	-2.4
#N/A	1056	55	994	33	1036	38	-6.3
#N/A	1032	101	990	32	1019	69	-4.2
#N/A	1073	56	993	15	1047	37	-8.1
#N/A	1043	35	988	31	1025	26	-5.6
#N/A	1044	56	992	33	1027	39	-5.3
#N/A	1043	36	1004	16	1030	25	-3.9
#N/A	1061	59	981	32	1035	40	-8.1
#N/A	1055	55	1023	30	1044	38	-3.1
#N/A	973	53	990	31	978	38	1.7
#N/A	1082	66	1032	19	1066	44	-4.9
#N/A	989	62	1066	56	1014	47	7.2
#N/A	1042	56	1037	32	1040	39	-0.5
#N/A	1054	57	996	73	1036	45	-5.8
#N/A	1063	37	987	35	1038	27	-7.7
#N/A	1060	34	978	32	1034	24	-8.3
#N/A	1023	54	992	31	1013	38	-3.1
#N/A	1023	93	980	37	1009	64	-4.4

Appendix 3.2:

SHRIMP spots on grain z6413

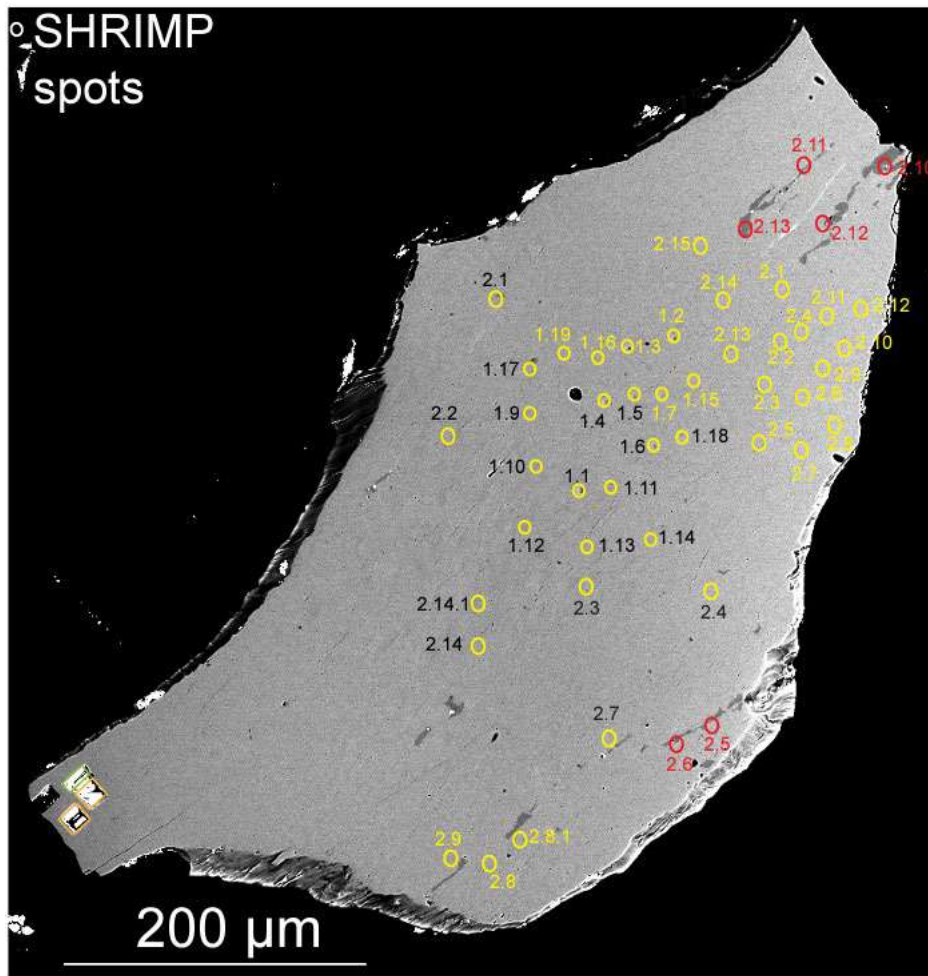
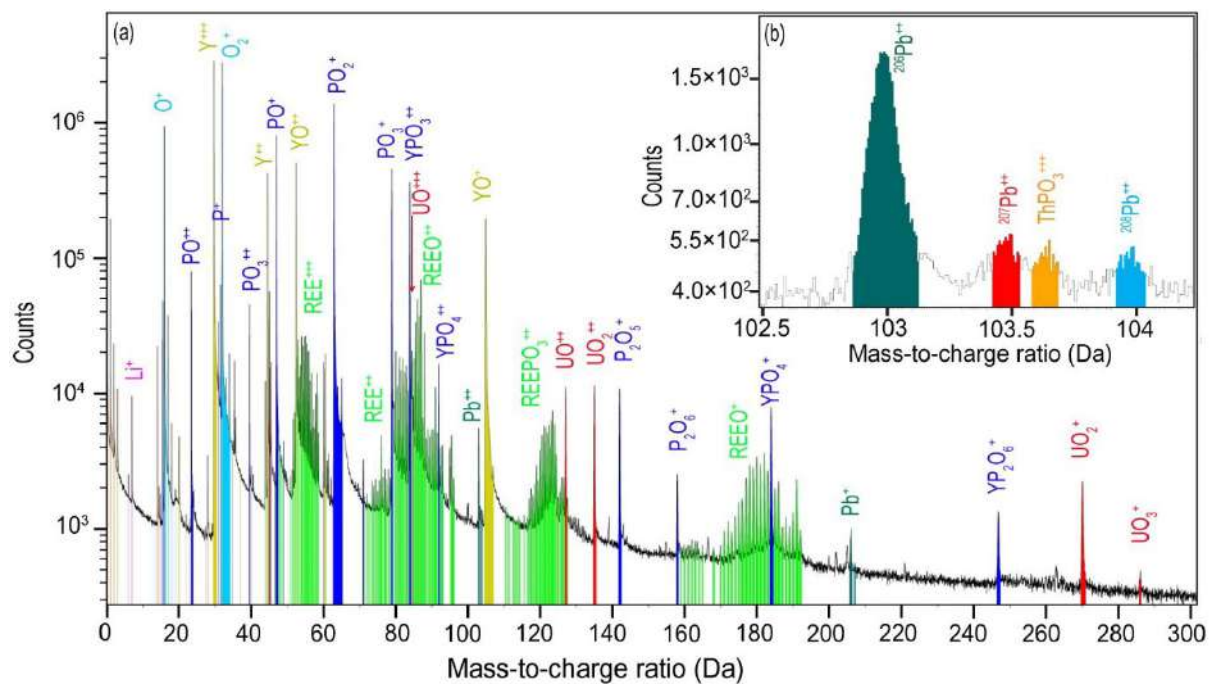


Figure 3.2 Spots for the SHRIMP analysis. Spots from day 1 is noted by the prefix 1 day 2 with the prefix 2 with the spot number and. Red ellipses represent spot in BSE dark domains, and yellow represents spots in the unaltered domain.

Appendix 3.3:

APT mass spectrum



Atom probe mass spectra of xenotime (sample – z6413). Peaks are colour-coded by atomic/molecular species. 1b. Inset showing Pb^{++} peaks and ThPO_3^{+++} peak.

Appendix 3.4

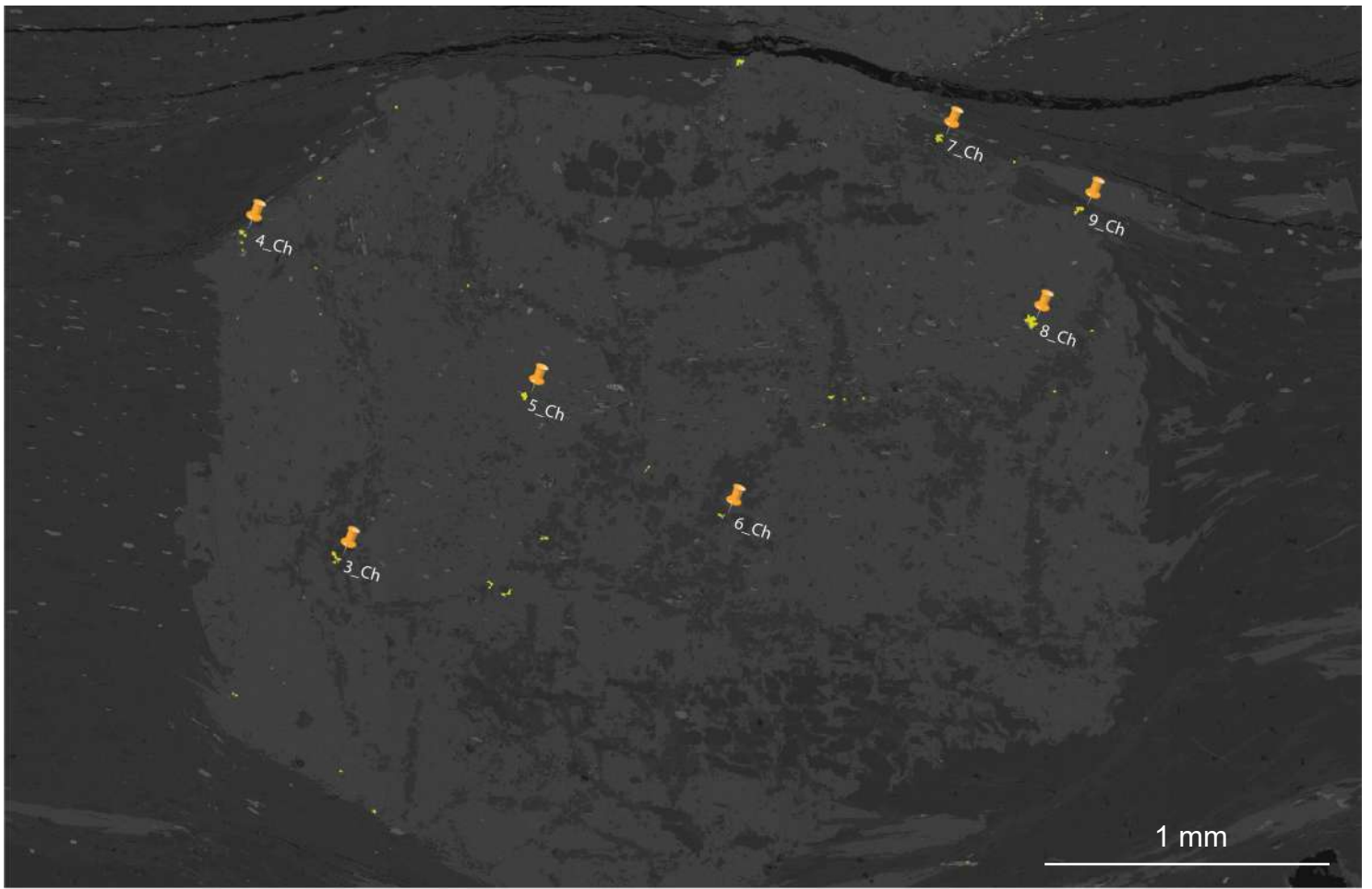
APT nanogeochronology results

Specimen	Run ID	Composition		Whole specimen		Matrix	
		Ca (at. %)	Pb (at. %)	$^{206}\text{Pb}/^{238}\text{U}$ Age (Ma)	2σ	$^{206}\text{Pb}/^{238}\text{U}$ Age (Ma)	2σ
M1	3541	0.015	0.038	932	38	872	37
M2	3542	0.005	0.042	971	52	937	51
M3	3669	0.007	0.037	920	63	860	61
M4	3672	0.002	0.034	No clusters, considered as matrix		832	83
M5	3673	0.010	0.039	859	87	830	42
M6	3676	0.007	0.039	857	43	851	27
M7	3679	0.004	0.036	910	29	870	38

Appendix 4.1

EPMA targets and results from Fanad

Targets for EPMA analysis from sample 1606.

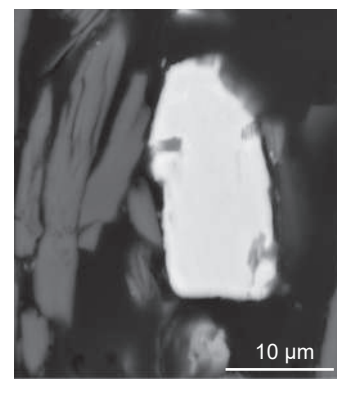
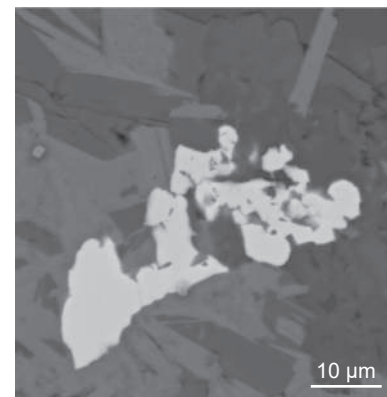
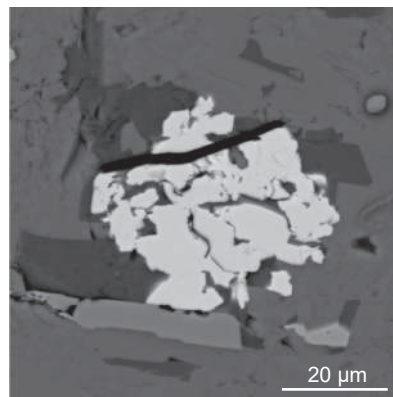
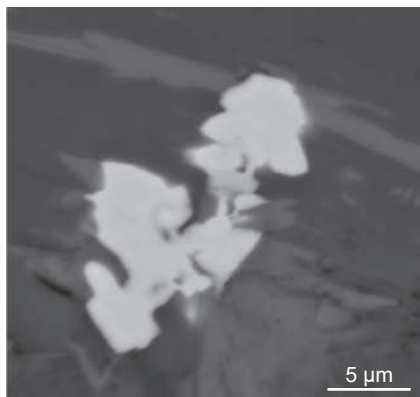
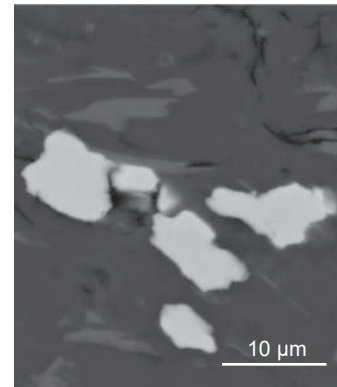
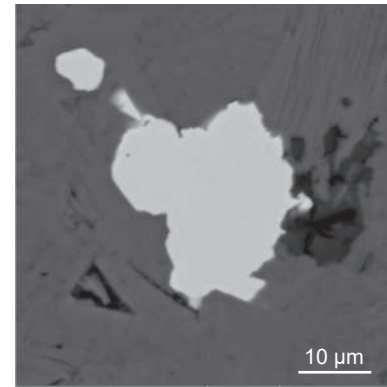
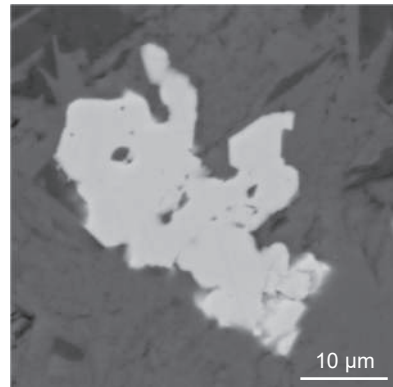
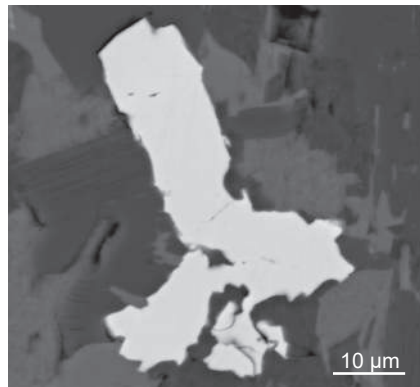


1606_Ch3

1606_Ch4

1606_Ch5

1606_Ch6

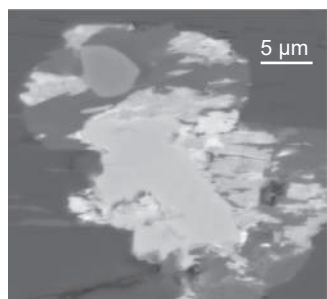


1606_Ch7

1606_Ch8

1606_Ch9

1606_M1



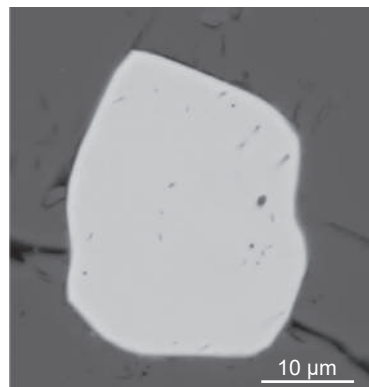
1606_M2

Ch - xenotime grains inside chlorite
M - xenotime in the rock matrix

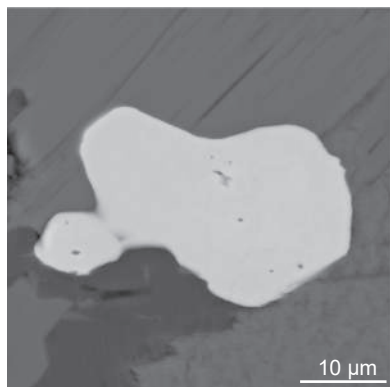
Oxide wt.%	1606-M1-01	1606-M1-02	1606-M2-01	1606-M2-02	1606-CH3-01	1606-CH3-02
P2O5	35.07	35.02	24.35	4.10	35.63	35.76
SiO2	0.27	0.27	1.99	38.51	0.04	0.13
ThO2	0.10	0.09	0.72	0.43	0.03	0.00
UO2	0.69	0.62	1.19	0.00	0.02	0.01
Y2O3	49.77	49.50	41.27	8.16	49.60	49.80
La2O3	0.00	0.00	2.39	0.81	0.00	0.00
Ce2O3	0.02	0.07	4.26	1.57	0.03	0.03
Pr2O3	0.04	0.00	0.92	0.36	0.07	0.00
Nd2O3	0.14	0.09	2.68	0.73	0.07	0.07
Sm2O3	0.19	0.10	0.51	0.12	0.04	0.22
Eu2O3	0.00	0.00	0.00	0.00	0.00	0.00
Gd2O3	4.39	4.68	3.29	0.85	4.51	3.76
Tb2O3	0.00	0.00	0.00	0.00	0.00	0.00
Dy2O3	7.48	7.66	4.61	1.00	6.17	6.09
Ho2O3	2.30	2.47	1.64	0.30	2.12	2.11
Er2O3	4.01	3.65	4.03	0.77	4.43	4.37
Tm2O3	0.34	0.48	0.45	0.07	0.57	0.62
Yb2O3	2.22	2.26	2.61	0.41	3.56	3.29
Lu2O3	0.91	0.70	0.69	0.09	0.96	0.79
CaO	0.01	0.02	3.43	0.37	0.01	0.00
PbO	0.42	0.37	0.30	0.06	0.36	0.34
Total	108.40	108.05	101.33	58.68	108.22	107.38
Element wt.%						
P	15.30	15.28	10.63	1.79	15.55	15.61
Si	0.13	0.13	0.93	18.00	0.02	0.06
Th	0.09	0.08	0.63	0.38	0.02	0.00
U	0.61	0.55	1.05	0.00	0.01	0.01
Y	39.19	38.98	32.50	6.42	39.06	39.21
La	0.00	0.00	2.04	0.69	0.00	0.00
Ce	0.02	0.06	3.64	1.34	0.02	0.03
Pr	0.03	0.00	0.78	0.31	0.06	0.00
Nd	0.12	0.07	2.29	0.63	0.06	0.06
Sm	0.16	0.09	0.44	0.10	0.03	0.19
Eu	0.00	0.00	0.00	0.00	0.00	0.00
Gd	3.81	4.06	2.86	0.74	3.92	3.26
Tb	0.00	0.00	0.00	0.00	0.00	0.00
Dy	6.52	6.68	4.02	0.87	5.37	5.31
Ho	2.01	2.16	1.43	0.26	1.85	1.84
Er	3.51	3.19	3.52	0.67	3.87	3.82
Tm	0.30	0.42	0.39	0.06	0.50	0.55
Yb	1.95	1.98	2.29	0.36	3.12	2.89
Lu	0.80	0.62	0.61	0.08	0.85	0.70
Ca	0.01	0.01	2.45	0.26	0.01	0.00
Pb	0.39	0.34	0.28	0.06	0.33	0.32
Total	74.96	74.70	72.79	33.01	74.67	73.83

1606-CH4-01	1606-CH4-02	1606-CH5-01	1606-CH5-02	1606-CH6-01	1606-CH6-02	1606-CH7-01
35.54	30.20	35.52	35.85	35.66	9.57	33.37
0.47	3.70	0.13	0.01	0.27	34.00	5.36
0.01	0.06	0.04	0.02	0.00	0.02	0.00
0.00	0.01	0.08	0.01	0.05	0.00	0.00
50.10	42.57	49.14	50.36	49.24	10.61	47.85
0.00	0.00	0.00	0.00	0.00	0.00	0.00
0.01	0.04	0.05	0.03	0.01	0.08	0.05
0.12	0.06	0.00	0.00	0.05	0.00	0.00
0.00	0.11	0.05	0.00	0.15	0.01	0.00
0.00	0.00	0.14	0.19	0.11	0.16	0.00
0.00	0.00	0.00	0.00	0.00	0.00	0.00
2.41	2.24	4.28	4.97	5.09	0.66	2.16
0.00	0.00	0.00	0.00	0.00	0.00	0.00
6.03	5.23	5.91	5.92	5.60	0.85	6.11
1.84	1.85	2.37	2.03	2.38	0.32	1.84
5.21	4.15	4.49	4.58	4.73	0.57	4.29
0.70	0.45	0.46	0.62	0.60	0.06	0.57
3.90	3.24	3.81	3.71	4.17	0.35	3.71
1.01	0.79	1.10	1.72	1.01	0.10	0.86
0.01	0.02	0.01	0.01	0.01	0.01	0.00
0.37	0.28	0.37	0.34	0.35	0.06	0.37
107.72	94.99186533	107.95	110.38	109.46	57.43	106.54
15.51	13.18	15.50	15.65	15.56	4.17	14.56
0.22	1.73	0.06	0.01	0.12	15.90	2.50
0.00	0.05	0.03	0.02	0.00	0.02	0.00
0.00	0.01	0.07	0.01	0.04	0.00	0.00
39.45	33.52	38.70	39.65	38.77	8.35	37.68
0.00	0.00	0.00	0.00	0.00	0.00	0.00
0.01	0.04	0.04	0.03	0.01	0.07	0.04
0.10	0.05	0.00	0.00	0.04	0.00	0.00
0.00	0.10	0.05	0.00	0.13	0.00	0.00
0.00	0.00	0.12	0.17	0.10	0.14	0.00
0.00	0.00	0.00	0.00	0.00	0.00	0.00
2.09	1.94	3.72	4.31	4.42	0.57	1.87
0.00	0.00	0.00	0.00	0.00	0.00	0.00
5.25	4.55	5.15	5.16	4.88	0.74	5.33
1.60	1.61	2.07	1.77	2.07	0.28	1.61
4.56	3.63	3.93	4.00	4.13	0.50	3.75
0.61	0.39	0.41	0.54	0.53	0.05	0.50
3.42	2.84	3.35	3.26	3.67	0.31	3.26
0.89	0.69	0.97	1.51	0.89	0.08	0.76
0.01	0.02	0.01	0.01	0.01	0.01	0.00
0.34	0.26	0.35	0.32	0.32	0.06	0.34
74.07	64.62	74.50	76.41	75.68	31.26	72.21

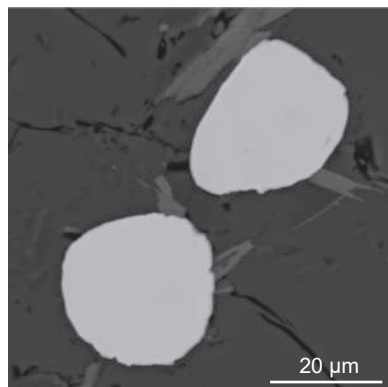
1606-CH7-02	1606-CH8-01	1606-CH8-02	1606-CH9-01	1606-CH9-02
35.26	34.43	35.62	35.62	35.45
0.54	0.08	0.00	0.09	0.03
0.00	0.03	0.00	0.00	0.02
0.00	0.01	0.03	0.00	0.01
50.78	47.02	49.53	50.74	50.43
0.00	0.00	0.00	0.00	0.00
0.07	0.04	0.02	0.01	0.02
0.00	0.02	0.00	0.01	0.00
0.02	0.05	0.09	0.00	0.00
0.17	0.04	0.12	0.05	0.13
0.00	0.00	0.00	0.00	0.00
2.48	4.39	3.77	3.87	3.63
0.00	0.00	0.00	0.00	0.00
5.98	6.18	6.07	5.93	5.91
1.98	2.30	2.10	2.16	2.03
4.63	4.19	4.68	4.37	4.37
0.67	0.66	0.61	0.54	0.55
3.50	3.14	3.96	3.61	3.49
0.98	0.92	1.54	0.83	0.94
0.03	0.01	0.01	0.01	0.01
0.36	0.39	0.37	0.37	0.44
107.44	103.90	108.54	108.20	107.46
15.39	15.03	15.55	15.55	15.47
0.25	0.04	0.00	0.04	0.01
0.00	0.02	0.00	0.00	0.02
0.00	0.01	0.03	0.00	0.01
39.99	37.02	39.00	39.95	39.71
0.00	0.00	0.00	0.00	0.00
0.06	0.03	0.02	0.01	0.02
0.00	0.02	0.00	0.01	0.00
0.01	0.05	0.08	0.00	0.00
0.15	0.03	0.10	0.04	0.11
0.00	0.00	0.00	0.00	0.00
2.16	3.81	3.27	3.36	3.15
0.00	0.00	0.00	0.00	0.00
5.21	5.38	5.29	5.16	5.15
1.73	2.01	1.84	1.88	1.77
4.05	3.66	4.09	3.82	3.82
0.58	0.58	0.53	0.47	0.48
3.08	2.76	3.48	3.17	3.06
0.86	0.81	1.36	0.73	0.83
0.02	0.01	0.01	0.01	0.01
0.33	0.36	0.34	0.34	0.40
73.86	71.63	74.99	74.55	74.03



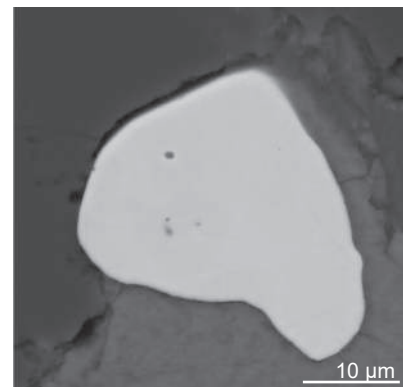
1630-1



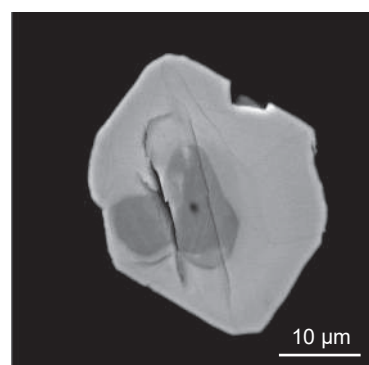
1630-2



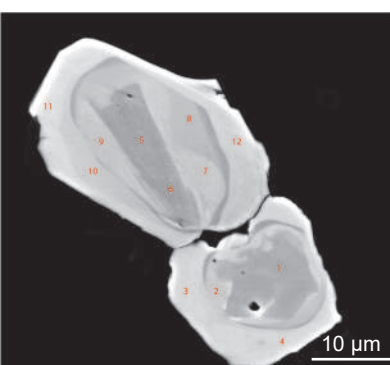
1630-3



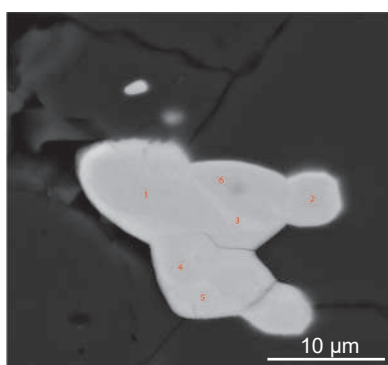
1630-4



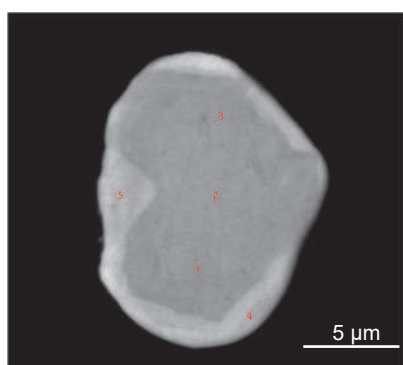
1642-1



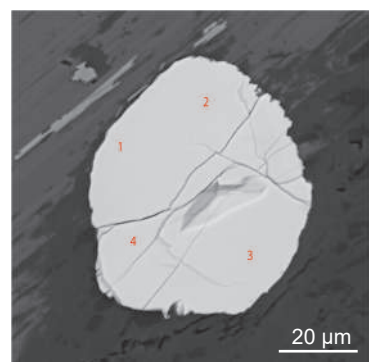
1642-2



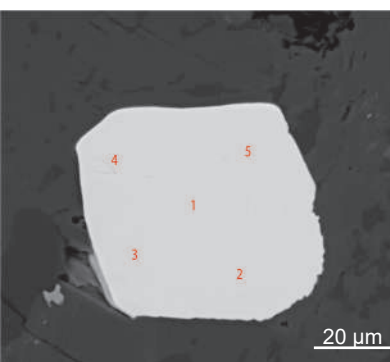
1642-3



1642-4



1642-5



1642-6

1630-1-01	1630-1-02	1630-2-01	1630-2-02	1630-3-01	1630-3-02	1630-4-01	1630-4-02
36.02	35.49	35.23	35.13	35.79	36.07	33.66	35.14
0.12	0.06	0.07	0.22	0.15	0.16	1.89	0.03
0.05	0.14	0.10	0.04	0.15	0.10	0.00	0.00
0.62	0.69	0.57	0.21	0.68	0.71	0.06	0.27
48.68	48.59	47.73	47.48	48.33	48.54	50.28	47.78
0.00	0.00	0.00	0.00	0.00	0.00	0.00	0.00
0.10	0.13	0.08	0.13	0.13	0.10	0.06	0.09
0.00	0.00	0.10	0.00	0.02	0.08	0.00	0.03
0.48	0.53	0.26	0.39	0.60	0.49	0.08	0.19
0.48	0.67	0.40	0.45	0.80	0.73	0.12	0.22
0.00	0.00	0.00	0.00	0.00	0.00	0.00	0.00
3.66	3.87	3.63	3.38	5.97	6.48	1.56	2.64
0.00	0.00	0.00	0.00	0.00	0.00	0.00	0.00
6.06	5.97	6.92	6.45	6.07	6.14	5.69	6.42
2.23	2.11	2.18	2.02	2.34	2.32	1.70	2.31
4.52	4.20	4.31	4.82	4.11	4.32	6.19	5.39
0.52	0.56	0.63	0.56	0.65	0.54	0.80	0.66
3.39	3.13	3.53	4.00	3.20	3.34	5.20	4.16
0.87	0.82	0.88	1.06	0.78	0.94	1.64	1.03
0.11	0.12	0.07	0.06	0.12	0.13	0.03	0.05
0.48	0.46	0.40	0.42	0.44	0.37	0.36	0.30
108.40	107.52	107.10	106.82	110.33	111.57	109.33	106.69
15.72	15.49	15.38	15.33	15.62	15.74	14.69	15.34
0.06	0.03	0.03	0.10	0.07	0.08	0.89	0.01
0.04	0.12	0.08	0.03	0.13	0.09	0.00	0.00
0.55	0.60	0.50	0.18	0.60	0.62	0.05	0.24
38.33	38.26	37.58	37.38	38.06	38.23	39.60	37.63
0.00	0.00	0.00	0.00	0.00	0.00	0.00	0.00
0.08	0.11	0.07	0.11	0.12	0.09	0.05	0.07
0.00	0.00	0.09	0.00	0.02	0.07	0.00	0.02
0.42	0.45	0.22	0.34	0.52	0.42	0.07	0.16
0.42	0.58	0.35	0.39	0.69	0.63	0.10	0.19
0.00	0.00	0.00	0.00	0.00	0.00	0.00	0.00
3.18	3.35	3.15	2.93	5.18	5.62	1.36	2.29
0.00	0.00	0.00	0.00	0.00	0.00	0.00	0.00
5.28	5.20	6.03	5.62	5.29	5.35	4.96	5.60
1.95	1.84	1.90	1.77	2.05	2.03	1.48	2.01
3.95	3.67	3.77	4.21	3.59	3.77	5.42	4.71
0.46	0.49	0.55	0.49	0.57	0.47	0.70	0.58
2.98	2.75	3.10	3.51	2.81	2.93	4.56	3.65
0.77	0.72	0.77	0.93	0.69	0.83	1.44	0.90
0.08	0.09	0.05	0.04	0.09	0.09	0.02	0.03
0.44	0.43	0.37	0.39	0.41	0.35	0.34	0.28
74.70	74.18	74.00	73.78	76.48	77.41	75.73	73.72

1642-1-01	1642-1-02	1642-1-03	1642-1-04	1642-1-05	1642-1-06
35.46	25.36	35.30	35.13	0.03	35.21
0.61	29.30	0.29	0.26	42.23	0.34
0.10	0.12	0.15	0.17	0.00	0.11
0.33	0.31	1.10	1.29	0.00	1.37
48.15	35.95	47.37	46.52	0.00	46.57
0.00	0.00	0.00	0.00	0.00	0.00
0.05	0.11	0.13	0.12	0.04	0.05
0.07	0.00	0.09	0.00	0.00	0.19
0.31	0.12	0.48	0.52	0.02	0.34
0.42	0.21	0.33	0.57	0.00	0.50
0.00	0.00	0.00	0.00	0.00	0.00
6.31	3.22	3.03	3.50	0.00	3.57
0.00	0.00	0.00	0.00	0.11	0.00
6.67	5.13	6.13	6.06	0.11	6.05
2.33	1.49	2.03	1.61	0.00	2.06
3.86	2.92	5.04	4.23	0.16	4.64
0.63	0.36	0.64	0.74	0.00	0.57
3.82	3.34	4.73	4.81	0.00	5.03
1.08	0.75	1.49	0.95	0.04	1.08
0.07	0.05	0.12	0.15	0.00	0.14
0.39	0.25	0.45	0.44	0.01	0.43
110.65	108.97	108.92	107.06	42.74	108.24
15.48	11.07	15.40	15.33	0.01	15.37
0.29	13.70	0.13	0.12	19.74	0.16
0.09	0.10	0.13	0.15	0.00	0.09
0.29	0.27	0.97	1.14	0.00	1.21
37.92	28.31	37.30	36.63	0.00	36.67
0.00	0.00	0.00	0.00	0.00	0.00
0.04	0.09	0.11	0.11	0.03	0.04
0.06	0.00	0.08	0.00	0.00	0.16
0.26	0.10	0.42	0.44	0.01	0.29
0.36	0.18	0.29	0.49	0.00	0.43
0.00	0.00	0.00	0.00	0.00	0.00
5.47	2.79	2.63	3.04	0.00	3.10
0.00	0.00	0.00	0.00	0.09	0.00
5.81	4.47	5.35	5.28	0.10	5.27
2.04	1.30	1.78	1.40	0.00	1.80
3.38	2.55	4.41	3.70	0.14	4.06
0.55	0.31	0.56	0.65	0.00	0.50
3.35	2.93	4.16	4.22	0.00	4.42
0.95	0.66	1.31	0.83	0.03	0.95
0.05	0.04	0.09	0.11	0.00	0.10
0.36	0.23	0.42	0.41	0.01	0.40
76.74	69.11	75.52	74.05	20.17	75.01

1642-2-01	1642-2-02	1642-2-03	1642-2-04	1642-2-05	1642-2-06
35.80	35.16	12.11	34.83	35.89	35.05
0.10	0.18	12.21	0.29	0.01	0.06
0.00	0.11	0.01	0.11	0.08	0.07
0.05	0.96	0.32	0.98	0.28	0.31
50.88	48.27	18.48	48.09	48.03	49.10
0.00	0.00	0.00	0.00	0.00	0.00
0.07	0.09	0.04	0.10	0.08	0.07
0.00	0.05	0.02	0.14	0.05	0.00
0.07	0.57	0.11	0.60	0.31	0.05
0.09	0.48	0.18	0.50	0.60	0.43
0.00	0.00	0.00	0.00	0.00	0.00
3.20	3.40	1.32	3.67	4.53	5.21
0.00	0.00	0.00	0.00	0.00	0.00
6.42	5.97	2.79	6.11	6.42	6.57
1.63	1.90	0.53	1.87	2.28	2.15
3.62	4.42	1.94	4.35	4.42	3.93
0.50	0.63	0.32	0.68	0.67	0.61
4.10	4.38	1.78	4.33	4.06	3.95
1.13	1.02	0.37	1.57	1.14	1.72
0.00	0.11	0.03	0.11	0.04	0.05
0.40	0.39	0.22	0.42	0.41	0.39
108.04	108.10	52.78	108.75	109.30	109.74
15.62	15.34	5.29	15.20	15.66	15.30
0.05	0.08	5.71	0.14	0.00	0.03
0.00	0.09	0.01	0.10	0.07	0.06
0.04	0.85	0.28	0.86	0.25	0.27
40.06	38.01	14.56	37.87	37.82	38.67
0.00	0.00	0.00	0.00	0.00	0.00
0.06	0.08	0.03	0.09	0.07	0.06
0.00	0.04	0.02	0.12	0.04	0.00
0.06	0.49	0.09	0.51	0.27	0.05
0.08	0.41	0.15	0.43	0.52	0.37
0.00	0.00	0.00	0.00	0.00	0.00
2.78	2.95	1.15	3.18	3.93	4.52
0.00	0.00	0.00	0.00	0.00	0.00
5.59	5.20	2.43	5.33	5.59	5.72
1.42	1.66	0.46	1.63	1.99	1.88
3.17	3.87	1.70	3.80	3.87	3.44
0.43	0.55	0.28	0.59	0.59	0.53
3.60	3.85	1.56	3.80	3.56	3.47
0.99	0.90	0.33	1.38	1.00	1.51
0.00	0.08	0.02	0.08	0.03	0.04
0.37	0.36	0.21	0.39	0.38	0.36
74.33	74.82	34.27	75.51	75.64	76.28

1642-2-07	1642-2-08	1642-2-09	1642-2-10	1642-2-11	1642-2-12
35.56	35.91	26.34	0.03	0.01	35.67
0.07	0.07	0.41	16.15	21.67	0.18
0.04	0.08	0.07	0.00	0.00	0.06
0.11	0.17	0.84	0.02	0.02	0.97
49.83	49.48	35.60	0.07	0.00	48.09
0.00	0.00	0.00	0.00	0.00	0.00
0.02	0.05	0.14	0.16	0.01	0.10
0.00	0.00	0.09	0.04	0.00	0.00
0.00	0.08	0.35	0.13	0.00	0.42
0.08	0.25	0.42	0.00	0.05	0.55
0.00	0.00	0.00	0.07	0.00	0.00
3.59	4.14	2.40	0.00	0.00	3.43
0.00	0.00	0.00	0.14	0.00	0.00
6.51	6.56	4.97	0.66	0.22	5.73
1.97	2.00	1.51	0.00	0.00	1.88
3.94	3.86	3.54	0.25	0.14	4.78
0.61	0.59	0.48	0.00	0.00	0.71
4.12	3.80	3.52	0.00	0.00	4.42
1.81	1.09	0.86	0.00	0.02	1.62
0.01	0.02	0.09	0.00	0.00	0.11
0.28	0.35	0.33	0.00	0.03	0.39
108.54	108.49	81.95	17.72	22.17	109.12
15.52	15.67	11.50	0.01	0.01	15.57
0.03	0.03	0.19	7.55	10.13	0.09
0.03	0.07	0.06	0.00	0.00	0.05
0.09	0.15	0.74	0.02	0.01	0.86
39.24	38.96	28.03	0.05	0.00	37.87
0.00	0.00	0.00	0.00	0.00	0.00
0.01	0.05	0.12	0.14	0.01	0.09
0.00	0.00	0.08	0.04	0.00	0.00
0.00	0.06	0.30	0.11	0.00	0.36
0.07	0.21	0.36	0.00	0.04	0.47
0.00	0.00	0.00	0.06	0.00	0.00
3.12	3.59	2.09	0.00	0.00	2.97
0.00	0.00	0.00	0.12	0.00	0.00
5.68	5.72	4.33	0.57	0.19	4.99
1.72	1.75	1.32	0.00	0.00	1.64
3.44	3.37	3.09	0.22	0.12	4.18
0.54	0.51	0.42	0.00	0.00	0.62
3.62	3.34	3.09	0.00	0.00	3.88
1.59	0.96	0.75	0.00	0.02	1.42
0.01	0.02	0.06	0.00	0.00	0.08
0.26	0.32	0.30	0.00	0.03	0.37
74.97	74.78	56.83	8.89	10.56	75.51

1642-3-1	1642-3-2	1642-3-3	1642-3-4	1642-3-5	1642-3-6
3.28	23.47	35.71	5.96	5.85	35.86
23.85	12.00	0.12	28.28	27.49	0.03
0.00	0.01	0.09	0.02	0.02	0.00
0.01	0.12	0.19	0.03	0.04	0.02
5.18	33.99	49.08	10.82	8.88	49.99
0.00	0.00	0.00	0.00	0.00	0.00
0.00	0.04	0.03	0.00	0.00	0.04
0.11	0.00	0.06	0.00	0.04	0.00
0.00	0.08	0.03	0.00	0.06	0.00
0.00	0.05	0.15	0.00	0.05	0.19
0.00	0.00	0.00	0.00	0.00	0.00
0.51	1.38	2.39	0.97	0.77	2.34
0.00	0.00	0.00	0.00	0.00	0.00
0.79	3.66	6.13	1.66	1.11	5.95
0.21	1.05	1.57	0.49	0.37	1.68
0.35	3.21	4.87	1.41	0.93	4.69
0.03	0.39	0.62	0.17	0.12	0.60
0.25	2.86	4.29	1.15	0.76	4.65
0.10	0.63	0.97	0.28	0.09	1.05
0.05	0.03	0.03	0.02	0.02	0.01
0.06	0.24	0.39	0.12	0.05	0.34
34.77	83.19	106.72	51.38	46.63	107.45
1.43	10.24	15.58	2.60	2.55	15.65
11.15	5.61	0.06	13.22	12.85	0.01
0.00	0.01	0.08	0.02	0.01	0.00
0.01	0.11	0.17	0.03	0.03	0.02
4.08	26.77	38.65	8.52	6.99	39.37
0.00	0.00	0.00	0.00	0.00	0.00
0.00	0.03	0.02	0.00	0.00	0.03
0.09	0.00	0.06	0.00	0.03	0.00
0.00	0.07	0.02	0.00	0.05	0.00
0.00	0.04	0.13	0.00	0.04	0.17
0.00	0.00	0.00	0.00	0.00	0.00
0.44	1.20	2.07	0.84	0.67	2.03
0.00	0.00	0.00	0.00	0.00	0.00
0.69	3.19	5.34	1.45	0.97	5.18
0.18	0.92	1.37	0.43	0.32	1.47
0.31	2.81	4.26	1.23	0.82	4.10
0.03	0.34	0.54	0.15	0.10	0.52
0.22	2.51	3.77	1.01	0.66	4.08
0.09	0.55	0.85	0.24	0.08	0.92
0.03	0.02	0.02	0.01	0.01	0.01
0.05	0.22	0.36	0.11	0.04	0.31
18.80	54.62	73.36	29.86	26.25	73.89

1642-4-1	1642-4-2	1642-4-3	1642-4-4	1642-4-5
35.88	35.91	26.34	6.97	35.12
0.25	0.30	10.40	27.61	0.80
0.01	0.00	0.12	0.06	0.06
0.13	0.10	0.10	0.05	0.11
49.66	50.06	36.07	11.11	49.22
0.00	0.00	0.00	0.00	0.00
0.03	0.04	0.03	0.02	0.02
0.00	0.00	0.00	0.00	0.00
0.01	0.00	0.22	0.10	0.13
0.00	0.09	0.09	0.14	0.12
0.00	0.00	0.00	0.00	0.00
2.28	1.90	2.96	1.38	2.32
0.00	0.00	0.00	0.00	0.00
5.82	5.60	5.16	2.01	6.06
1.66	1.59	1.38	0.67	1.88
5.37	5.14	3.43	1.23	5.17
0.65	0.73	0.49	0.18	0.71
4.80	4.92	3.38	1.08	4.86
1.56	1.43	0.82	0.30	0.95
0.01	0.01	0.02	0.01	0.02
0.36	0.36	0.29	0.08	0.38
108.48	108.19	91.29	53.01	107.92
15.66	15.67	11.49	3.04	15.33
0.12	0.14	4.86	12.91	0.38
0.01	0.00	0.10	0.05	0.05
0.11	0.09	0.09	0.04	0.10
39.10	39.42	28.41	8.75	38.76
0.00	0.00	0.00	0.00	0.00
0.03	0.03	0.03	0.02	0.02
0.00	0.00	0.00	0.00	0.00
0.01	0.00	0.19	0.08	0.11
0.00	0.07	0.08	0.12	0.10
0.00	0.00	0.00	0.00	0.00
1.97	1.65	2.57	1.20	2.01
0.00	0.00	0.00	0.00	0.00
5.07	4.88	4.50	1.76	5.28
1.45	1.39	1.21	0.58	1.64
4.69	4.50	3.00	1.07	4.52
0.57	0.64	0.43	0.16	0.62
4.22	4.32	2.97	0.95	4.27
1.37	1.26	0.72	0.26	0.83
0.01	0.01	0.01	0.01	0.02
0.33	0.33	0.26	0.08	0.35
74.72	74.41	60.91	31.09	74.37

1642-5-1	1642-5-2	1642-5-3	1642-5-4
35.03	35.12	35.39	35.56
0.20	0.08	0.21	0.22
0.20	0.18	0.15	0.10
1.09	1.06	0.99	1.03
48.65	47.57	47.75	47.81
0.00	0.00	0.00	0.00
0.05	0.09	0.08	0.12
0.06	0.00	0.03	0.06
0.55	0.54	0.53	0.36
0.58	0.60	0.44	0.54
0.00	0.00	0.00	0.00
3.26	3.73	3.18	3.28
0.00	0.00	0.00	0.00
6.16	6.37	6.09	5.92
1.92	1.99	1.99	1.93
4.80	4.50	5.07	4.70
0.67	0.59	0.74	0.72
4.50	4.49	4.95	4.50
1.63	1.04	1.21	1.03
0.13	0.13	0.09	0.11
0.33	0.38	0.37	0.46
109.79	108.46	109.25	108.45
15.29	15.33	15.44	15.52
0.09	0.04	0.10	0.10
0.18	0.16	0.13	0.09
0.96	0.94	0.87	0.91
38.31	37.46	37.60	37.64
0.00	0.00	0.00	0.00
0.04	0.07	0.06	0.11
0.05	0.00	0.02	0.05
0.47	0.47	0.45	0.31
0.50	0.51	0.38	0.47
0.00	0.00	0.00	0.00
2.83	3.24	2.76	2.85
0.00	0.00	0.00	0.00
5.37	5.55	5.31	5.16
1.67	1.74	1.74	1.68
4.19	3.93	4.44	4.11
0.59	0.51	0.65	0.63
3.95	3.95	4.35	3.95
1.43	0.92	1.06	0.91
0.09	0.09	0.07	0.08
0.30	0.35	0.35	0.42
76.32	75.25	75.77	74.99

1642-6-1	1642-6-2	1642-6-3	1642-6-4	1642-6-5
35.74	35.39	35.77	35.59	35.83
0.15	0.19	0.20	0.22	0.24
0.12	0.14	0.16	0.13	0.10
1.03	1.10	1.00	1.07	1.03
47.91	47.48	48.46	47.40	47.53
0.00	0.00	0.00	0.00	0.00
0.04	0.09	0.11	0.06	0.14
0.06	0.00	0.05	0.04	0.02
0.38	0.47	0.52	0.48	0.53
0.51	0.42	0.53	0.44	0.46
0.00	0.00	0.00	0.00	0.00
3.19	3.42	3.49	3.60	3.19
0.00	0.00	0.00	0.00	0.00
6.19	5.94	6.22	5.87	6.05
2.06	2.10	1.98	2.00	1.79
4.85	4.76	4.80	4.65	5.12
0.65	0.67	0.64	0.64	0.63
4.43	4.78	4.50	4.73	4.67
1.66	1.67	0.97	1.11	1.14
0.12	0.13	0.14	0.14	0.12
0.42	0.42	0.39	0.46	0.47
109.55	109.18	109.93	108.62	109.06
15.60	15.45	15.61	15.53	15.64
0.07	0.09	0.09	0.10	0.11
0.11	0.13	0.14	0.11	0.09
0.91	0.97	0.88	0.94	0.91
37.73	37.39	38.16	37.33	37.43
0.00	0.00	0.00	0.00	0.00
0.04	0.08	0.10	0.05	0.12
0.05	0.00	0.04	0.04	0.01
0.32	0.40	0.44	0.42	0.46
0.44	0.36	0.45	0.38	0.40
0.00	0.00	0.00	0.00	0.00
2.77	2.97	3.03	3.13	2.76
0.00	0.00	0.00	0.00	0.00
5.40	5.18	5.42	5.12	5.27
1.80	1.83	1.73	1.74	1.56
4.25	4.16	4.20	4.07	4.48
0.57	0.59	0.56	0.56	0.55
3.89	4.20	3.95	4.16	4.10
1.46	1.47	0.85	0.97	1.01
0.09	0.09	0.10	0.10	0.09
0.39	0.39	0.36	0.42	0.44
75.89	75.74	76.13	75.16	75.42

Appendix 4.2 Y1 SHRIMP results

Sample	Spot	U (ppm) ^c	Th (ppm) ^c	Th/U	²⁰⁶ Pb/ ²⁰⁴ Pt	± 2 s.e.	f206 (%)	εREE (%)
Y1	Y1.1	25771	10416	0.42	291392	237920	0.01	17.4
Y1	Y1.2	25191	10219	0.42	-433702	-433702	b.d.l.	17.8
Y1	Y1.3	25432	10316	0.42	112187	59967	0.02	17.2
Y1	Y1.4	5356	2672	0.52	-44095	-36003	b.d.l.	17.8
Y1	Y1.5	7976	4816	0.62	-62276	-48646	b.d.l.	17.1
Y1	Y1.6	12581	4101	0.34	-150770	-150770	b.d.l.	17.1
Y1	Y1.7	11682	3870	0.34	-123069	-123070	b.d.l.	16.7
Y1	Y1.8	12226	4240	0.36	-41858	-26473	b.d.l.	17.5
Y1	Y1.9	4424	3805	0.89	28136	22973	0.06	17.4
Y1	Y1.10	14041	4391	0.32	141136	141137	b.d.l.	17.5

Uncorrected ratios									
²⁰⁶ Pb*/ ²³⁸ U	± 2 s.e.	²³⁸ U/ ²⁰⁶ Pb	± 2 s.e.	²⁰⁷ Pb*/ ²⁰⁶ Pb	± 2 s.e.	²⁰⁸ Pb*/ ²³² Th	± 2 s.e.	²⁰⁸ Pb*/ ²⁰⁶ Pb	± 2 s.e.
0.20408	0.00815	4.89993	0.19557	0.07073	0.00042	0.06099	0.00362	0.12482	0.00256
0.20361	0.00797	4.91136	0.19229	0.07082	0.00038	0.06014	0.00306	0.12384	0.00332
0.20579	0.00810	4.85943	0.19127	0.07057	0.00131	0.06152	0.00310	0.12532	0.00320
0.14884	0.00702	6.71847	0.31670	0.06887	0.00166	0.04638	0.00356	0.16065	0.00904
0.17671	0.00795	5.65901	0.25452	0.07088	0.00138	0.04776	0.00289	0.16864	0.00328
0.18769	0.00853	5.32785	0.24221	0.07151	0.00118	0.05541	0.00421	0.09944	0.00565
0.18200	0.00870	5.49464	0.26280	0.07097	0.00129	0.05461	0.00314	0.10271	0.00231
0.17965	0.00896	5.56651	0.27766	0.07102	0.00139	0.05431	0.00409	0.10833	0.00552
0.17594	0.02707	5.68363	0.87462	0.07042	0.00104	0.03949	0.00678	0.19950	0.01442
0.18537	0.00914	5.39453	0.26585	0.06938	0.00122	0.05400	0.00320	0.09415	0.00208

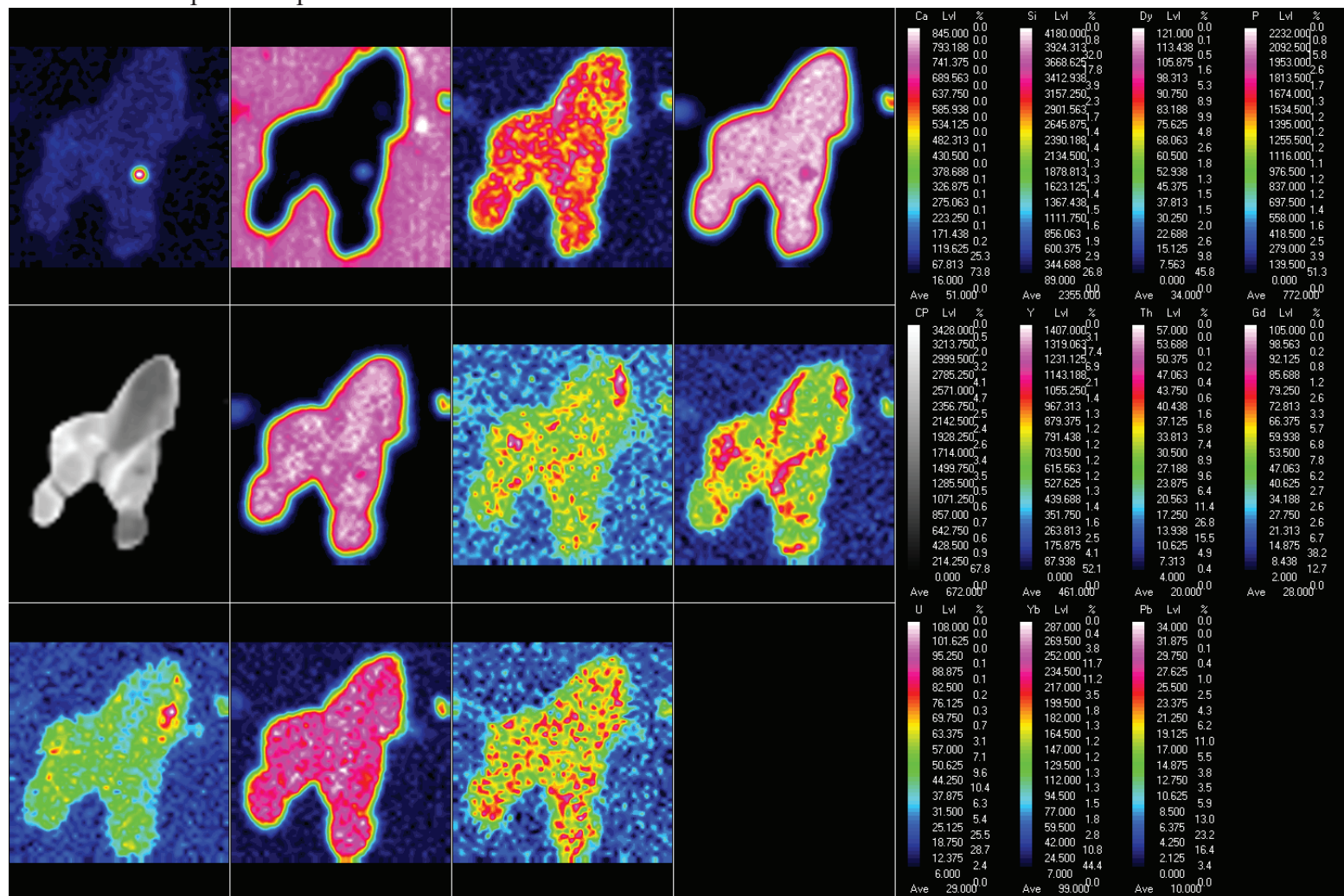
²⁰⁴ Pb-corrected ratios (not matrix-corrected)									
²⁰⁶ Pb*/ ²³⁸ U	± 2 s.e.	²³⁸ U/ ²⁰⁶ Pb*	± 2 s.e.	²⁰⁷ Pb*/ ²⁰⁶ Pb	± 2 s.e.	²⁰⁸ Pb*/ ²³² Th	± 2 s.e.	²⁰⁸ Pb*/ ²⁰⁶ Pb*	± 2 s.e.
0.20407	0.00815	4.90023	0.19559	0.07068	0.00043	0.06092	0.00362	0.12470	0.00257
0.20362	0.00797	4.91116	0.19229	0.07085	0.00038	0.06019	0.00306	0.12392	0.00332
0.20575	0.00810	4.86020	0.19130	0.07044	0.00132	0.06136	0.00309	0.12500	0.00320
0.14890	0.00702	6.71576	0.31658	0.06920	0.00168	0.04662	0.00358	0.16144	0.00906
0.17676	0.00795	5.65739	0.25445	0.07111	0.00139	0.04793	0.00290	0.16919	0.00331
0.18772	0.00853	5.32722	0.24218	0.07161	0.00118	0.05555	0.00422	0.09968	0.00565
0.18202	0.00871	5.49384	0.26276	0.07109	0.00129	0.05477	0.00315	0.10300	0.00233
0.17972	0.00896	5.56414	0.27755	0.07136	0.00141	0.05476	0.00413	0.10918	0.00554
0.17583	0.02706	5.68723	0.87518	0.06991	0.00112	0.03923	0.00674	0.19829	0.01447
0.18535	0.00913	5.39521	0.26589	0.06927	0.00123	0.05385	0.00319	0.09390	0.00210

²⁰⁴ Pb-corrected, matrix-corrected ratios ^d									
(²³⁸ U/ ²⁰⁶ Pb*) _m	± 2 s.e.	(²⁰⁷ Pb*/ ²⁰⁶ Pb*) _m	± 2 s.e.	(²⁰⁷ Pb*/ ²³⁸ U) _m	± 2 s.e.	(²⁰⁷ Pb*/ ²³⁵ U) _m	± 2 s.e.	(²⁰⁸ Pb*/ ²³² Th) _m	± 2 s.e.
6.25292	0.38557	0.07068	0.00043	0.15993	0.00986	1.55783	0.09652	#N/A	#N/A
6.24913	0.37819	0.07085	0.00038	0.16002	0.00968	1.56259	0.09493	#N/A	#N/A
6.16950	0.37411	0.07044	0.00132	0.16209	0.00983	1.57350	0.09984	#N/A	#N/A
7.08776	0.41552	0.06920	0.00168	0.14109	0.00827	1.34549	0.08534	#N/A	#N/A
6.10180	0.35134	0.07111	0.00139	0.16389	0.00944	1.60621	0.09767	#N/A	#N/A
5.93252	0.35589	0.07161	0.00118	0.16856	0.01011	1.66356	0.10352	#N/A	#N/A
6.05338	0.37510	0.07109	0.00129	0.16520	0.01024	1.61851	0.10453	#N/A	#N/A
6.20488	0.40333	0.07136	0.00141	0.16116	0.01048	1.58496	0.10765	#N/A	#N/A
5.96686	1.01599	0.06991	0.00112	0.16759	0.02854	1.61481	0.27618	#N/A	#N/A
6.10518	0.39856	0.06927	0.00123	0.16380	0.01069	1.56377	0.10578	#N/A	#N/A

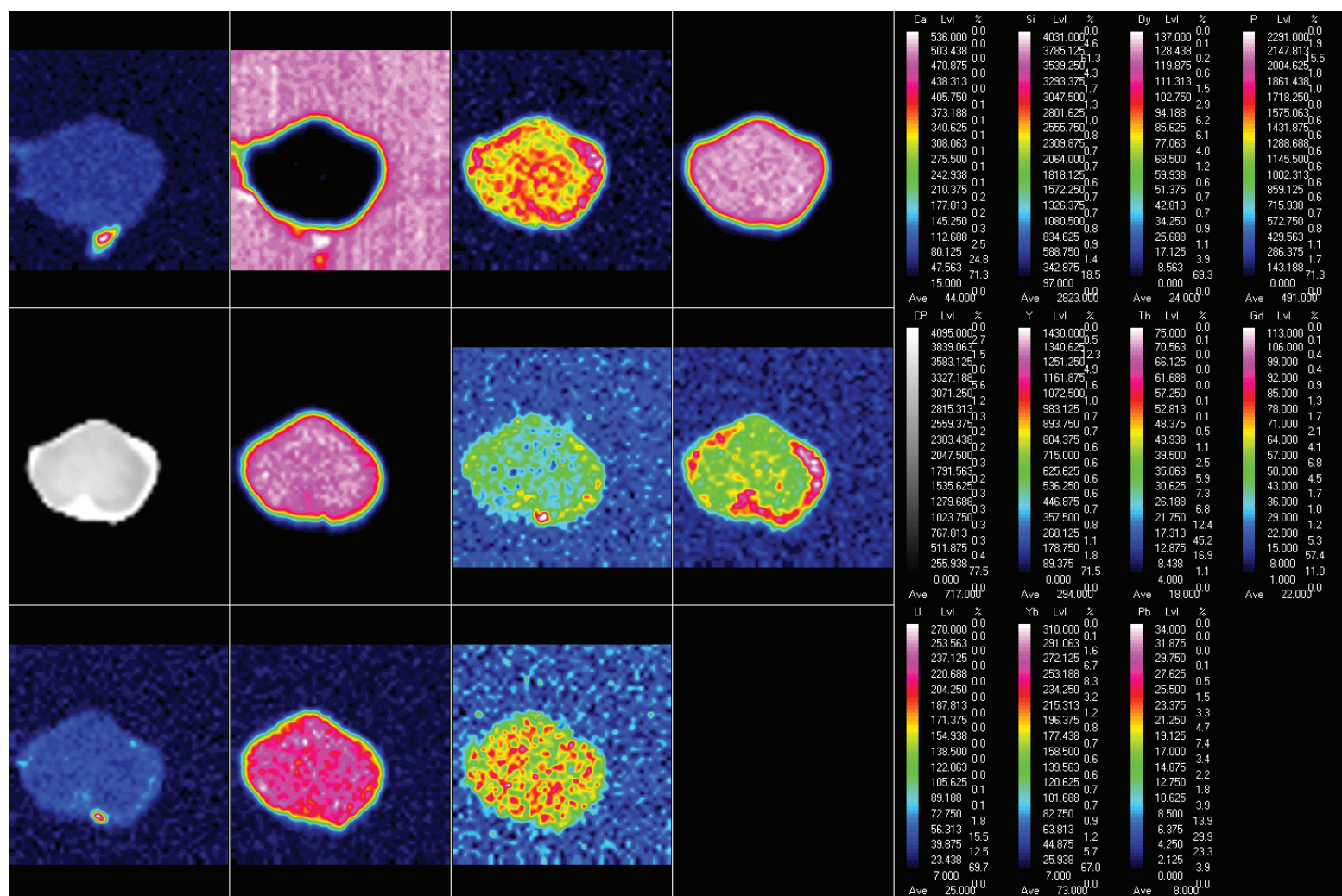
²⁰⁴ Pb-corrected, matrix-corrected dates ^d						
Pb*/ ²³⁸ U) _m Age (l)	± 2 s.e.	(²⁰⁷ Pb*/ ²⁰⁶ Pb*) _m Age (Ma)	± 2 s.e.	(²³⁵ U) _m Age (l)	± 2 s.e.	Disc. (%)
956	55	947	12	954	38	-1.0
957	54	952	11	955	38	-0.5
968	55	940	38	960	39	-3.0
851	47	904	50	866	37	5.8
978	52	960	40	973	38	-1.9
1004	56	974	34	995	39	-3.1
986	57	959	37	977	41	-2.8
963	58	967	40	964	42	0.4
999	158	925	33	976	108	-8.0
978	59	906	37	956	42	-7.9

Appendix 4.3

EPMS WDS maps of samples 1642-3 and 1642-4

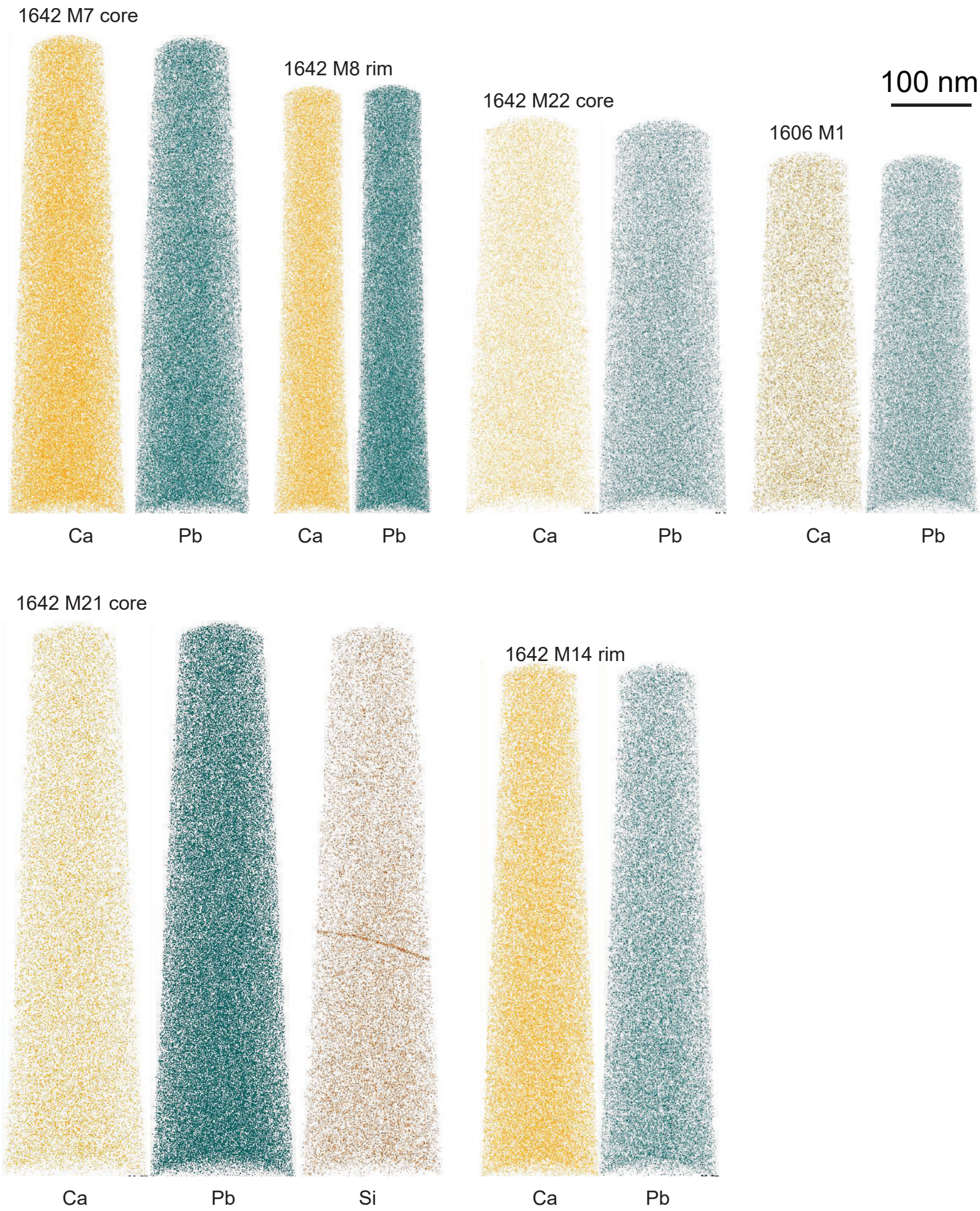


1642-4



Appendix 4.4

APT 3d reconstructions of specimens from Fanad metamorphic xenotime grains



Appendix 5.1

EBSD analysis conditions used for xenotime.

Site	Vredefort	Araguainha	Santa Fe
Grain	14DG14	all	all
Epoxy mount	SA21	SF20	
Date of collection	06-08-2022	31-12-2019	11/24/2021
Accelerating voltage (kV)	20	20	20
Sample tilt (degrees)	70	67	70
working distance (mm)	19.4	24.8 to 24.9	19.6 to 19.8
Acquisition speed (Hz)	200	199 to 333	95
Exposure setting (ms)	5.0	2.5 to 5.0	10
EBSD camera gain	2	2	2
Background correction	auto	static + auto	auto
Frame averaging	1	1	1
Binning mode	Speed 2	Speed 1	Speed 2
Indexing mode	Refined accuracy	Optimized BD	Refined accuracy
Hough resolution	60	60	50
Band detection mode	center	center	center
Band detected	11	11	11
Pixel size (nm)	75	60 to 100	75
Number of pixels in map	11.1M	0.6M to 10M	131,202 to 385,020
Noise reduction methods			
Wildspike	yes	yes	yes
<i>n</i> neighbour zero solution extrapolation	7	7	7
SEM Model: Tescan Mira3 FEG-SEM			
EBSD system: Oxford Symmetry,Oxford AZtec			
Match unit: Xenotime(Y), Inorganic Crystal Structure Database.			
Structural data from Milligan et al. (1982).			
Grains in epoxy, mounted flat, and grounded with Cu tape.			
Samples were coated with a thin (<5 nm) carbon coat.			
xeno = xenotime.			

Appendix 5.2

SHRIMP geochronology results

(Reference data provided in appendix 3.1)

10-12 January & 15-17 March 2022, Curtin University^a

#	Gr	Date	Sample	Spot	U (ppm) ^c	Th (ppm) ^c	Th/U	²⁰⁶ Pb/ ²⁰⁴ Pb	± 2 s.e.	f206 (%)	ΣREE ₂ O ₃ (wt. %)
6	D	10-12/01/2022	Araguainha	AR-X03.2	4318	7546	1.81	2525	2062	0.71	23.8
7	D	10-12/01/2022	Araguainha	AR-X03.5	4855	4623	0.98	5568	6430	0.32	20.1
8	D	10-12/01/2022	Araguainha	AR-X03.3	6447	13958	2.24	904	745	1.98	22.4
9	D	10-12/01/2022	Araguainha	AR-X02.5	4443	5362	1.25	3484	3484	0.51	22.3
10	D	10-12/01/2022	Araguainha	AR-X01.3	5266	7511	1.47	-5127	-3876	-0.35	22.2
11	D	10-12/01/2022	Araguainha	AR-X01.2	6013	8606	1.48	39008	78016	0.05	21.9
12	D	10-12/01/2022	Araguainha	AR-X02.1	4445	3140	0.73	4114	2743	0.44	17.7
13	IMP	10-12/01/2022	Araguainha	AR-X03.4	4761	4929	1.07	7992	11302	0.22	24.4
14	IMP	10-12/01/2022	Araguainha	AR-X03.6	5619	4443	0.82	4900	4900	0.37	23.3
15	Z	10-12/01/2022	Araguainha	AR-X03.1	4865	4658	0.99	9198	13008	0.19	19.5
16	Z	10-12/01/2022	Araguainha	AR-X02.2	4626	4388	0.98	846	314	2.12	20.5
17	Z	10-12/01/2022	Araguainha	AR-X02.3	5324	3943	0.77	2968	1790	0.60	21.0
18	Z	10-12/01/2022	Araguainha	AR-X01.6	5355	4765	0.92	5689	5089	0.32	20.1
19	Z	10-12/01/2022	Araguainha	AR-X01.1	4841	3879	0.83	4234	3201	0.42	21.7
20	Z	10-12/01/2022	Araguainha	AR-X01.5	7147	9905	1.43	19127	27050	0.09	21.6
21	Z	10-12/01/2022	Araguainha	AR-X02.4	3607	2586	0.74	1166	1175	1.54	20.6
22	Z	10-12/01/2022	Araguainha	AR-X02.6	4082	3183	0.81	8285	8285	0.22	20.7
23	I	10-12/01/2022	Araguainha	AR-X01.4	5164	4447	0.89	48996	97993	0.04	22.0
29	D	10-12/01/2022	Santa Fe	SF-X5-1	11219	4151	0.38	#####	218653	0.01	22.5
30	I	10-12/01/2022	Santa Fe	SF-X5-2	8131	3609	0.46	#####	396586	0.01	19.8
31	I	10-12/01/2022	Santa Fe	SF-X3	5845	1931	0.34	#####	#####	-0.01	20.7
32	I	10-12/01/2022	Santa Fe	SF-X4	4770	2677	0.58	80514	113864	0.02	22.1
33	I	10-12/01/2022	Santa Fe	SF-X5-3	10480	6751	0.67	#####	#####	0.00	21.8
34	D	15-17/03/2022	Vredefort	SA21.17	1526	3013	2.04	#####	-86496	b.d.l.	19.4
35	D	15-17/03/2022	Vredefort	SA21.15	1575	3123	2.05	#####	-15760	b.d.l.	19.8
36	D	15-17/03/2022	Vredefort	SA21.19	1452	3101	2.21	493	136	2.71	19.2
37	D	15-17/03/2022	Vredefort	SA21.8	1468	3072	2.16	7669	3439	0.17	19.3
38	D	15-17/03/2022	Vredefort	SA21.2	1253	2541	2.10	8692	4346	0.15	19.9
39	D	15-17/03/2022	Vredefort	SA21.4	1552	3114	2.07	43259	43260	b.d.l.	19.6
40	D	15-17/03/2022	Vredefort	SA21.11	1383	2754	2.06	#####	-39221	b.d.l.	19.3
41	D	15-17/03/2022	Vredefort	SA21.3	1915	3972	2.14	23094	15689	0.06	19.6
42	D	15-17/03/2022	Vredefort	SA21.9	1470	2768	1.95	#####	-9028	b.d.l.	19.9
43	D	15-17/03/2022	Vredefort	SA21.5	1404	2742	2.02	#####	323787	b.d.l.	19.6
44	D	15-17/03/2022	Vredefort	SA21.21	1701	3408	2.07	22204	14802	0.06	19.6
45	D	15-17/03/2022	Vredefort	SA21.6	1786	3201	1.85	11617	5635	0.11	19.8
46	D	15-17/03/2022	Vredefort	SA21.10	1449	2686	1.91	11619	6000	0.11	19.1
47	D	15-17/03/2022	Vredefort	SA21.12	1214	2477	2.11	9579	4790	0.13	19.1
48	P	15-17/03/2022	Vredefort	SA21.7	1689	3937	2.41	5138	5392	b.d.l.	18.6
49	P	15-17/03/2022	Vredefort	SA21.23	1715	3229	1.95	22539	15026	0.06	19.3
50	P	15-17/03/2022	Vredefort	SA21.16	1698	3445	2.10	#####	300909	b.d.l.	19.6
51	P	15-17/03/2022	Vredefort	SA21.22	1614	3051	1.95	#####	#####	b.d.l.	19.3
52	S	15-17/03/2022	Vredefort	SA21.14	1321	2813	2.20	14471	114298	b.d.l.	19.1
53	S	15-17/03/2022	Vredefort	SA21.20	1574	3020	1.98	42633	42633	b.d.l.	18.4
54	S	15-17/03/2022	Vredefort	SA21.13	1365	2765	2.09	#####	288874	b.d.l.	19.3
55	S	15-17/03/2022	Vredefort	SA21.18	1379	2771	2.08	10865	5808	0.12	19.2
56	S	15-17/03/2022	Vredefort	SA21.24	1842	3700	2.08	#####	-53606	b.d.l.	19.2
57	S	15-17/03/2022	Vredefort	SA21.1	1647	3650	2.29	54211	54211	b.d.l.	19.6

a Decay constants of Jaffey et al. (1971) used, $^{238}\text{U}/^{235}\text{U} = 137.818$ (Hiess et al., 2012). b.d.l, below detection; #N/A, not available. Uncertainties quoted without components related to systematic error unless otherwise stated.

Total extra systematic uncertainties: $^{206}\text{Pb}/^{238}\text{U} = 0.11\%$, $^{207}\text{Pb}/^{206}\text{Pb} = 0.14\%$ (2σ).

b I = Magmatic, M = Metamorphic, P = Concordant but with interpreted loss of radiogenic Pb, S = Detrital, D = Discordant or high common-Pb (f206 > 1%), Z = Physical mixture of ages, IMP = Age of impact event

c Concentration uncertainty ~20%.

d Data corrected for common Pb using contemporaneous common Pb compositions from Stacey & Kramers (1975).

e Discordance calculated as $100 * ([^{206}\text{Pb}-^{238}\text{U} \text{ age}-^{207}\text{Pb}-^{206}\text{Pb} \text{ age}]/^{207}\text{Pb}-^{206}\text{Pb} \text{ age})$.

Uncorrected ratios

Spot	$^{206}\text{Pb}/^{238}\text{U}$		$^{238}\text{U}/^{206}\text{Pb}$		$^{207}\text{Pb}/^{206}\text{Pb}$		$^{208}\text{Pb}/^{232}\text{Th}$		$^{208}\text{Pb}/^{206}\text{Pb}$	
	U	± 2 s.e.	± 2 s.e.	± 2 s.e.	Pb	± 2 s.e.	Th	± 2 s.e.	Pb	± 2 s.e.
AR-X03.2	0.04548	0.00235	21.98866	1.13605	0.07039	0.00649	0.01019	0.00063	0.40428	0.01198
AR-X03.5	0.04831	0.00240	20.69890	1.03028	0.07626	0.00652	0.01503	0.00124	0.30571	0.01939
AR-X03.3	0.05231	0.00378	19.11527	1.38152	0.11584	0.01362	0.01278	0.00198	0.55088	0.04979
AR-X02.5	0.04994	0.00259	20.02443	1.03777	0.06939	0.00663	0.01304	0.00114	0.32553	0.02230
AR-X01.3	0.05757	0.00410	17.37093	1.23597	0.06095	0.00390	0.01761	0.00143	0.44798	0.01644
AR-X01.2	0.06191	0.00535	16.15264	1.39695	0.05679	0.00186	0.01850	0.00175	0.43981	0.01591
AR-X02.1	0.06176	0.00269	16.19138	0.70415	0.06360	0.00408	0.01832	0.00147	0.21557	0.01121
AR-X03.4	0.04361	0.00215	22.93054	1.13005	0.05638	0.00556	0.01078	0.00162	0.26378	0.03059
AR-X03.6	0.04638	0.00211	21.56008	0.98110	0.05783	0.00530	0.01379	0.00141	0.24222	0.01670
AR-X03.1	0.04960	0.00603	20.15949	2.44915	0.05855	0.00551	0.01291	0.00179	0.25762	0.01714
AR-X02.2	0.05022	0.00214	19.91179	0.84984	0.06501	0.00516	0.01602	0.00157	0.31179	0.02714
AR-X02.3	0.05279	0.00213	18.94353	0.76531	0.06009	0.00416	0.01571	0.00107	0.22701	0.01202
AR-X01.6	0.05393	0.00232	18.54325	0.79801	0.05791	0.00988	0.01661	0.00120	0.28167	0.01571
AR-X01.1	0.05437	0.00551	18.39380	1.86304	0.05881	0.00872	0.01850	0.00214	0.28049	0.01497
AR-X01.5	0.05674	0.00221	17.62554	0.68679	0.05716	0.00378	0.01854	0.00153	0.46704	0.03343
AR-X02.4	0.06412	0.00311	15.59658	0.75634	0.07094	0.01526	0.02135	0.00428	0.24584	0.04769
AR-X02.6	0.06814	0.00285	14.67672	0.61311	0.05314	0.00686	0.02128	0.00141	0.25063	0.01234
AR-X01.4	0.08432	0.00344	11.85932	0.48398	0.06201	0.00725	0.02624	0.00165	0.27588	0.01111
SF-X5-1	0.29868	0.00874	3.34808	0.09799	0.08942	0.00168	0.08755	0.00637	0.11149	0.00267
SF-X5-2	0.30540	0.05236	3.27443	0.56138	0.08849	0.00557	0.08168	0.01472	0.12267	0.00350
SF-X3	0.27774	0.07880	3.60048	1.02155	0.08895	0.00217	0.07158	0.02171	0.08764	0.00329
SF-X4	0.25618	0.03339	3.90358	0.50876	0.09121	0.00138	0.07114	0.01424	0.16041	0.02434
SF-X5-3	0.24757	0.07634	4.03934	1.24556	0.09245	0.00742	0.05869	0.01812	0.15764	0.00192
SA21.17	0.48189	0.03193	2.07516	0.13748	0.19051	0.00393	0.13309	0.01201	0.56363	0.03044
SA21.15	0.51459	0.03199	1.94329	0.12081	0.19773	0.00406	0.14265	0.01010	0.56804	0.01111
SA21.19	0.50785	0.03392	1.96907	0.13150	0.22319	0.00464	0.15340	0.01331	0.66692	0.03581
SA21.8	0.47827	0.03037	2.09087	0.13277	0.20064	0.00401	0.13938	0.00997	0.63002	0.01165
SA21.2	0.49531	0.03210	2.01895	0.13086	0.20277	0.00904	0.13689	0.01181	0.57908	0.01159
SA21.4	0.51469	0.03277	1.94291	0.12369	0.20427	0.00386	0.13871	0.00969	0.55884	0.00502
SA21.11	0.49092	0.03201	2.03699	0.13281	0.20561	0.00408	0.14204	0.01124	0.59537	0.02066
SA21.3	0.52704	0.03161	1.89739	0.11379	0.20747	0.00854	0.14460	0.00981	0.58800	0.01026
SA21.9	0.52104	0.03371	1.91924	0.12417	0.20685	0.00409	0.14649	0.01076	0.54707	0.01074
SA21.5	0.51914	0.03253	1.92628	0.12071	0.20923	0.00404	0.14343	0.01017	0.55748	0.01046
SA21.21	0.49366	0.03201	2.02569	0.13135	0.21063	0.01060	0.13489	0.01193	0.56589	0.03008
SA21.6	0.53378	0.03131	1.87345	0.10990	0.21158	0.00372	0.15451	0.01317	0.53599	0.00955
SA21.10	0.51837	0.03276	1.92911	0.12190	0.21478	0.00222	0.14403	0.01038	0.53206	0.01033
SA21.12	0.57601	0.01826	1.73608	0.05503	0.22508	0.00427	0.16930	0.01213	0.61966	0.02429
SA21.7	0.46474	0.04935	2.15172	0.22851	0.18209	0.00375	0.12847	0.01430	0.66571	0.01220
SA21.23	0.53869	0.03138	1.85636	0.10813	0.20110	0.00362	0.14612	0.00971	0.52781	0.00943
SA21.16	0.50874	0.05605	1.96564	0.21658	0.20200	0.00401	0.14633	0.01721	0.60293	0.01871
SA21.22	0.51448	0.05674	1.94371	0.21438	0.20802	0.00387	0.14506	0.01676	0.55098	0.01035
SA21.14	0.52343	0.05439	1.91046	0.19853	0.20148	0.02940	0.15122	0.01634	0.63590	0.00590
SA21.20	0.53363	0.03507	1.87397	0.12314	0.21016	0.00964	0.15279	0.01266	0.56771	0.02360
SA21.13	0.54669	0.03565	1.82920	0.11927	0.21298	0.00428	0.14977	0.01107	0.57355	0.01137
SA21.18	0.52277	0.07104	1.91290	0.25996	0.21436	0.00422	0.14691	0.02046	0.58370	0.00546
SA21.24	0.57664	0.03511	1.73419	0.10559	0.21563	0.00370	0.14949	0.01030	0.53825	0.00954
SA21.1	0.56182	0.03255	1.77994	0.10313	0.21758	0.00625	0.15532	0.01260	0.63330	0.02285

²⁰⁴Pb-corrected ratios (not matrix-corrected)^d

Spot	²⁰⁶ Pb*/ ²³⁸ U		²³⁸ U/ ²⁰⁶ Pb		²⁰⁷ Pb*/ ²⁰⁶ Pb		²⁰⁸ Pb*/ ²³² Th		²⁰⁸ Pb*/ ²⁰⁶ Pb	
	⁸ U	± 2 s.e.	*	± 2 s.e.	Pb*	± 2 s.e.	Th	± 2 s.e.	Pb*	± 2 s.e.
AR-X03.2	0.04515	0.00235	22.14594	1.15147	0.06468	0.00805	0.00982	0.00068	0.39212	0.01567
AR-X03.5	0.04816	0.00240	20.76578	1.03650	0.07370	0.00718	0.01470	0.00127	0.29990	0.02058
AR-X03.3	0.05128	0.00380	19.50231	1.44659	0.10059	0.01891	0.01181	0.00200	0.51944	0.05727
AR-X02.5	0.04968	0.00259	20.12804	1.04832	0.06525	0.00786	0.01261	0.00119	0.31633	0.02425
AR-X01.3	0.05777	0.00411	17.31038	1.23250	0.06377	0.00443	0.01790	0.00147	0.45376	0.01695
AR-X01.2	0.06188	0.00535	16.16007	1.39768	0.05642	0.00201	0.01846	0.00175	0.43905	0.01599
AR-X02.1	0.06149	0.00268	16.26227	0.70882	0.06008	0.00473	0.01754	0.00150	0.20731	0.01255
AR-X03.4	0.04351	0.00215	22.98212	1.13495	0.05455	0.00614	0.01059	0.00161	0.25964	0.03122
AR-X03.6	0.04621	0.00211	21.63927	0.98791	0.05485	0.00610	0.01335	0.00144	0.23538	0.01811
AR-X03.1	0.04951	0.00602	20.19888	2.45457	0.05696	0.00596	0.01270	0.00179	0.25401	0.01792
AR-X02.2	0.04916	0.00213	20.34278	0.88351	0.04760	0.00845	0.01373	0.00159	0.27301	0.03139
AR-X02.3	0.05247	0.00213	19.05870	0.77313	0.05517	0.00514	0.01483	0.00114	0.21561	0.01394
AR-X01.6	0.05376	0.00232	18.60189	0.80226	0.05534	0.01018	0.01622	0.00122	0.27591	0.01658
AR-X01.1	0.05414	0.00549	18.47204	1.87190	0.05537	0.00914	0.01792	0.00211	0.27274	0.01615
AR-X01.5	0.05668	0.00221	17.64208	0.68783	0.05640	0.00394	0.01847	0.00152	0.46551	0.03353
AR-X02.4	0.06313	0.00322	15.84013	0.80757	0.05848	0.02007	0.01854	0.00467	0.21684	0.05681
AR-X02.6	0.06799	0.00284	14.70856	0.61527	0.05137	0.00710	0.02090	0.00144	0.24662	0.01301
AR-X01.4	0.08429	0.00344	11.86367	0.48424	0.06172	0.00728	0.02617	0.00165	0.27521	0.01119
SF-X5-1	0.29864	0.00874	3.34847	0.09800	0.08933	0.00169	0.08736	0.00636	0.11126	0.00269
SF-X5-2	0.30537	0.05235	3.27473	0.56143	0.08842	0.00558	0.08155	0.01470	0.12249	0.00352
SF-X3	0.27777	0.07881	3.60013	1.02145	0.08902	0.00217	0.07175	0.02177	0.08784	0.00331
SF-X4	0.25612	0.03338	3.90445	0.50888	0.09104	0.00140	0.07093	0.01420	0.15997	0.02435
SF-X5-3	0.24757	0.07634	4.03934	1.24556	0.09245	0.00742	0.05869	0.01812	0.15764	0.00192
SA21.17	0.48202	0.03193	2.07460	0.13744	0.19070	0.00393	0.13323	0.01202	0.56405	0.03044
SA21.15	0.51503	0.03202	1.94163	0.12071	0.19831	0.00408	0.14310	0.01014	0.56936	0.01115
SA21.19	0.48949	0.03308	2.04295	0.13807	0.19875	0.00850	0.13585	0.01274	0.61278	0.04026
SA21.8	0.47716	0.03030	2.09574	0.13310	0.19907	0.00409	0.13829	0.00991	0.62657	0.01178
SA21.2	0.49429	0.03204	2.02309	0.13114	0.20139	0.00908	0.13586	0.01173	0.57593	0.01172
SA21.4	0.51448	0.03275	1.94371	0.12374	0.20399	0.00387	0.13849	0.00968	0.55820	0.00506
SA21.11	0.49114	0.03202	2.03607	0.13275	0.20592	0.00409	0.14227	0.01126	0.59605	0.02066
SA21.3	0.52663	0.03158	1.89886	0.11388	0.20695	0.00856	0.14419	0.00979	0.58683	0.01030
SA21.9	0.52166	0.03375	1.91696	0.12403	0.20765	0.00411	0.14716	0.01082	0.54893	0.01079
SA21.5	0.51908	0.03253	1.92649	0.12072	0.20916	0.00404	0.14337	0.01017	0.55731	0.01047
SA21.21	0.49326	0.03198	2.02732	0.13146	0.21009	0.01061	0.13449	0.01189	0.56465	0.03012
SA21.6	0.53296	0.03127	1.87633	0.11008	0.21056	0.00375	0.15358	0.01310	0.53358	0.00964
SA21.10	0.51758	0.03271	1.93207	0.12209	0.21376	0.00229	0.14316	0.01032	0.52964	0.01042
SA21.12	0.57494	0.01823	1.73931	0.05515	0.22387	0.00432	0.16823	0.01207	0.61688	0.02438
SA21.7	0.46313	0.04921	2.15921	0.22944	0.17968	0.00454	0.12705	0.01422	0.66069	0.01333
SA21.23	0.53826	0.03135	1.85783	0.10822	0.20057	0.00364	0.14566	0.00969	0.52656	0.00947
SA21.16	0.50868	0.05605	1.96587	0.21660	0.20192	0.00401	0.14626	0.01720	0.60275	0.01871
SA21.22	0.51458	0.05675	1.94333	0.21433	0.20815	0.00388	0.14517	0.01678	0.55129	0.01035
SA21.14	0.52279	0.05456	1.91282	0.19964	0.20065	0.03016	0.15060	0.01699	0.63408	0.01553
SA21.20	0.53340	0.03505	1.87475	0.12319	0.20989	0.00965	0.15255	0.01264	0.56706	0.02362
SA21.13	0.54662	0.03564	1.82943	0.11928	0.21290	0.00429	0.14970	0.01106	0.57336	0.01138
SA21.18	0.52191	0.07093	1.91604	0.26040	0.21328	0.00427	0.14604	0.02034	0.58120	0.00563
SA21.24	0.57683	0.03512	1.73362	0.10556	0.21584	0.00370	0.14969	0.01031	0.53877	0.00956
SA21.1	0.56163	0.03254	1.78053	0.10317	0.21736	0.00626	0.15515	0.01259	0.63282	0.02286

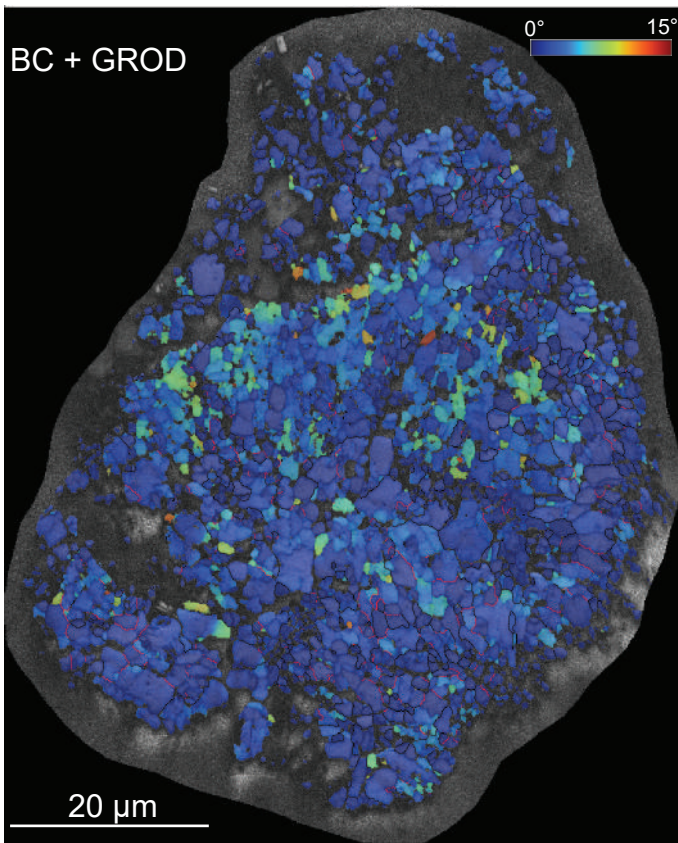
²⁰⁴Pb-corrected, matrix-corrected ratios^d

Spot	^{(238U/206Pb*)_m}		^{(207Pb*/206Pb*)_m}		^{(206Pb*/238U)_m}		^{(207Pb*/235U)_m}		^{(208Pb*/232Th)_m}	
	± 2 s.e.		± 2 s.e.		± 2 s.e.		± 2 s.e.		± 2 s.e.	
AR-X03.2	24.68074	1.66143	0.06468	0.00805	0.04052	0.00273	0.36116	0.05109	#N/A	#N/A
AR-X03.5	22.36557	1.40492	0.07370	0.00718	0.04471	0.00281	0.45413	0.05266	#N/A	#N/A
AR-X03.3	22.37416	2.11984	0.10059	0.01891	0.04469	0.00423	0.61960	0.13045	#N/A	#N/A
AR-X02.5	22.02111	1.45737	0.06525	0.00786	0.04541	0.00301	0.40838	0.05611	#N/A	#N/A
AR-X01.3	19.20134	1.69558	0.06377	0.00443	0.05208	0.00460	0.45771	0.05142	#N/A	#N/A
AR-X01.2	18.05340	1.91396	0.05642	0.00201	0.05539	0.00587	0.43068	0.04817	#N/A	#N/A
AR-X02.1	17.06135	0.93070	0.06008	0.00473	0.05861	0.00320	0.48529	0.04646	#N/A	#N/A
AR-X03.4	25.58971	1.64670	0.05455	0.00614	0.03908	0.00251	0.29381	0.03810	#N/A	#N/A
AR-X03.6	23.99637	1.43861	0.05485	0.00610	0.04167	0.00250	0.31504	0.03980	#N/A	#N/A
AR-X03.1	21.66397	3.01894	0.05696	0.00596	0.04616	0.00643	0.36238	0.06314	#N/A	#N/A
AR-X02.2	21.91018	1.22334	0.04760	0.00845	0.04564	0.00255	0.29942	0.05572	#N/A	#N/A
AR-X02.3	20.68957	1.09997	0.05517	0.00514	0.04833	0.00257	0.36752	0.03941	#N/A	#N/A
AR-X01.6	20.11042	1.12048	0.05534	0.01018	0.04973	0.00277	0.37927	0.07287	#N/A	#N/A
AR-X01.1	20.07831	2.39512	0.05537	0.00914	0.04980	0.00594	0.38005	0.07742	#N/A	#N/A
AR-X01.5	19.93420	1.06757	0.05640	0.00394	0.05017	0.00269	0.38992	0.03431	#N/A	#N/A
AR-X02.4	16.84912	1.06443	0.05848	0.02007	0.05935	0.00375	0.47835	0.16694	#N/A	#N/A
AR-X02.6	15.74079	0.84631	0.05137	0.00710	0.06353	0.00342	0.44977	0.06668	#N/A	#N/A
AR-X01.4	12.98176	0.69926	0.06172	0.00728	0.07703	0.00415	0.65521	0.08494	#N/A	#N/A
SF-X5-1	3.85350	0.16709	0.08933	0.00169	0.25950	0.01125	3.19467	0.15110	#N/A	#N/A
SF-X5-2	3.59455	0.70963	0.08842	0.00558	0.27820	0.05492	3.39004	0.70257	#N/A	#N/A
SF-X3	3.88719	1.22613	0.08902	0.00217	0.25726	0.08115	3.15617	0.99852	#N/A	#N/A
SF-X4	4.23618	0.63767	0.09104	0.00140	0.23606	0.03553	2.96173	0.44814	#N/A	#N/A
SF-X5-3	4.63713	1.68627	0.09245	0.00742	0.21565	0.07842	2.74778	1.02323	#N/A	#N/A
SA21.17	2.15712	0.16745	0.19070	0.00393	0.46358	0.03599	12.18360	0.97860	#N/A	#N/A
SA21.15	2.02645	0.14927	0.19831	0.00408	0.49347	0.03635	13.48708	1.03153	#N/A	#N/A
SA21.19	2.12106	0.16735	0.19875	0.00850	0.47146	0.03720	12.91419	1.15895	#N/A	#N/A
SA21.8	2.17691	0.16262	0.19907	0.00409	0.45937	0.03432	12.60290	0.97634	#N/A	#N/A
SA21.2	2.10418	0.16027	0.20139	0.00908	0.47524	0.03620	13.19039	1.16760	#N/A	#N/A
SA21.4	2.02541	0.15211	0.20399	0.00387	0.49373	0.03708	13.88045	1.07524	#N/A	#N/A
SA21.11	2.11159	0.16120	0.20592	0.00409	0.47358	0.03615	13.43964	1.06007	#N/A	#N/A
SA21.3	1.98892	0.14246	0.20695	0.00856	0.50278	0.03601	14.34035	1.18601	#N/A	#N/A
SA21.9	1.99836	0.15231	0.20765	0.00411	0.50041	0.03814	14.32054	1.12765	#N/A	#N/A
SA21.5	2.00211	0.14788	0.20916	0.00404	0.49947	0.03689	14.39768	1.09918	#N/A	#N/A
SA21.21	2.11564	0.16173	0.21009	0.01061	0.47267	0.03613	13.68603	1.25405	#N/A	#N/A
SA21.6	1.96111	0.13748	0.21056	0.00375	0.50991	0.03575	14.79734	1.07040	#N/A	#N/A
SA21.10	2.00088	0.14837	0.21376	0.00229	0.49978	0.03706	14.72370	1.10311	#N/A	#N/A
SA21.12	1.79750	0.07452	0.22387	0.00432	0.55633	0.02307	17.16487	0.78485	#N/A	#N/A
SA21.7	2.24135	0.26679	0.17968	0.00454	0.44616	0.05311	11.04827	1.34436	#N/A	#N/A
SA21.23	1.93471	0.13430	0.20057	0.00364	0.51687	0.03588	14.28749	1.02508	#N/A	#N/A
SA21.16	2.05245	0.25412	0.20192	0.00401	0.48722	0.06032	13.55846	1.70021	#N/A	#N/A
SA21.22	2.02117	0.24952	0.20815	0.00388	0.49476	0.06108	14.19324	1.77205	#N/A	#N/A
SA21.14	1.98030	0.23122	0.20065	0.03016	0.50497	0.05896	13.96397	2.65775	#N/A	#N/A
SA21.20	1.93593	0.14818	0.20989	0.00965	0.51655	0.03954	14.94175	1.33411	#N/A	#N/A
SA21.13	1.89704	0.14480	0.21290	0.00429	0.52714	0.04024	15.46723	1.22101	#N/A	#N/A
SA21.18	1.98621	0.29713	0.21328	0.00427	0.50347	0.07532	14.79876	2.23356	#N/A	#N/A
SA21.24	1.80869	0.13076	0.21584	0.00370	0.55289	0.03997	16.44687	1.22210	#N/A	#N/A
SA21.1	1.85969	0.12888	0.21736	0.00626	0.53773	0.03726	16.10848	1.20880	#N/A	#N/A

²⁰⁴Pb-corrected, matrix-corrected dates^d							Disc. (%)^e
Spot	(²⁰⁶Pb*/²³⁸U)_m Age (Ma)	± 2 s.e.	(²⁰⁷Pb*/²⁰⁶Pb*) _m Age (Ma)	± 2 s.e.	(²⁰⁷Pb*/²³⁵U)_m Age (Ma)	± 2 s.e.	
AR-X03.2	256	17	763	262	313	38	66.4
AR-X03.5	282	17	1032	197	380	37	72.7
AR-X03.3	282	26	1634	349	490	82	82.8
AR-X02.5	286	19	782	253	348	40	63.4
AR-X01.3	327	28	733	147	383	36	55.4
AR-X01.2	348	36	468	79	364	34	25.7
AR-X02.1	367	19	605	170	402	32	39.3
AR-X03.4	247	16	393	253	262	30	37.1
AR-X03.6	263	15	405	249	278	31	35.1
AR-X03.1	291	40	489	231	314	47	40.5
AR-X02.2	288	16	78	422	266	44	-266.8
AR-X02.3	304	16	418	208	318	29	27.2
AR-X01.6	313	17	425	410	327	54	26.4
AR-X01.1	313	36	426	368	327	57	26.5
AR-X01.5	316	16	467	155	334	25	32.4
AR-X02.4	372	23	547	750	397	115	32.0
AR-X02.6	397	21	256	318	377	47	-54.8
AR-X01.4	478	25	663	253	512	52	27.9
SF-X5-1	1487	58	1410	36	1456	37	-5.5
SF-X5-2	1582	277	1391	121	1502	164	-13.8
SF-X3	1476	417	1404	47	1447	249	-5.1
SF-X4	1366	185	1446	29	1398	115	5.6
SF-X5-3	1259	416	1476	152	1341	284	14.7
SA21.17	2455	159	2747	34	2619	76	10.6
SA21.15	2586	157	2812	34	2714	72	8.0
SA21.19	2490	163	2815	70	2673	85	11.6
SA21.8	2437	152	2818	34	2650	73	13.5
SA21.2	2507	158	2837	74	2693	84	11.6
SA21.4	2587	160	2858	31	2742	73	9.5
SA21.11	2499	158	2873	32	2711	75	13.0
SA21.3	2626	155	2881	67	2772	79	8.9
SA21.9	2616	164	2887	32	2771	75	9.4
SA21.5	2612	159	2898	31	2776	73	9.9
SA21.21	2495	158	2906	82	2728	87	14.1
SA21.6	2656	153	2909	29	2802	69	8.7
SA21.10	2613	159	2934	17	2798	71	10.9
SA21.12	2851	96	3008	31	2944	44	5.2
SA21.7	2378	237	2649	42	2527	114	10.2
SA21.23	2686	153	2830	30	2769	68	5.1
SA21.16	2559	262	2841	32	2719	119	9.9
SA21.22	2591	264	2890	30	2763	119	10.4
SA21.14	2635	253	2831	245	2747	182	6.9
SA21.20	2685	168	2904	75	2812	85	7.6
SA21.13	2729	170	2927	33	2844	75	6.8
SA21.18	2629	323	2930	32	2802	145	10.3
SA21.24	2837	166	2949	28	2903	71	3.8
SA21.1	2774	156	2961	46	2883	72	6.3

Appendix 5.3

GROD angle map of grain X3 (Araguainha)

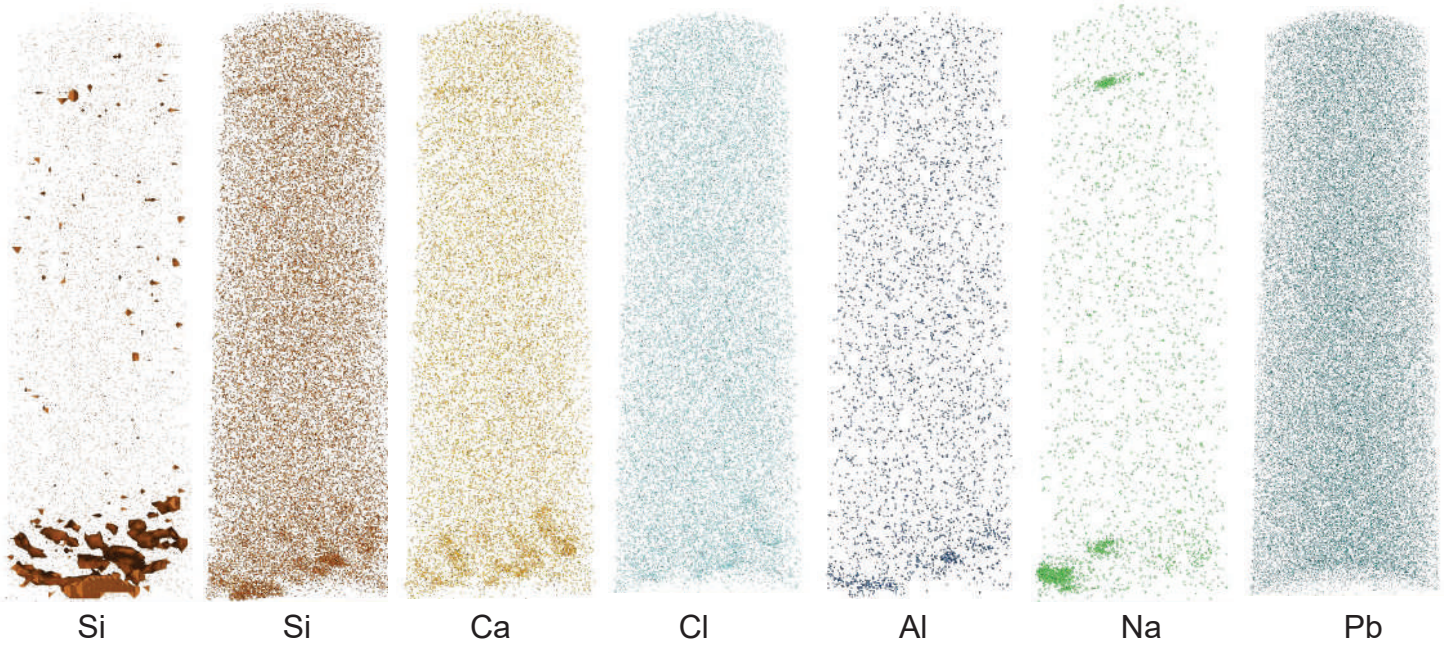


Appendix 5.4

APT 3d reconstructions of specimens from Vredefort

100 nm

V5



Si

Si

Ca

Cl

Al

Na

Pb

V3



Ca

Pb

Si

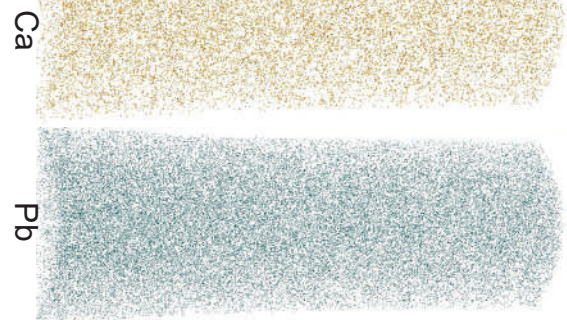
V9-Twin



Ca

Pb

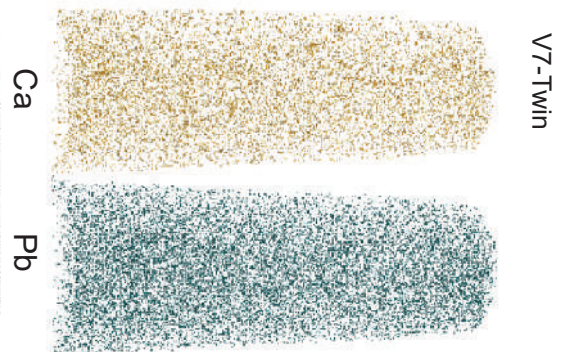
V2



Ca

Pb

V7-Twin



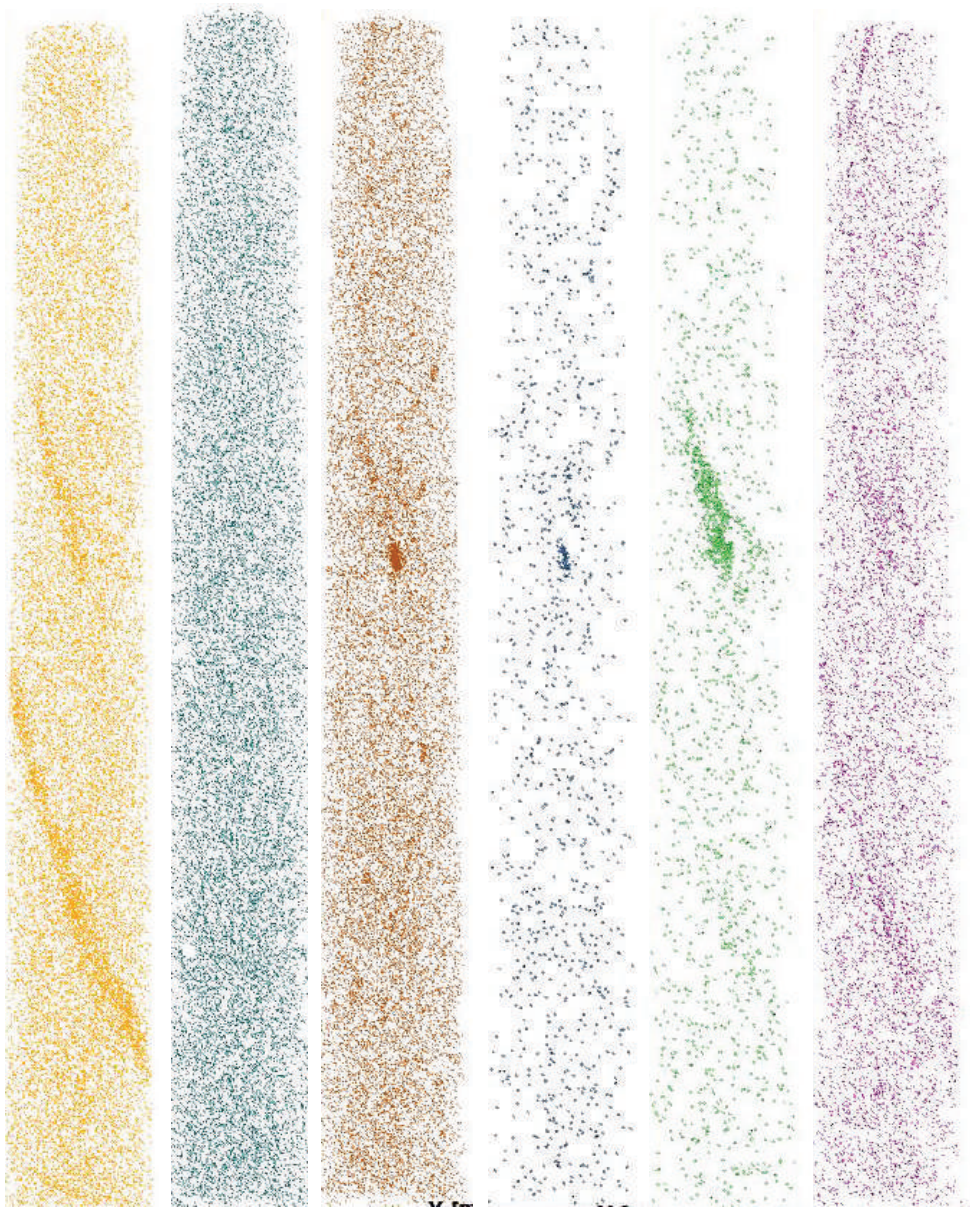
Ca

Pb

Appendix 5.4

APT 3d reconstructions of specimens from Araguainha

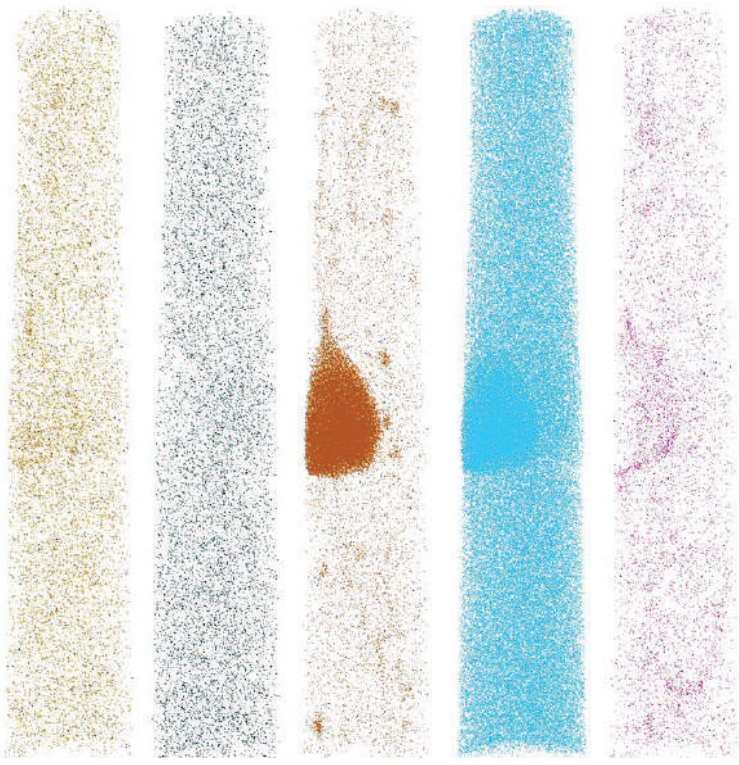
M5



100 nm

Ca Pb Si Al Na Mg

M2



Ca Pb Si O Mg

Appendix 5.5

APT nanogeochronology results

Impact structure	Needle	Feature	U-Pb age (Ma,2 σ)		Pb-Pb age (Ma,2 σ)	
			Whole needle	Matrix	Whole needle	Matrix
Vredefort	V7	twin <3-40>/70°	1319±322		1967±2769	
	V9	twin <3-41>/70°	1688±223	1665±222	2333±975	2186±1092
	V1	Host	1579±187	1539±184	3005±547	2859±618
	V2		1450±187		2647±780	
	V3		1633±251		2591±968	
	V4	Neoblast	1749±286	1611±276	3101±674	2519±1088
	V5	Host	1684±200		2411±777	
Santa Fe	M1	Host	1275±69			
	M2	Twin-grain boundary	1319±45			
	M3	Twin	1391±83	1329±81	1495±549	
	M4	Twin	1274±100	1213±98	1876±574	